Quasicrystals in two-dimensional ternary oxides

Habilitationsschrift

zur Erlangung des akademischen Grades

Doctor rerum naturalium habilitatus
(Dr. rer. nat. habil.)

vorgelegt von

Herrn Dr. rer. nat. Stefan Förster

der

Naturwissenschaftlichen Fakultät II - Chemie, Physik und Mathematik

Martin-Luther-Universität Halle-Wittenberg

Gutachter:

1. Prof. Dr. Wolf Widdra
   Martin-Luther-Universität Halle-Wittenberg

2. Prof. Dr. Ulrike Diebold
   Technische Universität Wien

3. Prof. Dr. Emilie Gaudry
   Université de Lorraine

Halle (Saale), verteidigt am 11.05.2023,

Probevorlesung gehalten am 27.06.2023

Contents

1 Introduction

The discovery of two-dimensional dodecagonal quasicrystals in oxides opened a new chapter in both, quasicrystal research and 2D materials sciences [1, 2]. Quasicrystals are long-range aperiodically ordered materials. Initially discovered in intermetallic alloys, quasicrystals extended the notion of a crystal by possessing 5-, 8-, 10- or 12-fold symmetries [3–7]. These kinds of symmetries are incompatible with tiling the two-dimensional plane with regular polygons or the three-dimensional space with regular polyhedra while obeying translational invariance. However by following aperiodic functions, the tilings of quasicrystals are well-determined which gives rise to diffraction pattern that are equally sharp as observed for periodic crystals.

Dodecagonal quasicrystals have been discovered for a multitude of materials systems [5, 8–14]. Characteristic to these quasicrystals is an aperiodic ordering in the plane that is periodically repeated in the perpendicular direction. This columnar nature allowed to gain insights to the quasicrystalline structure using atomic force microscopy and transmission electron microscopy [7, 10, 15]. The study of solely 2D dodecagonal quasicrystalline systems was enabled by their discovery in colloidal suspensions [16]. Together with the possibility to imprint aperiodic order into these suspensions by exposing them to laser interference patterns [17, 18], colloidal systems became a micro scale playground for studying the formation mechanism of quasicrystals and their properties in two dimensions [19–24]. In general, dodecagonal two-dimensional quasicrystals are stabilized by the competition of two length scales, which results in the formation of square-triangle tilings [25, 26].

Oxide quasicrystals (OQCs) are different: They represent the first 2D material that is aperiodically ordered on the atomic level. Furthermore, they are the first natural system exhibiting a dodecagonal tiling made from three tiling elements: equilateral triangles, squares and rhombuses. This habilitation thesis focusses on the prototypical OQC formed in Ba-Ti-O on Pt(111) [1]. Subjects of interest are the growth and structural properties of this OQC, its atomic and electronic structure, and its use as the template for molecular adsorption. Going beyond this particular materials system, also Sr-Ti-O layers and Pd(111) and Ru(0001) substrates have been investigated and a wealth of periodic oxide quasicrystal approximants have been explored.

2 Quasicrystals

The discovery of quasicrystals goes back to the first observation of a diffraction pattern of icosahedral symmetry in a Pd-Mn alloy [3]. The discretness of the diffraction spots of this compound showed that a long-range ordered phase must be present. This observation was astonishing because icosahedral space group symmetry is incompatible with lattice periodicity, a precondition for the definition of crystals at that time.

In crystallography, aperiodic structures in the form of incommensurately modulated phases had been known already. In 1972 de Wolff was the first to use the projection from a four-dimensional periodic lattice to describe the aperiodic structure in three dimensions [27]. Soon thereafter many incommensurately modulated phases have been discovered and the superspace-formalism has been generalized by Janner and Jannsen [28, 29], which defines space groups in higher dimensions.

In the same issue as where Shechtman's discovery appeared, computer simulations were reported by Levine and Steinhard that found a quasiperiodic orientational ordering in three dimensional structures and the term quasicrystal was coined [4]. The major difference between incommensurately modulated crystals and quasicrystals is that there is no periodic average structure for quasicrystals. The reader interested in a comprehensive mathematical introduction into aperiodic crystals is referred to the book by Jannsen, Chapius and deBoissieu [30].

2.1 The 1D Fibonacci chain

A simple and very illustrative model for a quasicrystal is the one dimensional Fibonacci chain. The Fibonacci chain is a sequence of long and short distances $\mathcal{L}$ and $\mathcal{S}$. It can be formed from a recursion rule in which $\mathcal{L}$ is substituted by $\mathcal{LS}$ and $\mathcal{S}$ by $\mathcal{L}$. One of the interesting properties of the Fibonacci chain is the frequency ratio for the elements $\mathcal{L}$ and $\mathcal{S}$ of $\tau : 1$, with τ being the golden mean. The golden mean is the positive root solving (2.1):

$$x^2 - x - 1 = 0, \quad x = (1 + \sqrt{5})/2 = 1.618... \tag{2.1}$$

It is the smallest of the Pisot-Vijayaraghavan (PV) numbers and the scaling factor for self-similarity in the Fibonacci chain, a property that applies also to icosahedral quasi-
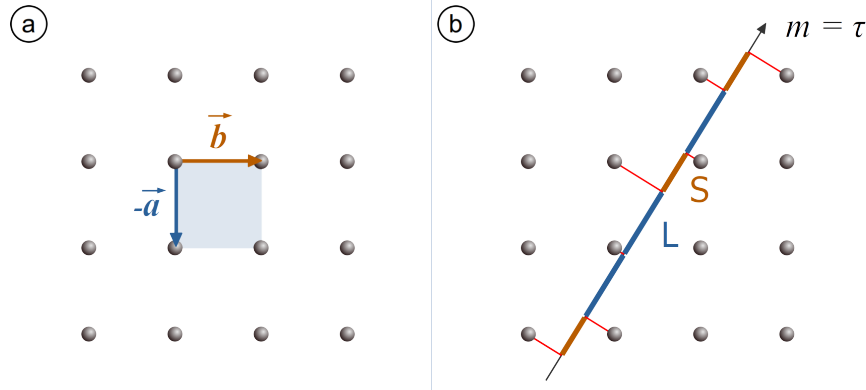
Figure 2.1: The projection of the nearby 2D lattice points onto a line with slope m results in a sequence of long and short distances $\mathcal{L}$ and $\mathcal{S}$.

crystals in three dimensions. An alternative way to construct the Fibonacci chain is by defining it as a series of elements $\mathcal{F}$ in which any new element is the sum of the two previous ones starting from $\mathcal{F}_0 = L$ and $\mathcal{F}_1 = S$ according to equation (2.2).

$$\mathcal{F}_{n+1} = \mathcal{F}_n + \mathcal{F}_{n-1} \tag{2.2}$$

Following this rule the Fibonacci chain rapidly grows.

$$
\begin{aligned}
\mathcal{L} + \mathcal{S} &= \mathcal{LS} \\
\mathcal{LS} + \mathcal{L} &= \mathcal{LSL} \\
\mathcal{LSL} + \mathcal{LS} &= \mathcal{LSLLS} \\
\mathcal{LSLLS} + \mathcal{LSL} &= \mathcal{LSLLSLSL}
\end{aligned}
\tag{2.3}
$$

The long and short distances in the Fibonacci chain can also be interpreted as the two tiles of this 1D QC. To derive the Fibonacci chain from higher dimensions, we consider a 2D square lattice as shown in Fig. 2.1(a). This lattice is spanned by the two linearly independent vectors $\vec{a}$ and $\vec{b}$. By cutting this lattice along a line of slope m and projecting the nearby lattice points onto that line as illustrated in Fig. 2.1(b), one dimensional structures are obtained that will consist of two segments of different length for all slopes $|m| \neq 1$. In the example given in Fig. 2.1(b), the projection of $\vec{a}$ results in $\mathcal{L}$ segments and the projection of $\vec{b}$ in $\mathcal{S}$ segments. Since the slope can be expressed by $\Delta a / \Delta b$ it immediately reflects the tiling element ratio of $\mathcal{L}$ and $\mathcal{S}$. This means the Fibonacci chain is obtained for the irrational slope $m = \tau$. More general, cutting at any irrational slope results in the formation of quasicrystals, while cutting at rational slopes results in periodic structures.

The direction parallel to the cut, in which the one-dimensional structure is obtained, is called the *physical space* (often also referred to as *parallel space*). What is meant above by *"the nearby lattice points"*, needs to be defined more precisely. Therefore, the direction perpendicular to the cut becomes relevant, which is called the *internal space* (or
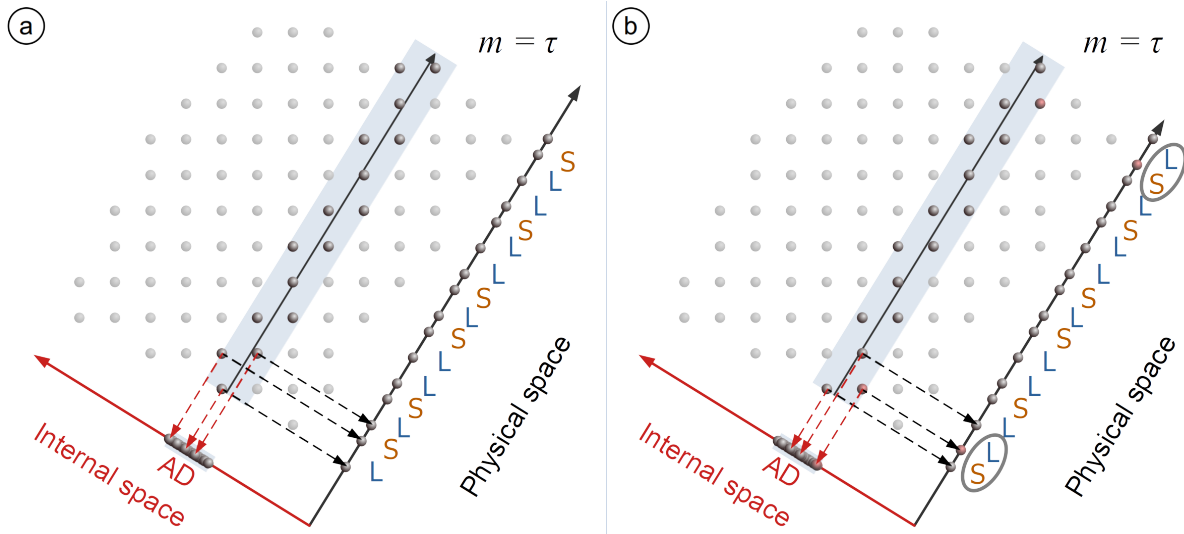
Figure 2.2: (a) Strip-projection method for constructing the Fibonacci chain from a 2D square lattice. The width of the strip is given from the projection of the square unit cell into the internal space called acceptance domain (AD). While the Fibonacci chain is infinitely long in the physical space, all atoms in the strip are confined in the internal space to the AD, which is densely filled. (b) Shifting the strip along the internal space selects different sets of 2D lattice points, which causes flips of elements $\mathcal{L}$ and $\mathcal{S}$ in the physical space (gray circles).

perpendicular space). The interval for the selection of lattice points is given by the projection of the unit cell of the higher-dimensional lattice into the internal space. This footprint of the higher-dimensional unit cell in the internal space of a quasicrystal is called its *acceptance domain*(*AD*). The latter is also often called *occupational domain* or *window*.

Upon introducing these important terms we can derive the Fibonacci chain from the higher-dimensional lattice using the strip-projection method illustrated in Figure 2.2(a). The Fibonacci chain evolves by projecting all atoms within a wide strip that cuts a 2D square lattice at a slope $m = \tau$ into the physical space. The internal space width of the strip is given by the AD. The resulting chain is gap-less tiling the physical space with $\mathcal{L}$ and $\mathcal{S}$ line segments, the quasicrystal tiling. Projecting all lattice points within the strip into the internal space results in constant atomic density for all points inside the acceptance domain and 0 elsewhere. In other words, the there is no overlap of the atomic positions of the quasicrystal in the acceptance domain but an infinitely dense filling.

For the physical space, lattice excitations are known that cause displacements from the ideal atomic position, called phonons. For quasicrystals also excitations in the internal space can occur upon displacements of the acceptance domain. In Fig. 2.2(b) the strip-projection for the generation of the Fibonacci chain is performed again, but this time the strip has been slightly displaced to the right. As a consequence, some atoms dropped out of the strip and new atoms entered (marked red). Upon project-
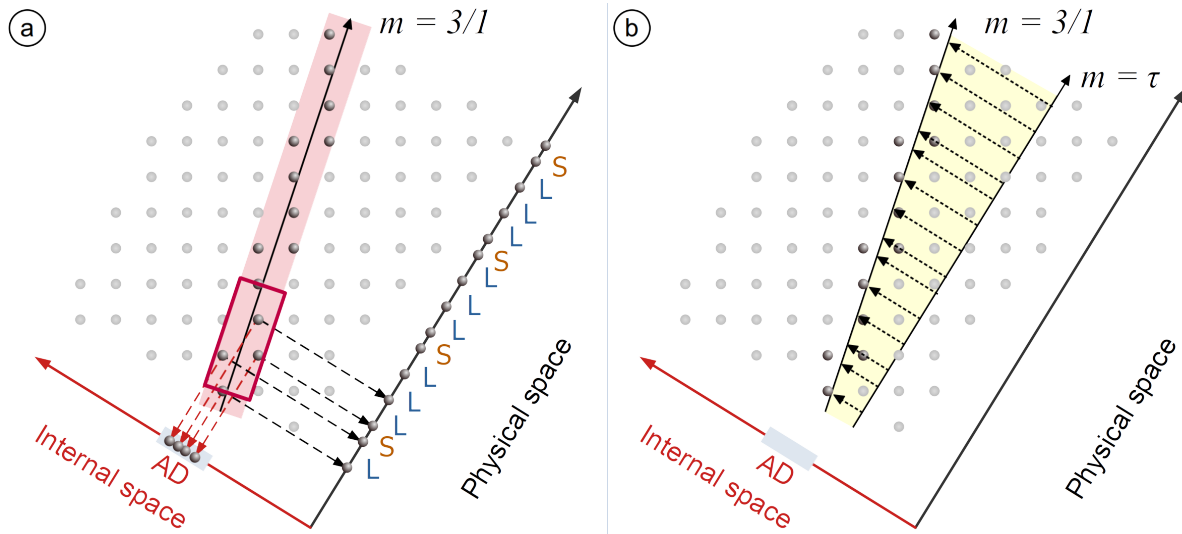
Figure 2.3: (a) Construction of a 3/1 approximant using the strip projection method. (b) The slope of the approximant is derived from that of the quasicrystal by a phason shift that linearly changes along the physical space axis emphasized by the shaded area.

ing the atoms in the strip into the physical space, the sequence of elements $\mathcal{L}$ and $\mathcal{S}$ is flipped at two positions as compared to Fig. 2.2(a) (gray circles). Upon flipping, the global tiling statistics is still obeyed since there was no change of the slope of the strip. Hence, we generate the Fibonacci chain, but the part we observe was at a different position in the infinite chain formed in (a). We could denote this as a phase shift, which is why excitations in the internal space are called phasons. More precisely, the given example is results from a constant phase shift. The swapping of tiling elements observed in physical space is called phason flips.

Finally, the implications to the internal and the physical space representation when cutting at a rational slope must be discussed. Figure 2.3(a) depicts the strip-projection at a slope of $m = 3$. The width of the strip is again given by the projection of the higher-dimensional unit cell to the direction perpendicular to the cut, which means for the given example it is reduced in comparison to the one used for the Fibonacci chain. The rational slope means that a staircase is formed in which for every three steps along $\vec{a}$ one step in $\vec{b}$ must be made. For the projection into the physical space of the quasicrystal this implies the formation of a periodic structure with four elements in the unit cell: $3 \times \mathcal{L}$ & $1 \times \mathcal{S}$. Upon projecting the atoms inside the strip into the internal space of the quasicrystal we also obtain a periodic structure, which exhibits the opposite ratio of long and short distances as compared to the physical space. In the internal space the atomic positions are not restricted to the acceptance domain any more but spread to infinity similar as found for the physical space. This implies that the analysis of the projected atomic positions into the internal space is the ideal tool to distinguish periodic from quasicrystalline structures [15].

As demonstrated above, the quasiperiodic tiling can be approximated by cutting at a rational slope, which is why these periodic structures are called approximants. The closer the rational slope approaches the irrational slope creating the quasicrystal, the larger the size of the unit cell will be and the closer the tiling statistics matches that of the quasicrystal. Starting from the cut through the higher-dimensional lattice at a slope of τ, the rational slope of the approximant is reached by applying a phase shift that linearly changes with the physical space as illustrated by the shaded area in Fig. 2.3(b). Mathematically, this corresponds to a shear deformation denoted as *linear phason strain*, which transforms the coordinate system of the quasicrystal into that of a given approximant [31].

2.2   Two-dimensional dodecagonal quasicrystals

Dodecagonal structures occur across all materials systems: intermetallics [5], chalcogenides [8], dendritic liquid crystals [9], co-polymers [10], inorganic nanoparticles [11], mesoporous silica [12], metal organic frameworks [13] and DNA molecules [14]. As reviewed by Ishimasa [25]: their formation is not stabilized by local interactions of conduction electrons as it is the case for icosahedral and decagonal intermetallic quasicrystals. Instead, the dodecagonal long-range order is governed by a different principle. It forms in systems exhibiting two competing length scales favouring hexagonally close-packed or square arrangements [26, 32]. By tailoring relative sizes and concentrations these systems can be driven towards a tiling element ratio of $N_{tr}/N_{sq} = 4/\sqrt{3}$ [25]. For this tiling element ratio the highest entropy structure is the dodecagonal tiling [33]. More recently, following the Lifshitz-Petrich model of frustrated two length scales for inducing aperiodic ordering a fine tuning of intermolecular interaction forces led to the formation of dodecagonal structures in metal-organic frameworks [34–36]. Note that all the examples listed here exclusively describe observations of square-triangle tilings.

Niizeki, Mitani and Gähler broadened the range of dodecagonal structures in two dimensions [37, 38]. In his construction of a dodecagonal lattice, Gähler obtained a star of twelve vectors $\{\vec{e}_1, ..., \vec{e}_{12}\}$ whose projections on the physical space ($\parallel$) and the internal space ($\perp$) can be expressed as

$$
\begin{aligned}
\vec{e}_i^{\parallel} &= a_{\parallel}(cos((i-1)\pi/6), sin((i-1)\pi/6)) \\
\vec{e}_i^{\perp} &= a_{\perp}(cos((i-1)\pi/6), sin((i-1)\pi/6)).
\end{aligned}
\tag{2.4}
$$

Using the relations $\vec{e}_{i+6} = \vec{e}_{-i}, \vec{e}_5 = \vec{e}_3 - \vec{e}_1$ and $\vec{e}_6 = \vec{e}_4 - \vec{e}_2$ all twelve vectors can be expressed as linear combinations of $\{\vec{e}_1, ..., \vec{e}_4\}$. Hence, these four vectors define the basis of a four dimensional lattice. The two symmetry operations which are connected to the higher-dimensional space group D24 are the twelvefold rotation $\mathcal{A}$ and the mirror

$\mathcal{B}$ [38]. With respect to the lattice basis they are expressed by

$$\mathcal{A} = \begin{pmatrix} 0 & 0 & 0 & -1 \\ 1 & 0 & 0 & 0 \\ 0 & 1 & 0 & 1 \\ 0 & 0 & 1 & 0 \end{pmatrix}, \mathcal{B} = \begin{pmatrix} 0 & 0 & 0 & 1 \\ 0 & 0 & 1 & 0 \\ 0 & 1 & 0 & 0 \\ 1 & 0 & 0 & 0 \end{pmatrix}. \tag{2.5}$$

From this four-dimensional periodic lattice different dodecagonal structures in two dimensions are obtained by using different shapes of the acceptance domain for the projection. The square-triangle tiling is obtained for a fractal acceptance domain [39, 40]. Figure 2.4 reproduces the various dodecagonal tilings derived by Gähler. He used a more simple dodecagon-shaped acceptance region (C_b) to derive a tiling of squares, triangles and asymmetric hexagons, which are often referred to as shields (Fig. 2.4-3). Upon expanding the area of that AD domain slightly to a short diameter of $2\vec{a}_\perp$ and a large diameter of $4cos(\pi/12)\vec{a}_\perp/\sqrt{3}$ and rotating it by 15° (C_a in Fig. 2.4-1) generates a tiling in which all shields are filled by one additional vertex that transforms the shield into one square, two triangles and one 30° rhomb. This way a square-triangle-rhomb tiling is obtained (Fig. 2.4-2). By further expanding the AD (C_c in Fig. 2.4-1), additional vertices are introduced into squares, which converts these squares and one neighboring triangle into pairs of rhombs, a transformation that is also discussed in the context of random square-triangle tilings [41].

In the context of oxide quasicrystals the square-triangle-rhomb tiling introduced by Niizeki and Gähler is of superior importance and will be denote as Niizeki-Gähler tiling (NGT) further-on. Taking a small patch of the NGT as an example, Fig. 2.5 illustrates how to utilize the higher-dimensional periodic lattice for the characterization of the two-dimensional quasicrystal tiling. In the physical space depicted in Fig. 2.5(a) the four projected unit vectors are given as colored arrows. They are rotated by 30° ($\pi/6$) with respect to each other. By starting from an arbitrary vertex of the tiling, using an integer linear combination of the projected lattice vectors each point in the tiling can be reached. The four vertices labeled as an example are reached from the center by subsequent steps along each of the lattice vectors. The four integer indices are unique and determine the coordinates of all lattice sites in the periodic hyperspace. In the internal space, shown in Figure 2.5(b), the projected lattice vectors are rotated by 150° ($5\pi/6$) against each other. These lattice vectors have the length of the short radius of the acceptance domain (shaded area). While in physical space the distance to the initial position increases in this example, the relative orientation of the four projected lattice vectors in the internal space results in an inward motion along the path.

Similar to the 1D Fibonacci chain, also the NGT can be derived from recursion [42]. Figure 2.6(a) illustrates the substitution rule for triangles, squares and rhombs. In each substitution cycle, triangles are replaced by seven triangles and three squares of smaller length. Each square is replaced by 16 triangles, five squares, and four rhombs.
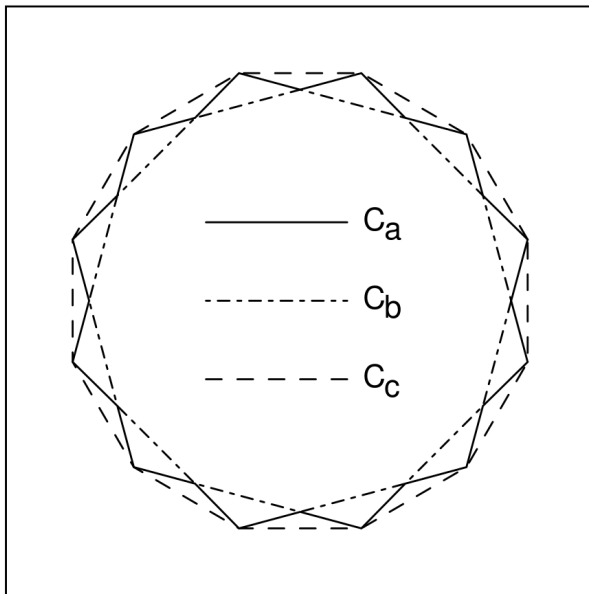
Fig. 1: Various acceptance regions
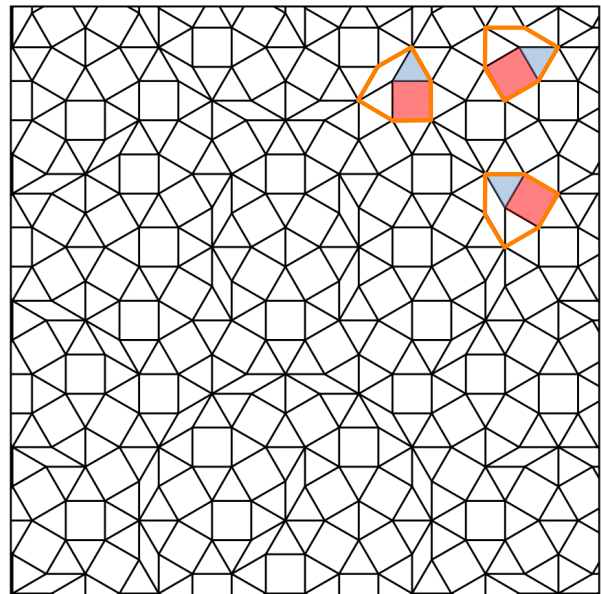
Fig. 2: Tiling with acceptance region C_a
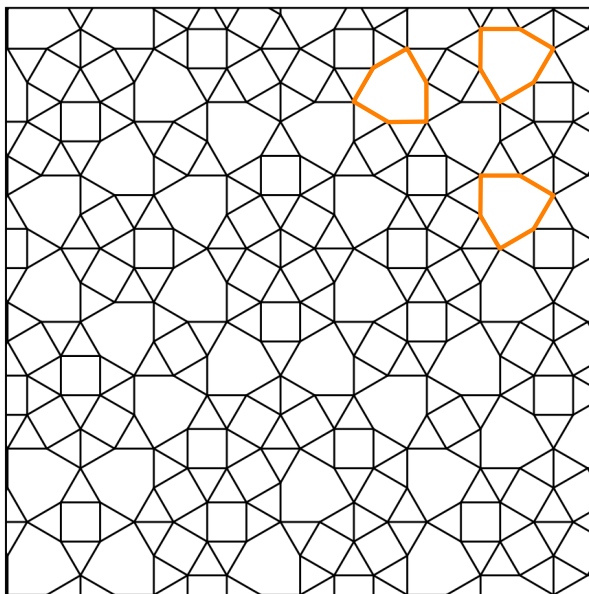
Fig. 3: Tiling with acceptance region C_b
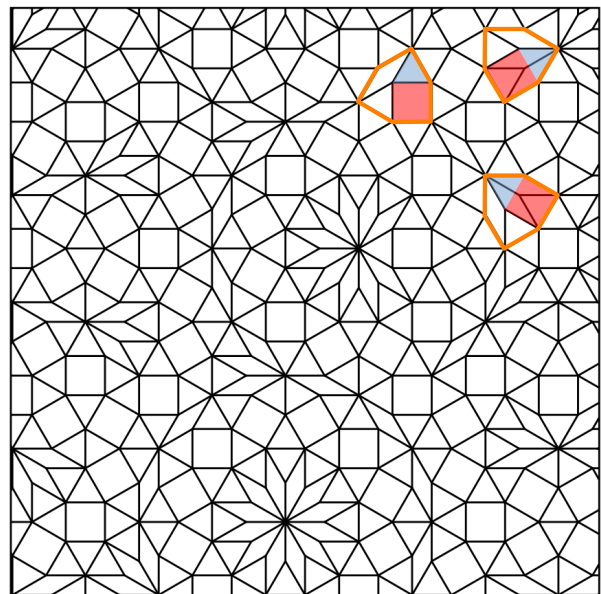
Fig. 4: Tiling with acceptance region C_c

Figure 2.4: Dodecagonal tilings consisting of three tiles constructed by F. Gähler by varying the acceptance domain. Selected tiling sequences are colored. Adapted from [38].

Finally, all rhombs are replaced by a combination of eight triangles, two squares, and three rhombs [43]. The shaded area marks the symmetry inherent ot the tiles. Upon inflation/deflation, self-similar structures are obtained. The scaling factor for dodecagonal quasicrystals is another PV number called the platinum mean [32]. It is the positive root solving

$$x^2 + 4x - 1 = 0, \quad x = 2 + \sqrt{3} = 3.732... \tag{2.6}$$
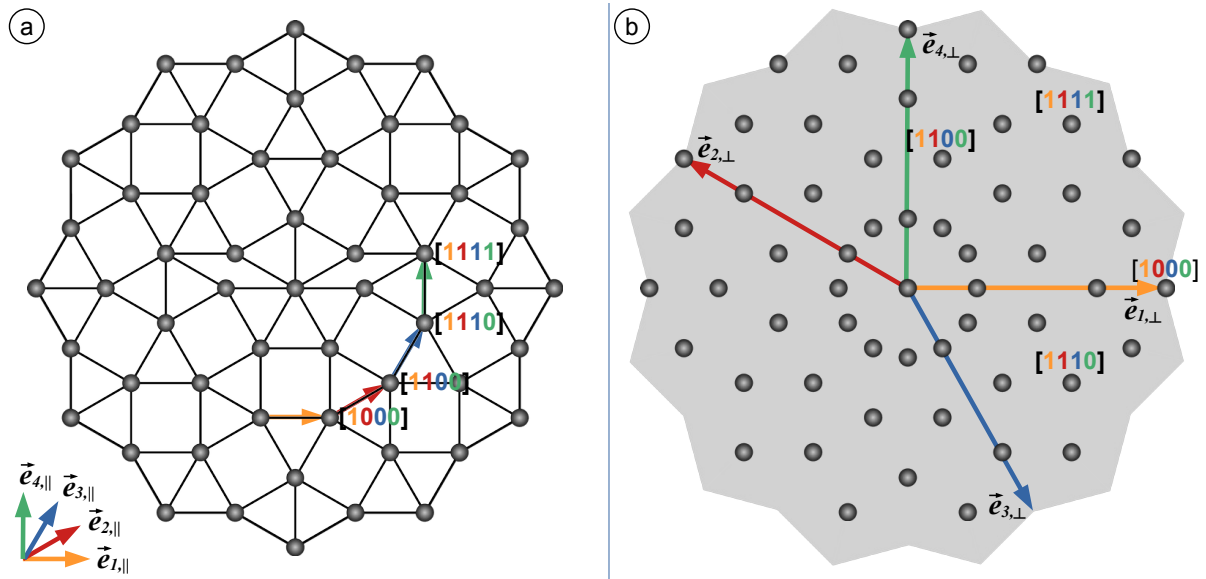
Figure 2.5: The dodecagonal Niizeki-Gähler tiling in (a) physical and (b) internal space. The four projected lattice vectors are given as colored arrows. The numbers in brackets illustrate the indexing of the physical space vertices and their mapping to the internal space.
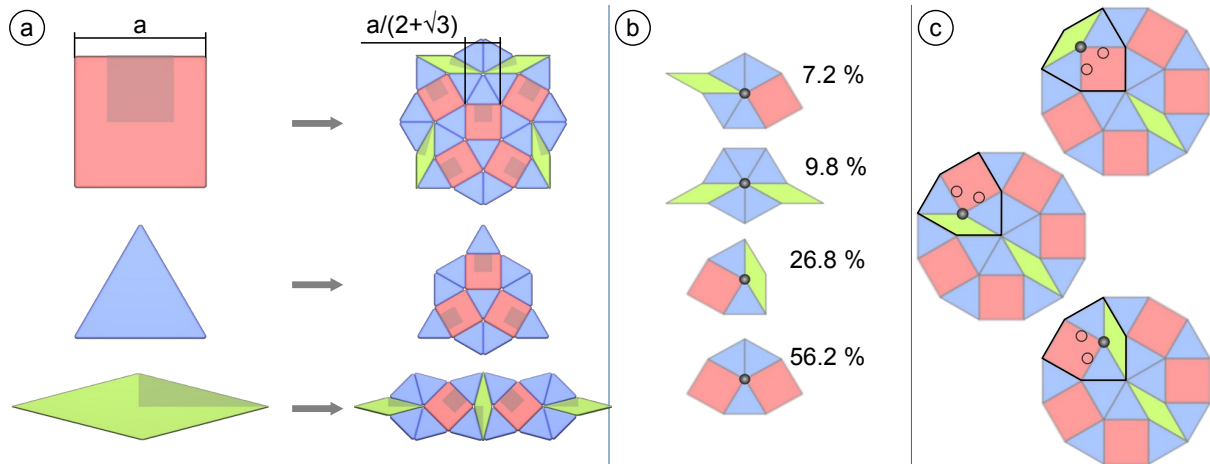
Figure 2.6: (a) Recursion rule for the dodecagonal NGT according to [42]. Upon substitution a self-similar square-triangle-rhomb tiling is generated, scaling with the platinum mean. The shaded area mark the symmetry of the tiles. (b) The four vertex configurations that occur in the NGT and their relative frequencies. (c) Phason flips in the NGT. The flipping between three equivalent positions inside the shield causes a 120° rotation of the interior tiling.

Mathematically, the substitution can be expressed by the deflation matrix $\mathcal{T}$, in which the rows of the matrix are assigned to the number of triangles, squares and rhombs involved in the substitution, respectively.

$$\mathcal{T} = \begin{pmatrix} 7 & 16 & 8 \\ 3 & 5 & 2 \\ 0 & 4 & 3 \end{pmatrix} \tag{2.7}$$

The scaling factor of self-similarity, the platinum mean, can also be calculated from the square root of the dominant eigenvalue of $\mathcal{T}$. The square root has to be taken since the

matrix and its eigenvalue are defined for the scaling of the area rather than the edge length. In addition, the corresponding dominant eigenvector of the deflation matrix represents the triangle : square : rhomb tiling element ratio in the NGT [43]:

$$\left[(1 + \sqrt{3}), 1, (1 + \sqrt{3})^{-1}\right] \simeq (2.73, 1, 0.37). \tag{2.8}$$

Despite a large number of possible combinations of the three tiling elements, only four vertex configurations exist in the NGT, which are shown in Fig. 2.6(b). These vertex configurations arise as corner points between four, five, six, or seven tiling elements, respectively. Most frequently a vertex is formed by five edges when three triangles and two squares meet (56.2 %). Roughly one quarter (26.8 %) of the vertices is a combination of the four edges of two triangles, one square and one rhomb. In 9.8 % of all vertices seven tiles merge namely five triangles and two rhombs. Least frequent (7.2 %) is the vertex formed from six edges of four triangles, one square and one rhomb. For completeness it should be mentioned that additional singular points exist in the ideal tiling with a different vertex configuration.

In the NGT, the vertices of the rhombs inside the shield elements are most sensitive to phasonic excitations. Gähler showed that the vertices defining the rhombs are defined by the outermost area of the acceptance domain in the internal space. However, the area of the internal space surrounding the acceptance domain of the NGT corresponds to additional positions inside the shield. This is also evident by the work of Gähler, where a slight increase in the size of the acceptance domain from C_a to C_c caused additional pairs of rhombs to occur. By looking carefully to the distribution of rhombs in the corresponding tiling in Fig. 2.5-4 three rhombs are frequently located next to each other. This is a consequence of the population of a shield element with two vertices. For phasonic excitations this means that any small displacements of the acceptance domain will immediately cause a depopulation of the vertices inside of some shields belonging to the NGT in favor of a population of an alternative vertex position in the shield. The consequences on the tiling level are illustrated in Fig. 2.6(c). The flipping between the three equivalent positions inside the shield element appears as a 120° rotation of the shield.

In the above paragraphs the special properties of dodecagonal QCs have been discussed. The following selection of results obtained for two-dimensional oxide quasicrystals will demonstrate that in these materials quasicrystal properties and concepts can be studied using the strong and powerful tools of surface science, especially using scanning probe techniques with atomic resolution.

3 Selected results

In this chapter the results of this habilitation thesis are highlighted covering the growth and structural properties of the prototypical OQC formed from Ba-Ti-O on Pt(111) (3.1), a summary of related periodic structures (3.2), the full atomic structure of oxide quasicrystals (3.3), the electronic structure of the OQC (3.4) and studies of molecular adsorption on these surfaces (3.5). The original publications reporting the work in full detail are collected in chapter 5.

3.1   Growth and structural properties

Oxide quasicrystals are formed from ternary oxide material on metal support upon high-temperature annealing in reducing environments [1, 2, 44]. The oxide material can be deposited on the metal by any means, e.g. rf magnetron sputtering, pulsed-laser deposition, or by using sequential or simultaneous evaporation in molecular beam epitaxy [45]. Upon thermal treatment fully oxidized films tends to de-wet the metal substrate to form three-dimensional islands, as has been reported for Pt(111), Pd(111), and Ru(0001) [1, 46, 47]. In reducing conditions, a two-dimensional wetting layer distributes the oxide material provided by the 3D islands until the metal substrate is fully covered. Figure 3.1 illustrates this wetting process for the Ba-Ti-O/Pt(111) system as monitored by low-energy electron microscopy (LEEM) [48]. In the top row of the figure the bare metal substrate gives rise to the bright contrast, the $BaTiO_3$ islands are light gray and the wetting layer is dark blue. In this system, the wetting process takes place at 1020 K in UHV. The wetted area does not develop any long-range ordering at this temperature. At 100 K higher temperatures, the quasicrystalline dodecagonal long-range order forms in the two-dimensional film and the residual 3D islands coalesce.

Figure 3.2 shows the diffraction pattern of the OQC obtained by μLEED. The dodecagonal pattern is obvious from the highest intensities, which correspond to the second order spots of the structure. This μLEED measurement performed in a LEEM system is the only measurement so far in which the first order spots have been clearly resolved. The pattern remains unchanged over a broad temperature range. In LEEM, even at 965 K the pattern is observed [48]. At higher temperatures electron emission
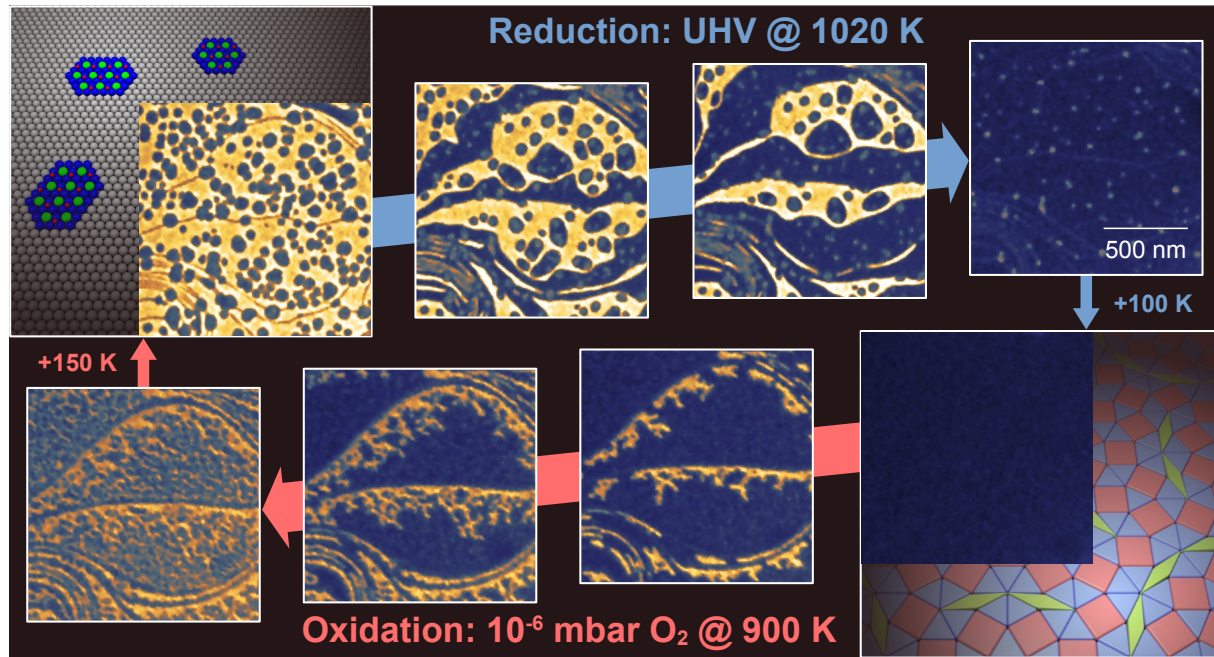
Figure 3.1: LEEM measurement of the wetting and de-wetting process of Ba-Ti-O on Pt(111). The top row shows the evolution of a two-dimensional wetting layer (dark blue) from 3D BaTiO$_3$ islands (light gray) on the metal surface (yellow) at 1020 K in UHV. The bottom row shows the decay of the OQC upon oxidation at 900 K. FOV $= 1.5\,\mu$m. Reprinted from **[F5.8]**.

sets in, which does not allow for further LEEM imaging. However, the OQC pattern has been observed by SXRD up to the formation temperature of 1150 K.

The OQC structure is stable upon O$_2$ adsorption - even at high temperatures: At a temperature of 900 K the OQC in the Ba-Ti-O/Pt(111) starts to decay only for pressures above 5×10^{-7} mbar [48]. The reason for the decay is the dissociation of O$_2$ into adsorbed atomic oxygen at free Pt defect sites. This oxygen leads to an oxidation of the two-dimensional wetting layer into perovskite islands. This conversion is monitored by LEEM in the bottom row of Fig. 3.1. Starting from the perfect OQC structure in the lower right, the decay proceeds in a dendritic fashion towards the lower left. The bright contrast appearing represents the bare metal substrate. The more metal is exposed to the O$_2$ atmosphere, the faster the conversion proceeds. By evaluating the time-dependence of the conversion, an exponential increase of the free metal area has been found [48]. This is the signature of an autocatalytic process as a consequence of the O$_2$ dissociation. Since the OQC layer terminates at the substrate step edges, free Pt sites will be initially available at the step edges on the higher-lying terrace, which is why the conversion starts there. In the course of time the two-dimensional OQC layer is locally converted into small islands, which necessarily extend to the third dimension. The conversion from a high density of smallest islands towards the lower islands density seen on the top right of Fig. 3.1 happens upon temperature increase via
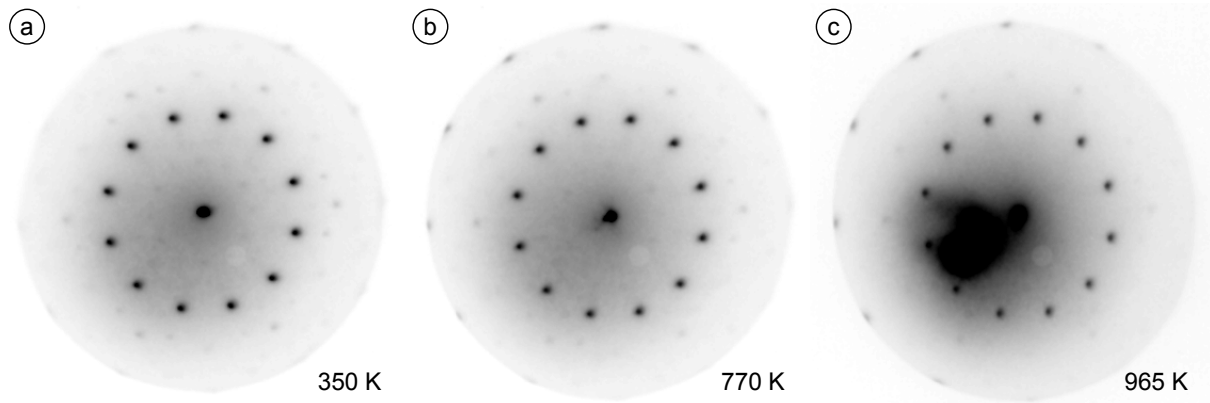
Figure 3.2: Dodecagonal diffraction pattern of the OQC in Ba-Ti-O/Pt(111). µLEED data reveals the thermal stability of the structure upon heating at $350\,\mathrm{K}$ (a), $770\,\mathrm{K}$ (b), and $965\,\mathrm{K}$ (c). Measurements at higher T were hindered by electron emission. Adapted from **[F5.3]**.

Ostwald ripening and coalescence. The growth and decay cycle presented in Fig. 3.1 demonstrates that these ternary oxide layers exhibit a prototypical strong-metal support interaction (SMSI), which has been thoroughly discussed for binary oxides in catalysis in the past [49–51].

On the atomic level, the dodecagonal structure is characterized by atomic vertices forming three basic tiles with a common edge length: equilateral triangles, squares, and rhombuses having 30° and 150° angles. As shown in Fig. 3.3, these basic tiles are combined to dodecagons consisting of 20 vertices arranged in 12 triangles, 5 squares, and two rhombs. These dodecagons are the basic building blocks of the tiling. They are combined on larger scales in an edge sharing fashion (top left in Fig. 3.3). The distance between two adjacent dodecagons sharing one edge is a factor of $(2 + \sqrt{3})$ larger than the edge length of the basic tiles. This factor of $(2 + \sqrt{3})$ is the inflation factor for dodecagonal tilings. The first mathematical description of a dodecagonal triangle-square-rhomb tiling has been presented by Niizeki and Gähler [37, 38]. Hence it is called Niizeki-Gähler tiling (NGT). A first inflation rule was given by Liao et al. [42]. Their work suffered from partially overlapping tiles upon recursion. This issue has been resolved by defining the recursion rule based on half elements [52]. Figure 3.4(a) illustrates how the second generation of the tiling is obtained based on combinations of the basic first generation tiles. The shaded area in the first generation tiles encodes the tiling element symmetry. In the second generation a proper orientation of the first generation tiles needs to be maintained. As a consequence of this substitution, tiling elements arise in the second generation, which are enlarged by the inflation factor $(2 + \sqrt{3})$. Every subsequent iteration of this inflation causes further enlargement of the supertiles by the same factor as shown in Fig. 3.4(b) for the third generation square. In this third generation the characteristic dodecagons can be recognized. Four of these dodecagons that decorate the vertices of the second generation square are marked in

blue in Fig. 3.4(b). By connecting all dodecagons an self-similar tiling will be constructed which is enlarged by the $(2 + \sqrt{3})$ compared to that of the basic tiles.

How closely oxide quasicrystals resemble the dodecagonal Niizeki-Gähler tiling model has been tested by an extensive statistical analysis [43]. Statistical measures are the frequencies of tiling elements and larger clusters and the distribution of their
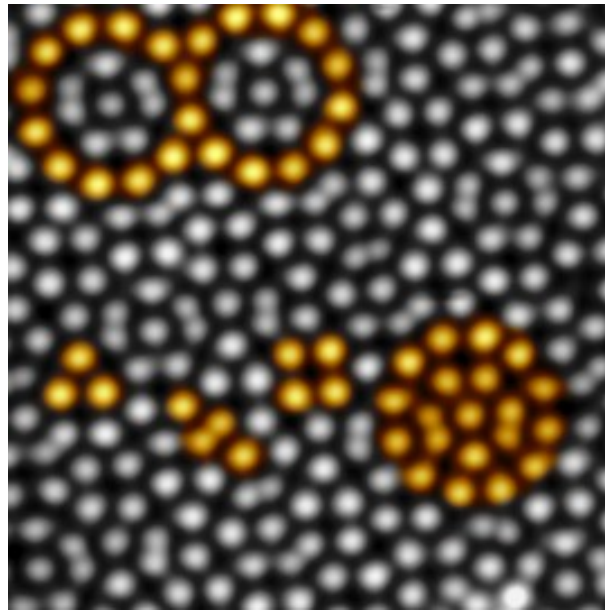
Figure 3.3: Atomically-resolved STM image of the OQC in Ba-Ti-O/Pt(111). The atomic vertices are arranged in triangles, squares and rhombs. These tiling elements are combined in dodecagons that are the characteristic building blocks of the dodecagonal tiling. $10 \times 10 \, \text{nm}^2$, $30 \, \text{pA}$, $0.15 \, \text{V}$. Reprinted from **[F5.8]**.
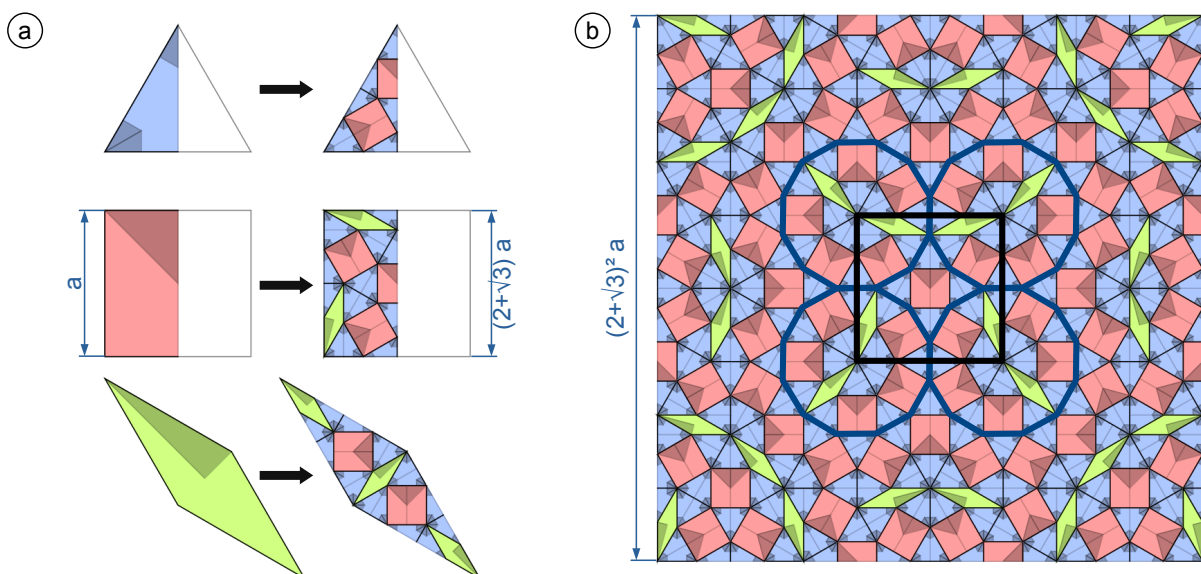
Figure 3.4: (a) Overlap free recursion rule for the three basic tiling elements of the dodecagonal Niizeki-Gähler tiling. (b) Third iteration of the recursion starting from a square. For further explanation see text. Adapted from **[F5.8]**.
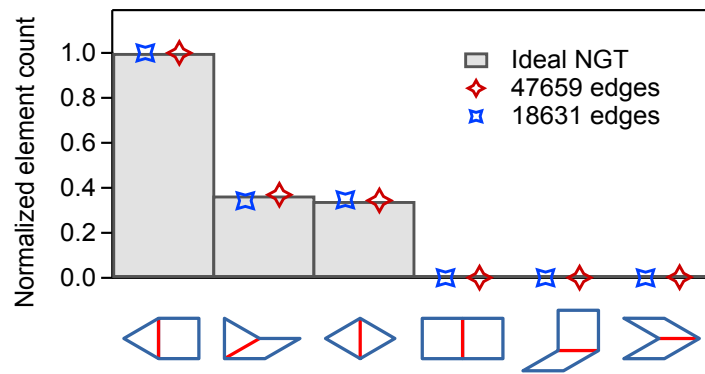
Figure 3.5: Distribution of shared edges between adjacent tiling elements of two experimental datasets compared to the ideal NGT (gray histogram). Reprinted from **[F5.7]**.

orientations. More elaborate, by analyzing the frequency of shared edges between neighboring tiles, information about the combination of elements in the global tiling can be obtained. This analysis has been performed for the prototypical OQC in Ba-Ti-O/Pt(111) [43, 53]. In the Niizeki-Gähler tiling only three combinations of the three tiling elements are allowed: A triangle can be combined with a square, a rhomb, or another triangle. No other combination should occur. Moreover, the relative frequency of these tiling element combinations is fixed. Figure 3.5 shows these frequencies for the NGT as grey bars. In addition, the data points obtained from two independent datasets of different size are included in the figure. These data points are obtained from atomically-resolved STM measurements containing 8100 and 20000 atomic vertices, respectively [43, 44, 53]. As can be read from the graph, tiling element combinations occur in the real oxide quasicrystals, which are not allowed in the NGT. However, these defects occur almost at zero measure - their total number amounts to 0.3 % of all atomic vertices for the larger dataset. Both, the tiling element ratio and the relative frequencies of the three NGT tiling element combinations are perfectly reproduced in the measured OQC systems, which proves that oxide quasicrystals are the first natural realization of a dodecagonal Niizeki-Gähler tiling. The only significant deviations from ideal statistics have been found in the orientation of the dodecagons in the Ba-Ti-O/Pt(111) system [43]. The twelvefold degeneracy in the orientation of the dodecagons is lifted and a preference for rotations every 60° are found. This observation is attributed to a stabilization mechanism for the OQC on the three-fold substrate, which is aligned parallel to the edges of the OQC tiling elements.

3.2 Periodic approximants

Besides oxide quasicrystals, a plethora of periodic structures is observed in 2D layers of Ba-Ti-O and Sr-Ti-O on Pt(111), Pd(111), and Ru(0001) surfaces [2, 47, 52, 54–57]. As illustrated for the example of the 2D hyperspace for the 1D Fibonacci quasicrystal in chapter 2, periodic structures related to quasicrystals exist for cutting the higher dimensional hyperspace at rational slopes. Each corresponding unit cell consists of a continuous patch of tiles, that also exist in the parent quasicrystal (pQC). The closer the rational slope approximates the irrational slope of the quasicrystal, the better the periodic tiling approximates the aperiodic tiling of the pQC. Consequently, these periodic structures are called approximants. Figure 3.6 illustrates the relation between approximant unit cells and the pQC for the NGT of oxide quasicrystals and the two single-phase approximants that have been reported first: the 4:2:0 approximant (also known as σ phase) and the 24:9:3 approximant [2, 55]. The nomenclature used for labeling these approximants encodes the triangle:square:rhomb tiling element ratio of the given unit cell, which is yet another measure for the complexity of a given periodic structure. In Fig. 3.6(a) a patch of four triangles and two squares is emphasized in the NGT tiling, which completely tiles the plane upon periodic repetition as shown in Fig. 3.6(b). The larger patch emphasized in Fig. 3.6(a) consisting of 24 triangles, 9 squares and 3 rhombs is periodically repeated in Fig. 3.6(c). Not just by visual inspection, but also by comparing the tiling element ratios of the approximants with that of the NGT, one clearly notes that the larger approximants resembles the OQC quite

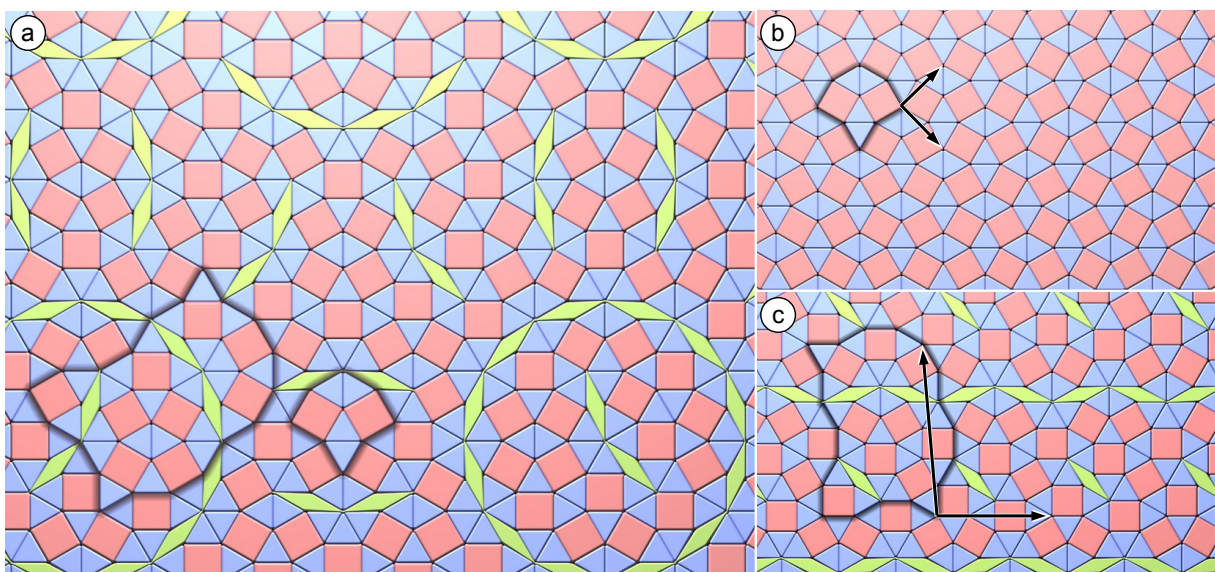**Figure 3.6:** (a) NGT tiling emphasizing two patches that exist in periodic repetition. (b) 4:2:0 σ-phase approximant observed for Ba-Ti-O on Pt(111), Ru(0001), and Pd(111). (c) 24:9:3 approximant found in Sr-Ti-O/Pt(111). Adapted from **[F5.8]**.

closely. Normalized to the number of squares the NGT tiling element ratio amounts to $(1 + \sqrt{3}) : 1 : (1 + \sqrt{3})^{-1} \approx 2.73 : 1 : 0.37$. While the σ phase with its ratio of $2 : 1 : 0$ deviates significantly, the 24:9:3 approximant with its ratio of $2.66 : 1 : 0.33$ already closely resembles the composition of the NGT.

In these ternary oxide systems, approximant structures have been identified that cannot be described with their relation to the pQC in a similar fashion as introduced above. One example is shown in Fig. 3.7. This hexagonal approximant structure contains not only the three tiling elements of the NGT in its unit cell, but five in total. In the center of the unit cell one finds a characteristic dodecagon of the NGT made from triangles, square, and rhombs. However, this dodecagon is surrounded by twelve trapezoids (black in Fig. 3.7) bridging to the neighboring cells. In addition, at the corner between three adjacent cells a lar-

Figure 3.7: Hexagonal approximant exhibiting five tiles in the unit cell (for further explanations see text). Adapted from **[F5.10]**.

ger triangle exists, that can be either decorated by an additional adatom (blue circle) or empty (red circle). Obviously, for structures like this the relation to the pQC that consists of less tiling elements is rather ill defined. Other examples exist that request a more subtle definition of the term approximant. In the Ba-Ti-O/Pd(111) system, another 24:9:3 approximant is observed, for which the distribution of rhombs within the unit cell is altered by phason flips within the same boundary as seen Fig. 3.6(c). As a result, the same patch cannot be found in the pQC at any position [58]. Furthermore, structures are found that exhibit vertex configurations that are not allowed in the pQC. One example is the hexagonal approximant in Sr-Ti-O/Pt(111), in which one vertex is surrounded by six triangles [57]. For this reasons, the approximant classification scheme shown in Fig. 3.8 is proposed.

According to this scheme, structures that consist solely from the basic tiling elements of the pQC are called approximants, whereas structures that contain other tiling elements are called pseudo approximants. The approximants are further subdivided into strict, flipped and vertex-relaxed. Strict approximants have an unit cell that includes full tiles. This unit cell is a compact patch of the pQC and it contains only vertex configurations that are allowed for the pQC. Flipped approximants also have a unit cell including full tiles. Its boundary equals that of a compact patch of the pQC
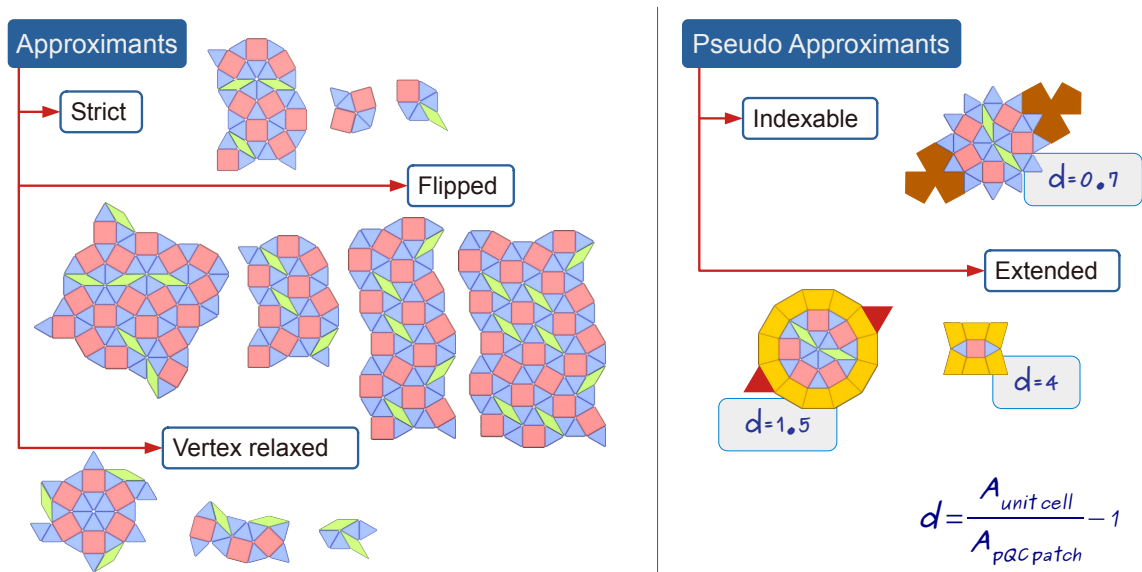
Figure 3.8: Generalized classification scheme for approximant structures inspired by the wealth of structures in two-dimensional ternary oxide layers (for further explanation see text). The indexable pseudo approximant is a hypothetical structure, all other structures have been observed experimentally.

and exhibits only vertex configurations of the pQC. The arrangement of tiles within the boundary is allowed to vary from the pQC. The mechanism causing these variations are phason flips that provide the name for this subclass of approximants. The third subclass of approximants are called vertex relaxed. These approximants have a unit cell of full tiles and all tiles must exist in the pQC. In other words, vertex configurations can be included in the unit cell, which are not present in the pQC and no restriction regarding the distribution of tiles exists. Pseudo approximants are divided into two subclasses: Indexable and extended ones. In the case of indexable pseudo approximants it is requested that all points in the lattice can be reached by adding one of the projected unit vectors of the pQC to the neighboring atom positions. This way all atomic positions can be expressed using the lattice vectors spanning the higher dimensional periodic lattice of the pQC. The definition of extended pseudo-approximants only requests that the unit cell contains a patch of the pQC. This definition allows also tiles that introduce a new length scale to the lattice which cannot be mapped to the higher-dimensional periodic lattice. The factor d shown in Fig. 3.8 defines a measure for the deviation from the pQC. It compares the area of a patch included in the pQC tiling with the unit cell area of the pseudo approximant. In absence of new tiles, which means for all strict approximants, this measure is 0. For all pseudo approximants d is larger than 0. The classification scheme presented here does not only have implications in the physical real space. The structural modification which lead to a division into the different subclasses do also modify the reciprocal physical and the internal
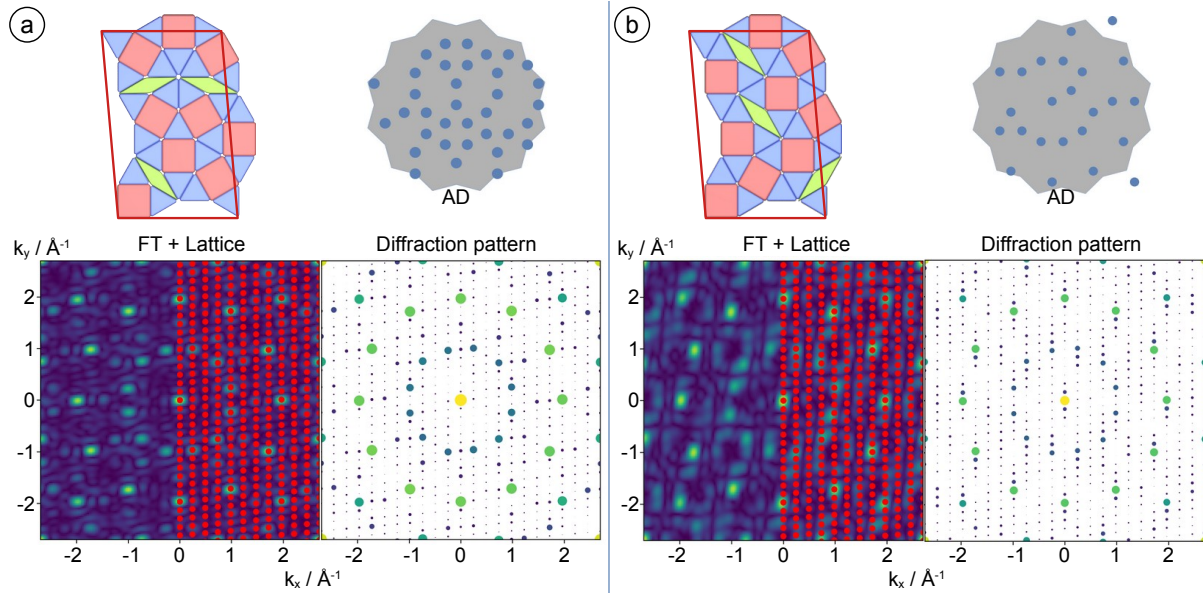
Figure 3.9: (a) Representation of a strict 24:9:3 approximant in real space (unit cell), internal space and reciprocal space. (b) Same characterization for a flipped 24:9:3 approximant. As a guide to the eye for the internal space, the acceptance domain of the pQC is given (AD). For illustrating the differences in reciprocal space, the Fourier-transform of the base is shown next to the diffraction pattern.

space properties. Two examples will be used to emphasize the important differences.

Figure 3.9 compares the two different variants of the 24:9:3 approximants that exist in Sr-Ti-O/Pt(111) and Ba-Ti-O/Pd(111) [2, 58]. The structure observed in Sr-Ti-O/Pt(111), shown in Fig. 3.9(a) is a strict approximant. The vertices in the unit cell are on identical positions as found in the NGT. By lifting the structure into the four-dimensional hyperspace one can get to the internal space representation, in which all points are found inside of the acceptance domain (AD) of the NGT. For simulating the diffraction intensities the squared modulus of the structure factor F, which accounts for the distribution of the vertex atoms in the unit cell, is multiplied with the squared modulus of the density distribution in the reciprocal space, which accounts for the lattice.

$$I = |F|^2 \cdot |L|^2 = |\sum_{j=1}^{J} f_0(\underline{k}_0, \underline{k}, \underline{r}_j)e^{ik r_j}|^2 \cdot |\sum_{j=1}^{N} e^{i\underline{K}\underline{R}_j}|^2 \tag{3.1}$$

In reciprocal space, the FT of the strict approximant closely resembles the intensity distribution of the OQC. This follows for the quite large number of tiles in the unit cell, which are perfectly ordered for this strict approximant. The deviations in the diffraction pattern arise from the discrete sampling of the reciprocal space as defined from the periodic lattice of the approximant, which does not allow to meet the points of highest intensity everywhere. Of course, the larger the unit cell of a strict approximant, the finer the k-space sampling and the better the approximation of the OQC diffraction
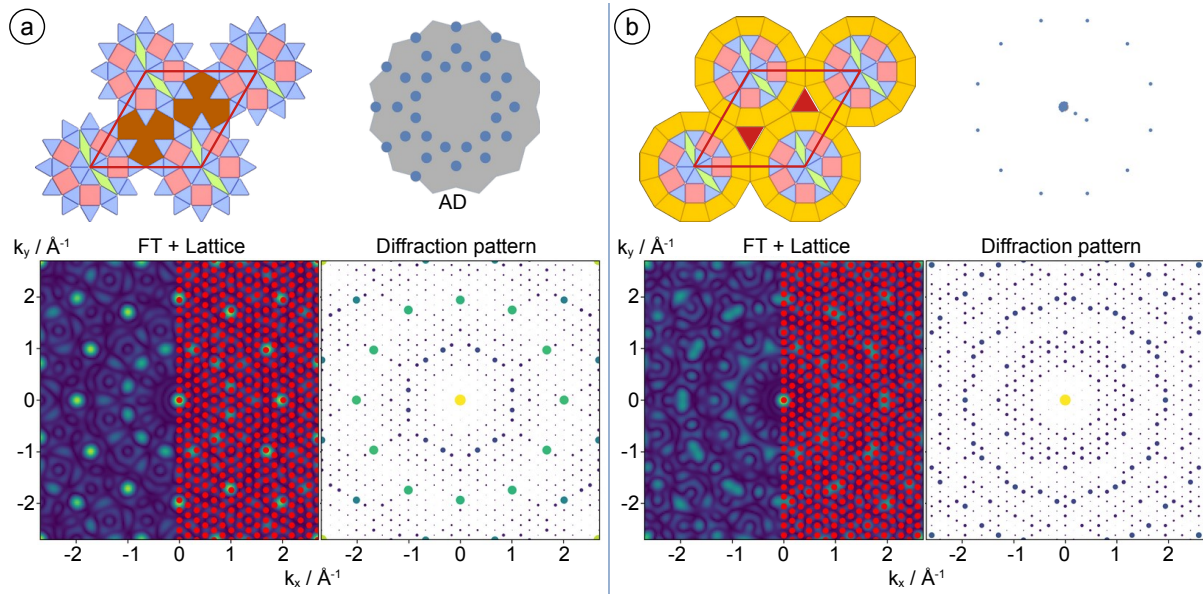
Figure 3.10: (a) Hypothetical indexable pseudo approximant represented in real, internal and reciprocal space. (b) Example of an extended pseudo approximant for comparison. The twelve non-indexable positions of the trapezoids reach far out in the internal space. Hence, the AD in the center is barely recognizable.

pattern. In the case of the flipped 24:9:3 approximant shown in Fig. 3.9(b), the tiles are rearranged wrt. the perfect OQC tiling. This is immediately seen in the internal space representation, in which two vertices reside outside the acceptance domain. Similar to disorder, the tiling rearrangement result in a smearing out of the reciprocal space intensity distribution calculated from the FT of the unit cell base. As a consequence, the k-space intensity is distributed amongst various neighboring spots in the diffraction pattern. The relative intensity distribution at the same reciprocal space coordinates differs significantly from the pattern of the strict approximant having the same lattice as given in Fig. 3.9(a).

As a second example, two pseudo approximants of hexagonal symmetry shown in Fig. 3.10 are discussed. The indexable pseudo-approximant contains a dodecagon surrounded by twelve triangles in its unit cell. This part of the motif is identically found in the NGT. By periodic repetition in a hexagonal fashion as indicated by the red unit cell, new tiles arise in-between three of the aforementioned patches that are not part of the NGT. Accordingly the structure is classified as a pseudo approximant. By sharing one vertex atom between neighboring dodecagons, the indexability of the structure is ensured. In the internal space all vertices fall into the AD of the NGT. Also in reciprocal space, this structure appears like a strict approximant, due to the perfect ordering of the atomic vertices forming the base of the unit cell. The extended approximant shown in Fig. 3.10(b) does also contain one full dodecagon in its unit cell, which is surrounded by twelve additional vertices. However, this outer ring of twelve vertices

is rotated by 15° with respect to the dodecagon in comparison to the pseudo approximant in Fig. 3.10(a). Thus, twelve trapezoids are formed instead of twelve triangles. This rotation by 15° does not allow to index the entire structure any more because the projected lattice vectors of the NGT incline 30° angles. The non-indexability implies in fact, that these points cannot be reached by any linear combination of the projected lattice vectors. Hence in the internal space representation only approximated positions can be given for these outermost vertices. They appear as twelve points on a circle far outside of the acceptance domain. It is important to note, that the presence of two trapezoids instead of two triangles on the connecting line between two large clusters causes a subtle modification of the distance between adjacent cluster centers. The new distances introduced by the trapezoids severely alter the reciprocal space intensity distribution. Although sampled with an almost identical reciprocal lattice, the diffraction pattern does not at all approximate a twelvefold symmetric pattern any more. It is purely hexagonal with small variations in the relative intensities of neighboring spots.

This short excursion aims on giving an overview about the variety of periodic structures that exist in two-dimensional ternary oxide made from Ba-Ti-O and Sr-Ti-O. Some of these approximants have played a major role in the exploration of the atomic structure of oxide quasicrystals because the application of the powerful tools of structure determination like surface x-ray diffraction and density functional theory is straight forward for periodic structures, which is the subject of the following section.

3.3 Atomic structure of oxide quasicrystals

The structural properties of oxide quasicrystals and their related approximants have been discussed in the previous chapter solely on the tiling element level. This tiling has been obtained by connecting the atomic vertices observed in STM images. The elemental nature of these atomic vertices remained the central question in the research on oxide quasicrystals since their discovery. The large interatomic spacing of 6.70 Å to 6.85 Å for the majority of vertices implied that only the sublattice of one single atomic species gives rise to the contrast in STM. All attempts in STM of varying the imaging conditions by altering the bias voltage to become sensitive to the density of states of the two other elements in these ternary compounds failed [1]. The ultimate tool for atomic level microscopy is non-contact atomic force microscopy (nc-AFM) in direct combination with STM by using conductive probes. It allows the simultaneous mapping of the density of states and interaction forces. Thus, it is capable of imaging atoms that do not contribute to the tunneling current at a given bias voltage. Figure 3.11 shows simultaneously recorded constant-height STM (left column) and nc-AFM images (right column) of the OQC. These measurements have been conducted at 5 K using a CO-functionalized tip as a probe [53]. At larger tip-sample distance, the constant-height
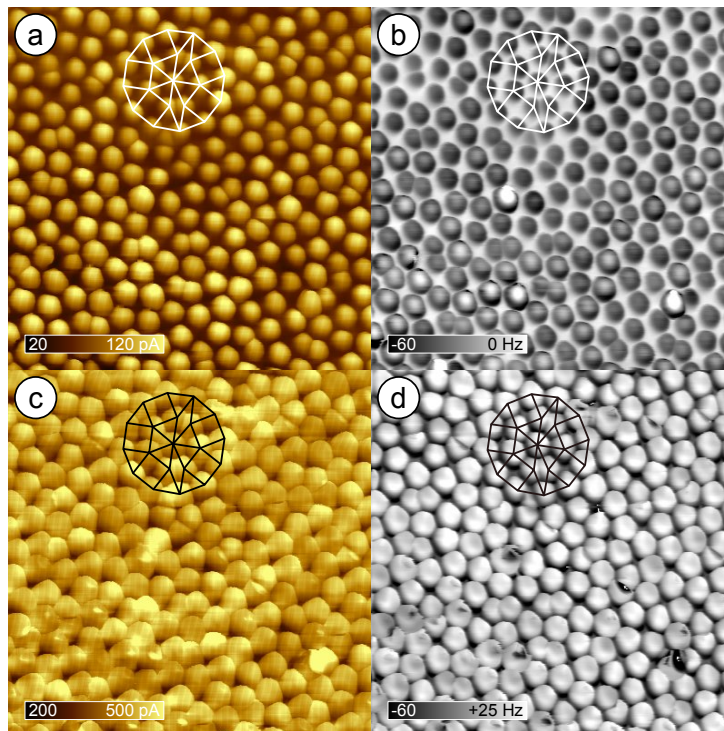

Figure 3.11: Simultaneously recorded constant-height STM (a,c) and nc-AFM images (b,d) of the OQC in Ba-Ti-O/Pt(111) using a CO-terminated tip. One of the characteristic dodecagons is emphasized for guidance. a-d) $7\times7\,\text{nm}^2$, $U = 20\,\text{mV}$, $A = 50\,\text{pm}$. The tip-sample distance has been reduce by $160\,\text{pm}$ between (a,b) and (c,d). Adapted from **[F5.7]**.

current image (a) shows the atomic vertices as well-separated spherical objects. In the frequency shift image (b) the same vertices are seen in a dark contrast reporting on an attractive interaction with the CO-terminated tip. However, no additional atoms are resolved in-between the vertex atoms seen in STM. By further approaching the tip to the surface, the absolute current in the current image (c) is strongly increased and the vertex atoms appear space filling. In the frequency shift image (d) the same atoms appear now with a bright contrast, which corresponds to a repulsive interaction with the tip. Even in this repulsive regime utilizing a CO molecule as the smallest-possible probe it is not possible to resolve any additional atomic species [53].

To solve the atomic structure of oxide quasicrystals, STM and LEED experiments have been complemented by surface x-ray diffraction and density functional theory calculations for the 48:18:6 approximant in Sr-Ti-O/Pt(111) [52]. Figure 3.12(a) shows the unit cell of this approximant, in which 48 vertex atoms form a tiling of 48 triangles, 18 squares and 6 rhombs. This structure is categorized as flipped approximant since its tiling (Fig. 3.12(b)) comprises rows of three rhombs, that do not occur in the ideal NGT. The large size of the unit cell makes this structure challenging for structure relaxation in DFT. However, in this structure two glide-planes exist, which increase the symmetry of the system to p2gg and reduce the size of the irreducible unit to one quarter of the unit cell (semi-transparent tiling in (a)). As a consequence of the large real-space unit cell dimensions of $4.4 \times 4.3 \, \text{nm}^2$, the reciprocal lattice is densely sampling the k-space. In addition, six domains of this structure form on the hexagonal substrate, which results in a very dense set of superstructure spots marked in black in the reciprocal space map shown in Fig. 3.12(c). The red circles in this map indicate the positions of the intense Bragg peaks of the dodecagonal OQC. Three spots appear from the different domains of the periodic structure at the OQC spot positions. From the reciprocal space mapping, 182 symmetry inequivalent spot intensities have been extracted for the 48:18:6
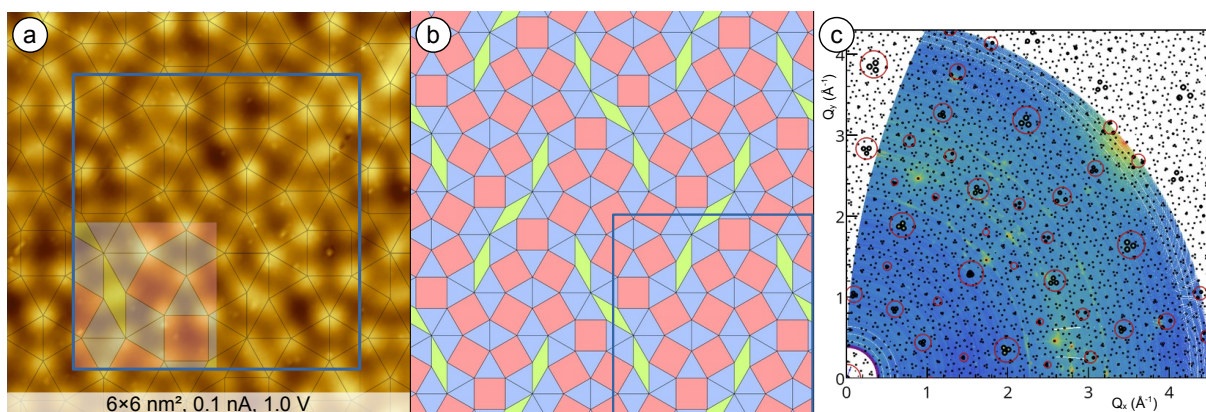

Figure 3.12: (a) The vertex configuration in the unit cell, (b) the tiling, and (c) the SXRD data for the 48:18:6 approximant in Sr-Ti-O/Pt(111). Adapted from **[F5.12]**.

approximant. This dataset has been used to test the different structures that have been proposed for oxide quasicrystals. An initial proposal has been put forward at the beginning of this habilitation work based on a combined STM, LEED, SXRD and DFT analysis of the 4:2:0 approximant in Ba-Ti-O/Pt(111) [55, 59]. At that time, the vertex atoms seen in STM have been assigned to the Ti atoms and a $Ba_4Ti_4O_{10}$ stoichiometry has been concluded. An alternative proposal has been made by Cockayne *et al.* in a theoretical work based on a tiling decoration approach [60]. Cockayne *et al.* assigned the vertices to the alkaline earth metal atoms hosted in a Ti_2O_3 network structure. In their model, the 4:2:0 approximant will have a stoichiometry of $Ba_4Ti_{12}O_{18}$. The availability of the 48:18:6 approximant SXRD data allowed for the first time to decide between the competing structural models [52]. By optimizing the atomic positions of the different metal cations for the two models in a least-squares refinement the measured SXRD data has been fitted with the two models. With regard to all agreement factors (Goodness of fit (GOF), weighted residuum (wR2), and unweighted residuum (R1)) [61], the structural model including alkaline earth metal atoms occupying the vertex positions leads to substantially better fits (GOF=1.5, wR2=0.21, R1=0.11) as compared to the alternative with Ti atoms at the vertices (GOF=4.2, wR2=0.73, R1=0.45). This clearly decides that the SXRD analysis is in agreement with the theoretical model developed by Cockayne *et al.* [60]. The arrangement of the Sr and Ti atoms can be directly visualized by the calculation of the charge density contour map, $\rho(x, y)$, which is shown in Fig. 3.13(a).
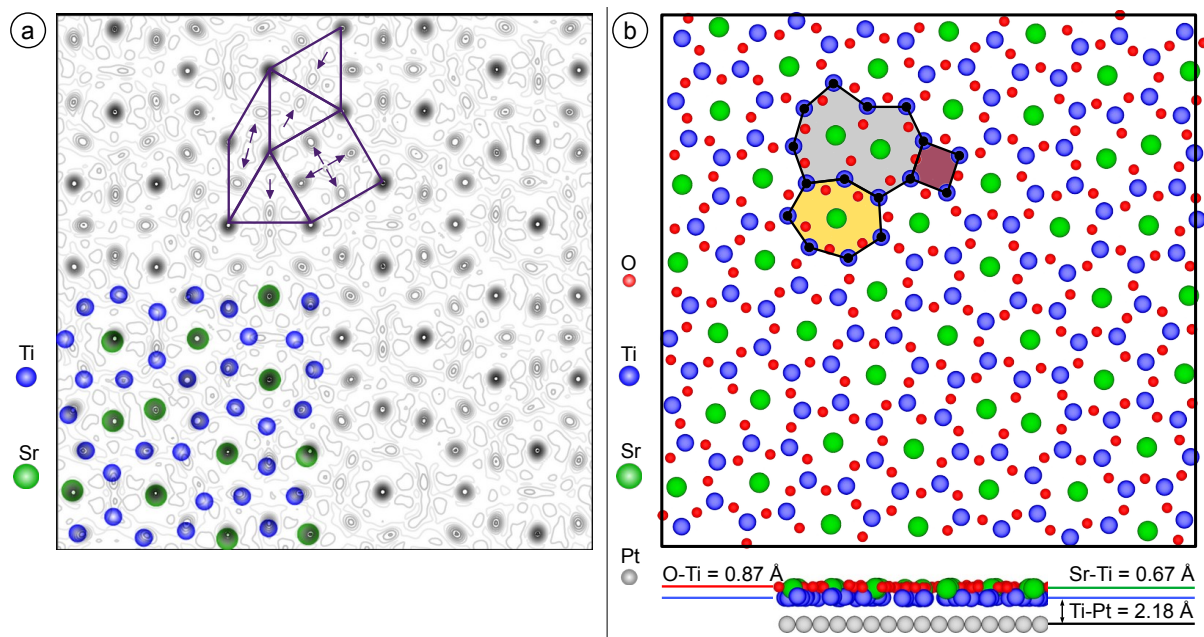

Figure 3.13: (a) Electron density distribution in the unit cell of the 48:18:6 approximant in Sr-Ti-O/Pt(111) calculated from SXRD. (b) Top and side view of the DFT relaxed structure of this approximant. For clarity the substrate atoms have been omitted in the top view. Reproduced from **[F5.12]**.

The highest-density features as marked in green correspond to the positions of the heaviest atom, the alkaline earth metal Sr. They form the vertices of the square-triangle-rhomb tiling. The Ti atoms are located at positions of the second highest electron density, as emphasized in blue and by the black arrows in Fig. 3.13(a). To identify the positions of the O atoms, DFT calculations have been performed by E. Cockayne. The relaxed structure of the 48:18:6 approximant is shown in Fig. 3.13(b). The essential feature of such two-dimensional ternary oxide layers is a Ti-O backbone that forms rings of four, seven, and ten Ti atoms, which are marked in magenta, orange and gray in Fig. 3.13(b), respectively. The seven membered rings are decorated with a single alkaline earth metal ion, whereas the ten membered rings host two alkaline earth metal ions and one additional O atom. The next-neighbor distance

Figure 3.14: The unit cell of the 48:18:6 approximant represented as decorated tiling. Sr, Ti, and O atoms are coloured green, blue, and red, respectively. The decoration the three tiles applies to all related structures including oxide quasicrystals.

between the two alkaline earth metal ions in the ten membered ring is strongly reduced due to the screening by the additional O atoms in-between. This structure is strongly interacting with the supporting substrate, which can be seen from the significant downward relaxation of the Ti atoms [52].

The atomic network structure obtained for the 48:18:6 approximant can be transferred to all periodic and aperiodic structures in two-dimensional ternary oxides via a tiling decoration scheme presented in Fig. 3.14, which has been proposed first by Cockayne *et al.* [60]. The backbone Ti_nO_n ring structure with $n = 4, 7$, and 10 is closely related to honeycomb networks. Figure 3.15(a) illustrates the Stone-Wales defect known for Carbon-based networks [62]. By rotating the central bond between four adjacent rings with $n = 6$, a combination of two rings with $n = 5$ and two with $n = 7$ is formed. In a subsequent transition of the same type a combination of four $n = 7$ rings surrounding one $n = 4$ ring can be realized. Stone-Wales defects are well-known for various honeycomb systems including binary oxides and their formation is accompanied with an energy penalty [63]. The complex networks in ternary oxide layers with rings of different sizes are stabilized by hosting the alkaline earth metal ions for ring sizes of $n > 6$. This has been proven by a comparative DFT study of a Ba decorated honeycomb Ti_2O_3 network and the 4:2:0 σ-phase approximant. In the two structures shown in Fig. 3.15 (b,c) 2/3 of all rings are decorated by Ba ions, i.e. all $n = 7$ rings
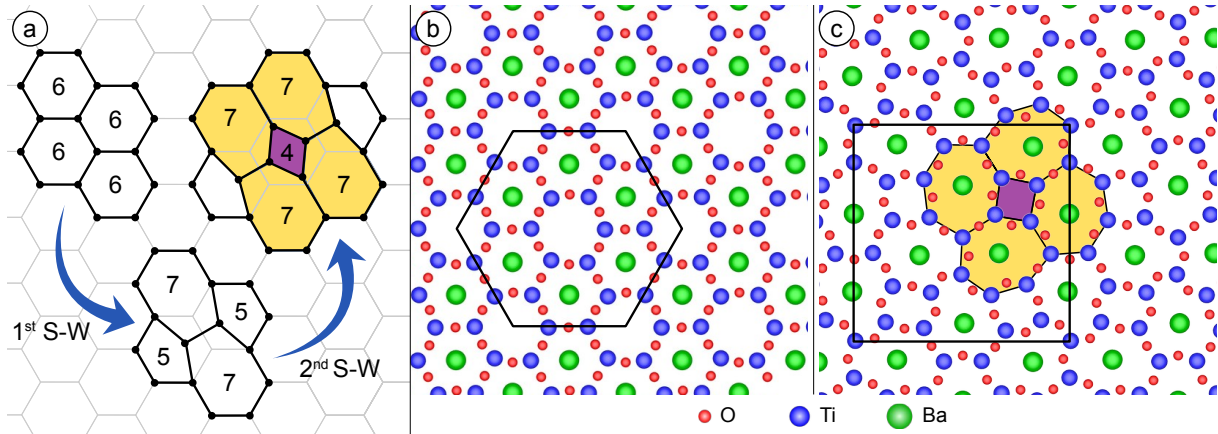
Figure 3.15: (a) Transition from a honeycomb lattice by subsequent Stone-Wales (S-W) transformations into a structure of four and seven member rings. (b) Comparison of the total energies of Ba-decorated Ti_2O_3 honeycomb structure and (c) the Ba-Ti-O σ-phase approximant on Pt(111) by DFT. The lowest energy phase is the σ-phase approximant. Reproduced from **[F5.12]**.

for the σ phase. Since both structures comprise the identical composition and comparable unit cell area upon relaxation, a comparison of their total energies is straight forward. It turns out that despite the unfavorable situation of strained $n = 4$ rings, the σ phase is the lower energy phase. Two main contributions are suggested that stabilize the complex network of "defects" in two-dimensional ternary oxides. First, the reduction of the absolute height of the Ba ions wrt. the Pt(111) substrate reduces the dipole connected to the ion and its image charge induced in the substrate. Second, the larger ring size in the σ phase results in an enlarged distance between adjacent Ba ions of about 15 % wrt. to the honeycomb, which reduces the Coulomb repulsion amongst the neighboring ions[52].

Now that the atomic structure is solved and the Cockayne model is validated the different phases observed in a given materials system can be put into a proper context. Most thoroughly investigated is the Ba-Ti-O/Pt(111) system. Already before the observation of the first oxide quasicrystal in this system, four different periodic approximant structures have been reported, which at that time have been observed in co-existence on the Pt(111) surface [54]. In the mean time, all of these structures have been prepared as single phases and two additional ones have been reported. With the knowledge of the atomic structure it is now possible to derive a phase-diagram of the system. The parameter that is decisive for the formation of a given structure is the Ba coverage of the Ti_2O_3 backbone. The survey of structures in the Ba-Ti-O/Pt(111) system presented in Fig. 3.16 starts with the pure honeycomb Ti_2O_3 on the left. Starting from a Ba coverage of 50 % of all honeycomb rings, i.e. $1.5\,Ba/nm^2$, the so-called Six-Network structure forms [54, 60]. In this structure single Stone-Wales transformations result in a network of equal amounts of Ti_nO_n rings with $n = 5$ and $n = 7$. The vertices of this
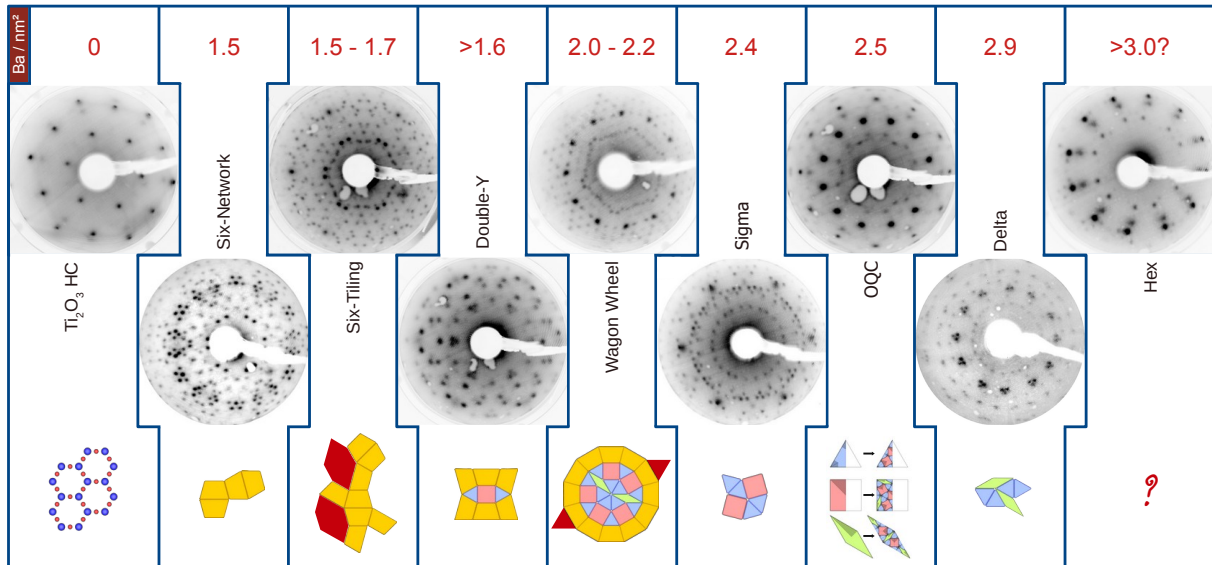
Figure 3.16: Collection of structures obtained in two-dimensional Ba-Ti-O films on Pt(111) ordered by increasing Ba ion density(top row). For all periodic structures the single-phase LEED pattern and the periodically repeating tiling motif are shown.

tiling are formed from Ba in $n = 7$ rings, while the empty $n = 5$ rings decorate the center of the trapezoidal tiling elements. The Six-Tiling structure contains one $n = 6$ ring in addition, which can be occupied by Ba or be empty. Thus, a small acceptance for Ba density variations is given. The Double-Y structure is the first to develop square and triangle tiling elements, which means also the first to contain $n = 4$ rings. In case of the Wagon-Wheel structure, $n = 6$ rings exist in the large triangles that can be either decorated by Ba or remain empty allowing also for a narrow range of Ba density variations [54, 56, 60]. Starting from the σ phase the trapezoidal tiling elements disappear. Now, exclusively $n = 4$ and $n = 7$ rings are formed. This structure corresponds to a 2/3 filling of the honeycomb pores by Ba as discussed above (Fig. 3.15(b,c)) [52, 54, 55, 60]. At slightly higher Ba density of 2.5 Ba/nm^2 the OQC is formed in the system, which includes the rhomb tile that is connected to $n = 10$ rings. At a density of 2.9 Ba/nm^2 a triangle-rhomb tiling is realized, the so-called Δ phase. This structure is solely made from $n = 10$ rings. It must be understood as a honeycomb network fully decorated by Ba. These n=10 rings arise from two adjacent $n = 6$ rings, when an extra oxygen is opening up the shared bond between these rings as illustrated in Fig. 3.17 [52]. Assuming the lattice parameter of the Ti$_2$O$_3$ honeycomb on Pt(111), a fully occupied

Figure 3.17: The formation of a Ba decorated Ti$_n$O$_n$ $n = 10$ ring upon incorporating an additional O atom into adjacent $n = 6$ rings. Adapted from **[F5.12]**.
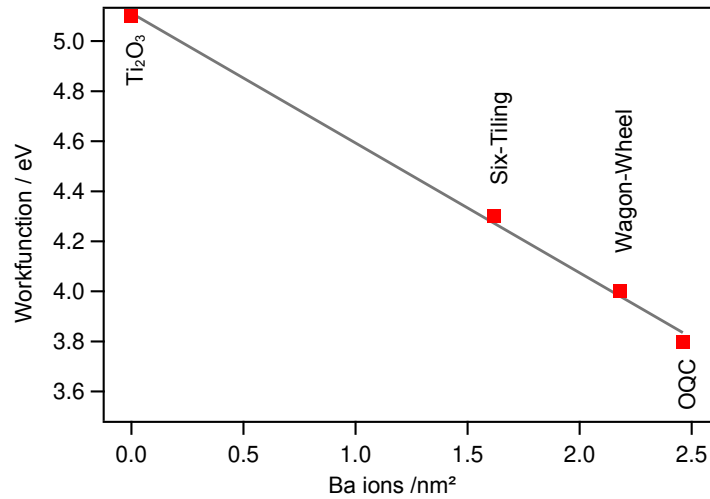
Figure 3.18: The workfunction of selected two-dimensional oxide phases as function of the Ba content in the layer. The gray line is a linear fit through the data.

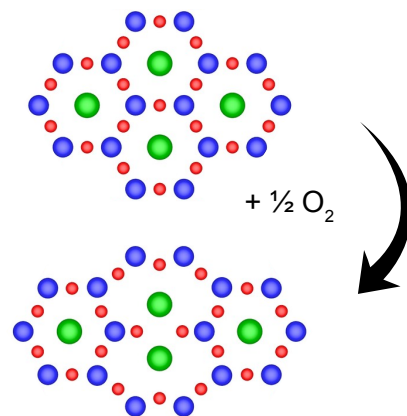honeycomb would correspond to a density of $3.2 \, \text{Ba}/\text{nm}^2$ [64]. However, this $n = 10$ ring network expands, which reduces the Ba density. At the high density limit a complex hexagonal phase has been identified, which could not yet been solved completely. Is there a way to prove the assignment made in Fig. 3.16? The variation of Ba ion density at the surface must alter the surface dipole, which is why a linear decrease of the workfunction (WF) with increasing Ba amount is expected [65]. This has been confirmed experimentally as shown in Fig. 3.18. Starting from the empty HC with a WF of 5.1 eV, we observe a linear decrease when going via the Six-Tiling and the Wagon-Wheel approximant all the way to the OQC.

The two-dimensional ternary oxide layer structures can be converted into one-another despite their different composition, mediated by the formation of three-dimensional $BaTiO_3(111)$ perovskite islands. By driving the formation of these islands, which have a significantly larger Ba content than all 2D phases, a reduction of the Ba content in the two-dimensional layers is obtained. These islands grow under oxidizing conditions and remain stable upon short term UHV annealing afterwards. In experiments it was possible to convert an OQC layer into a Wagon-Wheel approximant in a two-step preparation: In a first step, islands were formed by 20 min O_2 annealing in 1×10^{-6} mbar at 920 K. This treatment results in a complete de-wetting of the Pt(111) substrate as shown in Fig. 3.1. In a second step the metal substrate is wetted by the 2D oxide upon annealing for 5 min in UHV at 1070 K. Afterwards, the entire surface exhibited the single phase LEED pattern of the Wagon-Wheel structure. Upon further oxidation following the same recipe, the Wagon-Wheel structure has been converted into the Six-Tiling approximant. This process can be reversed by long-term UHV annealing above 1100 K. Given that this reversibility applies similarly to related systems, it offers a very efficient way of exploring the composition-dependent phase diagram.

The in-depth understanding of the atomic structure and the formation mechanism of oxide quasicrystals worked out in this thesis represents a milestone in the research on these two-dimensional systems. It allows to bridge to related materials to explore whether it will be possible to construct dodecagonal structures by rational design. Plenty of honeycomb structures are well-established in metal supported oxides [64–73]. In addition, two-dimensional oxide phases with broad ring size distributions forming vitreous structures have been found [74–78]. Studying the influence of large guest entities, e.g. alkaline earth metals or lanthanides, on these 2D network systems, shall pave the way to a tailor-made fabrication of new two-dimensional quasicrystalline materials targeting specific properties related to their aperiodic order.

3.4   Electronic structure of oxide quasicrystals

In scanning tunneling microscopy the OQC and related periodic structures exhibit a strong contrast upon all bias voltage conditions suggesting a metallic character of these two-dimensional oxide layers. On the local scale, the metallic behavior has recently been confirmed by measuring a finite differential conductance at the Fermi level in constant height scanning tunneling spectroscopy [79].

An integral measure for the metallicity of the OQC comes from angle-resolved photoemission applied to the Ba-Ti-O/Pt(111) system using momentum microscopy [80]. Figure 3.19 shows 2D momentum maps of the OQC covered and the bare Pt(111) substrate, recorded at the Fermi energy and at 0.5 eV binding energy. In the presence of OQC, the signature of the Pt bulk bands remains clearly visible, although these features are damped by the 2D overlayer. In addition, the OQC induces a strong enhancement of the photoelectron intensity around the $\bar{\Gamma}$ point at the Fermi level. With increasing

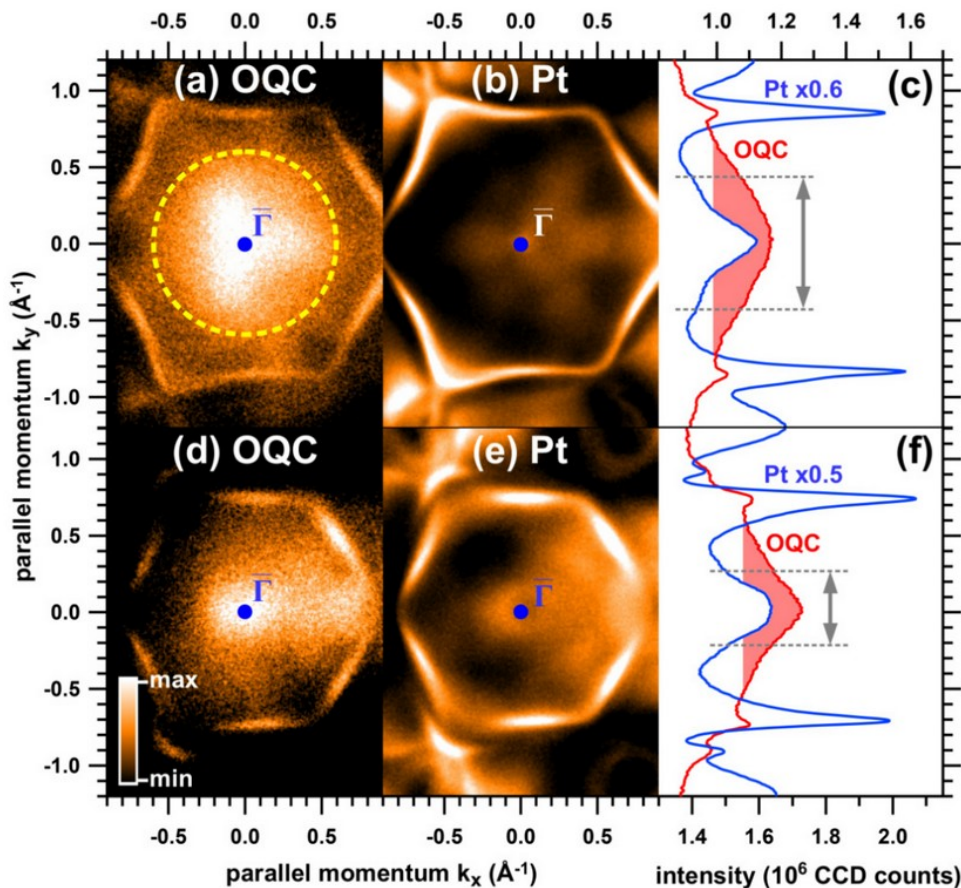**Figure 3.19:** 2D momentum map of (a, b) the OQC in Ba-Ti-O/Pt(111) in comparison with (d, e) bare Pt(111). (a, b) taken at E_F and (d, e) at $E_B = 0.5\,\text{eV}$. In (c), (f) their momentum distributions along k_y integrated over $k_x \pm 0.5\,\text{Å}$ are shown, and the full width at half maximum near $k_y = 0$ for OQC (filled regions) is estimated by the arrows. Reprinted from **[F5.5]**.

binding energy the intensity distribution becomes narrower indicating an $E(\vec{k})$ dispersion of the electronic states of the OQC. Regarding the filling of the electronic states, a lower bound of the Fermi wave vector of $0.6\,\text{Å}^{-1}$ could be estimated. This value is consistent with a lower bound for the charge carrier density of $2.5 \times 10^{14}\,\text{cm}^{-2}$. It originates from partially occupied Ti $3d$ bands that lead formally to a $3d^1$ state [80].

The metallic character of these 2D oxides is also reflected in the core level peak shape of the atomic species involved. The effect is best seen for the Ti $2p$ core level region shown in Fig. 3.20. The blue component in Fig. 3.20 is the formally 3+ charged Ti in the two-dimensional network structures, namely the Ti$_2$O$_3$ honeycomb, the OQC, the Wagon-Wheel and the Six-Tiling approximants. The yellow component relates to Ti^{4+} in 3D BaTiO$_3$ islands. From the data a Shirley background has been subtracted. The sum of the two components is giving the fit (red line) of the experimental data (black dots). A perfect fit of the Ti $2p$ doublet of 3+ component is obtained by using a Doniach-Sunjic lineshape [81]. This lineshape accounts for a strong asymmetry of the peak towards the higher binding energy side resulting from energetic losses of the photoelectrons upon excitations of valence electrons, which is typical for metal systems. This asymmetric peak shape also causes a strong contribution to the inelastic background at higher binding energies. The three spectra of the ternary 2D oxides shown in Fig. 3.20 illustrates the transformation from the OQC in lower Ba density structures upon oxidation and rewetting discussed in the previous section. With the growing higher binding energy Ti^{4+} component the formation of stable 3D islands can be monitored. From the area ratios of the two Ti species a surface model of the coexisting 3D and 2D phases can be designed and the 2D oxide's composition can be derived.
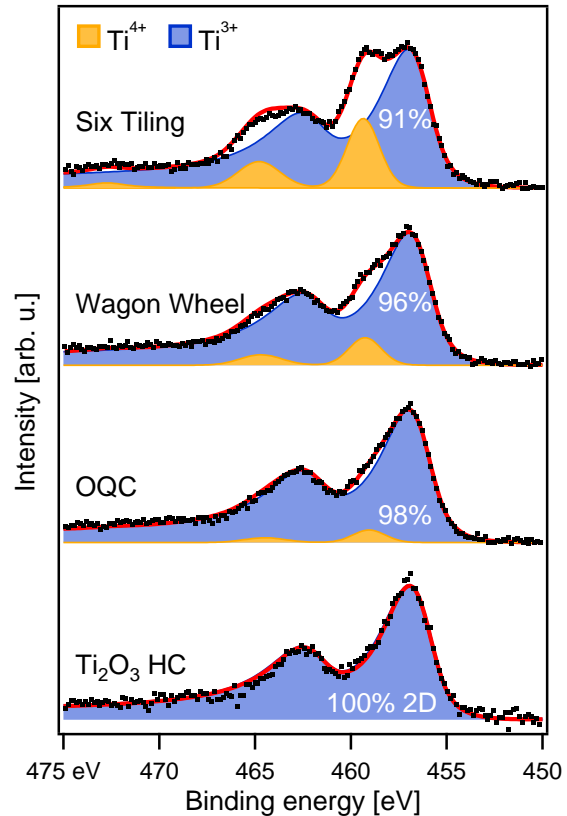

Figure 3.20: XPS spectra of Ti $2p$ for different two-dimensional oxide systems. The low binding energy component corresponds to the given 2D system. The percentage denotes the 2D oxide area fraction.

3.5 Molecular adsorption onto 2D ternary oxides

The extraordinary structure of oxide quasicrystals and their high degree of structural perfection especially in the Ba-Ti-O/Pt(111) system raised the interest in the transferability of their dodecagonal structure to overlayer systems. Our research focused on the use of oxide quasicrystals as templates for the growth of aperiodically-ordered molecular films. The special benefit of molecular systems is the availability of all kinds of intermolecular distances that allows to pick molecules matching the pitch of the template.

As a first example the adsorption of C_{60} molecules on the OQC in Ba-Ti-O/Pt(111) is presented [82, 83]. When adsorbing monolayer coverages onto the OQC at room temperature, close-packed two-dimensional C_{60} patches form. In LEED, rings are observed (Fig. 3.21(a)), from which a hexagonal structure with a lattice parameter of (9.9 ± 0.1) Å is determined, matching the van-der-Waals diameter of C_{60} molecules. Analyzing the intensity distribution of the first-order ring more closely (Fig. 3.21(b)), a preferred orientation of hexagonal C_{60} patches rotated by $15°$ against the tiling element edges of the OQC has been identified [82]. This is a first indication of a guided self-assembly in these inert molecular films. This effect becomes more pronounced when reducing the substrate temperature during adsorption. These experiments have been performed by in-situ deposition of the molecules onto the sample hosted in a variable temperature STM kept at 150 K. The result is shown in Fig. 3.22. At 150 K the molecular motion is strongly suppressed. In this submonolayer coverage, the molecules are not able to merge into close-packed islands. Instead, smallest patches exist in which the molecules adopt motifs of the underlying OQC template. Besides local hexagonal

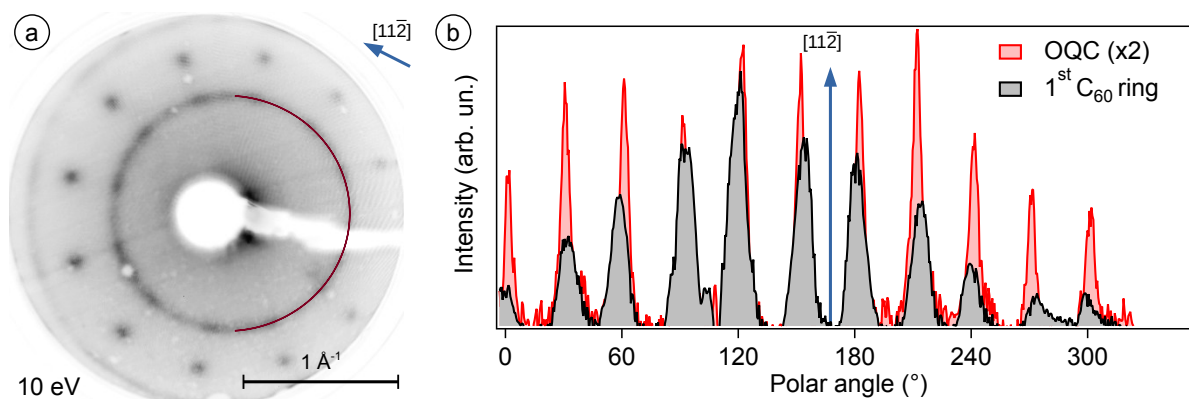**Figure 3.21:** (a) LEED pattern of one monolayer of C_{60} molecules upon room temperature deposition onto the OQC in Ba-Ti-O/Pt(111). (b) Comparison of the azimuthal intensity distribution of the OQC spots (red) and the ring corresponding to the first order C_{60} spots. A clear preference for an orientation at $15°$ rotation against the $\langle 11\bar{2} \rangle$ direction of Pt(111) is found. Adapted from **[F5.6]**.

arrangements (Fig. 3.22(b)), also squares are found (Fig. 3.22(c)) and even combinations of triangles and squares. The latter can be just a combination of one triangle and one square (Fig. 3.22(e)), a square sandwiched between two triangles (Fig. 3.22(f)) or two triangles and two squares (Fig. 3.22(g)). Even tiling elements involving five and six molecules are formed, like pentagons (Fig. 3.22(h)) and the characteristic shield element (Fig. 3.22(i)). These results show, that there must be a preferred adsorption site that allows to accommodate the large host molecule. To localize the preferred adsorption site of the C_{60} that allow to

Figure 3.22: (a) Small clusters of C_{60} molecules adsorbed at 150 K onto the OQC template. Various motifs (b-f) are obtained that reproduce the OQC tiling on the scale of C_{60}. Adapted from **[F5.6]**.

imprint the OQC tiling to the molecular layer, we made use of the least complex approximant structure, the σ phase. Figure 3.23(a) shows an extended patch of this square triangle tiling. This simple structure contains only two high symmetry adsorption sites: the centers of squares or pairs of triangles. Focussing on the squares, a well-determined set of next-neighbor C_{60} distances must occur for isolated molecules labeled 1-7 in Fig. 3.23(a). Having these possibilities in mind, a statistical analysis of the ranges of intermolecular distances and their angular distributions for low coverages of C_{60} has been performed. The results shown in Fig. 3.23(b-d) confirm the hypothesis of

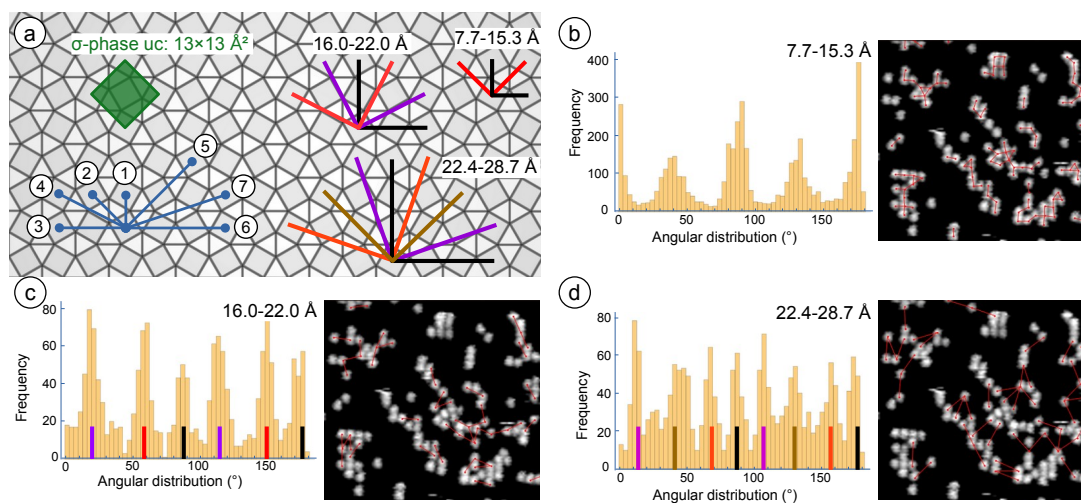**Figure 3.23:** (a) The σ-phase tiling as template for C_{60} adsorption. Potential NN distances for preferential adsorption in squares are indicated. (b-d) Angular distribution of intermolecular distances observed in STM for the three sets of distances emphasized in (a). Adapted from **[F5.6]**.

a preferential adsorption of squares which also explains the transfer of the OQC tiling motifs into the molecular layer at low coverages. However, the overall interaction of C_{60} is too small to induce a dodecagonal ordering in the molecular self-assembly, which would allow for further studies, e.g. on the modification of the electronic structure in aperiodically ordered organic films.

Other molecules, which were thought to bind more specifically to either Ti or Ba atoms in the OQC layer, have been tested in addition. Cyclopentadiene has been chosen to bind preferentially to the Ti sites, at a time before the Cockayne model of the OQC had been accepted and the STM contrast of the OQC was assigned to Ti still. At room temperature no specific binding could be seen and the OQC structure remained unaffected by the dosage of cyclopentadiene [83]. At 80 K multilayers of cyclopentadiene adsorb. Heating back to room temperature, monolayer cyclopentadiene is still adsorbed as shown by HREELS. However, no long-range ordering is obtained. Further annealing resulted in a degradation of the OQC layer and a loss of Ti from the surface, presumably due to the formation of volatile titanocene [83]. Since Ba is prone to from stable carbonate species, CO_2 adsorption has been tested as well [83]. At 83 K a saturation coverage is formed, for which the vibrational frequencies of the CO_2 molecules are found close to those of gas phase molecules. The desorption temperature is 95 K. Interestingly, the physisorbed CO_2 molecules are adopting the OQC structure as seen from LEED taken at 83 K [83].

As a last example CO adsorption should be mentioned. When flooding the OQC surface with CO molecules at temperatures below 60 K a dense layer of molecules is formed that exhibits the dodecagonal long-range order. However, the exact adsorption geometry has not been resolved [83].
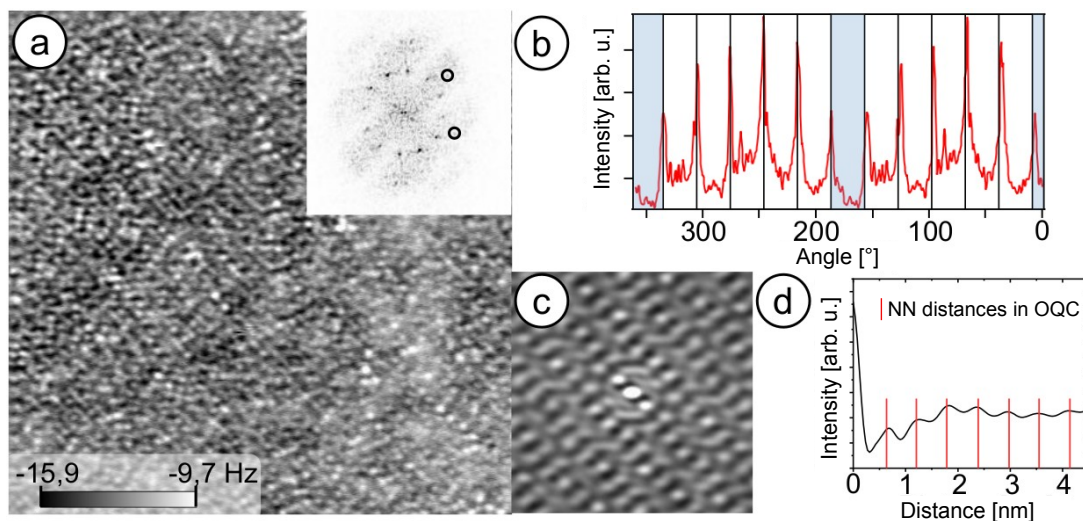

Figure 3.24: (a) NC-AFM measurement of a CO-covered OQC at 5 K exhibiting a twelvefold symmetric FT (inset). (b) Circular line profile taken from the FT image. Bars indicate intervals of 30°. (c) 2D autocorrelation image of (a) and (d) its radial distribution function [83].

4 Summary

In the course of this habilitation thesis an in-depth understanding covering various aspects of oxide quasicrystals has been developed: The growth of oxide quasicrystals, their detailed atomic structure, structural variations upon chemical modifications concerning the alkaline earth metal species and the substrate, their electronic structure and their use as template for molecular self-assembly. This work unraveled oxide quasicrystals as a fascinating materials system bridging between two fields of research. On one hand side in the field of surface science, these aperiodically-ordered two-dimensional oxide network structure complements periodic networks with unique ring sizes and vitreous networks with broad ring size distributions. On the other hand in field of quasicrystal research, OQCs have been established as a textbook quasicrystal model system with a degree of structural perfection that has never been obtained in dodecagonal quasicrystals before.

Two kinds of local interactions dominate OQCs on the atomic level: the stabilization of a reduced Ti-O network on a metal support involving a charge donation to the substrate. This is known to produce long-range ordered periodic structures of maximal symmetry, e.g. the sixfold Ti_2O_3 honeycomb lattice. In addition, in response to an additional interaction force induced from the dipoles related to the alkaline earth metal ions decorating the Ti-O network, the local symmetry is reduced by the formation of Ti_7O_7 rings. However, the Coulomb repulsion amongst neighboring dipoles forces global structures of higher, dodecagonal symmetry.

From the perspective of quasicrystal research OQCs represent a new class of quasicrystalline materials. They differ from the intermetallic alloys, which are stabilized by conduction electrons via the Hume-Rothery mechanism. OQCs do also not match the category of soft-matter quasicrystals, in which square-triangle tilings are establish due to the frustration of two competing length scales. Instead, the covalently bonded network of OQCs is the first natural representation of a square-triangle-rhomb tiling, which is well-described using the mathematical NGT model. Their structure might be rationalized as a packing density optimization for a certain concentration of repelling dipoles hosted by a Ti_nO_n network involving three competing length scales given by the three elementary tiles.

5 Original publications

This habilitation thesis is based on the peer-reviewed publications listed below.

notation	citation	page
[F5.1]	Observation and Structure Determination of an Oxide Quasicrystal Approximant, Phys. Rev. Lett. **117**, 095501 (2016).	40
[F5.2]	Observation of a dodecagonal oxide quasicrystal and its complex approximant in the SrTiO$_3$-Pt(111) system, J. Phys.: Condens. Matter **29**, 134002 (2017).	45
[F5.3]	Growth and decay of a two-dimensional oxide quasicrystal: High-temperature in situ microscopy, Ann. Phys. **529**, 1600250 (2017).	52
[F5.4]	Full real-space analysis of a dodecagonal quasicrystal, Acta Cryst. **A75**, 307 (2019).	59
[F5.5]	Electronic band structure of a two-dimensional oxide quasicrystal, Phys. Rev. B **100**, 125149 (2019).	66
[F5.6]	C$_{60}$ adsorption on a dodecagonal oxide quasicrystal, Phys. Rev. B **100**, 205414 (2019).	67
[F5.7]	Perfect Monolayers of the BaTiO3-derived 2D Oxide Quasicrystals Investigated by Scanning Tunneling Microscopy and Noncontact Atomic Force Microscopy, Phys. Status Solidi B **257**, 1900620 (2020).	85
[F5.8]	Quasicrystals and their Approximants in 2D Ternary Oxides, Phys. Status Solidi B **257**, 190624 (2020).	91
[F5.9]	Two-Dimensional Wetting Layer Structures of Reduced Ternary Oxides on Ru(0001) and Pt(111), Phys. Status Solidi B **257**, 1900655 (2020).	102
[F5.10]	Hexagonal approximant of the dodecagonal oxide quasicrystal on Pt(111), Phys. Rev. Materials **5**, 084006 (2021).	108
[F5.11]	Antiphase Domain Boundary Formation in 2D Ba–Ti–O on Pd(111): An Alternative to Phase Separation, Phys. Status Solidi B **259**, 2100389 (2022).	115
[F5.12]	2D honeycomb transformation into dodecagonal quasicrystals driven by electrostatic forces, Nat. Commun. **13**, 7542 (2022).	123

Observation and Structure Determination of an Oxide Quasicrystal Approximant,

PRL 117, 095501 (2016): http://dx.doi.org/10.1103/PhysRevLett.117.095501

Observation of a dodecagonal oxide quasicrystal and its complex approximant in the SrTiO₃-Pt(1 1 1) system

Sebastian Schenk[1], Stefan Förster[1], Klaus Meinel[1], René Hammer[1],
Bettina Leibundgut[1], Maximilian Paleschke[1], Jonas Pantzer[1],
Christoph Dresler[1], Florian O Schumann[1] and Wolf Widdra[1,2]

[1] Institute of Physics, Martin-Luther-Universität Halle–Wittenberg, Halle, Germany
[2] Max-Planck-Institut für Mikrostrukturphysik, Halle, Germany

E-mail: stefan.foerster@physik.uni-halle.de

Abstract

We report on the formation of a SrTiO₃-derived dodecagonal oxide quasicrystal (OQC) at the interface to Pt(1 1 1). This is the second observation of a two-dimensional quasicrystal in the class of oxides. The SrTiO₃-derived OQC exhibits strong similarities to the BaTiO₃-derived OQC with respect to the local tiling geometry. However, the characteristic length scale of the SrTiO₃-derived OQC is 1.8% smaller. Coexisting with the OQC a large scale approximant structure with a monoclinic unit cell is identified. It demonstrates the extraordinary level of complexity that oxide approximant structures can reach.

Keywords: oxide quasicrystal, SrTiO₃, STM, LEED

(Some figures may appear in colour only in the online journal)

1. Introduction

With the discovery of a two-dimensional oxide quasicrystal (OQC) derived from BaTiO₃ on the Pt(1 1 1) surface, a new class of quasicrystalline materials emerged [1]. For the first time, the formation of an aperiodic structure has been reported for an oxide material. Furthermore, it has been the first example of a spontaneous, epitaxial growth of a dodecagonal structure on a sixfold substrate, thus representing a special case of quasicrystal-crystal heteroepitaxy.

Recently, a single phase approximant was reported for the BaTiO₃-Pt(1 1 1) system, which reveals a 3².4.3.4 Archimedean tiling [2, 5]. This is the prototypical periodic square-triangle tiling, known already from Keplers 'Harmonices mundi' [2, 3]. This approximant develops within a wetting layer of reduced BaTiO₃ spreading across the Pt(1 1 1) surface at slightly higher temperatures as compared to the OQC [1, 2, 4]. A full structure determination of the approximant has proven the purely two-dimensional character of the reduced BaTiO₃-derived structures. Furthermore, it revealed that TiO₃ units reside at the vertices of the tiling and are separated by Ba atoms [2, 5].

The dodecagonal symmetry of the OQC is an interesting parallel to the majority of the soft matter QC systems [6–10]. In addition, both materials classes share a common approximant, the 3².4.3.4 Archimedean tiling. However, the soft-matter systems have been so far strongly limited to square-triangle tilings, whereas the OQC tiling includes a third element, which is the 30° rhomb.

Here we report an experimental approach to elucidate the importance of lattice mismatch between the oxide and the substrate for the OQC formation. This mismatch can be tuned in two ways: either by exchanging the substrate material, or by starting from different oxides. The most intuitive alteration of the BaTiO₃-Pt(1 1 1) system, is the substitution of Ba by Sr. Due to the smaller cation radius of Sr, the lattice constant of SrTiO₃ is 2% smaller as compared to BaTiO₃. Therefore, the lattice mismatch between BaTiO₃ and Pt of 2% vanishes for SrTiO₃ on Pt. Another advantage of this substitution is that this system is still a titanate in contact to Pt, which means only minor change to the chemical nature of the system.

In the following we will demonstrate the OQC formation from SrTiO₃ on Pt(1 1 1). This OQC shows a similar local

tiling structure although its characteristic length will differ. In the two-dimensional wetting layer, additionally, the formation of a complex approximant structure will be reported, which closely resembles the OQC.

2. Experimental

The experiments have been performed in two ultrahigh vacuum (UHV) systems operating at a base pressure of 10^{-10} mbar. One chamber is equipped with an Ar^+ ion sputtering facility, electron-bombardment assisted sample heating, and a fourfold evaporator (EBE4, SPECS, Germany) for the molecular beam epitaxy (MBE) preparation of oxide thin films. For sample characterization Auger-electron spectroscopy (AES) and spot-profile analysis low-energy electron diffraction (SPALEED) are available. The second chamber houses a home-built low-temperature scanning tunneling microscopy (STM) operating at 77 K in combination with low-energy electron diffraction (LEED).

A Pt(1 1 1) single crystal (MaTecK, Germany) with a miscut <0.1° has been used as substrate for the $SrTiO_3$ deposition. The sample has been cleaned by repeated cycles of 600 eV Ar^+ ion sputtering, UHV flashing at 1300 K, and annealing at 900 K in 10^{-6} mbar O_2. The MBE deposition of $SrTiO_3$ has been done by electron-beam assisted evaporation from a Nb-doped(0.05%) $SrTiO_3$ single crystal. From this source, a Ti deficient mixture of SrO and TiO_x arrives at the Pt(1 1 1) surface. The Ti deficiency is compensated by co-evaporation from a Ti rod. The deposition rates of the two sources are calibrated according to a $SrTiO_3$ single crystal AES reference spectrum. During the $SrTiO_3$ deposition, the substrate is kept at room temperature. The film composition is monitored by AES. The film thickness is determined from the damping of the Pt AES peak at a kinetic energy of 235 eV. A 4 Å thin $SrTiO_3$ film has been prepared on Pt(1 1 1) by subsequent deposition of 3 Å out of the $SrTiO_3$ source at an evaporation rate of 0.2 Å min^{-1} and 1 Å from the Ti rod at a rate of 0.5 Å min^{-1}. The deposition was performed in an O_2 atmosphere of 1×10^{-6} mbar and was followed by annealing 10 min at 900 K in 5×10^{-6} mbar O_2. Upon this final annealing step in oxygen, no long-range ordered structures have been detected in SPALEED measurements. Different as for conventional LEED, SPALEED scans the electron beam across the surface and the diffracted intensity is recorded via a channeltron detector, which has the advantage that the full k_x-k_y plane can be imaged. The measurement covers a surface area of 0.5×0.5 cm^{-2}. For further details see [11, 12].

3. Results

3.1. The SrTiO$_3$ derived oxide quasicrystal

Upon annealing the $SrTiO_3$ film at 900 K in UHV, first indications of a long-range ordered surface structures are obtained in the SPALEED measurements. Figure 1 shows SPALEED data upon UHV annealing at 1000 K recorded at different electron energies. The diffraction data show 12 equidistant sharp spots
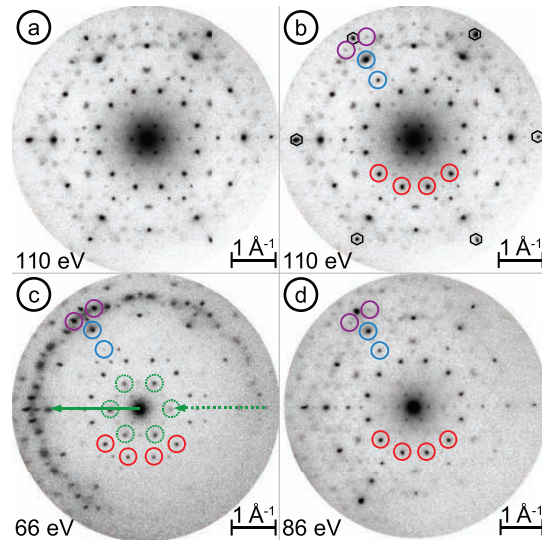

Figure 1. Diffraction pattern of the $SrTiO_3$-derived OQC on Pt(1 1 1) as measured by SPALEED at different electron energies. First, second, and third order OQC spots are marked in red, blue, and magenta, respectively. The black hexagons mark the Pt(1 1 1) first order substrate spots. The solid green arrow in (c) marks a (1100) OQC spot. The dashed green arrow and circles mark the six prominent inner spots as backfolded (1100) OQC spots.

at 1.05 Å^{-1} (marked red in figure 1). Additionally, 12 spots are observed at 1.48 Å^{-1} and at 2.03 Å^{-1}, which are rotated by 15° against the inner 12 spots (blue in figure 1). Other characteristic features are 24 spots at 2.51 Å^{-1} (magenta in figure 1), which can be seen best at 66 eV. Those correspond to the first, second, and third order diffraction spots of a dodecagonal structure, indicating the growth of an $SrTiO_3$-derived OQC. The dodecagonal structure is derived from a four-dimensional hyperhexagonal lattice, which means it is described by four independent lattice vectors [13, 14]. In the projection into the two-dimensional plane, these four lattice vectors are of equal length and seperated by 30° as marked by the four red circles in figure 1. At an electron energy of 66 eV, six additional spots are observed (green in figure 1(c)). These spots are (1100) OQC spots that are backfolded at the unit cell boundaries of the hexagonal substrate, as indicated by the green arrows. The remaining weak spots of sixfold symmetry seen at different energies, result from an additional phase, which will be discussed later.

The rotation of the first oder OQC spots reveals that the vertices of the real space tiling are aligned either parallel to the $\langle 1\,1\,\bar{2} \rangle$ high-symmetry directions of Pt(1 1 1), or parallel to the 30° rotated $\langle 1\,\bar{1}\,0 \rangle$ directions. The alignment of the $SrTiO_3$-derived OQC with respect to the hexagonal substrate is identical to the $BaTiO_3$-derived one [1].

For a quantitative comparison of the edge lengths of the tiling, spot profiles extracted from the diffraction data of the $SrTiO_3$- and the $BaTiO_3$-derived OQC are shown in figure 2. The profiles have been taken for three different symmetry equivalent $\langle 1\,1\,\bar{2} \rangle$ directions, to determine the positions of the
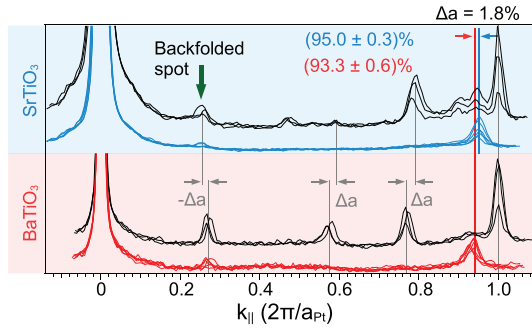
2

S Schenk *et al*

Figure 2. Comparison of SPALEED spot profiles of the SrTiO$_3$-derived OQC (top) and the BaTiO$_3$-derived OQC (bottom). Profiles along three different $\langle 1\,1\,\bar{2}\rangle$ directions of Pt are shown in black. The additional profile lines are taken at angles of $\pm 6.2°$ around the $\langle 1\,1\,\bar{2}\rangle$ directions cutting the (1011) OQC spots of SrTiO$_3$ (BaTiO$_3$) next to the Pt spots (magenta in figure 1).

Figure 3. (a) Atomically-resolved large-scale STM image of the SrTiO$_3$ derived OQC on Pt(111) and its Fourier-transform (FT) (b). The Regions 1 and 2 marked by black squares in (a) will be discussed in the next section. (a) Image size 75×50 nm^2, 20 pA, -0.1 V, height variation 40 pm.

first order substrate spots. In addition, spot profiles have been extracted at angles of $\pm 6.2°$ around these $\langle 1\,1\,\bar{2}\rangle$ directions, for the determination of the position of the (1011) OQC spots (magenta in figure 1). Due to their short distance relative to the Pt spots, the characteristic barrel distortion of SPALEED [12] can be neglected which allows a lattice parameter determination with high accuracy. The different variations of the OQC spot positions Δa at different $k_{\parallel}$ along the $\langle 1\,1\,\bar{2}\rangle$ directions (gray in figure 2) result from these barrel distortions. By this comparison, a 1.8% larger reciprocal edge length is determined for the SrTiO$_3$-derived OQC, as compared to the BaTiO$_3$-derived OQC. This transforms into a 1.8% reduced characteristic length of the SrTiO$_3$-derived OQC in real space, which corresponds to an edge length of 6.72 Å.

The local atomic arrangement of the SrTiO$_3$-derived OQC is shown in the STM image in figure 3(a) taken at 77 K. The FT of the STM image, figure 3(b), shows twelve sharp spots of equal distance to the origin every 30°, which is a first indication for the presence of a dodecagonal structure. However, the higher-order spots are weak. Patches of a well-ordered dodecagonal OQC can be found locally, as shown in the enlarged STM image figure 4. In this atomically-resolved STM image, bright protrusion are recognized, which arrange in equilateral triangles, squares, and 30° rhombs, all sharing a common edge length. These tiling elements are assembled in dodecagonal units, which are highlighted in gray in figure 4. Each dodecagon consists of five squares, twelve triangles, and two rhombs as indicated for the central one in figure 4. The two rhombs are pointing to the center and incline an angle of 150°. Such dodecagonal units are known as building blocks of the ideal Stampfli–Gähler tiling and have also been observed for the BaTiO$_3$-derived OQC [1, 13, 15]. Nine neighboring dodecagonal building blocks are marked in figure 4, which are again forming squares and triangles on $(2 + \sqrt{3})$ larger scale, corresponding to the inflation rule of a dodecagonal quasicrystal. The STM imaging contrast remains unchanged for variations of the sample bias between -1.5 and 1.9 V, which emphasizes that the Ti sublattice is imaged, as it has been proven recently for the BaTiO$_3$-derived structure [2].
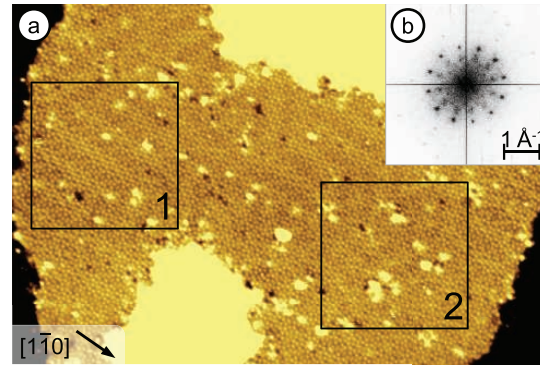
3.2. Identification of a large unit cell approximant

The well-ordered OQC is not the only structure that forms in the wetting layer of reduced SrTiO$_3$ on the Pt(111) surface. Additional and coexisting small domains of an approximant structure are observed. Figure 5(a) shows an enlarged view of Region 1 in figure 3(a). In this region, some darker appearing Ti atoms can be recognized, which form rows running from the upper left side to the lower right side along the $\langle 1\,\bar{1}\,0\rangle$ direction of the substrate. The exact tiling structure of the area in figure 5(a) is shown in figure 5(b). Figure 5(b) reveals that the darker appearing rows are formed by chains of rhombs. As indicated by the blue dodecagons in figure 5(b), these chains result from edge-sharing, equally rotated dodecagonal units. Between neighboring rows, single rhombs are seen, which make it easy to identify the unit cell of the periodic approximant structure. The unit cell is a monoclinic rectangle, which is marked black in figure 5(b).

An idealized approximant's unit cell is shown in figure 5(c), which is constructed from *equilateral* triangles, squares, and 30° rhombs. It contains 36 tiling elements, namely: 24 triangles, nine squares, and three rhombs. These tiling elements are arranged such that a full dodecagonal building block is included in the unit cell. The length of the short axis of the unit cell is 25.1 Å and corresponds to the diameter of the dodecagonal unit, which is $(2 + \sqrt{3})$ times the fundamental length of the OQC. The long side of the unit cell has a length of 37.7 Å and inclines an angle of 95.1° with the short side. The short axis of the approximant unit cell is aligned parallel to the $\langle 1\,\bar{1}\,0\rangle$ direction of the hexagonal substrate. The region shown in figure 5(a) contains ≈ 20 unit cells, which covers $\approx 50\%$ of the area. From the pattern of vertex points of figure 5(b), it is possible to extract a FT of the structure with reduced background intensity, which typically arises from irregularities in the measured STM image. The results are shown in figure 5(d). The positions of the most intense spots of the FT strongly remind on the first and second order spot arrangement of a dodecagonal structure, as marked in red and blue in figure 1(b). But here, these spots are higher-order
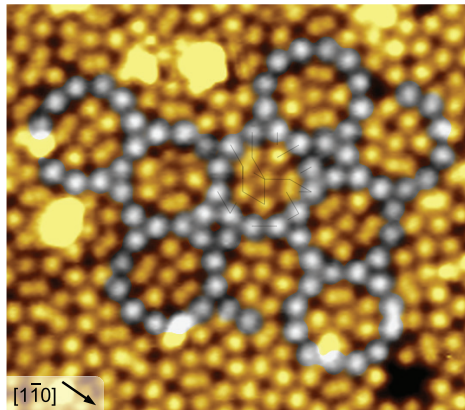
Figure 4. Atomically-resolved STM image of the SrTiO$_3$ derived OQC on Pt(1 1 1). Triangles, squares, and 30° rhombs assemble in dodecagonal units, which is superimposed in the center. These dodecagons arrange in triangles and squares on a $(2 + \sqrt{3})$ larger scale as indicated in gray. Image size 12.3×10.8 nm^{-2}, 20 pA, -0.1 V, height variation 20 pm.
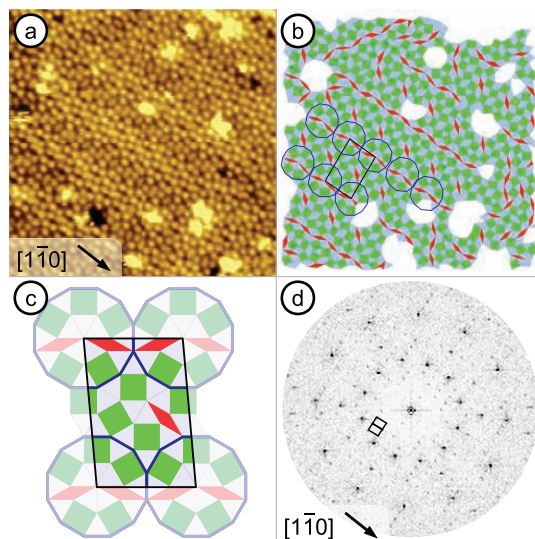

Figure 5. (a) Atomically-resolved STM image of an approximant structure in the SrTi$_3$ wetting layer on Pt(1 1 1). The image is a zoom into Region 1 in figure 3. (b) The local tiling created from triangles, squares, and rhombs as derived from (a). (c) Idealized unit cell of the approximant. (d) Fourier transform of the tiling calculated from the pattern of vertex points of (b).

spots of a fine grid of the monoclinic lattice of the approximant structure, as indicated in black.

Only a few nm appart from Region 1, a second region has been marked in figure 3(a). This Region 2 is shown enlarged in figure 6(a). In this region, a large number of individual dodecagonal building blocks exist. They can be easily identified in the adopted tiling structure shown in figure 6(b) by searching for pairs of rhombs. All observed pairs of rhombs reveal a characteristic geometrical relation: they are rotated by 30°
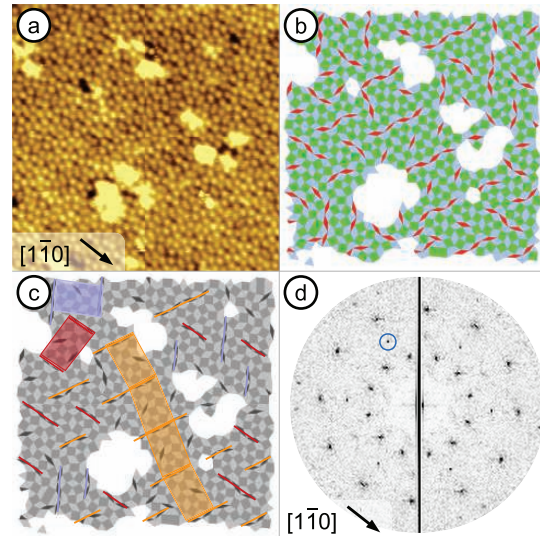

Figure 6. (a) Atomically-resolved STM image of the SrTi$_3$ wetting layer on Pt(1 1 1) in Region 2 of figure 3(a). (b) The local tiling created from triangles, squares, and rhombs as derived from (a). (c) The three occurring orientations of the dodecagonal units parallel to the high-symmetry directions of the substrate are color coded in the tiling of (b) and differently oriented approximant unit cells are highlighted accordingly. (d) FT of the tiling calculated from the pattern of vertex points of (b). The blue circle marks the inner second order spot position of a dodecagonal structure.

with respect to each other. As a consequence, the two rhombs share a straight edge at the connecting vertex, i.e. four of their eight edges are aligned parallel. This is the typical configuration of the dodecagonal building block of the OQC. In a few cases, two dodecagonal units are overlapping, or attached to each other, which result in short rows of three or four rhombs. All dodecagons of this region are rotated such that the four equally oriented edges of the rhombs are parallel to the high-symmetry directions of the substrate, i.e. only rotations of 60° and 120° are observed. To illustrate the parallel alignment of the rhombs to the substrate, the three different $\langle 1\ \bar{1}\ 0 \rangle$ directions of Pt(1 1 1) are represented by bars of different colors in figure 6(c). Individual unit cells of the approximant structure described above can also be identified in Region 2, which are superimposed in figure 6(c). Their color is related to the substrate orientation of the short unit cell vector. The approximant unit cells occur in all three possible rotations. Moreover, some unit cells are mirrored, as can be seen best at the position of the single rhombs inside of the orange cells in figure 6(c).

The FT has also been calculated for the tiling of Region 2, which is shown in figure 6(d). Since no extended domains of the approximant unit cells exist, the weak spots of the monoclinic unit cell at small reciprocal distances completely vanish. The only obvious difference of the FT from an ideal dodecagonal diffraction pattern is the inhomogeneous intensity distribution of the inner twelve second order QC spots, marked in blue in figure 6(d). From the twelve diffraction spots on this ring, only six intense spots every 60° can be recognized. However, these spots are the sharpest spots of the
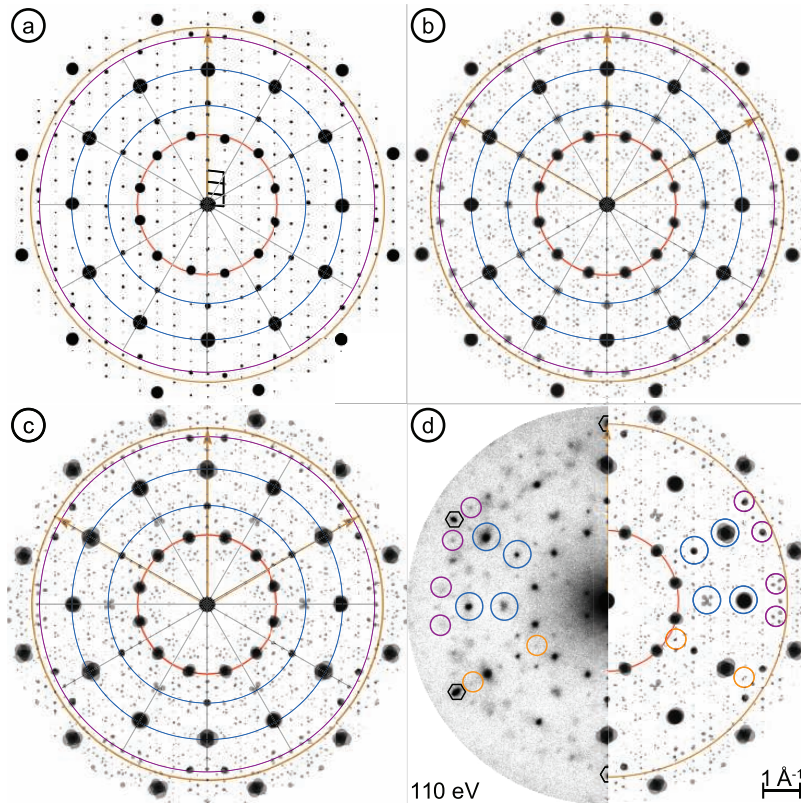
110 eV

1 Å^{-1}

Figure 7. (a) Calculated diffraction pattern of an SrTiO$_3$ approximant domain from the unit cell given in figure 5(c). (b) Superposition of three rotational and three mirror domains. (c) The six domains in registry with the Pt(1 1 1) substrate. (d) Comparison of the measured diffraction pattern of figures 1(a) and (c). The brown circle mark the inverse length of Pt(1 1 1) and the red, blue, and magenta circles mark the positions of the first, second, and third order spots of a dodecagonal lattice. The gray lines mark a 30° tiling of the reciprocal space. For further explanation see text.

whole pattern. The intensities of the six spots in between are smeared out and hard to distinguish from the background. This observation is again related to the differently rotated monoclinic approximant unit cells. All of them contribute equally to the six intense spots, whereas the 30° rotated spots are at slightly different positions for the different domains. Without the knowledge about the approximant, the FT might have been wrongly taken as an indication of a well-ordered OQC patch.

4. Discussion

The large unit cell approximant described in figure 5 is a complex approximant structure in the OQC system. So far, the existence of a 3^2.4.3.4 Archimedean tiling is reported for the BaTiO$_3$-Pt(1 1 1) system. From this rather simple approximant, created from only four triangles and two squares per unit cell, a structure model of the reduced BaTiO$_3$ rewetting layer has been derived recently [2, 5]. Comparing the complexity of the 3^2.4.3.4 Archimedean tiling with the approximant structure introduced here, one finds now six times more tiling elements in the unit cell, including also the rhombs and even a full dodecagon as known from the Stampfli–Gähler tiling. In

fact, the unit cell is an exact cut out of a perfect dodecagonal quasicrystal, which is repeated periodically.

In the following, a complete picture of the complex interplay of the approximant and the *p3m1* symmetry of the Pt(1 1 1) substrate is illustrated, and the consequences for the diffraction pattern are discussed. Using the idealized approximant's unit cell shown in figure 5(c), the calculated diffraction pattern of a single domain of the approximant structure is shown in figure 7(a). The brown circle represents all *k* vectors $k = \frac{2\pi}{a}$, where a is the Pt–Pt next-neighbor distance of the hexagonal Pt(1 1 1) substrate. The red, blue, and magenta circles emphasize the positions of the first, second, and third order diffraction of a dodecagonal grid, respectively. The substrate spots of the hexagonal lattice are observed in the ⟨11$\bar{2}$⟩ directions, indicated by the brown arrow in figure 7(a). In figure 5 it has been shown that the short side of the approximant's unit cell aligns in real space parallel to the ⟨1 $\bar{1}$ 0⟩ substrate directions. In reciprocal space, the short axis of the approximant's cell (marked in black) is oriented parallel to the ⟨1 1 $\bar{2}$⟩ direction. The spot diameter in figure 7(a) represents the relative spot intensities. Due to the structure factor, the pattern of the monoclinic structure exhibits an intensity distribution in the

higher-order spots, which closely resemble the diffraction pattern of a dodecagonal structure. Only slight deviations in the spot positions from the circles, which mark the diffraction orders of a dodecagonal OQC, are noticeable. However, for each of the prominent diffraction orders of the approximant, six symmetry inequivalent spots exist. Those differ in their distance to the origin and their angular spacing, which results from the monoclinic unit cell. This can be nicely seen at the circle according to the first order OQC spots (red), for the inner second order spots (small blue circle) and the third order spots (magenta circle). However, for the most prominent approximant's spots (large blue circle), almost no deviation from the corresponding QC position can be recognized. Deviations below 1% between their lengths and variations of their angles below 0.7% around the 30° positions are found. Due to a coincidence of the short unit cell vector with the $\langle 1\,1\,\bar{2} \rangle$ substrate direction (brown arrow) and the fact that the short diagonal of the unit cell inclines a 60° angle with the short axis, four of these intense higher-order spots exactly hit the 30° grid.

Three rotational domains and three mirror domains of the approximant result from the monoclinic structure on the three-fold-symmetric substrate. In figure 7(b), all six domains are superimposed such that spots of individual domain are drawn semi transparent. Thus, the gray level of the spots can represent added diffraction intensities from different domains. In the superposition of all six domains, many of the characteristic deviations in the diffraction pattern of the approximant with respect to the ideal dodecagonal pattern are averaged out. This can be seen for example in figure 7(b), where all spots on the red circle appear at equal distance from the origin and with equal 30° separation. Only the low-intensity spots clearly reveal the sixfold symmetry imposed by the substrate. Differences are, however, present and would lead to larger deviations at higher diffraction orders.

The lattice parameters of the idealized approximant's unit cell of $a = 25.1$ Å, $b = 37.7$ Å, and $\alpha = 95.1°$ as well as the alignment are close to achieve registry with the Pt(1 1 1) substrate. By changing the lattice parameters slightly to $a = 24.9$ Å, $b = 38.5$ Å, and $\alpha = 94.1°$, the approximant's unit cell can be expressed by a $\begin{pmatrix} 9 & 0 \\ 9 & 16 \end{pmatrix}$ superstructure with respect to Pt(1 1 1). These small differences in the lattice parameters cannot be determined from the STM measurements. However, in the diffraction pattern both unit cells are easily distinguishable. Figure 7(c) shows the calculated diffraction pattern for the $\begin{pmatrix} 9 & 0 \\ 9 & 16 \end{pmatrix}$ commensurate unit cell. The diffraction pattern of figure 7(c) reveals a more pronounced sixfold symmetry, i.e. for almost all orders of diffraction the spot positions along the $\langle 1\,1\,\bar{2} \rangle$ directions (brown arrow) differ significantly from the 30° rotated $\langle 1\,\bar{1}\,0 \rangle$ directions. Very pronounced is the change for the spots corresponding to the inner ring of second order QC reflections (inner blue circle). Here, the spots of all domains coincide along the substrate $\langle 1\,1\,\bar{2} \rangle$ directions, whereas the spots of the six domains are widely spread under 30° rotation. The same is observed for the spots corresponding to the third order QC reflections (magenta circle). Close to

the $\langle 1\,1\,\bar{2} \rangle$ directions, the spots of different domains overlap to sharp features, which is again not the case for the 30° rotated direction. The most intense spots of the approximant (large blue circle) are also strongly affected by changing the lattice parameters. Here, the spots along the $\langle 1\,\bar{1}\,0 \rangle$ directions are broadened significantly, whereas they remain sharp in the $\langle 1\,1\,2 \rangle$ directions.

The comparison of the measured diffraction data of the sample and the calculated diffraction pattern of the $\begin{pmatrix} 9 & 0 \\ 9 & 16 \end{pmatrix}$ approximant superstructure is shown in figure 7(d). It confirms that the approximant unit cell adopts to the Pt(1 1 1) lattice and forms a commensurate layer. All effects of snapping into registry as discussed before are clearly identified in the measured diffraction pattern: The approximant's spots at the position of the inner second order QC spots (blue circles) are sharpened along the sixfold axes and they are heavily smeared out inbetween. The opposite holds for the more intense outer spots, which are broadened along the sixfold axes and sharp inbetween. Additionally, the effect on spots at the third order QC position (magenta cirlces) of sharpening in the vicinity of the Pt spots and wide distribution around the 30° rotated directions is well visible. Moreover, the calculated approximant diffraction pattern allows a clear assignment of the additional spots present in the diffraction pattern (orange circles) to the approximant. At these positions several spots of different domains merge in the diffraction pattern. All residual spots of the measured diffraction pattern do also coincide with lattice points of the monoclinic approximant domains. However, their intensities are weak in the calculated pattern. Please note that the absolute intensities in the calculated diffraction pattern do not reflect the real system, as the calculations are based on the Ti sublattice seen by STM. The ignored Ba and O atoms do also affect the structure factor and thus the measured diffraction intensities.

The slight distortions of the unit cell for adopting commensurability to the Pt substrate have an interesting impact on the side lengths of the three tiling elements. Along the short axis, the length of the unit cell amounts to twice the height of the triangle plus two edge lengths (see figure 5(c)). Since the commensurate unit cell has a short axis of 24.9 Å, the edge length of the tiling elements needs to be 24.9 Å$/(2 + \sqrt{3}) = 6.69$ Å. The short diagonal of the unit cell has a length of three edges plus four times the triangle height. Therefore, the observed length of 44.0 Å, for the commensurate cell leads to an average side length of 6.81 Å in this direction. This describes significant distortions of the tiles within the commensurate unit cell of this large approximant.

The discussion above demonstrates that the measured SPALEED pattern of the SrTiO$_3$-derived wetting layer is dominated by epitaxial domains of a complex approximant. This statement seems to question the existence of a SrTiO$_3$-derived OQC as introduced at the beginning. However, patches as shown in figure 4 exist, in which a large number of adjacent dodecagonal building blocks are found. This arrangement is completely incompatible with the approximant structure, in which these dodecagons appear in well separated rows. Indications how to

6

50

Table 1. Tiling element ratios of the different observed structures in comparison to the ideal values of the OQC and the approximant.

	Triangles	Squares	Rhombs
Region 1	2.83	1	0.37
Region 2	2.79	1	0.36
OQC	$(1+\sqrt{3}) \approx 2.73$	1	$\frac{1}{(1+\sqrt{3})} \approx 0.37$
Approx.	2.66	1	0.33

interpret the atomic arrangement in the SrTiO$_3$ wetting layer can be derived from the evaluation of the local tiling composition. Table 1 compares the tiling frequencies as extracted from Regions 1&2 in figure 3(a), which are only 20 nm apart from each other, with those of the Stampfli–Gähler tiling and the ideal approximant. Both regions show only little deviations in the number of triangles to higher contents as compared to the ideal OQC tiling. For Region 1, 3.7% more triangles have been counted and for Region 2 2.5%. In absolute numbers, these are 31 triangles for Region 1 and 21 triangles in Region 2. Surely, these numbers have to be treated with care since the investigated ensembles in both regions are limited (R1: 1248, R2: 1261 tiles) and the image borders might falsify the overall statistics. Nevertheless, both regions are much closer to the ideal composition of the OQC as compared to the ideal approximant. Most interesting for the understanding of the actual surface structure is Region 2, in which isolated dodecagons coexist with isolated unit cells of the approximant.

All observations show that a strong tendency to assemble triangles, squares, and rhombs exists in the SrTiO$_3$ wetting layer, which follows closely the Stampfli–Gähler type arrangement. The dodecagonal units are influenced by the Pt(111) substrate, as can be seen in the uniform orientation of the rhombs along high-symmetry substrate directions. Depending on the very local tiling frequency, approximant unit cells can be favored, but also larger OQC patches are present. From the distinct orientation of the dodecagons along the Pt directions it is clear that the OQC patches do not form an ideal long-range ordered Stampfli–Gähler tiling. Instead, the OQC patches can be interpreted as random tiling QC, which fills the gaps inbetween small approximant patches.

5. Conclusion

Atomically-resolved STM images and high-resolution SPALEED data demonstrate the formation of an dodecagonal quasicrystal for a SrTiO$_3$ thin film on Pt(111) after an annealing procedure. STM identifies the Ti sublattice, which exhibits a Stampfli–Gähler tiling with an average fundamental length of 6.72 Å. This length is shorter by 1.8% as compared

to the fundamental length of the BaTiO$_3$-derived OQC. This observation highlights that two-dimensional OQCs can form with different lengths on the Pt(111) surface and that no specific lattice mismatch is needed.

Together with the SrTiO$_3$-derived OQC, domains of a complex monoclinic approximant structure coexist. The approximant's unit cell consists of 36 tiles, assembled exactly as in an ideal dodecagonal QC and, by that, including a full dodecagonal unit. For an undistorted approximant's unit cell, the six domains on the hexagonal substrate average out any deviations from the ideal dodecagonal lattice in the first and second order spots. Only for higher order spots small differences occur. The identification of the approximant succeeded due to its commensurate adaption to the Pt(111) lattice, which causes slight modifications of the diffraction pattern.

References

[1] Förster S, Meinel K, Hammer R, Trautmann M and Widdra W 2013 *Nature* **502** 215
[2] Förster S *et al* 2016 *Phys. Rev. Lett.* **117** 095501
[3] Kepler J 1619 *Harmonices Mundi*
[4] Förster S, Flege J I, Zollner E M, Schumann F O, Hammer R, Bayat A, Schindler K M, Falta J and Widdra W 2017 *Ann. Phys.* **529** 1600250
[5] Roy S, Mohseni K, Förster S, Trautmann M, Schumann F, Zollner E, Meyerheim H and Widdra W 2016 *Z. Kristallogr.* **231** 749
[6] Zeng X, Ungar G, Liu Y, Percec V, Dulcey A E and Hobbs J K 2004 *Nature* **428** 157
[7] Hayashida K, Dotera T, Takano A and Matsushita Y 2007 *Phys. Rev. Lett.* **98** 195502
[8] Fischer S, Exner A, Zielske K, Perlich J, Deloudi S, Steurer W, Lindner P and Förster S 2011 *Proc. Natl Acad. Sci.* **108** 1810
[9] Dotera T 2011 *Isr. J. Chem.* **51** 1197
[10] Urgel J I, Écija D, Lyu G, Zhang R, Palma C-A, Auwärter W, Lin N and Barth J V 2016 *Nat. Chem.* **8** 657
[11] Horn-von Hoegen M 1999 *Z. Kristallogr.* **214** 591
[12] Hammer R, Sander A, Förster S, Kiel M, Meinel K and Widdra W 2014 *Phys. Rev.* B **90** 035446
[13] Gähler F 1988 *Quasicrystalline Materials* (Singapore: World Scientific)
[14] Niizeki N and Mitani H 1987 *J. Phys. A: Math. Gen.* **20** L405410
[15] Stampfli P 1986 *Helv. Phys. Acta* **59** 1260

annalen der **physik**

Growth and decay of a two-dimensional oxide quasicrystal: High-temperature in situ microscopy

Stefan Förster[1,2,], Jan Ingo Flege[3,4], Eva Maria Zollner[2], Florian Otto Schumann[2], Rene Hammer[2], Alireza Bayat[2], Karl-Michael Schindler[2], Jens Falta[3,4], and Wolf Widdra[2,5]*

The recently discovered two-dimensional oxide quasicrystal (OQC) derived from $BaTiO_3$ on Pt(111) is the first material in which a spontaneous formation of an aperiodic structure at the interface to a periodic support has been observed. Herein, we report in situ low-energy electron microscopy (LEEM) studies on the fundamental processes involved in the OQC growth. The OQC formation proceeds in two steps via of an amorphous two-dimensional wetting layer. At 1170 K the long-range aperiodic order of the OQC develops. Annealing in O_2 induces the reverse process, the conversion of the OQC into $BaTiO_3$ islands and bare Pt(111), which has been monitored by in situ LEEM. A quantitative analysis of the temporal decay of the OQC shows that oxygen adsorption on bare Pt patches is the rate limiting step of this dewetting process.

1 Introduction

Two-dimensional materials have recently pioneered a new field of materials science. Their peculiar properties are often related to their lower dimensional periodic structure [1]. Aperiodicity is nowadays entering the solid state 2D materials with the recent discovery of a two-dimensional oxide quasicrystal (OQC) [2]. 2D quasicrystals are well-known for soft-matter systems [3–8]. However, the OQC is the only two-dimensional quasicrystal in solid materials, known so far. Common to most of the 2D materials is their formation due to a self-limited growth process catalyzed by a metal support. This holds also for the OQC, which develops in a reduced 2D wetting layer spreading from 3D $BaTiO_3$ islands on Pt(111) [2].

In previous work, a static characterization of the OQC film in coexistence with 3D $BaTiO_3$(111) islands at the Pt(111) surface has been reported [2]. Its dodecagonal structure had been resolved by low-energy electron diffraction, and its local structure has been determined by atomically resolved scanning tunneling microscopy. However, the OQC layer formation involves a massive materials transport across the Pt(111) interface on significantly larger length scales. A detailed knowledge on possible pathways for the OQC formation process, including the dynamics of the materials transport, is still lacking. Experimentally, this task is demanding due to the high formation temperatures of 800-1250 K and different length scales involved.

Here, we report the first in situ observation of the growth processes that lead to the formation of a long-range ordered quasicrystal. Using low-energy electron microscopy (LEEM), the OQC structure formation process has been followed from room-temperature up to 1170 K. Starting from the edges of the 3D $BaTiO_3$ islands, an amorphous 2D layer grows. Its front proceeds from the 3D islands until the entire Pt(111) surface is covered. At temperatures above 1150 K, long-range ordered structures develop in that wetting layer. For submonolayer coverages of $BaTiO_3$ exclusively periodic superstructures have been observed previously [9], whereas for larger initial coverages the long-range ordered OQC forms [2]. By exposing the 2D wetting layer at elevated temperatures to O_2 in situ LEEM reveals a rapid transition back into 3D $BaTiO_3$ islands. With the observed wetting and dewetting under reducing and oxidizing conditions, respectively, the $BaTiO_3$/Pt(111) system reveals parallels to inverse model catalysts in heterogeneous catalysis, for which the

* Corresponding author E-mail: stefan.foerster@physik.uni-halle.de
1 Physik-Institut, Universität Zürich, 8057, Zürich, Switzerland
2 Institute of Physics, Martin-Luther-Universität Halle-Wittenberg, Halle, Germany
3 Institute of Solid State Physics, University of Bremen, Bremen, Germany
4 MAPEX Center for Materials and Processes, University of Bremen, Bremen, Germany
5 Max-Planck-Institut für Mikrostrukturphysik, Halle, Germany

Wiley Online Library

so-called strong metal-support interaction (SMSI) has been found [17, 23].

Our work demonstrates that the OQC serves as ideal candidate for further studies of quasicrystal structure formation in general. Its complexity is significantly lower as compared to any other quasicrystal due to the reduced dimensionality and a smaller size of the building blocks involved [2, 10]. The herein reported nearly isothermal reversibility between a 2D quasicrystal and a periodic island structure (controlled by an external parameter as the oxygen chemical potential) presents ideal grounds for future in-depth studies of the mechanisms leading to the formation of quasicrystals on the nanoscale.

2 Experimental

Ultrathin films of $BaTiO_3$ have been grown on Pt(111) single crystal surfaces using RF magnetron sputtering as described previously [11]. The $BaTiO_3$ films are stable under ambient conditions, which allows for a sample transfer through air. Thus, ex-situ XPS and LEEM characterizations of the samples were performed. The XPS studies were conducted at the SuperESCA beamline of the Elettra third generation synchrotron radiation source in Trieste, Italy. The experimental chamber was equipped with a Phoibos hemispherical energy analyzer (SPECS GmbH) and had a background pressure of about 2×10^{-10} mbar. The LEEM experiments were carried out in a commercial Elmitec LEEM III at the University of Bremen, providing a base pressure of 1×10^{-10} mbar. After re-entering the UHV, annealing in 1×10^{-6} mbar O_2 at 900 K has been applied to remove adsorbates induced by the transfer. By this treatment the samples are free of any contaminations as proven by high-resolution XPS at the SuperESCA beamline in Trieste.

3 Results and discussion

Figure 1 shows the sample morphology of a thin film of $BaTiO_3$ on Pt(111) upon annealing at 1170 K in UHV, as measured by PEEM and LEEM. In the PEEM image in Fig. 1(a), a large number of islands of different size appear with dark contrast. In-between the islands, a continuous film is present, which appears bright due to a higher photoemission yield. Islands and film cover the entire Pt(111) surface as demonstrated in Fig. 1(a) with a field of view (FOV) of 50 μm. In the LEEM image of the same region in Fig. 1(b) taken with a FOV of 25 μm at an electron beam energy of 16.5 eV, the contrast between the islands and the film is inverted. Furthermore, the
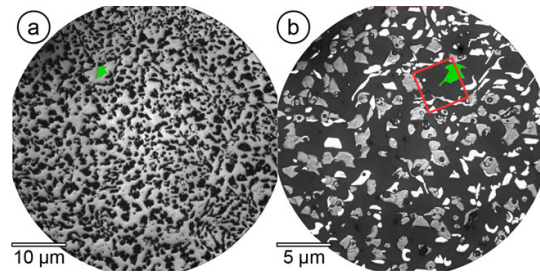

Figure 1 Large-scale photoemission electron microscopy (PEEM) and LEEM images of ultrathin $BaTiO_3$ on Pt(111) upon UHV annealing at 1170 K. The PEEM image (a) shows islands (dark) embedded in a continuous layer of a lower work function material (bright). In the enlarged LEEM image (b) the contrast is inverted. The reflectivity variations between different islands represent their structural inequivalence. The island marked in green serves as a guide to the eye. (a) $h\nu = 4.9$ eV. (b) $E_{kin} = 16.5$ eV.
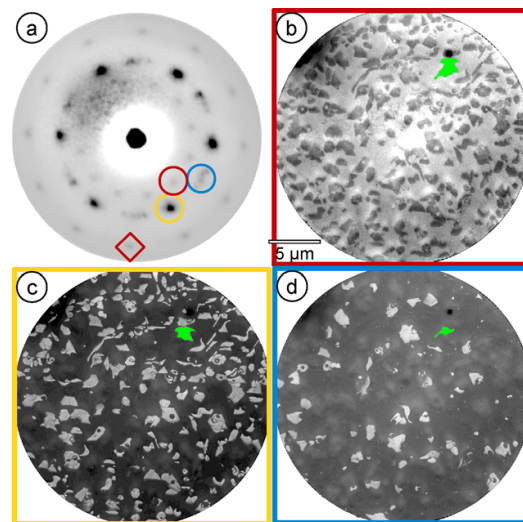
Figure 2 μLEED and dark field LEEM characterization of ultrathin $BaTiO_3$ on Pt(111) as shown in Fig. 1(b). The diffraction spots marked by red, yellow, and blue circles have been selected for the dark field imaging of the OQC (b), of non-rotated $BaTiO_3$ islands (c), and of rotated $BaTiO_3$ islands (d), respectively. (a) $E_{kin} = 19.5$ eV. (b) $E_{kin} = 14.6$ eV, (c) $E_{kin} = 14.1$ eV, (d) $E_{kin} = 13.9$ eV.

observed contrast in LEEM suggests the presence of several types of islands as indicated by the different gray levels.

The μLEED pattern of the region shown in Fig. 1(b) is shown in Fig. 2(a). It reveals the co-existence of several long-range ordered structures. Three rings of twelve

features can be distinguished in the diffraction diagram. The outer and the inner ring (marked red) are formed by twelve spots of matching intensity and sharpness. Both rings are rotated by 15° against each other and correspond to diffraction from the dodecagonal OQC. The twelve features at intermediate distance can be assigned to two hexagonal structures (marked yellow and blue) of identical reciprocal length in different orientations with respect to the substrate, whose first-order diffraction peaks lie outside the Ewald sphere at this low energy. The six spots of highest intensity (marked in yellow) originate from a BaTiO$_3$(111) lattice that is aligned along the high-symmetry directions of Pt(111) (see Supporting Information), called non-rotated BaTiO$_3$(111) from now on. The 30° rotated elongated features in the diffraction pattern (marked in blue) result from BaTiO$_3$(111) structures in different orientation at angles of $30 \pm 10°$ with respect to the substrate.

Dark field imaging has been used to relate the individual diffraction patterns of Fig. 2(a) to real-space features shown in Fig. 1(b). Upon selecting an individual spot of the diffraction pattern by an aperture in the diffraction plane of the microscope [12], all features of the related structure appear bright in the real-space image. Figure 2(b) shows the dark field LEEM image corresponding to the OQC (red in Fig. 2(a)). The continuous film in-between the islands appears with a homogeneous, bright contrast in Fig. 2(b) indicating the presence of a well-developed OQC structure here. For the PEEM image in Fig. 1(a) this observation allows to assign the high photoelectron yield to the OQC area. PEEM shows that the OQC layer extends to a scale of tens of micrometers at least. It proves that the OQC covers the entire surface between the BaTiO$_3$ islands. By selecting a spot of the non-rotated BaTiO$_3$(111) structure (yellow marked diffraction spot in Fig. 2(a)), the majority of the islands appears bright in the dark-field LEEM image as shown in Fig. 2(c). All additional islands have differently rotated BaTiO$_3$(111) structure as proven by the corresponding dark-field LEEM image in Fig. 2(d). Their orientation varies in an interval of $\pm 10°$ around a 30° rotation with respect to the Pt(111) lattice vectors.

Figure 3(a) and (b) show magnified views of the area inside the red rectangle in Fig. 1(b). In Fig. 3(a) the OQC covers the Pt(111) surface between the large BaTiO$_3$(111) islands. The large island on the right side is the one marked green in Fig. 1. Upon annealing in an O$_2$ atmosphere of 7×10^{-7} mbar, dewetting of the OQC film sets in, which is shown in detail in Fig. 3(b). In the area that was covered by the OQC before, small BaTiO$_3$ islands are formed that exhibit an intermediate intensity. The surroundings of the small islands appear bright in LEEM
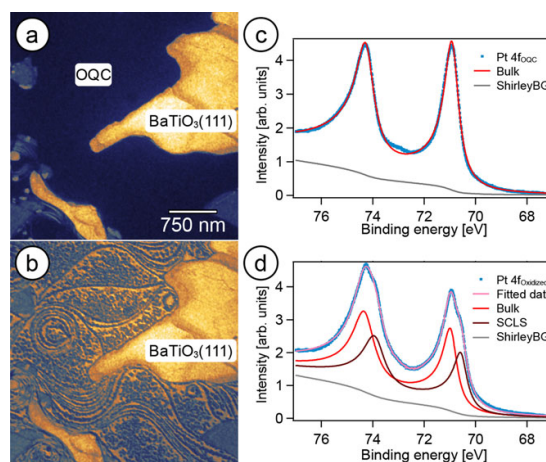

Figure 3 The two configurations of ultrathin BaTiO$_3$ on Pt(111) as measured with LEEM (a, b), and XPS (c, d). Upon annealing at 1170 K in UHV the OQC is present (a, c). By annealing at 900 K in 7×10^{-7} mbar O$_2$ the OQC is transformed into BaTiO$_3$ islands and bare Pt(111) (b, d). (a,b) E$_{kin}$ = 14.1 eV. (c, d) hν = 140 eV.

and will be assigned to areas of bare Pt(111) (see below). The large BaTiO$_3$(111) islands remain unchanged upon annealing in O$_2$. High-resolution XPS spectra for the Pt 4f core level, Fig. 3(c), show a single-component 4f doublet for the OQC covered surface with a Doniach-Sunjic line shape [13]. Upon annealing in O$_2$ a second doublet appears at 0.4 eV lower binding energy as shown in Fig. 3(d). Its appearance and energy fit well to the formation of areas of bare Pt(111) with the well-known Pt(111) surface core level shift [14, 15] (for details see Supporting Information). This observation implies that the OQC dewets the Pt(111) substrate and coalesces into BaTiO$_3$(111) islands.

Besides a static characterization, LEEM allows for a high-temperature in situ observation of the OQC structure *formation process* on a time scale of seconds as demonstrated in Fig. 4. The LEEM data provide direct insights into the high-temperature wetting process that leads to OQC formation. Our starting point for the wetting layer formation is a surface morphology as shown in Fig. 3(b), in which large and small BaTiO$_3$ islands are present and surrounded by bare Pt. Wetting occurs at 1020 K in an UHV environment with a total pressure below 5×10^{-9} mbar. Due to a temperature increase of 120 K in comparison to Fig. 3(b), the small islands coalesce due to Ostwald ripening, decreasing their number and increasing their individual areas. With increasing time from Fig. 4(a) to (f), a dark contrast develops in the
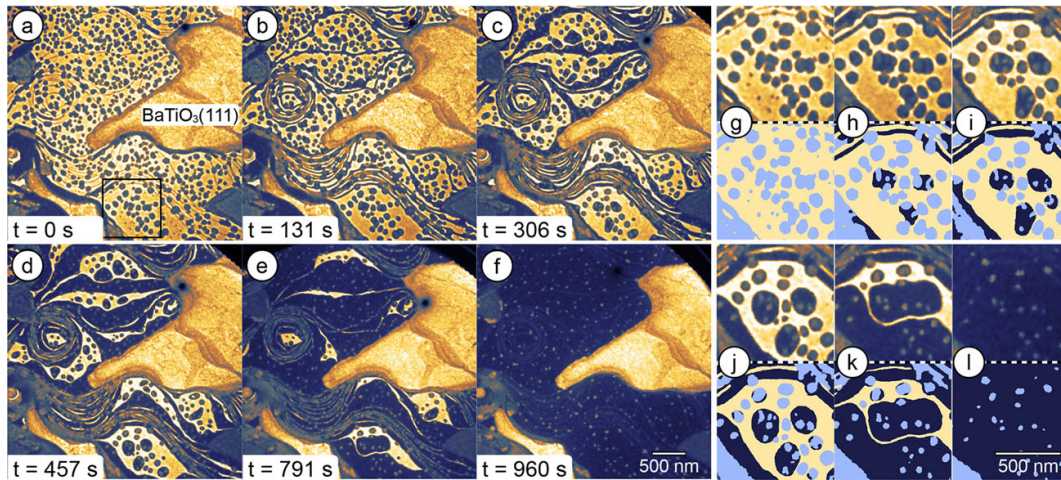
Figure 4 *In situ* LEEM measurement of the growth of the 2D OQC upon UHV annealing at 1020 K. (g)-(l) show magnified views of the area inside the black square in (a). For better recognition the three different phases are color coded in the schematic image below the measurement. Free Pt area is colored yellow, $BaTiO_3$ islands are light blue and the wetting layer is dark blue. Movies corresponding to the shown image sequences are available in the Supporting Information.

images, which spreads across the Pt terraces. This dark contrast is identical to that of the OQC in Fig. 3(a).

To follow the very details of the wetting process, the lower large terrace in Figs. 4(a)-(f) (marked with a black square in (a)) is shown enlarged in (g)-(l). The wetting layer nucleates at the islands. With time, the wetting layer grows as circular coronas around the islands with sharp boundaries to the hot Pt. As a consequence of a growing wetting layer the size of the islands reduces with time, which is best seen by comparing Figs. 4(g) and (l). At surface steps the wetting layer formation is different as seen at the top of Figs. 4(g)-(k). The excess material of the islands is wetting from the steps instead of forming a corona around the islands. When growing with time, patches of the 2D wetting layer merge to form a continuous film starting from the step edges as can be best seen in the upper part of Figs. 4(a)-(f). At the end of the wetting process the entire Pt area is covered by a continuous layer. Only few residual islands remain. The wetting process takes about 15 min at the given temperature and can be followed in full detail. However, at a temperature of 1020 K the wetting layer is disordered (see Supporting Information). Therefore, the wetting layer formation upon high-temperature annealing in UHV is a phase transition from small three-dimensional $BaTiO_3$ islands into a two-dimensional amorphous phase with liquid-like edge morphology.

Annealing at higher temperatures induces long-range ordering, and the OQC structure develops at 1170 K. The

LEEM image taken upon annealing at 1170 K as shown in Fig. 3(a) reveals a homogeneous OQC film in-between the large $BaTiO_3(111)$ islands. The residual material of the small islands, which is not completely consumed during the local wetting layer formation, disperses into the large $BaTiO_3(111)$ islands due to Ostwald ripening.

Once it has formed, the OQC layer is stable in UHV over a wide temperature range. From room temperature up to 865 K this has been followed using in situ μLEED as shown in Fig. 5. Besides the bright first-order diffraction spots of the OQC, a large number of weak spots can be recognized for temperatures up to 770 K. They can be assigned to higher order diffraction or to backfolded spots originating from the first order Pt(111) substrate spots as described elsewhere [2]. At 965 K the most intense spots are still well recognizable, but the secondary electron background has strongly increased (Fig. 5(c)). At even higher temperatures, the strong increase of the secondary electron background does not allow for further LEED measurements. It might be speculated here that the OQC will remain stable up to the formation temperature of 1170 K.

The reverse process, i. e., the decay of the OQC film into periodic $BaTiO_3$ islands during annealing in O_2 atmosphere, has also been followed by in situ LEEM as illustrated in Fig. 6. At a constant 900 K sample temperature, O_2 was introduced into the UHV chamber and the in situ changes of the surface morphology have been recorded. At a pressure of 7×10^{-7} mbar of O_2 the OQC

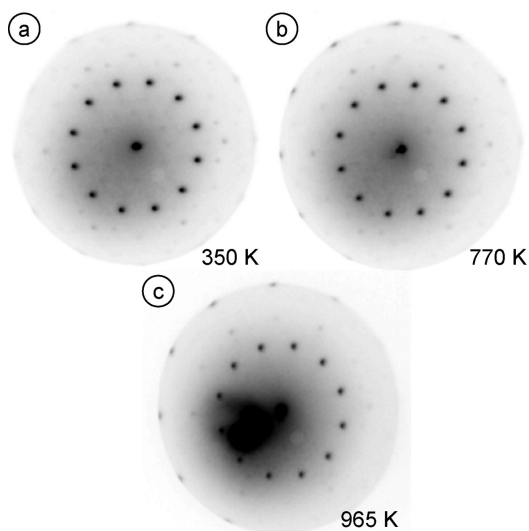**Figure 5** μLEED at elevated temperatures of 350, 779, and 965 K. $E_{kin} = 14.0$ eV. The inelastic background is strongly increased in (c), prohibiting LEED at even higher temperatures.

is starting to decay. Starting dominantly from the upper edges of the Pt(111) steps, the bright contrast of the bare Pt becomes visible. In a dendritic fashion, the bare Pt area is growing with time across the terraces replacing the OQC film. This can clearly be seen in the magnified images of Figs. 6(g)-(j), which focus on the lower central terrace of Figs. 6(b) to (e). They show that no sharp boundary between the OQC and the free Pt exists during dewetting. Instead, small islands form at the periphery of the free Pt area that can be recognized by an intermediate contrast.

At the given O_2 partial pressure of 7×10^{-7} mbar and a sample temperature of 900 K, the dewetting takes about 90 s. To characterize the dewetting process further, the change in morphology with time inside the white dotted rectangle of Fig. 6(f) has been evaluated. The increase in dewetted Pt(111) area with oxygen exposure is shown in Fig. 7. It clearly is a highly non-linear self-accelerating process. A quantitative analysis unveils an exponentially growing dewetted area (solid line in Fig. 7). This finding points to an oxygen-controlled dewetting process where oxygen adsorption takes place almost exclusively at bare Pt sites. In turn, it also demonstrates the relative inertness of the intact OQC structure against O_2 adsorption. In a series of experiments not shown here a strong dependence of the kinetics of the OQC decay on the adsorption probability of oxygen has been found, which is
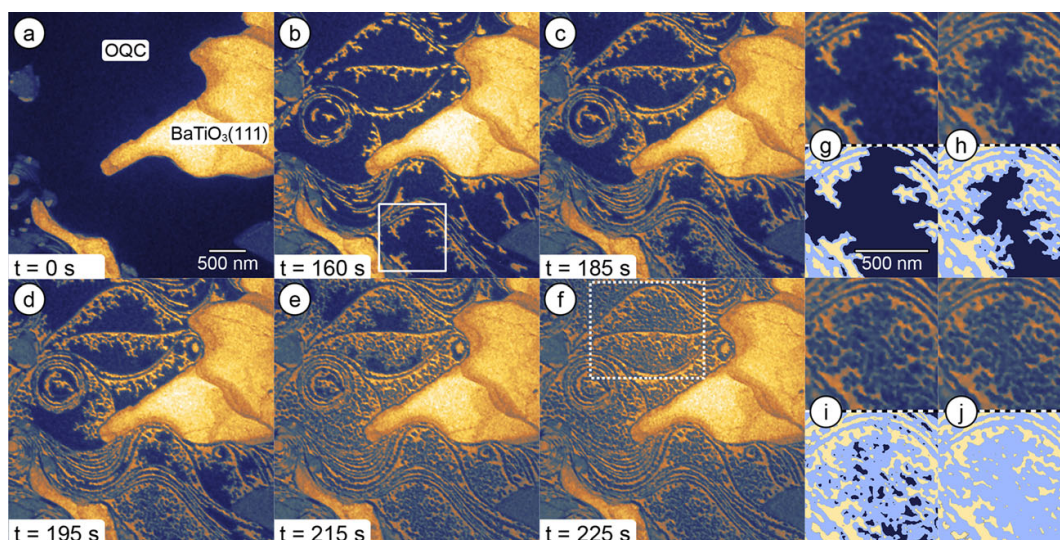
Figure 6 *In situ* LEEM measurement of the OQC decay by annealing in 7×10^{-7} mbar O_2 at 900 K. (g)-(j) show enlarged views of the area inside the white square in (b) for the time span from 160 s to 215 s. For better recognition the three different phases are color coded in the schematic image below the measurement. Bare Pt(111) regions are yellow, $BaTiO_3$ islands are light blue and the OQC is dark blue. Movies corresponding to the shown images are available in the Supporting Information. (a-f) Image size $3.5 \times 3.5 \mu m^2$.

Editor's Choice

Figure 7 Temporal evolution of the OQC dewetting process: The area of bare Pt(111) that was covered by the OQC before was evaluated from the LEEM data inside the dashed rectangle of Fig. 6(f).

influenced by both, temperature and O_2 partial pressure. This is in line with the interpretation that bare Pt catalyzes the dissociation of molecular oxygen, which leads t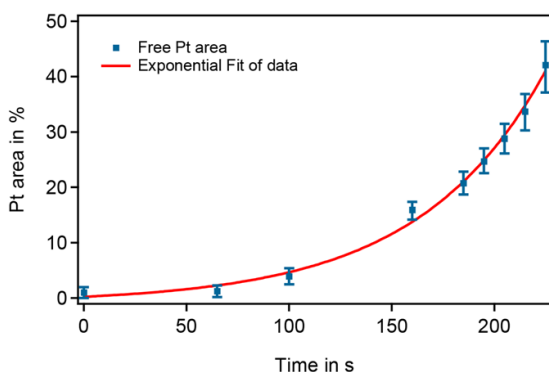o an oxidation of the OQC starting from the edges. The result of the oxidation is stoichiometric $BaTiO_3$, which locally transforms into 3D islands.

The high-temperature wetting of a metal surface under reducing conditions and dewetting in an oxidizing environment as observed here for ultrathin $BaTiO_3$, is well-known for a number of binary oxides in heterogeneous catalysis and is related there to the so-called "strong metal-support interaction" (SMSI) [16]. SMSI refers to changes in the chemisorption properties, and thus the catalytic activity of a given system, upon a morphological transformation, typically the encapsulation of a metal nanoparticle by the oxide support. Originally discovered for group VIII noble metal nanoparticles on TiO_2 support [17] the SMSI effect has been found for a number of binary transition metal oxides [18–20] and more recently also in ternary oxide systems [21, 22]. The migration of a reduced oxide thin film onto the metal surface, often called the SMSI state, has also been observed for low coverages of transition metal oxides on a metal support [23]. This configuration is commonly referred to as an inverse model catalyst [24], which resembles the situation of ultrathin $BaTiO_3$ on Pt(111) as described here. The rich phase diagram of complex monolayer structures of $BaTiO_x$ on Pt(111) [2, 9, 25] is an interesting analog to the observations for ultrathin TiO_x on Pt(111) [26–29], which emphasizes that it might be worth investigating the catalytic properties of the chemically yet unexplored $BaTiO_x$/Pt(111) system.

4 Conclusion

The first mesoscale characterization of an OQC under growth conditions is presented, covering length scales from 50 nm to 50 μm. We demonstrate the reversible isothermal transformation between a two-dimensional aperiodic quasicrystalline film and a three-dimensional crystalline island structure. Controlled by the oxygen partial pressure, the $BaTiO_3$-derived OQC decays at temperatures above 900 K into $BaTiO_3$ islands and bare Pt(111) in-between. Oxygen dissociation on bare Pt patches is identified as the rate-limiting step for this dewetting process. Starting from defect sites of the OQC at step edges, the dewetting proceeds in a dendritic fashion with an exponential time dependence. The reverse transformation, the formation of long-range aperiodic order, has been shown to proceed via an amorphous two-dimensional precursor layer. The OQC has been found to be the equilibrium structure of the 2D layer that is formed at temperatures above 1170 K. In situ μLEED reveals the stability of the OQC structure in the entire temperature range down to room temperature. Furthermore, the in situ LEEM studies reveal that the large $BaTiO_3(111)$ islands act as a materials reservoir only and are not involved in the OQC formation process. This paves the way to the fabrication of perfect OQC monolayers.

References

[1] S. Z. Butler, S. M. Hollen, L. Cao, Y. Cui, J. A. Gupta, H. R. Gutiérrez, T. F. Heinz, S. S. Hong, J. Huang, A. F. Ismach, E. Johnston-Halperin, M. Kuno, V. V. Plashnitsa, R. D. Robinson, R. S. Ruoff, S. Salahuddin, J. Shan, L. Shi, M. G. Spencer, M. Terrones, W. Windl, and J. E. Goldberger, ACS Nano **7**, 2898 (2013).

[2] S. Förster, K. Meinel, R. Hammer, M. Trautmann, and W. Widdra, Nature **502**, 215 (2013).

[3] X. Zeng, G. Ungar, Y. Liu, V. Percec, A. E. Dulcey, and J. K. Hobbs, Nature **428**, 157 (2004).

[4] K. Hayashida, T. Dotera, A. Takano, and Y. Matsushita, Phys. Rev. Lett. **98**, 195502 (2007).

[5] J. Mikhael, J. Roth, L. Helden, and C. Bechinger, Nature **454**, 501 (2008).

annalen der **physik**

[6] S. Fischer, A. Exner, K. Zielske, J. Perlich, S. Deloudi, W. Steurer, P. Lindner, and S. Förster, Proc. Natl. Acad. Sci. **108**, 1810 (2011).

[7] N. A. Wasio, R. C. Quardokus, R. P. Forrest, C. S. Lent, S. A. Corcelli, J. A. Christie, K. W. Henderson, and S. A. Kandel, Nature **507**, 86 (2014).

[8] J. I. Urgel, D. Écija, G. Lyu, R. Zhang, C.-A. Palma, W. Auwärter, N. Lin, and J. V. Barth, Nat. Chem. **8**, 657 (2016).

[9] S. Förster, K. Meinel, K.-M. Schindler, and W. Widdra, Surf. Interface Anal. **44**, 628 (2012).

[10] W. Steurer, Chem. Soc. Rev. **41**, 6719 (2012).

[11] S. Förster and W. Widdra, Surf. Sci. **604**, 2163 (2010).

[12] J. I. Flege, W. X. Tang, and M. S. Altman, in: Characterization of Materials, edited by E. N. Kaufmann (John Wiley & Sons, Inc., 2012), 1–22.

[13] S. Doniach and M. Sunjic, J. Phys. C: Solid State Phys. **3**, 285 (1970).

[14] M. Shek, P. Stefan, C. Binns, I. Lindau, and W. Spicer, Surf. Sci. **115**, L81 (1982).

[15] K. Dückers, H. Bonzel, and D. Wesner, Surf. Sci. **166**, 141 (1986).

[16] S. J. Tauster, Acc. Chem. Res. **20**, 389 (1987).

[17] S. J. Tauster, S. C. Fung, and R. L. Garten, J. Am. Chem. Soc. **100**, 170 (1978).

[18] S. J. Tauster, S. C. Fung, R. T. K. Baker, and J. A. Horsley, Science **211**, 1121 (1981).

[19] Z. Hu, K. Kunimori, H. Asano, and T. Uchijima, J. Catal. **112**, 478 (1988).

[20] Y. N. Sun, Z. H. Qin, M. Lewandowski, E. Carrasco, M. Sterrer, S. Shaikhutdinov, and H. J. Freund, J. Catal. **226**, 359 (2009).

[21] Z. Wang, B. Liu, and J. Lin, Appl. Cat. A **485**, 130 (2013).

[22] Z. Wang, J. Lin, R. Wang, and K. Wei, Catal. Commun. **32**, 11 (2013).

[23] C. S. Ko and R. J. Gorte, Surf. Sci. **161**, 597 (1985).

[24] K. Hayek, M. Fuchs, B. Klötzer, W. Reichl, and G. Rupprechter, Top. Catal. **13**, 55 (2000).

[25] S. Förster, M. Trautmann, S. Roy, W. A. Adeagbo, E. M. Zollner, R. Hammer, F. O. Schumann, K. Meinel, S. K. Nayak, K. Mohseni, W. Hergert, H. L. Meyerheim, and W. Widdra, Phys. Rev. Lett. **117**, 095501 (2016).

[26] F. Sedona, M. Eusebio, G. A. Rizzi, G. Granozzi, D. Ostermann, and K. Schierbaum, Phys. Chem. Chem. Phys. **7**, 697 (2005).

[27] G. Barcaro, S. Agnoli, F. Sedona, G. A. Rizzi, A. Fortunelli, and G. Granozzi, J. Phys. Chem. C **113**, 5721 (2009).

[28] E. Cavaliere, L. Artiglia, G. Barcaro, G. A. Rizzi, F. Bondino, A. Fortunelli, L. Gavioli, and G. Granozzi, Phys. Chem. Chem. Phys. **13**, 17171 (2011).

[29] G. Barcaro, E. Cavaliere, L. Artiglia, L. Sementa, L. Gavioli, G. Granozzi, and A. Fortunelli, J. Phys. Chem. C **116**, 13302 (2012).

[30] Q. Fu, F. Yang, and X. Bao, Acc. Chem. Rec. **46**, 1692 (2012).

Supporting Information

Additional supporting information may be found in the online version of this article at the publisher's website.

Full real-space analysis of a dodecagonal quasicrystal

Sebastian Schenk,[a] Eva Maria Zollner,[a] Oliver Krahn,[a] Berit Schreck,[a] René Hammer,[a] Stefan Förster[a]* and Wolf Widdra[a,b]

[a]Institute of Physics, Martin-Luther-Universität Halle-Wittenberg, Halle, Germany, and [b]Max-Planck-Institut für Mikrostrukturphysik, Halle, Germany. *Correspondence e-mail: stefan.foerster@physik.uni-halle.de

The atomically resolved real-space structure of a long-range-ordered dodecagonal quasicrystal is determined based on scanning tunnelling microscopy. For the BaTiO$_3$-derived oxide quasicrystal which spontaneously forms on a Pt(111) surface, 8100 atomic positions have been determined and are compared with an ideal Niizeki–Gähler tiling. Although the Niizeki–Gähler tiling has a complex three-element structure, the abundance of the triangle, square and rhomb tiling elements in the experimental data closely resembles the ideal frequencies. Similarly, the frequencies of all possible next-neighbour tiling combinations are, within the experimental uncertainty, identical to the ideal tiling. The angular and orientational distributions of all individual tiling elements show the characteristics of the dodecagonal quasicrystal. In contrast, the analysis of the orientation of characteristic and more complex tiling combinations indicates the partial decomposition of the quasicrystal into small patches with locally reduced symmetry. These, however, preserve the long-range quasicrystal coherence. The symmetry reduction from dodecagonal to sixfold is assigned to local interaction with the threefold substrate. It leads to atomic flips which preserve the number of quasicrystal tiling elements.

1. Introduction

A real-space analysis of quasicrystal (QC) tilings is in general a very difficult task. For icosahedral QCs, that are aperiodic in all three dimensions, averaging methods like high-resolution transmission electron microscopy (HRTEM) cannot be applied. Instead, the information on the QC tiling has typically been obtained from atomically resolved scanning tunnelling microscopy (STM) measurements (Cai *et al.*, 2002; Papadopolos *et al.*, 2008; McGrath *et al.*, 2010). However, systematic statistical studies of icosahedral tilings based on atomic vertex positions have not been reported so far. Dodecagonal QCs exhibit aperiodic order within the dodecagonal plane, but periodic order in the perpendicular direction. This reduced complexity allows the averaging along atomic rows perpendicular to the dodecagonal plane which has led to dodecagonal structure determination in intermetallic alloy QCs (Ishimasa *et al.*, 1985, 2015; Chen *et al.*, 1988; Krumeich *et al.*, 1998; Iwami & Ishimasa, 2015). For an Mn–Cr–Ni–Si alloy, Ishimasa *et al.* recently pushed the limit of QC tiling analysis to the 10 nm range using HRTEM (Ishimasa *et al.*, 2015). In their work QC domains of roughly 2000 vertices have been analysed in physical and phason space. Besides intermetallic systems, dodecagonal structures are also observed in soft matter (Zeng *et al.*, 2004; Hayashida *et al.*, 2007; Talapin *et al.*, 2009; Steurer, 2012; Chanpuriya *et al.*, 2016; Fischer *et al.*, 2011; Iacovella *et al.*, 2011; Engel & Trebin, 2007; Dotera *et al.*, 2014) as well as in
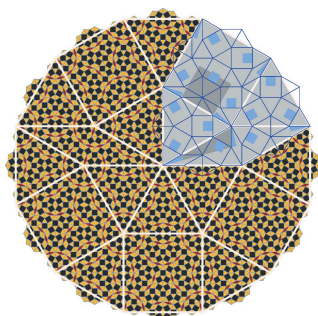
aperiodic 2018

ultrathin 2D adlayers on ideal metal surfaces (Förster *et al.*, 2013; Urgel *et al.*, 2016; Paßens *et al.*, 2017).

Here we present a large-area real-space analysis for the 2013-discovered oxide quasicrystal (OQC), which is derived from an ultrathin $BaTiO_3$ layer on a single-crystal Pt(111) substrate (Förster *et al.*, 2013). Its atomic structure is imaged directly by means of scanning tunnelling microscopy (STM). This technique is used for the first time to analyse a QC on an atom-by-atom basis and to address local defects as well as structural coherence on a 50 nm length scale. 8100 atomic positions within a dodecagonal OQC are analysed and compared with high-resolution electron diffraction from the same structure.

2. The dodecagonal Niizeki–Gähler tiling

2D OQCs as derived from $BaTiO_3$ and $SrTiO_3$ on the Pt(111) surface are constructed from three tiling elements of common edge length, namely equilateral triangles, squares and rhombs inclining 30° and 150° angles. Using these elements an ideal dodecagonal tiling can be constructed as introduced independently by Niizeki & Mitani (1987) and Gähler (1988). We will refer to this tiling as Niizeki–Gähler tiling (NGT). The NGT exhibits a characteristic higher-order building block, which is a dodecagon, that consists of 12 triangles, five squares and two rhombs as drawn in white in Fig. 1.

The NGT can be generated by recursion (Liao *et al.*, 2013) starting from one of the elementary tiling elements or, as shown in Fig. 1, from the characteristic dodecagon. In a single deflation step, each triangle is replaced by seven triangles and three squares of smaller length. Each square is replaced by 16 triangles, five squares and four rhombs, whereas each rhomb is replaced by eight triangles, two squares and three rhombs. These substitutions give rise to the blue tiling in the upper
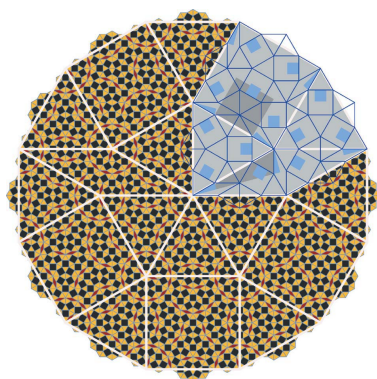
right of Fig. 1. According to the recursion rule, the symmetry of squares and rhombs is reduced. The squares have only mirror symmetry due to their decoration with rhombs in the next generation of the tiling. This reduced symmetry is emphasized by the shaded grey and blue areas in Fig. 1. The presence of squares inside the rhombs upon recursion likewise lowers the symmetry of the rhombs to C_1.

The substitution can be expressed mathematically using a deflation matrix T:

$$T = \begin{pmatrix} 7 & 16 & 8 \\ 3 & 5 & 2 \\ 0 & 4 & 3 \end{pmatrix}. \tag{1}$$

In this representation of T the rows of the matrix are assigned to the number of triangle, square and rhomb tiles, respectively, and thus every vector operation on T depends on this representation. The eigensystem solution of T reveals two important properties of the NGT. Firstly, one can derive the scaling factor of self-similarity in the NGT of $(2 + 3^{1/2})$ from the square root of the eigenvalue. Secondly, the corresponding eigenvector of the deflation matrix T

$$[(1 + 3^{1/2}), 1, (1 + 3^{1/2})^{-1}] \simeq (2.73, 1, 0.37) \tag{2}$$

represents the tiling element ratio in the NGT: the numbers of triangles relative to the numbers of squares and of rhombs. For a finite tiling from any start configuration, the number of tiling elements will converge to these values upon multiple deflation iterations. By deflating the white dodecagon in Fig. 1 twice, one derives a tiling consisting of 2708 vertices, which contains 2640 triangles (gold), 953 squares (black) and 338 rhombs (red). The corresponding tiling frequency of 2.75:1:0.38 already closely resembles the ideal value.

3. Experimental

Ultrathin $BaTiO_3$ films were grown on Pt(111) by radio-frequency-assisted magnetron sputter deposition as reported elsewhere (Förster & Widdra, 2010). The OQC develops upon annealing the $BaTiO_3$ films at temperatures above 1150 K in ultrahigh vacuum (UHV) (Förster *et al.*, 2013). The long-range order has been confirmed by low-energy electron diffraction. For low-temperature STM measurements the sample has been transferred into a home-built STM chamber using an UHV suitcase. The data have been recorded at 77 K.

For conducting the statistical analysis of the length and angular distributions, the STM images have been corrected for piezo-scanner creep and thermal drift in the scanning tunnelling microscope. The background-subtracted data have been corrected by using a plugin to the opensource software *ImageJ* (Schneider *et al.*, 2012) developed by Michael Schmid (TU Vienna). This plugin applies higher-order non-linear corrections to remove the creep-induced distortions from the STM data by maximizing the intensity of selected spots in the Fourier transform of the image. Subsequently, linear corrections have been applied using *Gwyddion* (Nečas & Klapetek, 2012). The final STM image has been scaled to meet an average next-neighbour distance of 6.85 Å. This length has

Figure 1
Niizeki–Gähler tiling on different length scales as generated from recursion, emphasizing its self-similarity. The white lines represent a first-generation tiling. In the upper right part the substitution rule for the three elements is given. The symmetry of rhombs and squares is reduced as indicated by the shaded areas. The blue lines represent the tiling deflated once, which scales with $(2 + 3^{1/2})^{-1}$. The smallest scale tiling, indicated by black squares, golden triangles and red rhombs, results from a second deflation.

been previously evaluated from low-energy electron diffraction (Förster *et al.*, 2013). The further analysis was done with the help of the image and mesh processing capabilities of *Mathematica* (Wolfram Research).

4. Statistical analysis

Fig. 2(*a*) shows an atomically resolved STM image of the $BaTiO_3$-derived OQC. Two terraces are present in this region separated by a monoatomic step [white line in the lower left part of Fig. 2(*a*)]. The contrast has been adjusted to make the detailed atomic structure of each terrace visible. A purely background-subtracted version of this image is available in the supporting information. The bright protrusions in the STM image arise from the Ti grid of the OQC as previously demonstrated for the sigma phase approximant (Förster *et al.*, 2016).

The few large white features on the upper terrace are adsorbates that might decorate defects. For all Ti atoms, the atomic coordinates have been determined by fitting the protrusion with 2D Gaussian profiles. From these coordinates the Fourier transform (FT) has been calculated as depicted in Fig. 2(*b*). The FT shows a pronounced long-range order in the OQC tiling due to the presence of a large number of high-order reflections. Based on the atomic positions, the OQC tiling is extracted as shown in Fig. 2(*c*). The structure is determined by triangles, squares and rhombs, but also a small number of shield elements can be recognized [grey in Fig. 2(*c*)]. The latter element results from one missing Ti atom in the structure, which would otherwise be filled by two triangles, one square and one rhomb.

The tiling elements in Fig. 2(*c*) sum up to 7773 triangles, 2806 squares and 981 rhombs. These numbers correspond to a ratio of 2.77:1:0.35, which is close to that of the ideal NGT. If one additionally takes the 57 shield defects into account, which equal 114 triangles, 57 squares and 57 rhombs, the tiling element ratio will change to 2.75:1:0.36. This even more closely approaches the NGT ratio of 2.73:1:0.37.

Besides counting the tiling elements, an analysis of the angular distribution of the Ti neighbours around each vertex has been conducted. This distribution is plotted in Fig. 3.

It gives a statistical measure of the interior angles of triangles, squares and rhombs. The angular distribution of the interior angles for triangles is well described by a Gaussian centred at 60.1° with a full width at half-maximum (FWHM) of 8.3°. For squares, the distribution is asymmetrically broadened to higher angles. From fitting with a Gaussian, the maximum is found at 89.2° and the FWHM is 9.4°. The interior angles of the rhombs strongly deviate from their expected values of 30° and 150°. Instead, two Gaussians can be fitted at 32.7° and 147.3°. Their widths have been determined to 5.2° and 11.5°, respectively. The angular variations as expressed by the broadening of all distributions reflect local distortions of all elements. In the case of triangles and squares, the distortions are balanced. However, the shift of the maximum in the angular distribution of rhombs reflects a systematic deformation. The shift by 2.7° corresponds to a change in the aspect ratio of the diagonals of 9% when assuming constant edge lengths.

The distributions of side lengths which are shown in Fig. 4(*a*) for three combinations of neighbouring tiling elements also reveal small deviations from the ideal tiling.

From fitting the histograms with Gaussian distributions, average side lengths of 6.95, 6.72 and 6.79 Å are determined for the combination of triangles with squares, triangles and rhombs, respectively. With an FWHM of 0.95 Å these distributions are again quite broad. The average triangle–square side length is slightly longer than the others. However, its distribution also contains a few short distances around 5.7 Å, which are not covered by the Gaussian. In total, these variations are well within the scattering of the data.

Neighbouring tiling elements in an ideal NGT contain only a negligible number of rhomb–rhomb, rhomb–square or square–square contacts. The only relevant combinations are triangle–square, triangle–rhomb and triangle–triangle, where the first of these has the highest abundance as indicated in Fig. 4(*b*) as a grey bar chart. The experimentally determined frequencies for the OQC are marked by crosses for all six tiling combinations. The experimental values are in perfect agreement with those of an ideal NGT. This includes the correct relative frequency of the triangle–

Figure 2
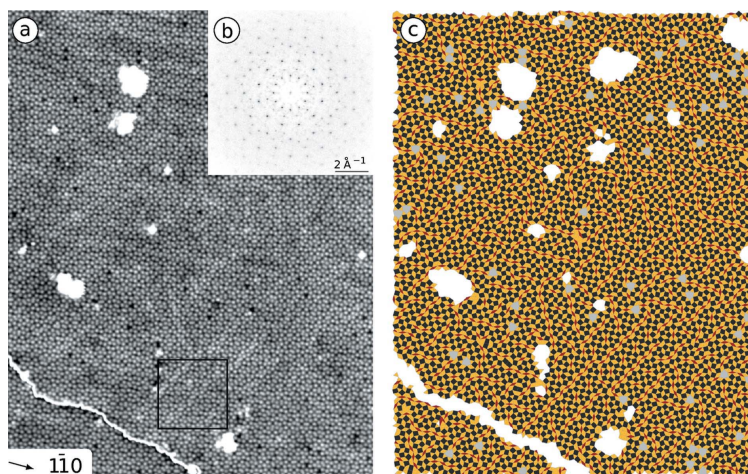(*a*) STM measurement of $BaTiO_3$-derived OQC on Pt(111) showing the sublattice of the Ti atoms. The region marked in black is discussed in more detail in Fig. 8. (*b*) Fourier transform of the atomic positions extracted from (*a*). (*c*) The OQC tiling as extracted from the atomic coordinates showing triangles (gold), squares (black), rhombs (red) and shields (grey). (*a*) 52 × 67 nm, 15 pm, −1 V.

aperiodic 2018

square, triangle–triangle and triangle–rhomb edges as well as the absence of rhomb–rhomb, rhomb–square and square–square edges.

Besides the tiling statistics, the rotational alignment of the different elements with respect to the $\langle 1\bar{1}0 \rangle$ Pt(111) substrate directions has been analysed in detail. Figs. 5, 6 and 7 show the orientation of squares, rhombs and the characteristic dodecagons, respectively. In all cases the results taken from the STM image are compared with the arrangement of these units in an ideal NGT.

The detailed analysis for the squares is given in Fig. 5(a) in which their orientational distribution and the variations in the length of their diagonals are plotted. Within each type of square, a spreading of the orientation and of the lengths is observed, which might emphasize distortions within the tiling.
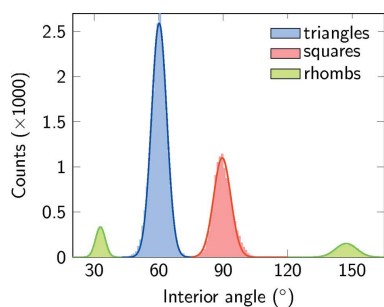
However, the distribution reveals no correlation between the fluctuations in length and bond direction. From diffraction, the orientation of the OQC with respect to the underlying substrate is known (Förster *et al.*, 2013). It turns out that the diagonals of the squares are rotated by 15° with respect to the atomic rows of Pt(111) along the $\langle 1\bar{1}0 \rangle$ directions. Correspondingly, each square is oriented with one edge along this high-symmetry direction.

Figure 3
Distribution of interior angles in the triangles, squares and rhombs as derived from the drift-corrected STM data of the OQC tiling in Fig. 2.
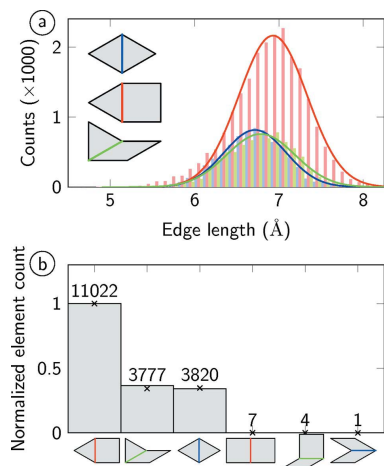

Figure 4
(a) Side length distribution of the OQC tiling elements as derived from Fig. 2. The histograms show the lengths of edges shared between adjacent triangles, between triangles and squares, and between triangles and rhombs in classes of 0.1 Å. The representation in classes causes an off-centring of blue and green bars. (b) Number of neighbouring tiling combinations: crosses and absolute numbers mark the experimental values, whereas the grey bar chart indicates the ideal NGT values.
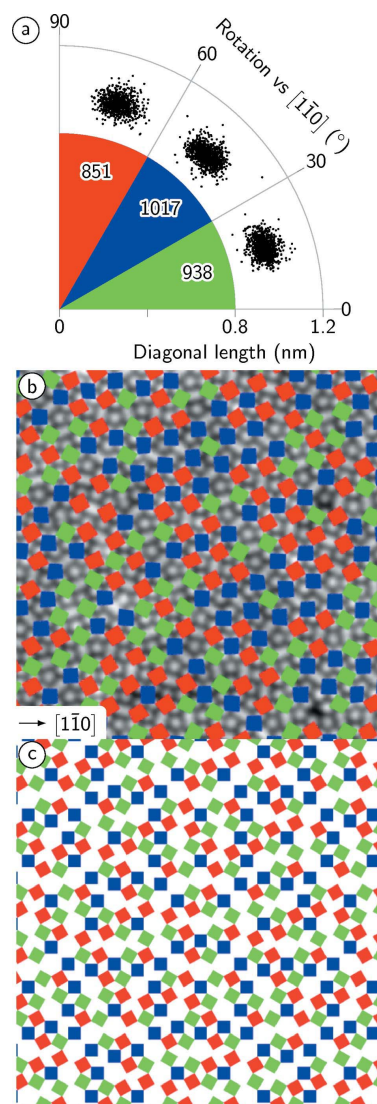

Figure 5
(a) The distribution of squares from Fig. 2. The length of the diagonals is determined and their rotational distribution relative to the [$1\bar{1}0$] substrate direction is given in classes of 30°. (b) Superposition of differently oriented squares to a cut of Fig. 2(a) for comparison with (c) the ideal NGT.

Fig. 5(a) reveals a 10% variation in the frequency of differently oriented squares. In the ideal NGT the orientation of squares is homogeneously distributed as shown in Fig. 5(c) with the same frequency in all three rotations. In contrast, the OQC data in Fig. 5(b) show an arrangement where locally one orientation is suppressed. In the ideal NGT and in the measured data, no square shares a corner with a second one of the same orientation. In the ideal NGT a square is never connected to more than two squares of common orientations, and up to four neighbours of identical orientation are found in the real OQC tiling.

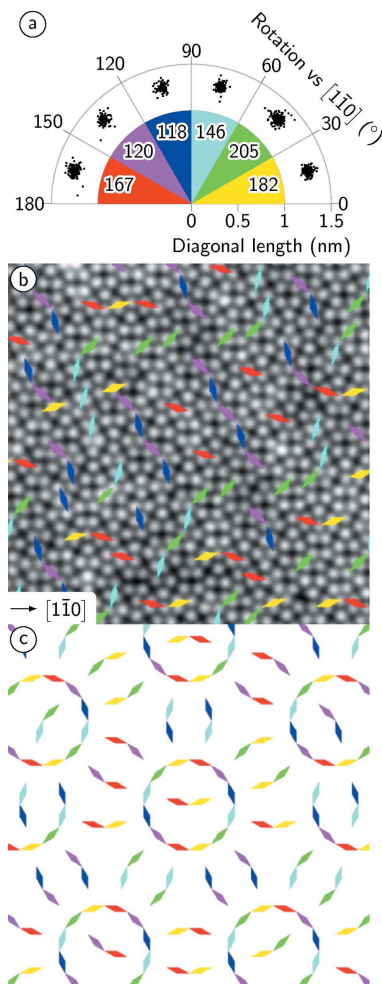The rhombs occur in six different orientations every 30°. Their distribution has been determined from their long axis

which is shown as raw data in Fig. 6(a). The variations of lengths and bond angles are similar to the case of squares discussed before.

Note that the frequency of the six different orientations as given by the numbers in Fig. 6(a) reveals deviations up to 30% from the mean value. By comparing the local orientation of rhombs within the real OQC data in Fig. 6(b) with that of the ideal NGT (Fig. 6c), three major differences can be recognized. Firstly, in the OQC isolated rhombs are present, which is not the case in the ideal NGT. Secondly, the rhombs in the OQC tiling tend to arrange in lines with two edges parallel to the ⟨1̄10⟩ directions. Along these lines their long diagonals are alternately oriented in ±150°. In the ideal NGT, those chains do not occur; instead the rhombs tend to form circles or occur in isolated pairs. Thirdly, the distribution of rhombs within the ideal NGT is equal in all directions for symmetry reasons.

Finally, the orientation of the characteristic dodecagons of the NGT tiling has been evaluated. We define the orientation of the dodecagon based on its mirror symmetry axis with a direction given as shown schematically in Fig. 7(a). The symmetry of the dodecagon allows 12 orientations.

The histogram of Fig. 7(b) shows the orientational distribution of dodecagons in the OQC and reveals clearly a preference for six out of the 12 directions. Almost all dodecagons are found under 30° rotations against the ⟨1̄10⟩ substrate directions. Two orientations at 30° and 210° relative to the [1̄10] direction occur only half as often in the OQC tiling of Fig. 2(a) as compared with 90°, 120°, 270° and 330°, which emphasizes a correlation of dodecagons with opposite orientations. This becomes more obvious when superimposing the dodecagons to the STM data as shown in Fig. 7(c). The lines that have been recognized in the distribution of rhombs are a consequence of an overlapping of adjacent dodecagons of opposite orientations. This is in strong contrast to the cluster

Figure 6
(a) Raw data of the rotational distribution of rhombs from Fig. 2. The frequency of rhomb orientations taken from their long axes in classes of 30° relative to the [1̄10] direction of Pt(111) is given. (b) Superposition of differently oriented rhombs to a cut of Fig. 2(a) for comparison with (c) the ideal NGT.
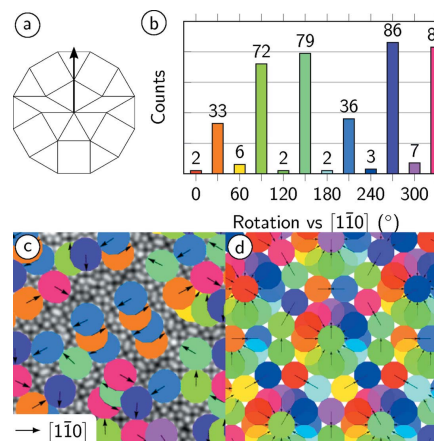
Figure 7
(a) Definition of the orientation in the characteristic dodecagon of the NGT. (b) Frequency of dodecagon orientations in the OQC in classes of 30° relative to the [1̄10] direction of Pt(111). (c) Superposition of differently oriented dodecagons to the measured STM data for comparison with (d) the ideal NGT.

aperiodic 2018

distribution in the ideal NGT, which must again be equally balanced along every 30° shown in Fig. 7(d).

5. Discussion

In the previous section we have presented a detailed statistical analysis for a large area of the dodecagonal BaTiO$_3$-derived OQC on Pt(111). The structure has only a very small number of defects and consists mainly of triangle, square and rhomb configurations. Their frequency and rotational orientation are very close to those of the NGT. In addition, the frequencies of the six possible nearest-neighbour configurations, as dominated by triangle–triangle, triangle–square and triangle–rhomb configurations, match perfectly those of the NGT.

However, a number of deviations from the ideal NGT are also reported here. Variations of the average side lengths of the three tiling elements by roughly ±2% around the value of 6.85 Å have been observed. The average spreading of these side lengths is in the order of ±0.5 Å, which is quite substantial. From evaluating the angles between adjacent edges a stretching along the short diagonal of the rhombs by 9% is expected. These deviations from an ideal geometry most likely relate to an adaptation to preferential adsorption sites

on the atomic level. These are hard to determine precisely, since only the Ti grid of the BaTiO$_3$-derived 2D structure is imaged in STM. The information about the positions of Ba and O atoms is still lacking.

In addition, a clear sixfold signature is found in the rotational distribution of dodecagons in the OQC tiling. This symmetry reduction is accompanied by the formation of rows of dodecagons in opposite orientations as seen in Fig. 7(c). As a consequence, the circular arrangements of rhombs within the NGT are transformed into a row-like structure. The detailed analysis of the local OQC tiling along these rows identifies individual unit cells of a giant approximant structure that was recently reported for the SrTiO$_3$–Pt system (Schenk et al., 2017). Fig. 8(a) shows a close-up of the STM image of Fig. 2(a). In this area three approximant unit cells are marked by black lines. Their short unit-cell vector is aligned parallel to the [1$\bar{1}$0] direction. Additionally, the 36 tiling elements within the approximant unit cell are indicated. Interestingly, the unit cell includes one of the characteristic dodecagons discussed in Fig. 1. Whereas the unit cell is a motif of the ideal NGT, the periodic repetition is not. Therefore, a larger periodic repetition of this unit cell would correspond to an approximant domain embedded in the OQC. In the area given in Fig. 8(a), this motif is repeated a few times along the short unit-cell vector, which produces the row-like structure of the rhombs and oppositely oriented dodecagons. Therefore, it is important to compare the tiling statistics for the ideal NGT, the ideal approximant structure and the experimentally observed structure. The triangle:square:rhomb ratios for the NGT are 2.73:1:0.37, whereas the approximant ratios are 2.66:1:0.33. In the approximant are fewer triangles and fewer rhombs in comparison with the NGT. The experimentally observed ratios are 2.75:1:0.36 and are very close to those of the NGT. In fact, the small deviations cannot be explained by approximant domains within the NGT, since the frequency of triangles is slightly higher in the experiment as compared with the NGT. Note that the triangle frequency is lower in the approximant. Therefore, we conclude that the approximant patches are in the limit of vanishing domain size. A second proof of the very local nature of the symmetry reduction to a sixfold structure comes from the comparison of the FT of the atomic grid as determined in the STM image and the global diffraction pattern obtained by spot-profile analysis of low-energy electron diffraction (SPALEED) as shown in Fig. 8(b). Whereas the FT has been calculated from 3500 nm^2, the diffraction data are collected from an area of 5 mm × 5 mm. The major difference between both patterns is the intensities of the ⟨1110⟩ higher-order spots, marked by red circles in Fig. 8(b). Their intensity distribution implies a local symmetry reduction to sixfold in the FT of this STM image. However, the real diffraction data in Fig. 8(b) show clearly the long-range coherence for a dodecagonal quasicrystal.

On the one hand, the giant approximant structure is very *locally* present in different orientations. On the other hand, the long-range dodecagonal order and coherence are *globally* maintained despite the observed local fluctuations. One scenario which can combine both aspects arises from an
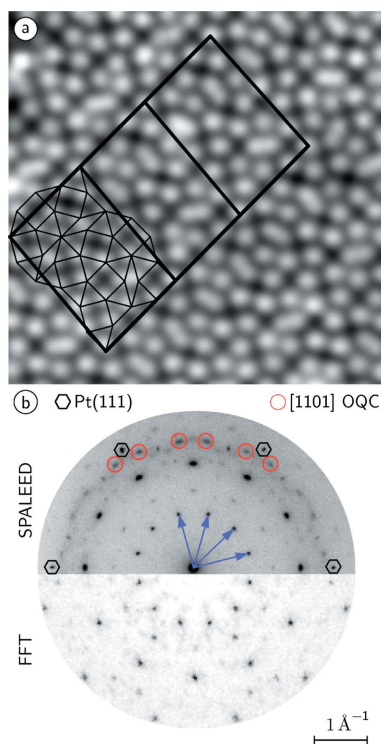
Figure 8
(a) Close-up STM image of the BaTiO$_3$-derived OQC tiling taken within the black square of Fig. 2(a). Locally, patches of an approximant unit cell can be identified, which consists of 36 tiling elements. (b) SPALEED image of the OQC in comparison with the FT from Fig. 2(b).

initially very well developed QC at growth temperatures. At these higher temperatures, the QC can be additionally stabilized by the enhanced QC entropy. Upon cooling, the interaction with the substrate favours specific adsorption sites. The QC structure transforms locally into approximant-like geometries if these structures match the substrate lattice. However, these changes can occur only without significant mass transport, *e.g.* by local site changes. In fact, such local changes of atomic positions in a QC that leave the number of tiling elements unchanged, as we observe here, are known as phason flips.

6. Conclusion

An in-depth statistical analysis of the dodecagonal tiling of the $BaTiO_3$-derived oxide quasicrystal on the Pt(111) substrate is presented. The tiling ratio which is determined from almost 11 500 elements created from 8100 vertex positions unambiguously identifies the ideal NGT formed from equilateral triangles, squares and rhombs as the host structure of the $BaTiO_3$-derived OQC. For different elements of the OQC tiling strong distortions are found, both in their interior angles and their edge lengths, which most likely occur due to local preferences to specific adsorption sites on an atomic scale. The rotational distribution of squares, rhombs, and the characteristic dodecagons of the NGT reveal a clear preference for an alignment of edges parallel to the $\langle 1\bar{1}0 \rangle$ directions of the hexagonal substrate. This is a consequence of individual unit cells of an approximant structure. These approximant patches are locally reducing the symmetry in the 2D layer. Despite these local features, the dodecagonal symmetry remains on global scales as confirmed by the tiling element ratio and by diffraction.

Funding information

References

Cai, T., Fournée, V., Lograsso, T., Ross, A. & Thiel, P. A. (2002). *Phys. Rev. B*, **65**, 140202.

Chanpuriya, S., Kim, K., Zhang, J., Lee, S., Arora, A., Dorfman, K. D., Delaney, K. T., Fredrickson, G. H. & Bates, F. S. (2016). *ACS Nano*, **10**, 4961–4972.

Chen, H., Li, D. X. & Kuo, K. H. (1988). *Phys. Rev. Lett.* **60**, 1645–1648.

Dotera, T., Oshiro, T. & Ziherl, P. (2014). *Nature*, **506**, 208–211.

Engel, M. & Trebin, H.-R. (2007). *Phys. Rev. Lett.* **98**, 225505.

Fischer, S., Exner, A., Zielske, K., Perlich, J., Deloudi, S., Steurer, W., Lindner, P. & Förster, S. (2011). *Proc. Natl Acad. Sci. USA*, **108**, 1810–1814.

Förster, S., Meinel, K., Hammer, R., Trautmann, M. & Widdra, W. (2013). *Nature*, **502**, 215–218.

Förster, S., Trautmann, M., Roy, S., Adeagbo, W. A., Zollner, E. M., Hammer, R., Schumann, F. O., Meinel, K., Nayak, S. K., Mohseni, K., Hergert, W., Meyerheim, H. L. & Widdra, W. (2016). *Phys. Rev. Lett.* **117**, 095501.

Förster, S. & Widdra, W. (2010). *Surf. Sci.* **604**, 2163–2169.

Gähler, F. (1988). *Quasicrystalline Materials. Proceedings of the ILL/CODEST Workshop*, p. 13. Singapore: World Scientific.

Hayashida, K., Dotera, T., Takano, A. & Matsushita, Y. (2007). *Phys. Rev. Lett.* **98**, 195502.

Iacovella, C. R., Keys, A. S. & Glotzer, S. C. (2011). *Proc. Natl Acad. Sci. USA*, **108**, 20935–20940.

Ishimasa, T., Iwami, S., Sakaguchi, N., Oota, R. & Mihalkovič, M. (2015). *Philos. Mag.* **95**, 3745–3767.

Ishimasa, T., Nissen, H.-U. & Fukano, Y. (1985). *Phys. Rev. Lett.* **55**, 511–513.

Iwami, S. & Ishimasa, T. (2015). *Philos. Mag. Lett.* **95**, 229–236.

Krumeich, F., Conrad, M., Nissen, H.-U. & Harbrecht, B. (1998). *Philos. Mag. Lett.* **78**, 357–367.

Liao, L.-G., Zhang, W.-B., Yu, T.-X. & Cao, Z.-X. (2013). *Chin. Phys. Lett.* **30**, 026102.

McGrath, R., Smerdon, J. A., Sharma, H. R., Theis, W. & Ledieu, J. (2010). *J. Phys. Condens. Matter*, **22**, 084022.

Nečas, D. & Klapetek, P. (2012). *Cent. Eur. J. Phys.* **10**, 181–188.

Niizeki, N. & Mitani, H. (1987). *J. Phys. A Math. Gen.* **20**, L405–L410.

Papadopolos, Z., Widmer, R. & Gröning, O. (2008). *Philos. Mag.* **88**, 2083–2093.

Paßens, M., Caciuc, V., Atodiresei, N., Feuerbacher, M., Moors, M., Dunin-Borkowski, R. E., Blügel, S., Waser, R. & Karthäuser, S. (2017). *Nat. Commun.* **8**, 15367.

Schenk, S., Förster, S., Meinel, K., Hammer, R., Leibundgut, B., Paleschke, M., Pantzer, J., Dresler, C., Schumann, F. O. & Widdra, W. (2017). *J. Phys. Condens. Matter*, **29**, 134002.

Schneider, C. A., Rasband, W. S. & Eliceiri, K. W. (2012). *Nat. Methods*, **9**, 671–675.

Steurer, W. (2012). *Chem. Soc. Rev.* **41**, 6719–6729.

Talapin, D. V., Shevchenko, E. V., Bodnarchuk, M. I., Ye, X., Chen, J. & Murray, C. B. (2009). *Nature*, **461**, 964–967.

Urgel, J. I., Écija, D., Lyu, G., Zhang, R., Palma, C.-A., Auwärter, W., Lin, N. & Barth, J. V. (2016). *Nat. Chem.* **8**, 657–662.

Zeng, X., Ungar, G., Liu, Y., Percec, V., Dulcey, A. E. & Hobbs, J. K. (2004). *Nature*, **428**, 157–160.

Electronic band structure of a two-dimensional oxide quasicrystal

Phys. Rev. B 100, 123149 (2019):

https://doi.org/10.1103/PhysRevB.100.125149

C$_{60}$ adsorption on a dodecagonal oxide quasicrystal

Phys. Rev. B 100, 205414 (2019):

https://doi.org/10.1103/PhysRevB.100.205414

ORIGINAL PAPER

Perfect Monolayers of the BaTiO$_3$-Derived 2D Oxide Quasicrystals Investigated by Scanning Tunneling Microscopy and Noncontact Atomic Force Microscopy

Eva Maria Zollner, Sebastian Schenk, Martin Setvin, and Stefan Förster*

The atomic structure of the BaTiO$_3$-derived 2D oxide quasicrystals (OQCs) is investigated using scanning tunneling microscopy (STM) and noncontact atomic force microscopy (nc-AFM). It is demonstrated that these extraordinary films can easily be prepared as single-phase monolayers on a Pt(111) support. From analyzing almost 20 000 atomic vertices, an extended statistical dataset of the OQC tiling is collected. It manifests that the OQC obeys the statistics of the Niizeki–Gähler tiling, which is a dodecagonal triangle–square–rhomb model system. The atomic structure shown by nc-AFM is identical to the contrast obtained in STM images. The results are discussed with respect to the existing structural models.

1. Introduction

When approaching the 2D limit, oxides are known to exhibit strong variations in their structures and properties compared with the respective bulk materials.[1] One of most peculiar examples is the 2D oxide quasicrystals (OQCs) formed from ternary oxides on periodic metal substrates which have been reviewed in this issue by Förster et al.[2–4] Those structures are developed at high temperatures in reducing environment in atomically thin networks on metal supports.[5] Examples for periodic or aperiodic structures in such 2D layers are found in many systems, e.g., SrTiO$_3$/Pt(111), BaTiO$_3$/Pt(111), and BaTiO$_3$/Ru(0001).[2,3,6–8] The preparation of OQCs in extended monolayers is challenging, as an exact amount of material needs to be deposited on the

E. M. Zollner, S. Schenk, Dr. S. Förster
Institute of Physics
Martin-Luther-Universität Halle-Wittenberg
D-06099 Halle, Germany
E-mail: stefan.foerster@physik.uni-halle.de
Dr. M. Setvin
Institute of Applied Physics
TU Wien
Wiedner Hauptstraße 8-10/E134, 1040 Wien, Austria

substrate in the correct stoichiometry. Previous reports suffered from this difficulty, and OQCs were found in coexistence with periodic islands formed from excess material. This limited the applications of area-averaging analysis methods and required complex data analysis.[9] Here, we demonstrate how to succeed in the preparation of perfect monolayers of this new kind material for the case of BaTiO$_3$/Pt(111). These OQCs films extend across the entire surface, and no material is left to form periodic islands.

We make use of these perfect monolayer templates for structural investigations using a combined scanning tunneling microscopy (STM)/noncontact atomic force microscopy (nc-AFM). At the atomic level, the structure of the Ti subgrid had previously been resolved by STM.[2,3] An in-depth analysis of the Ti positions identified the OQC as a disordered Niizeki–Gähler tiling (NGT).[10–12] In STM, the Ba and O grids are not accessible, due an energetic position of Ba- and O-related bands far from the Fermi level. However, from a combination of STM, surface X-ray diffraction (SXRD) and density functional theory (DFT) calculations performed for a related periodic approximant, a decoration of the triangle and square tiling elements with all three atomic species has been proposed.[6,7] Based on this model, all Ti atoms are threefold coordinated by O atoms. Furthermore, the sublattice of Ba and some of the O ions should buckle outward of the surface.[6,7] Therefore, nc-AFM is supposed to be ideally suited for imaging Ba and O ions. However, the constant-height nc-AFM measurements presented here using either metallic or CO functionalized tips show the exactly same contrast as seen in the simultaneously recorded tunneling current images. This implies that the Ti atoms buckle outward from the surface and AFM does not allow to determine the decoration of the dodecagonal tiling by Ba and O.

2. OQC Monolayers on Pt(111)

Perfect monolayers of the BaTiO$_3$-derived OQCs are fabricated by subsequent deposition of 2.0 ± 0.1 Å of BaO and 2.0 ± 0.1 Å of TiO$_x$ in an oxygen atmosphere of 10^{-6} mbar to the Pt(111) substrate. The deposited material is fully oxidized by annealing in 10^{-5} mbar O$_2$ for 20 min at 920 K. OQC monolayers are formed by a single 5 min ultrahigh vacuum (UHV) flash of the as-prepared samples at 1100 K. **Figure 1**a–d shows a series of low-energy

Figure 1. a–d) LEED pattern of the dodecagonal OQC derived from $BaTiO_3$ on Pt(111) at different kinetic energies. e) The measured data are a super-position of the dodecagonal pattern originating from the first BZ and f) a set of backfolded spots originating from the six neighboring BZs of Pt(111). The backfolded spots along the $[11\bar{2}]$ direction are marked with blue circles in parts (a)–(c).

electron diffraction (LEED) images of the OQC taken at different electron kinetic energies right after this single heating step.

In addition to the Pt(111) substrate spots (marked with hexagons in Figure 1d), all LEED spots are related to the dodecagonal OQC. In the LEED pattern, OQC spots of different origin can be distinguished. The dominating contribution are spots of the dodecagonal structure originating from the first Brillouin zone (BZ). A scheme of such spots is shown in Figure 1e. This pattern represents a 2D projection of a 4D hyperhexagonal lattice, which is the reason for the description with four unit

vectors (black arrows in Figure 1e).[13] The first-order spots are typically very weak and only observed at energies below 10 eV (not shown here). The most intense feature is the ring of 12 spots corresponding to the second-order of diffraction (red in Figure 1e). For guidance, this order of diffraction is marked in the measured LEED data in red. At larger reciprocal distances, the rings of third- and fourth-order spots appear with 15° rotation against the second-order ring. At the highest electron energy of 66 eV in Figure 1d, additional pairs of fifth-order reflections are observed at every 30°. Theoretically, the reciprocal space of

a OQC consists of an infinitely dense mesh of points, as every point in the 2D space can be approached by the superposition of integer numbers of the four unit vectors. However, for the OQC, only a small number of reflections of nonzero intensity are observed.

The second contribution to the LEED pattern originates from multiple scattering events, which occur at these low electron energies. Electrons that are subsequently scattered at the OQC and the Pt(111) substrate produce additional spots originating from neighboring BZs of the Pt(111) substrate.[2] This so-called backfolding is schematically shown in Figure 1f. All backfolded spots that have been observed experimentally are drawn here. Each of the neighboring BZs contributes with two second-order reflections (red in Figure 1f), one third-order spot and five spots of the fourth order of diffraction (blue in Figure 1f). In the experimental data, the backfolded spots are exemplary marked along the [11$\bar{2}$] direction in Figure 1a–c. The superposition of the two contributions shown in Figure 1e,f reduces the symmetry of the observed LEED pattern. The presented OQC pattern extends over the entire sample surface demonstrating an OQC coating of the surface on millimeter scales. Because no additional phase is seen in LEED, the deposited material was completely consumed to form the OQC monolayer.

For atomic-scale characterization using STM and nc-AFM, the sample needed to be transferred through air. To remove adsorbates after re-entering the UHV chamber, the sample has been annealed in 10^{-6} mbar O_2 for 10 min at 920 K. Flashing the sample in UHV afterward to 1100 K for 5 min recovers the OQC structure. **Figure 2**a shows the homogeneity of the surface in the presence of the OQC layer. On the scale of 200×200 nm^2 flat terraces separated by monoatomic steps are seen. These substrate terraces are completely covered with the OQC layer. Due to its alignment along the high-symmetry substrate directions, the OQC grows as a single-domain overlayer. Accordingly, no domain boundaries are formed on the terraces. The image has been recorded at a resolution of 1500×1500 points, which allows to atomically resolve the OQC structure in the entire area. The Fourier transform of this image is shown in Figure 2b. Twelve intense spots are seen, which correspond to the second-order spots seen in LEED. In addition, higher-order spots at larger and smaller reciprocal distances are resolved. All details of the OQC tiling can be derived from smaller-scale STM images. One example is shown in Figure 2c, which maps a surface region of 40×40 nm^2. In this image, one recognizes the construction principle of the dodecagonal tiling, which is a combination of equilateral triangles, squares, and rhombs. Figure 2c is cut out from a larger dataset and contains about 4000 atomic vertices out of a total number of 19 840. From this large dataset, all atomic positions have been extracted, and a detailed statistical analysis of the atomic tiling has been performed as recently introduced by Schenk et al.[12] There, it has been shown that the OQC tiling is a first experimentally observed realization of the ideal NGT, which can be constructed by the cut and project method or by recursion.[10,11,14] The benchmark parameters for this assignment are the total tiling element frequencies and the frequencies of shared edges between adjacent tiles. Schenk et al. conducted this analysis for a system of 8100 atomic vertices and report perfect match between the OQC statistics and that of the ideal NGT. The dataset that is analyzed here is almost a factor of
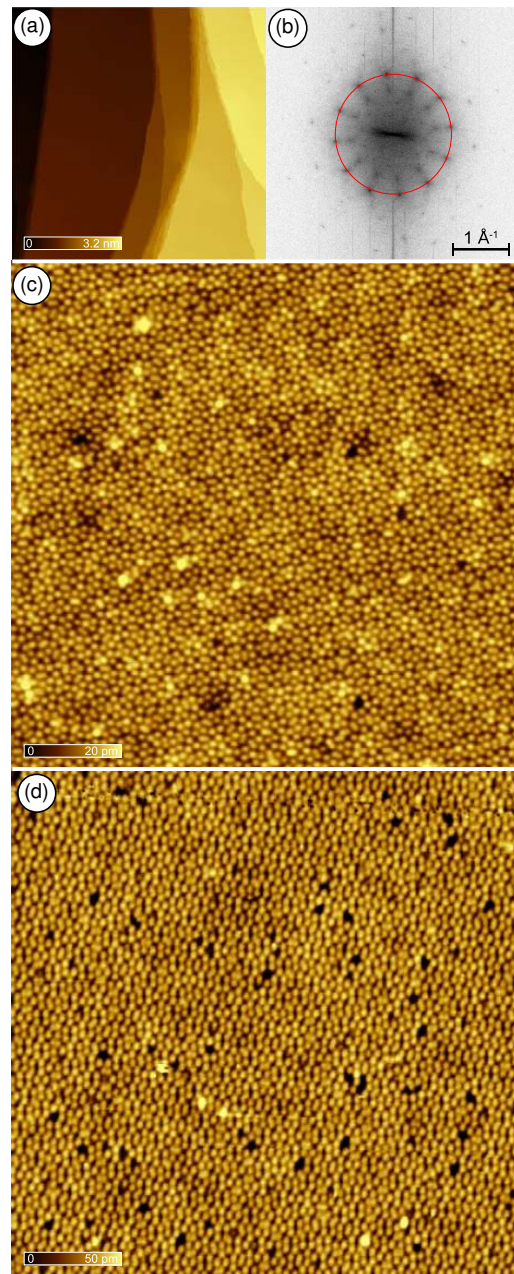
Figure 2. STM data of a perfect monolayer of the BaTiO$_3$-derived OQC on Pt(111) measured at a–c) 4.8 K and d) at room temperature. a) High-resolution large-scale image showing a homogeneous surface with monoatomic steps covered by the OQC. b) Fourier transform of part (a) on logarithmic scale. Atomic resolution of the OQC structure at c) 4.8 K and d) at room temperature. a) 200×200 nm^2, 30 pA, 0.5 V; c) 40×40 nm^2, 25 pA, 1.0 V; and d) 40×40 nm^2, 100 pA, 1.0 V.

2.5 larger. In total, 19 840 atomic vertices form 19 309 triangles, 7006 squares, and 2634 rhombs, which translates into a triangle: square:rhomb ratio of 2.76:1:0.38. The ideal tiling element ratio of the NGT is 2.73:1:0.37. Only 65 squares are missing in the real system to meet the ideal value, which is less than 1%. The very good match confirms the quasicrystalline nature of the observed tiling. An even stronger benchmark parameter to compare the OQC tiling with the NGT is the frequency of

Figure 3. Comparison of the frequencies of shared edges between adjacent tiles in the OQC derived from analyzing 19 840 atomic vertices (red crosses) and the ideal NGT (bars).

shared edges between adjacent tiles, because it reflects the way how the tessellation is created from the different tiles. It will strongly differ from a tiling determined by a recursion rule such as the NGT to, e.g., a random tiling. **Figure 3** shows the comparison of these frequencies for the OQC dataset with those of the NGT.

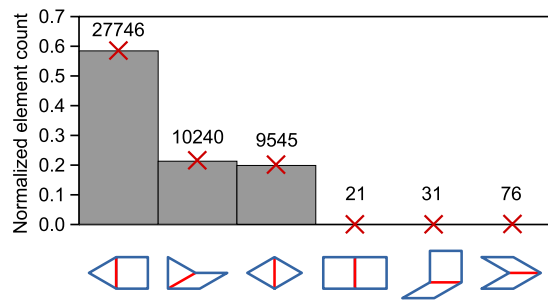The agreement is again excellent. Only a minor number of defects is found in the tiling, which are edges shared between two adjacent squares, two rhombs, or a square and a rhomb. Those tiles should not meet in the NGT. However, the total number of such defects is below 0.3%, which means it is negligible. A profound understanding of the observed slight deviations from the ideal tiling configurations and the differences between the OQC preparations analyzed here and published by Schenk et al. would require a proper model for the decoration of tiles with all three atomic species. This is still lacking, which motivated additional nc-AFM measurements as discussed in the following paragraphs.

For the determination of these structural details as derived earlier, the STM measurements do not necessarily need to be performed at liquid helium temperatures. The large interatomic spacing of the Ti atoms of 6.85 Å also allows resolving the structure at room temperature using standard equipment, as shown in Figure 2d. From these measurements, all statistical information, as obtained from the low temperature dataset, could

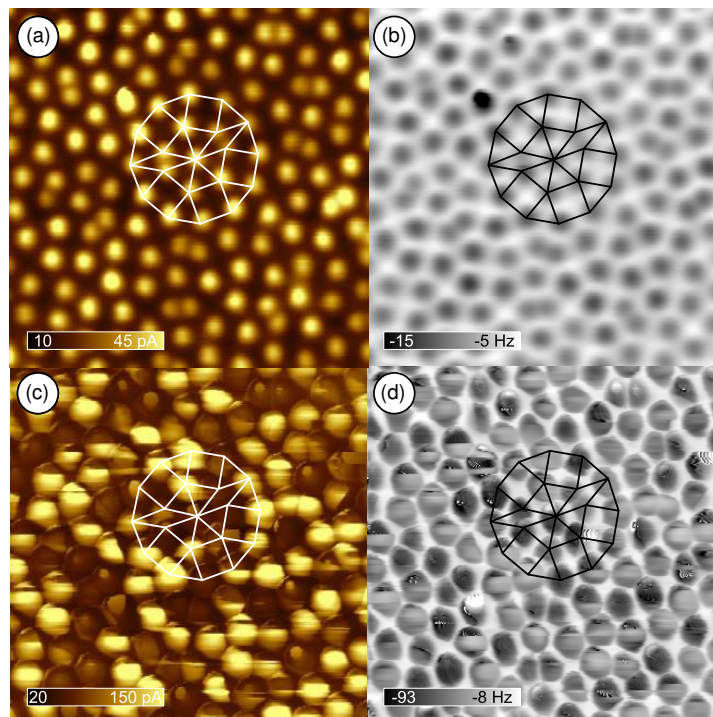**Figure 4.** Simultaneously recorded constant-height STM (left column) and nc-AFM images (right column) of the OQC using a metallic tip. One of the characteristic dodecagons of the OQC is emphasized for guidance. $7 \times 7 \, nm^2$, a,b) $U = -0.03 \, V$, $A = 120 \, pm$, c,d) $U = -0.01 \, V$, $A = 60 \, pm$. The tip–sample distance in parts (c) and (d) is 1 Å which is smaller than in parts (a) and (b).

be extracted in a similar fashion with equal precision. The only noticeable difference between this measurement compared with Figure 2c is the slightly increased number of larger dark holes. At these positions, one or two Ti atoms are missing. Such defects are most likely related to preparational issues, e.g., small deviations in the composition, rather than to the measurement temperature.

3. ncAFM Measurements of the OQC Tiling

As the OQC layers do not have an established structural model, nc-AFM measurements have been performed on the aforementioned perfect OQC monolayers with the aim to resolve the cation and anion sublattices. For ionic lattices, AFM can typically show attractive forces above cations and repulsive forces above anions, assuming that the tip apex has a negative electric charge.[15–18] Positively terminated tips show an inverted contrast.

The nc-AFM measurements presented here have been performed with a variety of tip functionalizations, but the obtained contrast appeared very robust and independent of the tip. **Figure 4** shows typical results obtained with metallic tips. Here, the tip was functionalized by applying voltage pulses above a Cu (001) surface. The AFM images reveal a strong attraction above the atoms that have been identified as Ti by STM. To clearly recognize this, one of the characteristic motifs of the NGT, a dodecagon build from 12 triangles, 5 squares, and 2 rhombs is marked by white lines in the STM image of Figure 4a. At the very same position, the AFM image reveals a dark contrast indicating the attractive tip–sample interaction. Surprisingly, no additional features appear in the frequency shift image of Figure 4b. This observation holds even upon approaching closer to the surface and entering the repulsive regime as shown in Figure 4c,d. The only change in the STM and AFM image contrast is the apparent width of the Ti atoms.

Another frequently used tip functionalization is a CO-tip.[19] CO was dosed on the surface at $T \approx 60\,K$, and the molecule was picked by applying voltage pulses. The tip functionalization was verified by imaging the adsorbed CO molecules. In the AFM image of **Figure 5**b, the adsorbed CO molecules appear as bright spots due to the repulsive CO–CO interaction.[20] The OQC surface imaged by the CO tip is shown in Figure 5c–h. The sequence of images shows the same spot of the sample at low and medium attractive forces and in the repulsive regime. In comparison with the metallic tip, the maximum attractive forces between the CO tip and the OQC template are somewhat smaller. However, the overall appearance of the OQC tiling remains unchanged. Even in the largest voids of the Ti grid, which are the centers of the squares with a nominal width of $6.85 \times 6.85\,nm^2$, no additional features can be identified.

The identical AFM contrast has also been achieved when functionalizing the tip directly at the OQC layer. Such behavior is unusual for ionic surfaces; there, it is typically possible to invert the imaging contrast.[16,18,21] Also, the magnitude of the frequency shifts obtained on the OQC is significantly higher than typically measured on ionic surfaces. Such robust attractive forces are characteristic for surfaces that form covalent bonds, such as the prototypical silicon surfaces.[22–24] The domination of the OQC AFM contrast by the Ti atoms independent of the tip
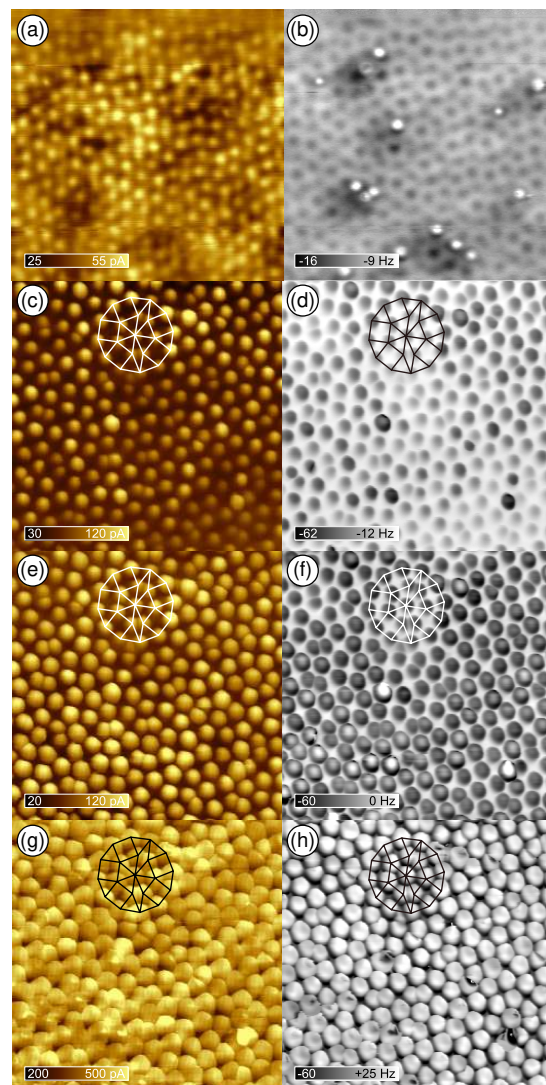
Figure 5. Simultaneously recorded constant-height STM (left column) and nc-AFM images (right column) of the OQC using a CO-terminated tip. One of the characteristic dodecagons of the OQC is emphasized for guidance in parts (c)–(h). a,b) $10 \times 10\,nm^2$, $U = +0.04\,V$, $A = 60\,pm$. The bright spots in the AFM image correspond to the adsorbed CO molecules. c–h) $7 \times 7\,nm^2$, $U = +0.002\,V$, $A = 50\,pm$. The tip–sample distance with respect to parts (a) and (b) is c,d) $\Delta Z = +100\,pm$, e,f) $\Delta Z = +190\,pm$, and g,h) $\Delta Z = +350\,pm$.

configuration suggests an significant outward buckling of the Ti site. Alternatively, it could result from the reduction of the film. In the OQC, the Ti 3d orbitals are singly occupied, as recently shown by valence band photoemission.[9] This could be the origin of a strongly enhanced reactivity at the Ti sites as seen in AFM.

4. Conclusion

We report on STM and nc-AFM investigations of the $BaTiO_3$-derived OQC. The AFM data show the identical atomic pattern derived from simultaneously recorded STM images. Previous studies identified these sites as the Ti subgrid of the OQC. The Ti atoms are very dominant in the interaction with AFM tips of different terminations. No other atoms have been detected in the AFM images, even at very close tip–sample distances corresponding to a strongly repulsive interaction. Consequently, the AFM data do not provide a clear lead for solving the OQC structure. However, the high structural quality of single-phase OQC monolayers that is demonstrated here allows for performing surface X-ray standing waves experiments to access the positions of Ba and O atoms in this 2D ternary compound.

5. Experimental Section

Monolayer coverages of $BaTiO_3$ were prepared on Pt(111) substrates by MBE. BaO and Ti were evaporated in an atmosphere of 10^{-6} mbar of O_2 out of an three-pocket electron beam evaporator (EFM3, Omicron). The Ti was supplied from a metal rod and BaO from heating a stoichiometric $BaTiO_3$ ceramic fixed in an Ta crucible. The deposition rate of each source was routinely calibrated using a quartz-crystal micro balance. After subsequent deposition of a given amount of BaO and TiO_x, the ultrathin oxide film was fully oxidized in 10^{-5} mbar O_2 at 920 K for 20 min. The OQC template was prepared by annealing the ultrathin $BaTiO_3$ film for 5 min at 1100 K in UHV.

The combined STM/AFM experiments were performed at $T = 4.8$ K in an UHV chamber (base pressure $<2 \times 10^{-11}$ mbar) equipped with a commercial Omicron q-Plus LT head and a custom-design cryogenic preamplifier.[25] Tuning-fork-based AFM sensors with a separate wire for the tunneling current[26] were used; $f_0 = 31$ kHZ, $Q \approx 20\,000$. Electrochemically etched W tips were glued on the tuning fork and cleaned in situ by field emission and self-sputtering in 10^{-6} mbar AR.[27]

Conflict of Interest

The authors declare no conflict of interest.

[1] F. Netzer, S. Fortunelli, *Oxide Materials at the Two-Dimensional Limit*, Springer, Cham **2016**.
[2] S. Förster, K. Meinel, R. Hammer, M. Trautmann, W. Widdra, *Nature* **2013**, *502*, 215.
[3] S. Schenk, S. Förster, K. Meinel, R. Hammer, B. Leibundgut, M. Paleschke, J. Pantzer, C. Dresler, F. O. Schumann, W. Widdra, *J. Phys.: Condens. Matter* **2017**, *29*, 134002.
[4] S. Förster, S. Schenk, E. M. Zollner, O. Krahn, C.-T. Chiang, F. O. Schumann, A. Bayat, K.-M. Schindler, M. Trautmann, R. Hammer, K. Meinel, W. A. Adeagbo, W. Hergert, J. I. Flege, J. Falta, M. Ellguth, C. Tusche, M. DeBoissieu, M. Muntwiler, T. Greber, W. Widdra, *Phys. Status Solidi B* **2019**, https://doi.org/10.1002/pssb.201900624.
[5] S. Förster, J. I. Flege, E. M. Zollner, F. O. Schumann, R. Hammer, A. Bayat, K.-M. Schindler, J. Falta, W. Widdra, *Ann. Phys. (Berlin)* **2017**, *529*, 1600250.
[6] S. Förster, M. Trautmann, S. Roy, W. A. Adeagbo, E. M. Zollner, R. Hammer, F. O. Schumann, K. Meinel, S. K. Nayak, K. Mohseni, W. Hergert, H. L. Meyerheim, W. Widdra, *Phys. Rev. Lett.* **2016**, *117*, 095501.
[7] S. Roy, K. Mohseni, S. Förster, M. Trautmann, F. O. Schumann, E. M. Zollner, H. L. Meyerheim, W. Widdra, *Z. Kristallogr.* **2016**, *231*, 749.
[8] E. M. Zollner, F. Schuster, K. Meinel, P. Krause, S. Schenk, B. Allner, S. Förster, W. Widdra, *Phys. Status Solidi B* **2019**, https://doi.org/10.1002/pssb.201900655.
[9] C.-T. Chiang, M. Ellguth, F. O. Schumann, C. Tusche, R. Kraska, S. Förster, W. Widdra, *Phys. Rev. B* **2019**, *100*, 125149.
[10] N. Niizeki, H. Mitani, *J. Phys. A: Math. Gen.* **1987**, *20*, L405.
[11] F. Gähler, in *Proc. of the ILL/CODEST Workshop*, World Scientific, Singapore, **1988**, p. 13.
[12] S. Schenk, E. M. Zollner, O. Krahn, B. Schreck, R. Hammer, S. Förster, W. Widdra, *Acta Crystallogr.* **2019**, *A75*, 307.
[13] A. Yamamoto, *Acta Crystallogr.* **1996**, *A52*, 509.
[14] L.-G. Liao, W.-B. Zhang, T.-X. Yu, Z.-X. Cao, *Chin. Phys. Lett.* **2013**, *30*, 026102.
[15] R. Bechstein, C. Gonzalez, J. Schütte, P. Jelinek, R. Pérez, A. Kuhnle, *Nanotechnology* **2009**, *20*, 505703.
[16] A. Yurtsever, D. Fernandez-Torre, C. Gonzalez, P. Jelinek, P. Pou, Y. Sugimoto, M. Abe, R. Perez, S. Morita, *Phys. Rev. B* **2012**, *85*, 125416.
[17] M. Reticcioli, M. Setvin, X. Hao, P. Flauger, G. Kresse, M. Schmid, U. Diebold, C. Franchini, *Phys. Rev. X* **2017**, *7*, 031053.
[18] M. Ellner, N. Pavlicek, P. Pou, B. Schuler, N. Moll, G. Meyer, L. Gross, R. Perez, *Nanoletters* **2016**, *16*, 1974.
[19] L. Gross, F. Mohn, N. Moll, P. Liljeroth, G. Meyer, *Science* **2009**, *325*, 1110.
[20] M. Reticcioli, I. Sokolovic, M. Schmid, U. Diebold, M. Setvin, C. Franchini, *Phys. Rev. Lett.* **2019**, *122*, 016805.
[21] I. Sokolovic, M. Schmid, U. Diebold, M. Setvin, *Phys. Rev. Mater.* **2019**, *3*, 034407.
[22] F. J. Giessibl, *Science* **1995**, *267*, 68.
[23] Y. Sugimoto, P. Pou, M. Abe, P. Jelinek, R. Perez, S. Morita, O. Custance, *Nature* **2007**, *446*, 64.
[24] M. Emmrich, F. Huber, F. Pielmeier, J. Welker, T. Hofmann, M. Schneiderbauer, D. Meuer, S. Polesya, S. Mankovsky, D. Kodderitzsch, H. Ebert, F. J. Giessibl, *Science* **2015**, *348*, 308.
[25] F. Huber, F. J. Giessibl, *Rev. Sci. Instrum.* **2017**, *88*, 073702.
[26] F. J. Giessibl, *Rev. Sci. Instr.* **2019**, *90*, 01101.
[27] M. Setvin, J. Javorsky, D. Tucinkova, I. Matolinova, P. Sobotik, P. Kocan, I. Ostadal, *Ultramicroscopy* **2012**, *113*, 152.

FEATURE ARTICLE

www.pss-b.com

Quasicrystals and their Approximants in 2D Ternary Oxides

Stefan Förster,* Sebastian Schenk, Eva Maria Zollner, Oliver Krahn,
Cheng-Tien Chiang, Florian O. Schumann, Alireza Bayat, Karl-Michael Schindler,
Martin Trautmann, René Hammer, Klaus Meinel, Waheed A. Adeagbo,
Wolfram Hergert, Jan Ingo Flege, Jens Falta, Martin Ellguth, Christian Tusche,
Marc DeBoissieu, Matthias Muntwiler, Thomas Greber, and Wolf Widdra

2D oxide quasicrystals (OQCs) are recently discovered aperiodic, but well-ordered oxide interfaces. In this topical review, an introduction to these new thin-film systems is given. The concept of quasicrystals and their approximants is explained for $BaTiO_3-$ and $SrTiO_3-$derived OQCs and related periodic structures in these 2D oxides. In situ microscopy unravels the high-temperature formation process of OQCs on Pt(111). The dodecagonal structure is discussed regarding tiling statistics and tiling decoration based on the results of atomically resolved scanning tunneling microscopy and various diffraction techniques. In addition, angle-resolved ultraviolet photoemission spectroscopy and X-ray photoelectron spectroscopy results prove a metallic character of the 2D oxide.

1. Introduction

2D oxide quasicrystals (OQCs) emanate from research dedicated to functional oxide interfaces. Oxide thin films are known to exhibit a wide range of functionalities. When the film thickness is reduced, the impact of the interfacial layer on the film properties increases and additional functionalities can arise, which extend the materials properties with respect to the bulk counterparts. Famous examples are the voltage-driven magnetization switching in multiferroics[1–3] and the formation of a 2D electron gas at the $LaAlO_3/SrTiO_3$ interface.[4,5]

In addition to these functionalities, the observation of a 2D OQC added long-range aperiodic order to perovskite-derived oxide interfaces—two years after the Nobel prize in chemistry was awarded to Dan Shechtman for the discovery of quasicrystals.[6] OQCs form spontaneously from perovskite oxide thin films on a metal substrate with sixfold symmetry.[6,7] These interfaces between a periodic substrate and the aperiodic thin film add a new facet to the known forms of interface epitaxy.

Dr. S. Förster, S. Schenk, E. Maria Zollner, O. Krahn, Dr. C.-T. Chiang,
Dr. F. O. Schumann, Dr. A. Bayat, Dr. K.-M. Schindler, Dr. M. Trautmann,
Dr. R. Hammer, Dr. K. Meinel, Dr. W. A. Adeagbo, Prof. W. Hergert,
Prof. W. Widdra
Institute of Physics
Martin-Luther-Universität Halle-Wittenberg
D-06099 Halle, Germany
E-mail: stefan.foerster@physik.uni-halle.de

Dr. C.-T. Chiang, Dr. M. Ellguth, Dr. C. Tusche, Prof. W. Widdra
Max-Planck-Institut für Mikrostrukturphysik
D-06120 Halle, Germany

Prof. J. Ingo Flege
Applied Physics and Semiconductor Spectroscopy
Brandenburg University of Technology
Cottbus-Senftenberg 03046 Cottbus, Germany

Prof. J. Falta
Institute of Solid State Physics
University of Bremen
Bremen, Germany

Prof. J. Falta
MAPEX Center for Materials and Processes
University of Bremen
Bremen, Germany

Dr. C. Tusche
Peter Grünberg Institut (PGI-6)
Forschungszentrum Jülich
D-52425 Jülich, Germany

Dr. M. DeBoissieu
Univ. Grenoble Alpes, CNRS, SIMaP
F-38000 Grenoble, France

Dr. M. Muntwiler
Paul Scherrer Institut
Villigen, Switzerland

Prof. T. Greber
Physik-Institut, Universität Zürich
8057 Zürich, Switzerland

Quasicrystals are materials without the translational symmetry known to periodic crystals, but with a long-range order and a well-defined rotational symmetry visible in diffraction. Often they exhibit an 8-, 10-, or 12-fold rotational symmetry, which is incompatible with translational symmetry.[8–11] Therefore, fundamental concepts in solid-state physics, e.g., the description of electrons by delocalized Bloch states or the concept of extended phonons do not apply for quasicrystals. This makes this class of materials highly interesting also from a fundamental science point-of-view.

Figure 1a shows the first electron diffraction data of an aperiodic oxide structure. The low-energy electron diffraction (LEED) pattern of the OQC clearly shows a 12-fold symmetric pattern. On the atomic scale, this unique structure is built from motifs of equilateral triangles, squares and rhombs, that arrange in characteristic dodecagons, as seen in the scanning tunneling microscopy (STM) image of Figure 1b.[6] We enroll the formation process of the quasicrystalline layers, which follows a self-limiting encapsulation process of the metal surface by the oxide monolayer known as the strong metal support interaction (SMSI) effect of binary oxides on metals.[12–18] Atomically resolved STM images allow for a detailed understanding of the real space tiling of OQCs. It will be demonstrated how a statistical analysis of the real space tiling can be used to identify the Niizeki–Gähler tiling (NGT) as the idealized model system which describes the structure.[19–21] Recursion rules for the NGT are discussed and it is described how the self-similarity, which follows directly from recursion, is altered in the as grown OQC due to phason flips.[21,22] In addition to the real space structure, insights into various diffraction experiments are given. With respect to the electronic structure, we present evidence for unpaired electron spins at the vertices of the dodecagonal tiling as derived from angle-resolved photoemission.[23] Today OQCs can be prepared as perfect monolayer extending over the entire substrate surface and have been successfully tested as template for adsorption experiments.[24,25]

In the field of quasicrystals, a variety of approximant structures are frequently found. These are long-range periodic structures in which the tiling elements or even larger patches of the quasicrystal tiling are cut and form the repeating unit cell. For the ternary oxide monolayers, a variety of approximants to the
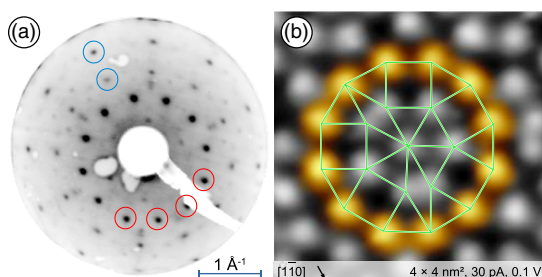
Stefan Förster received his Ph.D. in physics in 2012 at the Martin-Luther-Universität Halle- Wittenberg (MLU). He was awarded a P.R.I.M.E. postdoctoral fellowship of the German Academic Exchange Service and worked from 2014 to 2016 in the group of Greber and Osterwalder at the University of Zurich. Since 2016, he is leading a young researchers group focusing on oxide quasicrystals in the group of Wolf Widdra at the MLU.

Eva Maria Zollner graduated in physics at the Martin-Luther-Universität Halle-Wittenberg. Her Ph.D. in the surface science group at the MLU is devoted to the growth of 2D oxide quasicrystals and their use as templates for molecular adsorption studies.

Wolf Widdra received his Ph.D. in physics in 1991 at the Philipps-Universität Marburg. After a Post-doc at the UC Santa Barbara, he became an Assistant Professor in the group of Dietrich Menzel at the TU Munich in 1994. From 2001 to 2003, he worked as an Associate Professor at the TU Berlin and headed the Department "Synchrotron Radiation, Micro- and Nanostructures" at the Max Born Institute for Nonlinear Optics and Short Pulse Spectroscopy in Berlin. Since 2003, he is a Full Professor at the Martin-Luther-Universität Halle-Wittenberg as head of the Surface Science department.

dodecagonal NGT have been reported.[7,26–31] With increasing size of the unit cell of the approximant, the structures resemble the OQC more closely. Approximants are of special interest due to their periodic nature, as the Bloch theorem applies here and all standard methods of solid-state physics can be used. Especially, surface X-ray diffraction (SXRD) investigations have proven to be most valuable for establishing a complete structural model for OQCs, that goes beyond investigations of the Ti sublattice seen in STM images.[28–30]

2. Preparation and Stability

For the preparation of OQCs, less than 1 nm of a given ternary oxide needs to be deposited on the Pt(111). By annealing the oxide layer at temperatures above 900 K, the material rearranges at the surface, which ultimately can lead to the OQC formation. This structural transformation process has been studied in great detail for the prototypical OQC system of $BaTiO_3$ on Pt(111).[12,32,33] For temperatures around 900 K, a long-range

Figure 1. a) Dodecagonal low-energy electron diffraction pattern of the 2013 discovered oxide quasicrystal derived from $BaTiO_3$ on Pt(111) and b) scanning tunneling microscopy image with the characteristic building blocks marked for the dodecagonal OQC (4 × 4 nm²). Adapted with permission.[6] Copyright 2013, Springer Nature.

ordered BaTiO₃(111) structure develops. Upon annealing to higher temperatures under oxidative conditions, BaTiO₃ tends to reduce the interfacial contact to Pt, which results in the growth of 3D islands. In surplus of oxygen, all BaTiO₃ segregates in the islands with bare Pt(111) between the islands. Recently, it has been found that depending on the islands' thickness, a hexagonal BaTiO₃ structure can be stabilized in the islands, rather than a simple perovskite stacking along the (111) directions.[34] This structure is the high-temperature phase of bulk BaTiO₃.[35]

Under reducing conditions, the annealing of a periodic or amorphous BaTiO₃ layer leads to islands formation as well. However, in this case, the Pt(111) substrate will be covered by an ultrathin $BaTiO_{3-x}$ wetting layer. **Figure 2** shows a series of in situ low-energy electron microscopy (LEEM) images of this wetting process for an area of $1.4 \times 1.4\,\mu m^2$. The bright area in the top left image corresponds to bare Pt(111); the gray contrast resembles BaTiO₃(111) islands. The faint wavy horizontal lines are the substrate step edges. The wetting layer starts to form locally at the rim of the BaTiO₃(111) islands at 1020 K and appears with darker contrast in the LEEM images of Figure 2. Due to the enhanced mobility at the substrate step edges, a growth front of the wetting layer starts there, which connects the local patches to a homogeneous layer with time. At 1020 K, this wetting layer is amorphous. It fully covers the Pt(111) substrate as confirmed by the suppression of the surface core-level shift of Pt in photoemission experiments using synchrotron radiation.[12] Upon temperature increase, a series of

long-range ordered structures is formed in the wetting layer. The OQC is typically found for temperatures ranging from 1070 to 1170 K.[6,12,24,28] At higher temperatures, the film rearranges into a small unit cell periodic approximant structure, which will be discussed in detail in Section 6.

This wetting process can be reversed by reoxidation as shown in the lower sequence of LEEM images in Figure 2. The OQC layer itself is stable against dosing 10^{-6} mbar of molecular oxygen at 900 K. However, with time the bright contrast of the Pt(111) substrate becomes visible and the wetting layer transforms into tiny BaTiO₃ islands (bottom left). Due to the initiation at the step edges and the auto-catalytic character, the dewetting is attributed to a reoxidation of the wetting layer using atomic oxygen, that results from a dissociation at Pt sites.[12] The wetting and dewetting cycle shown in Figure 2 is completed by annealing to higher temperatures in O₂. This reduces the island density due to Ostwald ripening and coalescence. This cycling is fully reversible. For the case of BaTiO₃ on Pt(111), even upon multiple cycling, no Ba or Ti is lost by re-evaporation from the surface or diffusion into the Pt bulk.

For the preparation of OQC films, no special deposition technique is needed. Surface roughening as a consequence of sputter deposition or pulsed-laser deposition will not hinder the OQC formation, as surface defects will be healed out during the high-temperature treatment involved in the OQC formation process. However, the highest level of precision in the preparation of OQC monolayers has been reached using molecular beam
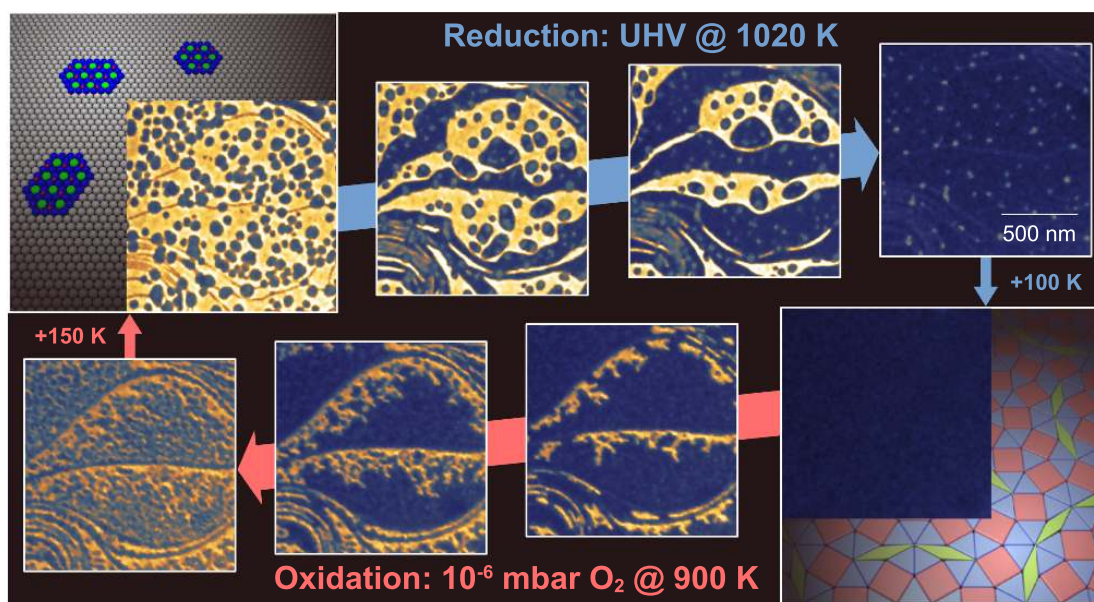
Figure 2. In situ LEEM observation of the wetting and dewetting process of a monolayer of BaTiO₃ on Pt(111). At 1020 K, small hexagonal BaTiO₃(111) islands on bare Pt (top left) are transformed into a complete wetting layer encapsulating the metal surface (top right) under reducing conditions. This proceeds by a spreading of the material from the 3D islands across the Pt substrate in a 2D layer, which continuously grows with time to full coverage. At 100 K higher UHV annealing temperature, this wetting layer develops into the homogeneous dodecagonal OQC (bottom right). For high oxygen chemical potentials, the OQC decays into smallest BaTiO₃ islands (bottom left). This process starts from the substrate step edges and destroys the wetting layer in a dendritic fashion. At 150 K higher temperatures, the small islands grow by coalescence and ripening, which closes the redox-cycle. A movie of this transition is available in the Supporting Information.

epitaxy (MBE).[24] By calibrating independent Ba and Ti sources using a quarz-crystal micro balance (QMB), the right composition and coverage can be guaranteed. As demonstrated in this issue by Zollner et al., perfect monolayers can be grown that extend over the entire surface, which have been already successfully tested as templates for molecular adsorption.[24,25]

When depositing more than the required monolayer $BaTiO_3$ equivalent or having an off-stoichiometric metal composition, a phase separation occurs at the substrate surface. In coexistence to the OQC, the excess material will form additional islands of perovskite-related structures. For the $BaTiO_3$/Pt system, it turned out that the OQC will be formed for higher coverages even if the overall metal composition varies by $\pm 15\%$ around the stoichiometric value. This implies that the OQC stoichiometry is fixed and the islands can act as a materials reservoir that compensates deviations from the optimal composition. This formation of 2D wetting layers of reduced ternary oxides in coexistence with 3D islands is not unique for $BaTiO_3$ on Pt(111). It has also been reported recently for $SrTiO_3$ on Pt(111) as well as $BaTiO_3$ on Ru(0001) and emphasizes a rather universal scheme for ternary oxides on metals.[7,31]

3. Electronic Structure

According to the preparation conditions for the wetting and dewetting cycle introduced earlier, the OQC should have a reduced character. This is confirmed by the Ti-2p core-level binding energies. **Figure 3** shows two X-ray photoelectron spectroscopy (XPS) spectra of the Ti-2p region for a 1 nm thin $BaTiO_3$ film on Pt(111) after 3D island formation and rewetting. The two spectra have been recorded with synchrotron radiation at photon energies of 670 and 1000 eV, respectively.[36] The spectra are normalized to the low binding energy background and offset for clarity. At the given film thickness, a coexistence of $BaTiO_3$ islands with a periodic structure and the OQC is observed upon ultrahigh vacuum (UHV) annealing, as confirmed by LEED (not shown). In these two structures, the titanium atoms are chemically different as evidenced by XPS, which shows a superposition of two Ti-2p doublets. For the higher binding energy component, the Ti-2$p_{3/2}$ peak is centered at 459.0 eV. For the lower binding energy component, this peak is observed at 456.3 eV. The doublet at 459.0 eV
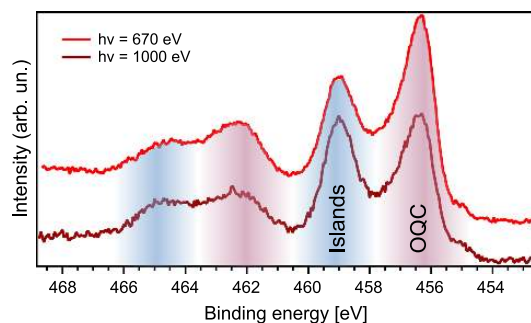
is assigned to the $BaTiO_3$ islands, as its binding energy is in perfect agreement with that of Ti^{4+} in bulk $BaTiO_3$.[37] The intensity decrease in this component upon reducing the photon energy as observed in Figure 3 furthermore confirms that this signal relates to 3D islands. The large downshift in energy of 2.7 eV for the second component, which corresponds to Ti atoms in the OQC, clearly indicates a reduction of this 2D layer. However, this shift is much larger than typically observed for reduced $BaTiO_3$ or TiO_2. There the introduction of oxygen vacancies causes the formation of a Ti^{3+} component, which is shifted by maximal 2 eV.[37–39] A shift that is comparably large as for the OQC has been reported for Ti ions in 2D binary oxides on metal surfaces.[40–43] The energetic position might also reflect a distinct variation in the binding geometry rather than a formal oxidation state. As a consequence of the reduction, Ti-3d states that are located at the Fermi level are filled, which induces a metallic character to the OQC layer. A first hint toward this direction comes from a peak asymmetry of the OQC component, which can be well described using a Doniach–Sunjic line shape.[44]

The direct evidence of the metallic character of the OQC comes from angle-resolved photoemission using momentum microscopy.[23] **Figure 4** shows 2D momentum maps of the bare and the OQC covered Pt(111) substrate, recorded at the Fermi energy and at 0.5 eV binding energy. In the presence of OQC, the signature of the Pt bulk bands remains clearly visible, although these features are damped by the 2D overlayer. In addition, the OQC induces a strong enhancement of the photoelectron intensity around the $\bar{\Gamma}$ point at the Fermi level. Its energetic and momentum position nicely matches that of occupied Ti-3d states in oxygen-deficient $BaTiO_3$ films forming 2D electron gases.[45] With increasing binding energy the intensity distribution becomes narrower indicating an $E(\vec{k})$ dispersion of the Ti-3d states

Figure 3. XPS data for the Ti-2p core level region for the OQC in presence of $BaTiO_3$(111) islands. Due to the increased surface sensitivity at 670 eV photon energy, the photoelectron intensity of the 3D islands is reduced.
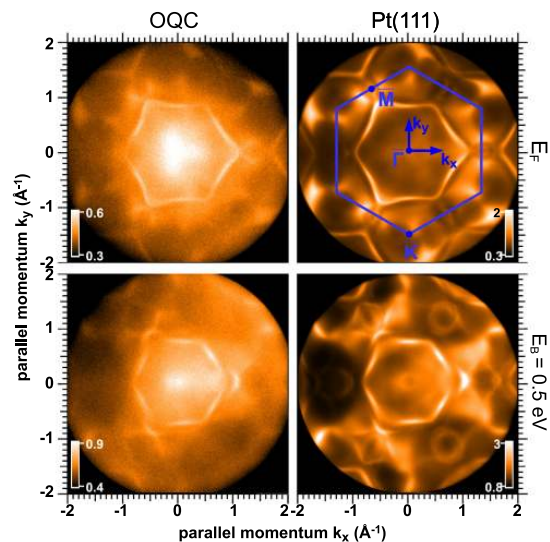
Figure 4. Comparison of the 2D momentum maps of the $BaTiO_3$-derived OQC on Pt(111) and of the bare Pt(111) substrate at the Fermi energy and 0.5 eV below. Color scale in 10^4 CCD counts.

1900624 (4 of 11)

of the OQC. Regarding the filling of the Ti-$3d$ states, the Fermi wave vector has been estimated. From the full-width-at-half-maximum of the momentum distribution along the k_y direction, a lower bound of the Fermi wave vector of $0.4\,Å^{-1}$ could be estimated. This value is consistent with the $0.6\,Å^{-1}$ of a $3d^1$ configuration for each Ti atom within the OQC structure and in agreement with the reduction seen by XPS.[23] The assignment of an unpaired electron spin on each Ti site is an exciting finding, which paves the way into future studies of the magnetic ordering in the OQC layer.

4. Real Space Structure

The real space structure of the OQC has been determined from atomically resolved STM images. **Figure 5** shows an example on
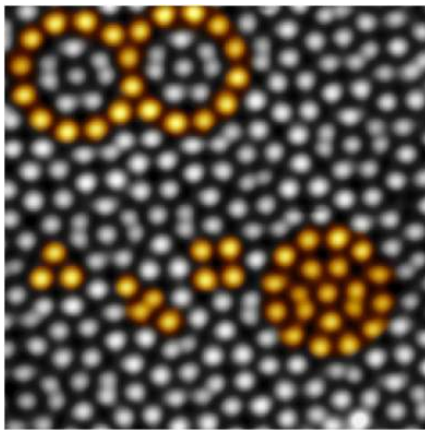

Figure 5. Atomically resolved STM image of the $BaTiO_3$-derived OQC on Pt(111). The structure forms from three different tiling elements that build a characteristic dodecagon. The 2D tiling is created from overlapping dodecagons. The coloring has been added to emphasize the building blocks. $10 \times 10\,nm^2$, 30 pA, -0.15 V.

the scale of $10 \times 10\,nm^2$. The OQC appears as bright protrusions with an interatomic spacing of $6.85\,Å$. This imaging contrast is robust upon bias voltage variations away from the Fermi level and does not depend on bias polarity within a range from -1.0 to 1.0 V.[6] These tunneling characteristics can be explained by tunneling out or into the Ti $3d$ states, which is in line with the photoemission results. A detailed inspection of the atomically resolved features in the STM image reveals three different tiling elements within the OQC: equilateral triangles, squares, and rhombs inclining $30°$ and $150°$ angles. The vertices of these tiling elements are decorated by Ti. These three tiling elements are frequently found in groups of twelve triangles, five squares, and two rhombs that arrange in a characteristic dodecagon as emphasized in color in Figure 5. The 2D layer builds up from overlapping dodecagons.

A mathematical description of a 2D dodecagonal quasicrystal with these building blocks has been reported by Niizeki, Mitani, and Gähler in the late 1980s, why we denote this structure as the NGT.[19,20] This tiling can be generated by the cut-and-project method from a 4D periodic lattice, which is the general scheme to rationalize quasicrystals.[46–48] Alternatively, it can also be generated by recursion.[22] The recursion rule is shown in **Figure 6**a. In each deflation step, a triangle is substituted by seven triangles and three squares of smaller length. Each square is replaced by 16 triangles, five squares, and four rhombs. The rhombs are replaced by eight triangles, two squares, and three rhombs. The shaded areas in the rhombs and the squares indicate, that a given orientation of these tiles needs to be respected, which reduces their symmetry.[21,22] Mathematically, this substitution rule can be formulated by a deflation matrix T

$$T = \begin{pmatrix} 7 & 16 & 8 \\ 3 & 5 & 2 \\ 0 & 4 & 3 \end{pmatrix}. \tag{1}$$

The rows of T are assigned to the number of triangle, square, and rhomb tiles in each replacement, respectively. The Eigensystem solution of T reveals two important properties of
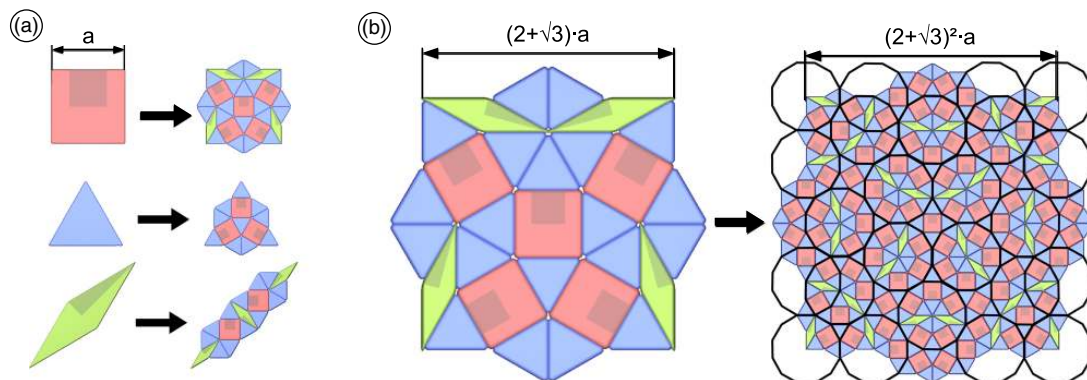

Figure 6. Substitution rules for the dodecagonal NGT: a) First recursion step.[22] b) Second recursion step for the square element: By multiple iterations, the recursion generates self-similar tilings that scale with $(2 + \sqrt{3})$. The higher-hierarchical tiling connects the centers of dodecagons formed in the lower generation instance (black circles).

the NGT: The square root of the eigenvalue gives the scaling factor of self-similarity in the NGT of $(2 + \sqrt{3})$. Furthermore, the corresponding Eigenvector of the deflation matrix T

$$((1 + \sqrt{3}), 1, (1 + \sqrt{3})^{-1}) \approx (2.73, 1, 0.37) \tag{2}$$

represents the tiling element ratio in the NGT: the numbers of triangles relative to the numbers of squares and of rhombs. This ratio can be used to derive other entities that can be used for a statistical analysis of the NGT, e.g., the frequency of shared edges between the different tiles.

Figure 6b shows that the subsequent application of the recursion rule not only increases the size of the grown patch according to the scaling factor but also results in a self-similarity of the tiling. In the third-generation tiling shown in Figure 6b on the right, the subsequent application of the recursion rule has led to the formation of characteristic dodecagons of the NGT. By connecting the centers of these dodecagons, a triangle-square-rhomb tiling is formed on next-larger scale as emphasized in black in Figure 6b.

Recently, a systematic statistical analysis of the BaTiO₃-derived OQC tiling has been conducted for a system of 8100 vertex positions as determined from an atomically resolved large-scale STM image.[21] In this issue, Zollner et al. repeat this analysis for an even larger dataset of almost 20 000 vertices.[24] The comparison of both systems to the statistics of the ideal NGT regarding tiling element ratio and frequency of shared edges clearly reveals that the OQC is the first realization of this ideal dodecagonal model system. To the best of our knowledge, these are the largest real space datasets of any quasicrystal analyzed so far.

First of all, an almost perfect match of the OQC tiling element ratios of 2.75:1:0.36 (8100 vertices) and 2.75:1:0.38 (20 000 vertices) to that of the ideal NGT of 2.73:1:0.37 has been found. Even more intriguing is the superior agreement in the frequency of shared edges. **Figure 7** summarizes the values obtained for the three systems. In the NGT, only triangle-square, triangle-triangle, and triangle-rhomb edges occur. Their relative frequencies agree perfectly with those of the experimentally determined ones for the real OQC. Due to defects that are intrinsically present in real systems, also rhomb-rhomb, rhomb-square, and square-square
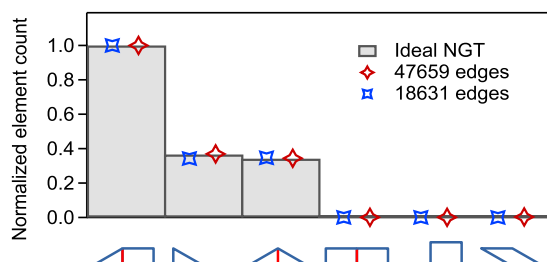
edges occur. However, they amount to 12 out of 18 631 edges (8100 vertices) and 128 out of 47 659 (20 000 vertices) in total, which is a remarkably low number of defects and underlines the perfectness of quasicrystalline order here.[21,24]

Deviations of the OQC statistics from the NGT have been reported with respect to the rotation of rhombs and dodecagons.[21] The combination of both facts, namely, variations in the rotation of building blocks and an ideal edge frequency, points toward a significant amount of phason flips in the tiling. Phasons flips are changes of vertex positions in real space between well-determined positions as a consequence of excitations in the higher-dimensional hyperspace.[49–51] This small displacement of a vertex results in exchanged positions of the surrounding tiles. Please note that the edge-sharing frequencies of the NGT are preserved upon single phason flips. In this way, the quality of the quasicrystal can be assessed in the presence of the specific disorder of phason flips.

The presence of phason flips makes the recognition of the higher-hierarchical tiling in STM images more challenging. By neglecting the location and the orientation of rhombs and locating rings of twelve atoms that create a framework of adjacent dodecagons, the higher-hierarchical tiling were identified in **Figure 8**a. For a better comparison to the ideal NGT, the selected area in the STM image corresponds to the tiling shown on the right in Figure 6b. The Ti atomic positions of the OQC
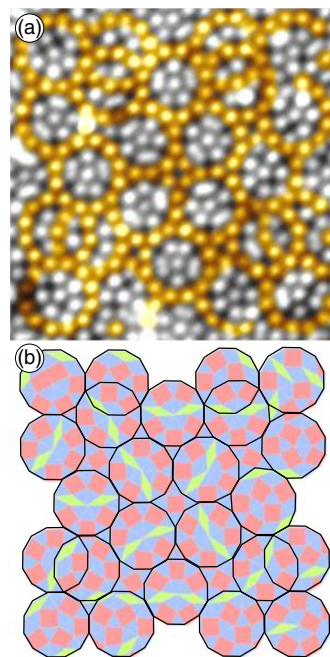
Figure 8. a) The higher-hierarchical tiling of the BaTiO₃-derived OQC measured by STM and b) the corresponding tiling scheme. Rings of 12 atoms at the outer ring of the characteristic dodecagons are emphasized in yellow color in the STM image and as black rings in (b). The apparent disorder in the orientation of rhombs within these dodecagons is caused by phason flips. (a) 13 × 13 nm², 25 pA, 1.0 V.

Figure 7. Statistical analysis of the OQC based on STM images: Frequencies of shared edges between adjacent tiles in the mathematically defined NGT (bars) and for two extended data sets of different OQC preparations on different Pt(111) crystals (red and blue marker).[21,24]

tiling as extracted from the STM image are shown in Figure 8b. It clearly indicates strong deviations of the inner structure of the characteristic dodecagons from the ideal NGT. For only half of the dodecagons, the two rhombs point toward the center in agreement with the NGT. For all the others, at least one of the rhombs has moved toward the rim or even left the dodecagon. This motion of rhombs is the signature of multiple phason flips.

5. Diffraction

Oxide quasicrystals were discovered due to the observation of a twelvefold-symmetric diffraction pattern in LEED, as shown for the example of the $BaTiO_3$-derived OQC on Pt(111) in Figure 1 and **9**a. This clear dodecagonal pattern, instead of diffraction rings, reports on an epitaxial alignment of the OQC along the high-symmetry directions of the substrate. The LEED pattern of the OQC is characterized by twelve sharp and intense spots at $1.03\,Å^{-1}$ as shown in Figure 9a, which has been recorded by spot-profile analysis low-energy electron diffraction (SPALEED). The intense spots correspond to the second diffraction order, in correction to the initial report in ref. [6]. Indeed, the first-order spots are only seen at kinetic energies below 10 eV (not shown here). Two additional rings of twelve spots are found at larger **q** vectors under a rotation of 15° with respect to the first ring. Additionally, close to the first-order spots of the Pt substrate pairs of spots occur in twelve directions. In addition to this characteristic dodecagonal pattern, the sixfold symmetry of the substrate leads to a backfolding of intense QC spots from neighboring surface Brillouin zones of the hexagonal substrate, as has been explained in great detail recently.[24] The backfolding at the substrate superimposes a sixfold symmetric pattern to the original dodecagonal diffraction of the OQC. An

example for a backfolded spot, which is extraordinary intense at the given electron kinetic energy, is marked by the black open circle in Figure 9a.

An alternative approach to the momentum space can be obtained from FT of atomically resolved STM images as shown in Figure 9b for a dataset with 20 000 atomic positions. The use of identical scatterers at these atomic coordinates results in a reduced background on the FT and unravels the long-range dodecagonal symmetry of the OQC tiling nicely. In comparison to the LEED pattern of Figure 9a, many higher diffraction orders of nonzero intensity are seen in the FT. Keeping in mind that the FT was calculated from the Ti subgrid only, whereas the LEED pattern additionally contains the information about the Ba and O grids; the lower number of observed spots in LEED points toward systematic extinction of diffraction spots.

The diffraction pattern of the ideal and infinitely extended NGT is shown in Figure 9c. It has been derived by Fourier transforming the acceptance domain of the NGT in internal space.[20,52] Positions and intensities of the diffraction peaks of the NGT in Figure 9c agree reasonably with the FT in Figure 9b. Surprisingly, the relative intensities of the three inner rings of 12 spots seen in LEED are also in good agreement with those of the NGT tiling. From the additional atomic decoration of the NGT by Ba and O, larger intensity differences are expected as compared with the pure Ti grid.

One way to possibly access the tiling decoration is the use of SXRD. There, due to the small scattering cross-section of the X-rays, only single scattering needs to be considered. Consequently, the measured intensities can be directly compared with model calculations. A reciprocal space map of the $BaTiO_3$-derived OQC on Pt(111) measured by SXRD is shown in **Figure 10**. The small full-width-at-half-maximum of the OQC in the order of $0.03\,Å^{-1}$ reports of the high quality of the

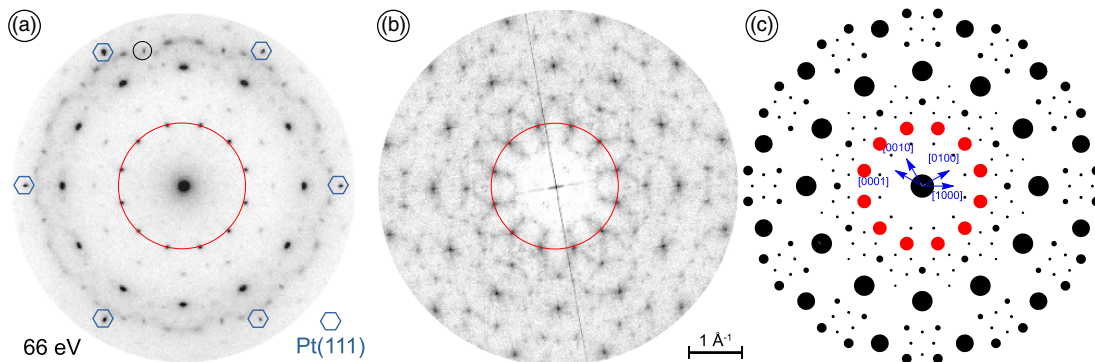**Figure 9.** a) Low-energy electron diffraction of the $BaTiO_3$-derived OQC on Pt(111) (SPA-LEED at 66 eV). b) FT of an atomically resolved STM image with almost 20 000 Ti atoms. c) Calculated diffraction pattern of the ideal NGT. The second-order diffraction is marked in red for comparison. The black open circle in (a) emphasizes a backfolded spot originating from the next Brillouin zone of the Pt(111) substrate.
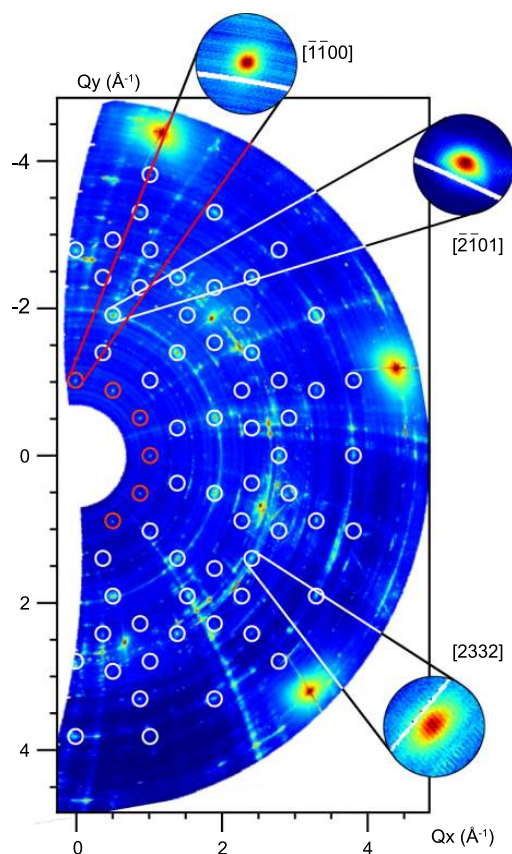
Figure 10. Reciprocal space map of the BaTiO$_3$-derived OQC on Pt(111) measured by SXRD. The circles emphasize the diffraction spots of the OQC. The second-order diffraction spots are marked in red. The three Bragg peaks [$\bar{1}\bar{1}00$], [$\bar{2}\bar{1}01$], and [2332] are shown on a 20× enlarged scale in the insets from top to bottom, respectively.

dodecagonal layer. The establishment of a complete structural model of the OQC is one of the current topics of research on this system. Note that the theoretical model reported by Cockayne et al. is able to predict a dodecagonal Ba–Ti–O structure with a Ba$_{0.37}$Ti$_1$O$_{1.55}$ stoichiometry where the NGT is formed by the Ba atoms.[27] Experimentally, we find a stoichiometry close to Ba$_1$Ti$_1$O$_{3-x}$ and observe a NGT in STM, which is formed by Ti atoms.

6. Approximants

A common scheme to all quasicrystal systems is their formation within a small temperature window in the multidimensional composition phase diagram. Upon deviations from the optimal formation conditions of quasicrystals, periodic structures are typically formed that are created from the same building blocks

as the related quasicrystal. They often have unit cells that are smaller or larger patches of the parent aperiodic structure and are called approximants. Also for OQCs, such approximants have been reported as shown in **Figure 11**.[7,26,28,29,31] Within the ideal NGT shown in Figure 11a, two clusters are highlighted. By translating these clusters along two unit vectors in the plane, periodic tilings arise as shown in Figure 11b,c. The larger the cluster is, i.e., its unit cell, the closer it resembles the aperiodic structure.

The small unit cell approximant shown in Figure 11b was observed for the BaTiO$_3$/Pt system.[28,29] This triangle-square tiling is called σ-phase approximant or snub-square tiling and contains a combination of six tiles as found in the OQC. It is also known as $3^2.4.3.4$ Archimedean tiling[53] and was described for the first time 400 years ago by Johannes Kepler.[54] On the Pt(111) substrate, it forms a commensurate superstructure under 8° rotation out of the substrate high-symmetry directions. By a combination of STM, LEED, SXRD, and calculations by means of density functional theory (DFT), its structure has been determined as also presented in this issue by Meyerheim et al.[28,30] The same superstructure has been observed recently for BaTiO$_3$ on Ru(0001), as reported in this issue by Zollner et al.[31] This indicates the broader concept of OQC and approximants in the field of perovskites on metal substrates.

The large unit cell approximant shown in Figure 11c has been discovered in the SrTiO$_3$/Pt(111) system.[7] Its unit cell includes all motifs that are essential for the description of the OQC tiling. In addition to the three basic building blocks, even the characteristic dodecagon is part of the unit cell. In total it contains 36 tiles and 24 Ti atoms. Anticipating the similar stoichiometry as reported for the σ-phase approximant of Ba:Ti:O = 1:1:2.5, the large unit cell approximant contains 108 atoms in the unit cell.[28,29] Similar to the σ-phase approximant, this large unit cell approximant is in registry with the substrate. It forms a $\begin{pmatrix} 9 & 0 \\ 9 & 16 \end{pmatrix}$ superstructure with respect to Pt(111). Due to the symmetry mismatch, six domains of the approximant contribute to the LEED pattern, which is shown in **Figure 12**. At the position corresponding to the second-order diffraction of the OQC, which is marked by the red circle in Figure 12, the approximant and the OQC pattern are identical. However, a clear sixfold symmetry is seen at the positions of the third- and fourth-order OQC diffraction spots marked by the blue circles. The different domains contribute to common spots every 60° along these circles, whereas their diffraction spots are located at slightly different positions with 30° rotations in between. As a consequence, the diffraction intensities are smeared out in the reciprocal space. An additional difference to the diffraction pattern of the OQC is the much higher number of intense diffraction spots. This could be related to the substrate registry that slightly distorts the unit cell.[7] As a consequence, small deviations in lengths and angles of the tiling elements occur that might lift the prerequisites for destructive interference, which increases the number of observed spots.

Within the tiling of the BaTiO$_3$-derived OQC on Pt(111), a small number of repeating units of the large unit cell

1900624 (8 of 11)
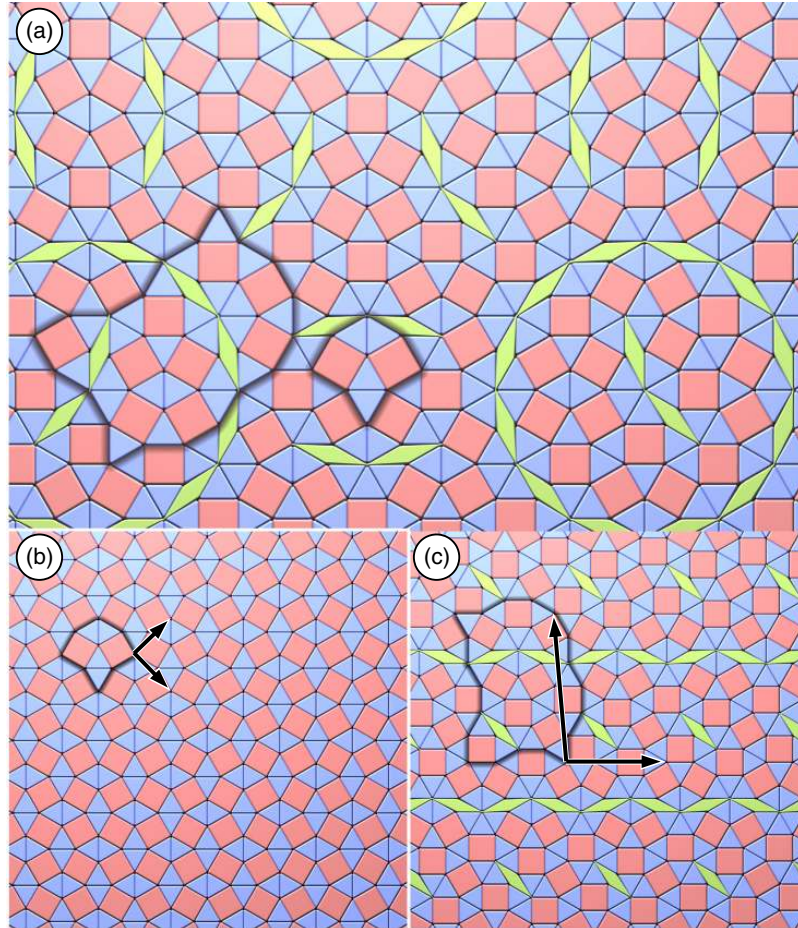
Figure 11. Illustration of the concept of the relationship of quasicrystals and their approximants. The building blocks of the OQC tiling highlighted in (a) are forming periodic structures of different unit cell dimensions (b, c). The unit vectors of the periodic structures are indicated by arrows.

approximant are locally present in multiple orientations.[21] At the current level of understanding, these units help to stabilize the epitaxial alignment of the OQC on the Pt(111) substrate.

In adddition to the two examples of approximants discussed earlier in detail, a variety of additional approximant structures is known to exist in the various combinations of ternary oxide monolayers on metal surfaces.[26,31] These experimental findings stimulated calculations that try to find a unique decoration scheme for the tiling elements to explain all observed structures.[27] Whereas this model gives interesting insights into formation of possible dodecagonal oxide structures, it fails to predict the experimentally determined 1:1 stoichiometry for Ba and Ti in the OQC and the σ-phase approximant.[28] Nevertheless, the approach to explain all observed structures by one unique decoration seems to be the key to reach a

complete understanding of the binding concept for 2D ternary oxide monolayers.

7. Conclusion and Outlook

As we discuss in this review, the field of aperiodic oxide monolayers that are formed from ternary perovskites has developed into a broad research area. All aspects and peculiarities of quasicrystals can be studied here in a textbook-like fashion for a 2D system. Especially, the combination of different diffraction techniques with real-space imaging by STM allows new insights as all atomic coordinates within a real quasicrystalline tiling are accessible and deliver via Fourier transform (FT) a microscopic picture of diffraction.

Figure 12. Diffraction pattern of the large unit cell approximant derived from $SrTiO_3$ on Pt(111).[7] The approximant forms a commensurate superstructure on the sixfold 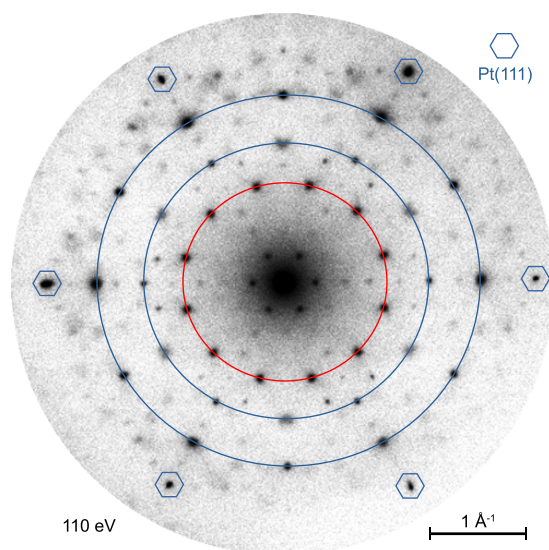substrate. The position of the second- to fourth-order diffraction spots of the OQC is indicated by red and blue circles. Along the blue circles the sixfold symmetry induced by the superposition of six approximant domains is clearly seen.

The presence of well-defined quasicrystalline structures adds another degree of freedom to perovskite oxide interfaces beyond the formation of 2D electron gases, new forms of topology, and new ferroic coupling mechanisms.

Supporting Information

Supporting Information is available from the Wiley Online Library or from the author.

Conflict of Interest

The authors declare no conflict of interest.

[1] F. Zavaliche, T. Zhao, H. Zheng, F. Straub, M. P. Cruz, P.-L. Yang, D. Ha, R. Ramesh, *Nano Lett.* **2005**, *5*, 1793.
[2] R. Ramesh, N. A. Spaldin, *Nat. Mat.* **2007**, *6*, 21.
[3] V. Garcia, M. Bibes, L. Bocher, S. Valencia, F. Kronast, A. Crassous, X. Moya, S. Enouz-Vedrenne, A. Gloter, D. Imhoff, C. Deranlot, N. D. Mathur, S. Fusil, K. Bouzehouane, A. Barthélémy, *Science* **2010**, *327*, 1106.
[4] A. Ohtomo, H. Y. Hwang, *Nature* **2004**, *427*, 423.
[5] R. Pentcheva, W. Pickett, *Phys. Rev. B* **2006**, *74*, 035112.
[6] S. Förster, K. Meinel, R. Hammer, M. Trautmann, W. Widdra, *Nature* **2013**, *502*, 215.
[7] S. Schenk, S. Förster, K. Meinel, R. Hammer, B. Leibundgut, M. Paleschke, J. Pantzer, C. Dresler, F. O. Schumann, W. Widdra, *J. Phys. Condens. Matter.* **2017**, *29*, 134002.
[8] D. Shechtman, I. Blech, D. Gratias, J. W. Cahn, *Phys. Rev. Lett.* **1984**, *53*, 1951.
[9] L. Bendersky, *Phys. Rev. Lett.* **1985**, *55*, 1461.
[10] T. Ishimasa, H.-U. Nissen, Y. Fukano, *Phys. Rev. Lett.* **1985**, *55*, 511.
[11] N. Wang, H. Chen, K. Kuo, *Phys. Rev. Lett.* **1987**, *59*, 1010.
[12] S. Förster, J. I. Flege, E. M. Zollner, F. O. Schumann, R. Hammer, A. Bayat, K.-M. Schindler, J. Falta, W. Widdra, *Ann. Phys.* **2017**, *529*, 1600250.
[13] S. J. Tauster, S. C. Fung, R. L. Garten, *J. Am. Chem. Soc.* **1978**, *100*, 170.
[14] C. S. Ko, R. J. Gorte, *Surf. Sci.* **1985**, *161*, 597.
[15] S. J. Tauster, S. C. Fung, R. T. K. Baker, J. A. Horsley, *Science* **1981**, *211*, 1121.
[16] Z. Hu, K. Kunimori, H. Asano, T. Uchijima, *J. Catal.* **1988**, *112*, 478.
[17] Y. N. Sun, Z. H. Qin, M. Lewandowski, E. Carrasco, M. Sterrer, S. Shaikhutdinov, H.-J. Freund, *J. Catal.* **2009**, *266*, 359.
[18] O. Dulub, W. Hebenstreit, U. Diebold, *Phys. Rev. Lett.* **2000**, *84*, 3646.
[19] N. Niizeki, H. Mitani, *J. Phys. A Math. Gen.* **1987**, *20*, L405.
[20] F. Gähler, in *Proceedings of the ILL/CODEST Workshop*, World Scientific, Singapore **1988**, p. 13.
[21] S. Schenk, E. M. Zollner, O. Krahn, B. Schreck, R. Hammer, S. Förster, W. Widdra, *Acta Cryst.* **2019**, *A75*, 307.
[22] L.-G. Liao, W.-B. Zhang, T.-X. Yu, Z.-X. Cao, *Chin. Phys. Lett.* **2013**, *30*, 026102.
[23] C.-T. Chiang, M. Ellguth, F. O. Schumann, C. Tusche, R. Kraska, S. Förster, W. Widdra, *Phys. Rev. B* **2019**, *100*, 125149.
[24] E. M. Zollner, S. Schenk, M. Setvin, S. Förster, *Phys. Stat. Sol. B* **2019**, https://doi.org/10.1002/pssb.201900620.
[25] E. M. Zollner, S. Schenk, S. Förster, W. Widdra, *Phys. Rev. B* **2019**, *100*, 205414.
[26] S. Förster, K. Meinel, K.-M. Schindler, W. Widdra, *Surf. Interface Anal.* **2012**, *44*, 628.
[27] E. Cockayne, M. Mihalkovič, C. L. Henley, *Phys. Rev. B* **2016**, *93*, 020101(R).
[28] S. Förster, M. Trautmann, S. Roy, W. A. Adeagbo, E. M. Zollner, R. Hammer, F. O. Schumann, K. Meinel, S. K. Nayak, K. Mohseni, W. Hergert, H. L. Meyerheim, W. Widdra, *Phys. Rev. Lett.* **2016**, *117*, 095501.

[29] K. Mohseni Roy, S. Förster, M. Trautmann, F. Schumann, E. Zollner, H. Meyerheim, W. Widdra, *Z. Kristallogr.* **2016**, *231*, 749.

[30] K. Mohseni, H. L. Meyerheim, *Phys. Stat. Sol. B* **2019**, https://doi.org/10.1002/pssb.201900605.

[31] E. M. Zollner, F. Schuster, K. Meinel, P. Krause, S. Schenk, B. Allner, S. Förster, W. Widdra, *Phys. Stat. Sol. B* **2019**, Unpublished.

[32] S. Förster, W. Widdra, *Surf. Sci.* **2010**, *604*, 2163.

[33] S. Förster, W. Widdra, in *Oxide Materials at the Two-Dimensional Limit*, (Eds: F. P. Netzer, A. Fortunelli), Springer, Cham, Switzerland **2016**, Ch. 13.

[34] F. Schumann, K. Mohseni, S. Förster, E. M. Zollner, R. Felici, W. A. Adeagbo, W. Hergert, H. L. Meyerheim, W. Widdra, Unpublished.

[35] H. T. Evans Jr., R. D. Burbank, *J. Chem. Phys.* **1948**, *16*, 634.

[36] M. Muntwiler, J. Zhang, R. Stania, F. Matsui, P. Oberta, U. Flechsig, L. Patthey, C. Quitmann, T. Glatzel, R. Widmer, E. Meyer, T. A. Jung, P. Aebi, R. Fasel, T. Greber, *J. Synchrotron. Radiat.* **2017**, *24*, 354.

[37] L. T. Hudson, R. L. Kurtz, S. W. Robey, D. Temple, R. L. Stockbauer, *Phys. Rev. B* **1993**, *47*, 1174.

[38] W. Göpel, J. A. Anderson, D. Frankel, M. Jaehnig, K. Phillips, J. A. Schäfer, G. Rocker, *Surf. Sci.* **1984**, *139*, 333.

[39] J. T. Mayer, U. Diebold, T. E. Madey, E. Garfunkel, *J. Electron Spectrosc. Relat. Phenom.* **1995**, *73*, 1.

[40] F. Sedona, G. A. Rizzi, S. Agnoli, F. X. Llabrés i Xamena, A. Papageorgiou, D. Ostermann, M. Sambi, P. Finetti, K. Schierbauk, G. Granozzi, *J. Phys. Chem. B* **2005**, *109*, 24411.

[41] G. Barcaro, S. Agnoli, F. Sedona, G. A. Rizzi, A. Fortunelli, G. Granozzi, *J. Phys. Chem. C* **2009**, *113*, 5721.

[42] D. Ragazzon, A. Schaefer, M. H. Farstad, L. E. Walle, P. Palmgren, A. Borg, P. Uvdal, A. Sandell, *Surf. Sci.* **2013**, *617*, 211.

[43] M. H. Farstad, D. Ragazzon, H. Grönbeck, M. D. Strømsheim, C. Stavrakas, J. Gustafson, A. Sandell, A. Borg, *Surf. Sci.* **2016**, *649*, 80.

[44] S. Doniach, M. Sunjic, *J. Phys. C Solid State Phys.* **1970**, *3*, 285.

[45] P. Lutz, S. Moser, V. Jovic, Y. J. Chang, R. J. Koch, S. Ulstrup, J. S. Oh, L. Moreschini, S. Fatale, M. Grioni, C. Jozwiak, A. Bostwick, E. Rotenberg, H. Bentmann, F. Reinert, *Phys. Rev. Mater.* **2018**, *2*, 094411.

[46] N. G. de Bruijn, *Indagationes Math.* **1981**, *43*, 38.

[47] P. Kramer, R. Neri, *Acta Cryst. A* **1984**, *40*, 580.

[48] T. Janssen, *Phys. Rep.* **1988**, *168*, 55.

[49] P. Bak, *Phys. Rev. Lett.* **1985**, *54*, 1517.

[50] J. E. S. Socolar, T. C. Lubensky, P. J. Steinhardt, *Phys. Rev. B* **1986**, *34*, 3345.

[51] M. Widom, *Phil. Mag.* **2008**, *88*, 2339.

[52] A. Yamamoto, *Acta Cryst.* **1996**, *A52*, 509.

[53] B. Grünbaum, G. C. Shepard, *Math. Magazine* **1977**, *50*, 227.

[54] J. Kepler, *Harmonices Mundi*, Linz, **1619**.

1900624 (11 of 11)

ORIGINAL PAPER

physica **pss**b
status solidi

Two-Dimensional Wetting Layer Structures of Reduced Ternary Oxides on Ru(0001) and Pt(111)

Eva Maria Zollner, Fabian Schuster, Klaus Meinel, Philine Stötzner, Sebastian Schenk, Bettina Allner, Stefan Förster,* and Wolf Widdra

Long-range ordered structures of reduced oxide films with monolayer thickness derived from $BaTiO_3$ and $SrTiO_3$ on Ru(0001) and Pt(111) are investigated by scanning tunneling microscopy (STM) and low-energy electron diffraction (LEED). Upon ultrahigh vacuum annealing at 1100 K, a hexagonal phase is observed for $BaTiO_3$ on Ru(0001), which forms similarly from $SrTiO_3$ on Pt(111). At higher temperatures, a triangle–square tiling called σ-phase develops in the $BaTiO_3$/Ru(0001) system, with a unit cell rotation of 15° against the Ru(0001) substrate. Furthermore, it is shown that this 15° rotated σ-phase also forms in the $BaTiO_3$/Pt(111) system in addition to the already known 8° rotated σ-phase. The results emphasize a strong flexibility in the structural parameters of the reduced oxide wetting layers in response to the substrate interaction strength.

1. Introduction

The discovery of a 2D quasicrystalline structure derived from $BaTiO_3$ on the Pt(111) surface opened a new chapter in the heteroepitaxy at interfaces.[1] This system is the first example for a spontaneous formation of a dodecagonal symmetry on a sixfold substrate on the atomic level.

The opposite, the formation of periodic structures on quasicrystal surfaces, is known from the beginning of quasicrystal research: periodic overlayers emerged at the surfaces of bulk-quasicrystals upon slightly altering the sample composition at the surface.[2–4] They have also been formed in many investigations of solid films deposited on quasicrystal surfaces.[5–7]

E. Maria Zollner, F. Schuster, Dr. K. Meinel, P. Stötzner, S. Schenk, B. Allner, Dr. S. Förster, Prof. W. Widdra
Institute of Physics
Martin-Luther-Universität Halle-Wittenberg
D-06099 Halle, Germany
E-mail: stefan.foerster@physik.uni-halle.de
Prof. W. Widdra
Max-Planck-Institut für Mikrostrukturphysik
D-06120 Halle, Germany

The epitaxial alignment of an overlayer to the substrates has many ingredients. It results from an interplay of interactions within the overlayer and between the overlayer and the substrate. They are linked to the chemical nature of the constituents, the symmetry, or the misfit between the two systems and can induce significant strain in the overlayer.[8] Different types of crystal–crystal epitaxy are classified according to their superstructure matrix coefficients. Integer coefficients report on a commensurate alignment, fractional coefficients describe higher-order-commensurate structures, and irrational coefficients are the signature of incommensurate structures. Additional types can be distinguished in reciprocal space, e.g., the point-on-line symmetry for which substrate and superstructure spots coincide along a line.[9] The basics theory to describe epitaxy in periodic systems is the coincidence-site-lattice (CSL) theory.[10–12] This theory has been expanded to interfaces of periodic structures with quasicrystals in the formulation of the coincidence reciprocal lattice planes (CRLP) theory.[13] The observation of a coincidence of reciprocal lattice points of a periodic overlayer on a bulk quasicrystal is an even stronger criterion for stabilizing an epitaxial quasicrystal–crystal interface.[14]

The peculiar long-range order of oxide quasicrystals (OQCs) develops in a wetting layer of reduced $BaTiO_3$ or $SrTiO_3$ that forms upon annealing in ultrahigh vacuum on the Pt(111) surface.[1,15–17] A comprehensive introduction into different aspects ranging from a statistical tiling analysis to electronic properties is given by Förster et al. in this issue.[18] For higher preparation temperatures, a transition of the wetting layer toward a periodic approximant structure is observed for $BaTiO_3$/Pt(111).[19] This approximant forms a σ-phase tiling with four triangles and two squares in the unit cell. It is described by a $\begin{pmatrix} 27/5 & 2 \\ 3/4 & 5 \end{pmatrix}$ superstructure matrix corresponding to a 8° rotation.[19–21] Its higher-order commensurate cell described by $\begin{pmatrix} 27 & 10 \\ 3 & 20 \end{pmatrix}$ contains a patch of 4×5 primitive unit cells. In the closely related system of $SrTiO_3$/Pt(111), small patches of the OQC develop embedded in extended domains of a larger unit cell approximant.[15] This approximant contains 36 tiles of the OQC in its unit cell and forms a commensurate lattice described by a $\begin{pmatrix} 9 & 0 \\ 16 & 9 \end{pmatrix}$ matrix.

Here, we report on 2D wetting layer structures formed from $BaTiO_3$ on Ru(0001), which we also found in $SrTiO_3$/Pt(111) and $BaTiO_3$/Pt(111). Upon annealing an initially 0.4 nm thin $BaTiO_3$ layer on Ru(0001) to 1100 K, we observe the formation of a long-range ordered wetting layer structure. Its nature is different as compared with the aforementioned OQC and its approximants, as the interatomic distance of the Ti ions in the layer is a factor of two smaller. This structure also forms in slightly Ti-enriched layers of $SrTiO_3$ on Pt(111). Upon annealing $BaTiO_3$ on Ru(0001) at 1250 K, this structure is transformed into the σ-phase. The latter forms a commensurate lattice on Ru(0001) and is rotated by 15° against the Ru(0001) substrate. As reported here, this orientation can also occur for $BaTiO_3$/Pt(111), in addition to the already known 8° rotation of the σ-phase in this system.[19]

2. Results

For fabricating 2D layers of $BaTiO_3$ on Ru(0001), 0.4 nm of $BaTiO_3$ have been deposited by molecular beam epitaxy (MBE) at room temperature (RT). The as-deposited $BaTiO_3$ has been fully oxidized by annealing to 900 K in 10^{-5} mbar O_2. Upon subsequent annealing in ultrahigh vacuum (UHV) at 1100 K, a long-range ordered superstructure is formed. In large-scale scanning tunneling microscopy (STM) images, the surface exhibits extended terraces separated by monoatomic steps. On smaller scale, a superstructure is observed that entirely covers the Ru(0001) terraces. **Figure 1**a shows this structure at atomic resolution on a scale of 25×12.5 nm². Up to four atoms are grouped together at the surface. On the first glance, their arrangement seems random. However, the Fourier transform (FT) of the image shown as inset in Figure 1a reveals a long-range hexagonal order. In the close-up image in Figure 1b, the hexagonal unit cell is shown. It consists of individual atoms that are the center atoms of a windmill-like building block. Six rhombs of four atoms are arranged around these centers. This structure arises as shown in Figure 1c from a small-scale hexagonal lattice. By displacing the atoms to groups of four around a central atom, a $\begin{pmatrix} 4 & 1 \\ 3 & 4 \end{pmatrix}$ superstructure is created. According to the matrix, the superstructure lattice is enlarged by a factor of $\sqrt{13} \times (\approx 3.6)$ and rotated by 12.1°. In the FT of the STM image of Figure 1a, both lattices can be recognized. In addition to the superstructure lattice marked by the red circles, the primitive hexagonal mesh gives rise to the high intensities of the outer spots marked by the blue circles.

This structure exhibits a chirality with respect to the arrangement of rhombs. In Figure 1b,c, a windmill with clockwise rotation is indicated. In addition, windmills with a counter clockwise rotation have been found on other terraces (not shown here). However, the rotation remains constant on one terrace and there are no phase boundaries on a terrace. From previous STM studies for 2D superstructures of reduced $BaTiO_3$ on Pt(111), it is known that the Ti sublattice of the ternary oxide is seen in STM for bias voltages close the Fermi level.[1,19,22] These tunneling conditions apply here as well. Thus the contrast in STM is attributed to Ti atoms.

The low-energy electron diffraction (LEED) pattern of the structure is shown in Figure 1d. It reveals a flower-like diffraction
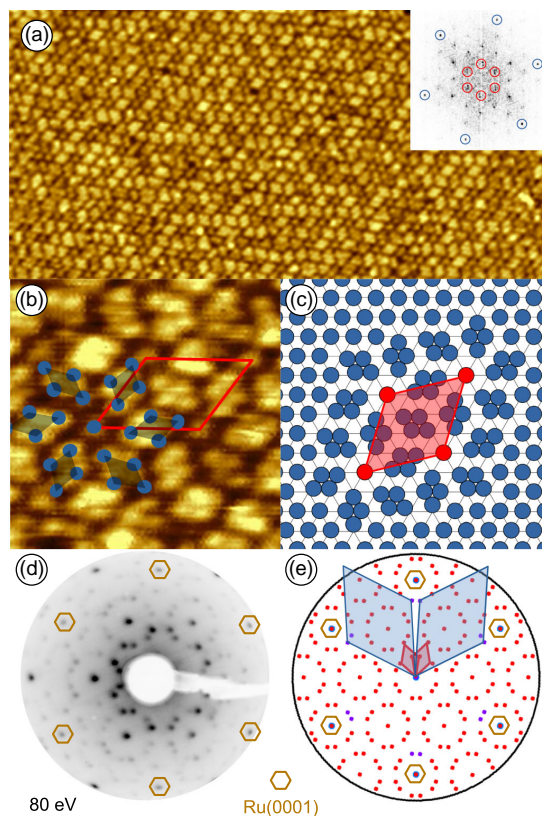
Figure 1. Hexagonal superstructure in a 2D network derived from $BaTiO_3$ on Ru(0001). The STM images (a,b) reveal a windmill-like pattern on the atomic scale. The hexagonal order is seen in the FT of the image (inset in (a)). The superstructure arises from systematic displacements of the atoms from a primitive hexagonal lattice as shown in (c). The d) measured and e) calculated LEED patterns show the formation of two rotational domains of a commensurate $\begin{pmatrix} 5 & 1 \\ 4 & 5 \end{pmatrix}$ superstructure. The unit cell of the windmill-like structure is marked red in (b,c,e), that of the primitive hexagonal cell of the overlayer is marked blue. a) 25×12.5 nm², b) 3.2×3.2 nm², a,b) 170 pA, 1.1 V.

pattern that consists of groups of 12 equidistant spots around the substrate lattice spots and the respective $(\sqrt{3} \times \sqrt{3})R30°$ positions. In contrast to the fast Fourier transform (FFT) of the STM image, the LEED pattern represents a superposition of all rotational superstructure domains. A simulation of the LEED pattern determines a $\begin{pmatrix} 5 & 1 \\ 4 & 5 \end{pmatrix}$ superstructure in the reduced oxide layer with respect to Ru(0001). This corresponds to a lattice vector of 1.24 nm. The simulated LEED pattern is shown in Figure 1e. Two rotational domains of the superstructure exist at ±10.6° with respect to Ru(0001). These two domains give rise to the circles of 12 spots. In addition to the superstructure unit cell marked in red, the unit cell of the primitive hexagonal structure is marked in blue in the simulated pattern. In this
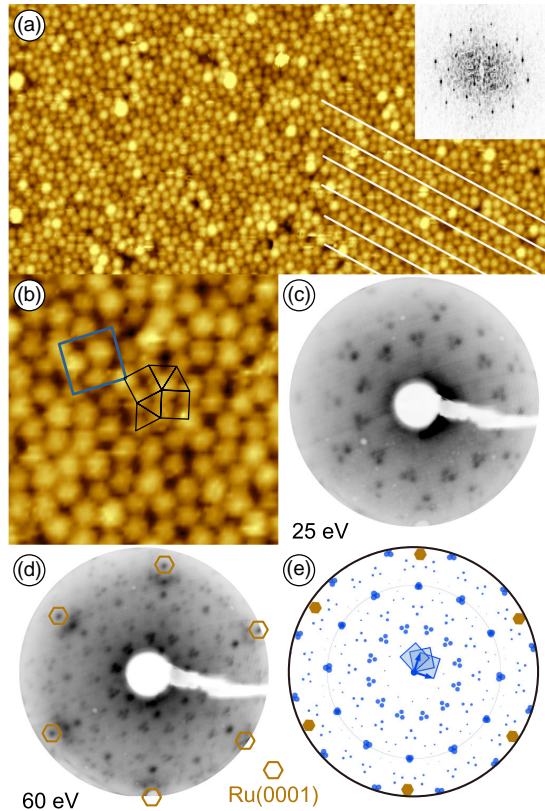
Figure 2. a,b) STM data of the σ-phase derived from BaTiO$_3$ on Ru(0001). The FT of (a) shown as an inset emphasizes a quadratic unit cell. The close-up image (b) reveals a triangle-square tiling. The unit cell is marked in blue and the characteristic motif of four triangles and two squares in black. c,d) The measured LEED pattern is characterized by triangular groups of spots every 30° at various reciprocal lengths. e) The simulated pattern was calculated using a $\begin{pmatrix} 4 & -1.5 \\ 4 & 5.5 \end{pmatrix}$ superstructure matrix. The pattern results from three domains as indicated in (e). The circle at 2.0 Å^{-1} in (e) marks a diffraction order with systematic deviations from 12-fold symmetry. a) 19.3×9.7 nm^2, b) 6.6×6.6 nm^2, a,b) 130 pA, −2.6 V.

smallest scale hexagonal lattice of the overlayer, the next-neighbor Ti distance is 344 pm and this structure is rotated by ±15° with respect to Ru(0001).

Upon annealing in UHV to 1250 K, the material rearranges in a different periodic structure. The STM image of **Figure 2**a reveals a homogeneous dense packing of the atoms at the surface. Minor height variations occur that result in stripe-like trenches as emphasized by the white lines in Figure 2a. The FT of (a) shown as an inset unravels a quadratic structure of this phase. The close-up STM image in Figure 2b reveals the formation of a five vertex structure on the atomic scale: Each protrusion is surrounded by five next neighbors at equal distance. The repeating motif of this structure is an arrangement of four triangles and two squares as marked in black in Figure 2b. The

resulting unit cell containing four Ti atoms is marked in blue. The stripe-like height modulation seen in the STM of Figure 2a is linked to the unit cell dimensions. The stripes occur under 45° and have a spacing corresponding to the unit cell diagonal. This structure is called σ-phase in the context of periodic approximant structures related to quasicrystals as described by Förster et al.[18] Previously, a σ-phase structure has been reported in the BaTiO$_3$/Pt(111) system.[19–21] In a detailed analysis involving STM, LEED, surface X-ray diffraction (SXRD), and density functional theory calculations, the tiling has been identified as the Ti sublattice of the 2D reduced BaTiO$_3$ layer. The STM data presented in Figure 2a,b has been recorded at a high negative bias voltage of −2.6 V, which shows that the Ti atoms dominated the STM contrast even far from the Fermi level.

Figure 2c–e show two LEED pattern as well as a simulation of the measured LEED data of the σ-phase structure derived from BaTiO$_3$ on Ru(0001). At low kinetic energies (Figure 2c), the pattern of the σ-phase on Ru(0001) is characterized by a 12-fold arrangement of triangular sets of spots. This apparent 12-fold symmetry results from a coexistence of three rotational domains of this structure at the Ru(0001) surface as indicated in Figure 2e. In the intensity distribution of higher-order spots at 2.0 Å^{-1} (marked by the circle in Figure 2e), a clear reduction of the 12-fold to a 6-fold symmetry is seen. In alternating sequence every 30° three spots are either almost completely overlapping, or well-separated from each other. The pattern is simulated with a commensurate superstructure as it was the case for the hexagonal structure discussed previously. The σ-phase unit cell is described by a $\begin{pmatrix} 4 & -1.5 \\ 4 & 5.5 \end{pmatrix}$ superstructure matrix with respect to Ru(0001). This unit cell is almost quadratic. It has equal unit vectors with a length of 1.33 nm that incline to an angle of 90.6°. The unit cell is rotated by ±15.3° out of the high symmetry directions of the substrate. The coincidence cell of the σ-phase with the Ru(0001) substrate is given by $\begin{pmatrix} 8 & -4 \\ 7 & 0 \end{pmatrix}$. This is a $(\sqrt{2} \times \sqrt{2})R45°$ superstructure with respect to the σ-phase. The periodicity of systematic height variation of the σ-phase seen in STM (Figure 2a) is determined by the coincidence cell unit vector.

The reported sequence of structures is robust upon cycles of oxygen and UHV annealing. For BaTiO$_3$/Pt(111), it has been demonstrated that these cycles corresponds to a reversible transformation of the oxide material from fully oxidized periodic islands to reduced 2D wetting layers.[16] This is also the case for BaTiO$_3$ on Ru(0001). Upon oxygen annealing, the 2D wetting layer disappears and 3D oxide islands are formed. During subsequent UHV annealing, the hexagonal superstructure is observed in the lower temperature regime, and with increasing temperature, the σ-phase develops. This procedure has been repeated multiple times without a noticeable change in the Ba:Ti composition on Ru(0001).

The hexagonal phase also develops in ultrathin reduced SrTiO$_3$ on Pt(111). There, a monoclinic approximant to the OQC has been observed for stoichiometric monolayers, which is characterized by a unit cell formed from 36 tiles out of the OQC tiling.[15] Upon increasing the Ti content by roughly 15%, the hexagonal superstructure occurs. **Figure 3**a shows a
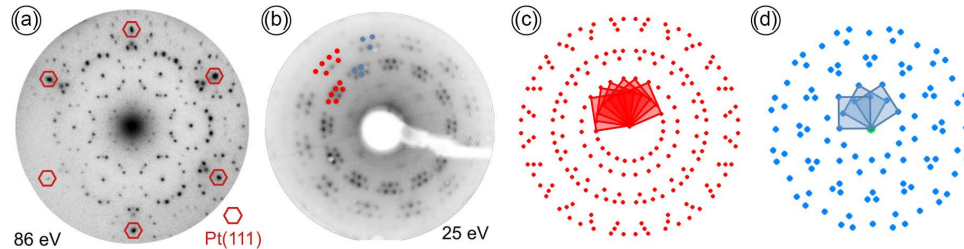
Figure 3. a) SPALEED image recorded for a 2D reduced $SrTiO_3$ layer on Pt(111) at an energy of 86 eV. It shows a similar hexagonal superstructure as seen in Figure 1d. b) LEED image with a superposition of two different σ-phase orientations derived from $BaTiO_3$ on Pt(111) taken at 25 eV. In red the spots of the previously reported 8° rotated σ-phase approximant are marked. The spots in blue correspond to a 15.1° rotated σ-phase. c,d) LEED simulation of the 8° and the 15.1° rotated σ phase, respectively. The solid red and blue squares indicate the different domains that contribute in LEED.

spot-profile analysis low-energy electron (SPALEED) diffraction pattern taken upon UHV annealing to 1100 K. The structure is described by a $\begin{pmatrix} 5 & 1 \\ 4 & 5 \end{pmatrix}$ superstructure matrix, which is identical with the one reported for this structure on Ru(0001). Due to a 2.6% increased substrate lattice constant when substituting Ru(0001) by Pt(111), the unit cell dimensions change by this value. This results in a lattice parameter of 1.27 nm for the superstructure and changes the interatomic spacing for the primitive hexagonal lattice of neighboring Ti atoms from 344 to 353 pm.

The σ-phase superstructure reported previously for $BaTiO_3$ on Ru(0001) is also formed as additional phase in the $BaTiO_3$/Pt(111) system. Figure 3b shows a LEED pattern recorded upon annealing a 0.3 nm thin $BaTiO_3$ layer to 1200 K in UHV. In this particular preparation, the well-established σ-phase on Pt(111) which is rotated by ±8° against the Pt(111) substrate has formed[19] (marked in red in Figure 3b). However, the LEED pattern shows additional spots, which originate from a ±15° rotated σ-phase as discussed previously for $BaTiO_3$ on Ru(0001). The spots of both rotations of the σ-phase on Pt(111) are aligned on circles in the LEED pattern of Figure 3b, indicating a similar lattice constant. The simulated LEED pattern of both orientations are shown in Figure 3c,d. The unit cell of this new rotational variant of the σ-phase on Pt(111) is given by $\begin{pmatrix} 3.8 & -1.4 \\ 3.8 & 5.2 \end{pmatrix}$. It is rotated 15.1° against the substrate. Its unit vectors have a

common length of 1.29 nm and incline to an angle of 90.2°. This unit vector length is identical to the short unit cell vector of the 8° rotated σ-phase.[19] The coincidence cell of the 15° rotated σ-phase is described by $\begin{pmatrix} 19 & -7 \\ 19 & 26 \end{pmatrix}$ and contains a patch of 5×5 σ-phase units. The difference in the number of spots for the different rotations results from a coincidence of the mirror domain spots. This is illustrated by the solid squares representing the different domains in the calculated pattern of Figure 3c,d.

3. Discussion

Table 1 summarizes the structural parameters of the 2D wetting layer structures derived above for $BaTiO_3$ on Ru(0001), $BaTiO_3$ on Pt(111), and $SrTiO_3$ on Pt(111).[15,19]

The two superstructures that are formed from $BaTiO_3$ on Ru(0001) show strong variations in the spacing of Ti atoms. For the hexagonal phase, a Ti–Ti distance of 344 pm has been determined. In contrast, upon annealing to higher temperatures, a twice as large spacing of 688 pm develops. The smaller value is close to the lattice spacing in pure TiO_x monolayer structures on metal surfaces like Pt,[23–25] Mo,[26,27] Cu,[28] Ni,[29] Au,[30,31] and Pd.[32] However, two facts clarify that the hexagonal superstructure is formed indeed by the ternary oxide and not from a binary TiO_x. First, the σ-phase structure is known to form at a 1:1 ratio of the Ba and Ti.[19] Consequently, from the ability to reversibly

Table 1. Structural parameters of periodic superstructures observed for $BaTiO_3$/Ru(0001), $BaTiO_3$/Pt(111), and $SrTiO_3$/Pt(111): the average distance of neighboring Ti atoms, the superstructure matrices for the coincidence cells, the number of primitive unit cells of the σ-phase per coincidence cell and the superstructure matrices of the primitive cells with respect to Pt(111)/Ru(0001), and the orientation of Ti pairs with respect to the given substrate.

	Hexagonal phase	σ-phase				
	Ti–Ti distance	Coincidence cell	σ-phase units		Ti–Ti orientation	Ti–Ti distance [pm]
$BaTiO_3$/Ru(0001)	344 pm	$\begin{pmatrix} 8 & -4 \\ 7 & 0 \end{pmatrix}$	$(\sqrt{2} \times \sqrt{2})R45°$	$\begin{pmatrix} 4 & -1.5 \\ 4 & 5.5 \end{pmatrix}$	‖ to substrate	688
$BaTiO_3$/Pt(111)	–	$\begin{pmatrix} 19 & -7 \\ 19 & 26 \end{pmatrix}$	5×5	$\begin{pmatrix} 3.8 & -1.4 \\ 3.8 & 5.2 \end{pmatrix}$	‖ to substrate	668
$BaTiO_3$/Pt(111)[19]	–	$\begin{pmatrix} 27 & 10 \\ 3 & 20 \end{pmatrix}$	5×4	$\begin{pmatrix} 27/5 & 2 \\ 3/4 & 5 \end{pmatrix}$	7° versus substrate	673
$SrTiO_3$/Pt(111)	353 pm	36 tiles approximant[15]			‖ to substrate	672

change between the two structures by oxidation and subsequent UHV annealing, an equal metal composition must apply to the hexagonal phase. Second, the structure was not reported earlier, although ultrathin films of TiO_2 have been a topic of research for decades. From the literature, it is known that TiO_2 on Ru(0001) forms a $(5\sqrt{3} \times 5\sqrt{3})R30°$ superstructure for 0.68 ML Ti deposited in O_2 atmosphere[33] or a $(6\sqrt{3} \times 6\sqrt{3})$ superstructure after flash annealing 1 ML to 1000 K in O_2 atmosphere.[34] The atypical wide interatomic spacing in the σ-phase, which is, for example, much larger than the distance of Ti atoms in a hexagonal plane of $BaTiO_3(111)$ of 566 pm, results from a planar arrangement of Ba, Ti, and O atoms in the 2D layer. In turn, the short distance as determined for the hexagonal superstructure points toward a vertical stacking of Ba and Ti atoms in the layer. To further support this structural model, complementary methods, e.g., SXRD or photoelectron diffraction, are needed.

Surprisingly, the Ti–Ti distance in the hexagonal phase of $SrTiO_3$ on Pt(111) of 353 pm is 2.6% larger as compared with that found for $BaTiO_3$ on Ru(0001). From the cation exchange in the wetting layer, a decrease in the wetting layer lattice parameter could have been expected, as the ionic radius of Sr is smaller as compared with that of Ba. A change in the opposite direction indicates a large flexibility in the wetting layer structure and emphasizes a stronger interaction with the Ru(0001) substrate as compared with Pt(111).

A comparison of the structural parameters of the σ-phase on different substrates in Table 1 pinpoints a significantly increased wetting-layer-substrate interaction for the Ru(0001) surface in comparison to Pt(111). The σ-phase on Ru(0001) realizes the smallest coincidence cell in this list. A patch of only twice the area of the σ-phase unit cell is needed to be commensurate with the substrate. To achieve this match, the Ti–Ti distance is significantly expanded as compared with the σ-phase formed by $BaTiO_3$ on Pt(111). It is more than 2% larger on Ru(0001) despite a decrease in the substrate lattice constant. In addition to the small coincidence cell, also the parallel alignment of the Ti–Ti

pairs to the high-symmetry substrate directions indicates a strong wetting-layer-substrate interaction. **Figure 4** shows the σ-phase alignment for the coincidence cells of the σ-phase on Ru(0001), the 8° rotated σ-phase on Pt(111), and the 36 tiles approximant of $SrTiO_3$ on Pt(111). The latter is included in the comparison of Table 1 and in Figure 4, as its unit cell contains a large patch of the σ-phase as marked by the enlightened area in Figure 4. In case of $SrTiO_3$/Pt(111), the Ti–Ti distance is comparable to the σ-phase observed on Pt(111). This fact shows, that the cation exchange from Ba to Sr does not alter the wetting layer structure and does not affect the wetting-layer-substrate interaction. An additional manifestation of the comparably weaker interaction of the wetting layer with the Pt(111) surface are the large coincidence cells of the σ-phase. Figure 4 shows the example for the 8° rotated σ-phase for which a patch of 4×5 σ-phase is needed to achieve a substrate registry. In case of the 15° rotated σ-phase on Pt(111), even a mesh of 5×5 units is needed.

Although ultrathin films of $BaTiO_3$ on Ru(0001) have been prepared in slightly varying compositions and by different deposition techniques (rf magnetron sputtering and MBE), no other structures have been observed in this system, especially no OQC is formed. This is surprising, as the diffraction pattern of the σ-phase under 15° rotation against the substrate resembles a very good approximation to the dodecagonal structure of OQCs. In case of a transformation into a dodecagonal structure, the triangular sets of spots in the LEED pattern would collapse into a single spot in the centers of the triangles. The presented facts emphasize that the strong epitaxial stabilization of the σ-phase on Ru(0001) suppresses an OQC formation of $BaTiO_3$ on Ru(0001).

4. Conclusion

2D structures in reduced wetting layers of $BaTiO_3$ on Ru(0001) and Pt(111) and $SrTiO_3$ on Pt(111) are reported. Upon UHV
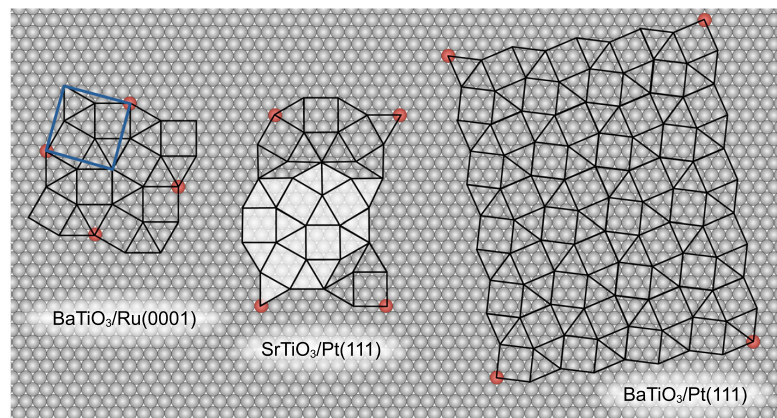
Figure 4. Wetting layer structures observed for ternary oxides on Ru(0001) and Pt(111). The meshes drawn in black mimic the sublattices of Ti atoms in these structures. The red balls mark the size of the coincidence cells. The blue rectangle marks a primitive unit cell of the σ-phase of $BaTiO_3$ on Ru(0001). The enlightened area in the unit cell of $SrTiO_3$/Pt(111) marks a tiling patch similar to the σ-phase. The large patch on the right depicts the coincidence cell of the 8° rotated σ-phase of $BaTiO_3$ on Pt(111).

1900655 (5 of 6)

annealing at 1100 K, a hexagonal superstructure with a Ti–Ti distance of 344 pm is observed in BaTiO$_3$/Ru(0001). A similar superstructure develops in SrTiO$_3$/Pt(111) for which the Ti–Ti distance is increased by 2.9%. For BaTiO$_3$/Ru(0001), a transformation into a triangle-square tiling with a Ti–Ti of distance 688 pm is observed upon annealing at 1250 K in UHV. This triangle-square tiling is known as σ-phase approximant to the OQC discovered in BaTiO$_3$/Pt(111).[1,19] A 2.2 % expansion of the Ti–Ti distance and a small area $\begin{pmatrix} 8 & -4 \\ 7 & 0 \end{pmatrix}$ coincidence cell for the σ-phase of BaTiO$_3$/Ru(0001) emphasize a stronger interaction of the reduced oxide to Ru(0001) as compared to Pt(111). The epitaxial stabilization of the σ-phase on Ru(0001) seems to suppress the formation of a dodecagonal structure in the BaTiO$_3$/Ru(0001) system.

5. Experimental Section

The experiments were performed in UHV systems operating at a base pressure of 10^{-10} mbar. Pt(111) substrates (Mateck, Germany) were cleaned by repeating cycles of Ar$^+$ ion sputtering and annealing as described in ref. [1]. The Ru(0001) substrate was also cleaned by cycles of Ar$^+$ ion sputtering and annealing. Each annealing step contained multiple cycles of the following annealing procedure: 1) annealing to 670 and 870 K in 2×10^{-8} mbar O$_2$ for 2 min, respectively. 2) Cooling down to RT for 3 min in UHV. 3) Flash to 1470 K in 6×10^{-9} mbar O$_2$ for 1 min. For temperature measurements, a pyrometer (Cyclops 52, Minolta, $\lambda = 520$ nm) was used at $\varepsilon = 0.1$ optimized to the Pt and Ru substrates. Ultrathin films of SrTiO$_3$ and BaTiO$_3$ were deposited by MBE from a Nb-doped (0.05%) SrTiO$_3$ single crystal and a stoichiometric BaTiO$_3$ ceramic as described in detail in ref. [15,35].

Conflict of Interest

The authors declare no conflict of interest.

[1] S. Förster, K. Meinel, R. Hammer, M. Trautmann, W. Widdra, *Nature* **2013**, *502*, 215.

[2] K. Urban, N. Moser, H. Kronmüller, *Phys. Status Solidi A* **1985**, *91*, 411.

[3] Z. Zhang, K. Urban, *Scr. Metall. Mater.* **1989**, *23*, 1663.

[4] Y. Zhuang, Z. Zhang, D. B. Williams, *J. Non-Cryst. Solids* **1993**, *153*, 119.

[5] V. Fournée, P. A. Thiel, J. Phys, *D: Appl. Phys.* **2005**, *38*, 83.

[6] H.-R. Sharma, M. Shimoda, A. P. Tsai, *Adv. Phys.* **2007**, *56*, 403.

[7] V. Fournée, J. Ledieu, M. Shimoda, M. Kraj, H.-R. Sharma, R. McGrath, *Isr. J. Chem.* **2011**, *51*, 1314.

[8] F. C. Frank, J. H. van der Merwe, *Proc. R. Soc. Lond. A* **1949**, *198*, 205.

[9] A. Hoshino, S. Isoda, H. Kurata, T. Kobayashi, *J. Appl. Phys.* **1994**, *76*, 4113.

[10] G. Friedel, *Lecon De Cristallographie* Berger Levrault, Paris, **1926**.

[11] M. L. Kronberg, F. H. Wilson, *Trans. AIME* **1949**, *185*, 501.

[12] N. H. Fletcher, *J. Appl. Phys.* **1964**, *35*, 234.

[13] E. J. Widjaja, L. D. Marks, *Philos. Mag. Lett.* **2003**, *83*, 47.

[14] K. J. Franke, P. Gille, K.-H. Rieder, W. Theis, *Phys. Rev. Lett.* **2007**, *99*, 036103.

[15] S. Schenk, S. Förster, K. Meinel, R. Hammer, B. Leibundgut, M. Paleschke, J. Pantzer, C. Dresler, F. O. Schumann, W. Widdra, *J. Phys.: Condens. Matter* **2017**, *29*, 134002.

[16] S. Förster, J. I. Flege, E. M. Zollner, F. O. Schumann, R. Hammer, A. Bayat, K.-M. Schindler, J. Falta, W. Widdra, *Ann. Phys. (Berlin)* **2017**, *529*, 1600250.

[17] S. Schenk, E. M. Zollner, O. Krahn, B. Schreck, R. Hammer, S. Förster, W. Widdra, *Acta Cryst.* **2019**, *A75*, 307.

[18] S. Förster, S. Schenk, E. M. Zollner, O. Krahn, C.-T. Chiang, F. O. Schumann, A. Bayat, K.-M. Schindler, M. Trautmann, R. Hammer, K. Meinel, W. A. Adeagbo, W. Hergert, J. I. Flege, J. Falta, M. Ellguth, C. Tusche, M. DeBoissieu, M. Muntwiler, T. Greber, W. Widdra, *Phys. Status Solidi B* **2019**, 1900624.

[19] S. Förster, M. Trautmann, S. Roy, W. A. Adeagbo, E. M. Zollner, R. Hammer, F. O. Schumann, K. Meinel, S. K. Nayak, K. Mohseni, W. Hergert, H. L. Meyerheim, W. Widdra, *Phys. Rev. Lett.* **2016**, *117*, 095501.

[20] K. Mohseni Roy, S. Förster, M. Trautmann, F. Schumann, E. Zollner, H. Meyerheim, W. Widdra, Z. Kristallogr, *Z. Kristallogr. Cryst. Mater.* **2016**, *231*, 749.

[21] K. Mohseni, H. L. Meyerheim, *Phys. Status Solidi B* **2019**, 1900605.

[22] C.-T. Chiang, M. Ellguth, F. O. Schumann, C. Tusche, R. Kraska, S. Förster, W. Widdra, *Phys. Rev. B* **2019**, *100*, 125149.

[23] A. B. Boffa, H. C. Galloway, P. W. Jacobs, J. J. Benitez, J. D. Batteas, M. Salmeron, A. T. Bell, G. A. Somorjai, *Surf. Sci.* **1995**, *326*, 80.

[24] F. Sedona, G. A. Rizzi, S. Agnoli, F. X. Llabres i Xamena, A. Papageorgiou, D. Ostermann, M. Sambi, P. Finetti, K. Schierbaum, G. Granozzi, *J. Phys. Chem.* **2005**, *109*, 24411.

[25] G. Barcaro, E. Cavaliere, L. Artiglia, L. Sementa, L. Gavioli, G. Granozzi, A. Fortunelli, *J. Phys. Chem. C* **2012**, *116*, 13302.

[26] Q. Guo, W. S. Oh, D. W. Goodman, *Surf. Sci.* **1999**, *437*, 49.

[27] W. S. Oh, C. Xu, D. Y. Kim, D. W. Goodman, *J. Vac. Sci. Technol. A* **1997**, *15*, 1710.

[28] T. Maeda, Y. Kobayashi, K. Kishi, *Surf. Sci.* **1999**, *436*, 249.

[29] T. V. Ashworth, G. Thornton, *Thin Solid Films* **2001**, *400*, 43.

[30] Z. Song, J. Hrbek, R. Osgood, *Nano Lett.* **2005**, *5*, 1327.

[31] C. Wu, M. S. J. Marshall, M. R. J. Castell, *J. Phys. Chem. C* **2011**, *115*, 8643.

[32] R. A. Bennett, C. L. Pang, N. Perkins, R. D. Smith, P. Morrall, R. I. Kvon, M. Bowker, *J. Phys. Chem. B* **2002**, *106*, 4688.

[33] J. P. S. Badyal, A. J. Gellman, R. W. Judd, R. M. Lambert, *Catal. Lett.* **1988**, *1*, 41.

[34] A. Männig, Z. Zhao, D. Rosenthal, K. Christmann, H. Hoster, H. Rauscher, R. J. Behm, *Surf. Sci.* **2005**, *576*, 29.

[35] E. M. Zollner, S. Schenk, M. Setvin, S. Förster, *Phys. Status Solidi B* **2019**, 1900620.

Hexagonal approximant of the dodecagonal oxide quasicrystal on Pt(111)

Check for updates

Antiphase Domain Boundary Formation in 2D Ba–Ti–O on Pd(111): An Alternative to Phase Separation

Friederike Elisa Wührl, Oliver Krahn, Sebastian Schenk, Stefan Förster,* and Wolf Widdra

2D oxide quasicrystals (OQCs) are unique structures arising from atoms positioned at the vertices of a dodecagonal triangle–square–rhombus tiling. The prototypical example for OQCs is derived from BaTiO$_3$ on Pt(111). Herein, scanning tunneling microscopy (STM) and low-energy electron diffraction (LEED) investigations of 2D oxide layers derived from BaTiO$_3$ on Pd(111) are reported. Upon ultrahigh vacuum (UHV) annealing, different long-range ordered structures are observed with a base of four vertex atoms forming two edge-sharing equilateral triangles. By a periodic repetition of this base in either quadratic or rectangular unit cells, a triangle–square tiling (known as σ-phase approximant or $3^2.4.3.4$ Archimedean tiling) or a triangle–rhombus tiling is formed. Both structures vary strongly in their vertex density. In addition, the formation of antiphase domain boundaries in the σ phase is observed resulting in a well-ordered incorporation of rhombuses in the triangle–square tiling. A systematic variation of the frequency of these domain boundaries is identified as a mechanism for an incremental increase in the global vertex density, mediating between pure triangle–square and triangle–square–rhombus tilings.

1. Introduction

The discovery of a quasicrystalline phase in ultrathin films derived from BaTiO$_3$ on Pt(111) opened a new field of research for ternary oxides on metal substrates.[1] These oxide quasicrystals (OQCs) are the first observation of spontaneous formation of long-range ordered dodecagonal structures on-top of hexagonal substrates. The dodecagonal structure results from a close-packed tiling of equilateral triangles, squares, and rhombuses that had been theoretical defined as dodecagonal Niizeki-Gähler tiling, a quarter century before the first experimental evidence.[1–5] In the OQC, the cation species which shows strong

F. E. Wührl, O. Krahn, S. Schenk, S. Förster, W. Widdra
Institute of Physics
Martin-Luther-Universität Halle-Wittenberg
Halle D-06099, Germany
E-mail: stefan.foerster@physik.uni-halle.de

contrast in atomically resolved STM decorates all vertex positions of the dodecagonal tiling. The full structure of the OQC is not yet solved, which is why an assignment of the STM contrast to either Ti or Ba atoms remains currently a matter of debate.[6,7] In the context of the OQC, several periodic approximant structures have been reported which share common tiling elements of the parent OQC. Upon variations of the preparation conditions of BaTiO$_3$-derived films on Pt(111), such periodic structures are observed as a consequence of compositional changes affecting the vertex density.[6–12] While some structures have been successfully prepared as single phases, also the coexistence of phases of varying vertex density in neighboring domains has been reported.[8] This phase separation mechanism is commonly observed upon compositional changes, e.g., in monolayer oxides[13–16] and in metal–organic coordination networks,[17] or for coverage variations in noble gas adlayers[18] and self-assembled molecular layers.[19,20]

To elucidate the role of the lattice mismatch between the parent ternary oxide and the metal support toward the stabilization of dodecagonal oxide layers, different oxide layer/substrate combinations have been studied previously.[5,21] Between BaTiO$_3$ and Pt, which are the two components forming the prototypical OQC, the lattice mismatch amounts to −2.0%. So far, mismatches of −4.5% and vanishing mismatch conditions have been realized by combining BaTiO$_3$ with Ru(0001) and SrTiO$_3$ with Pt(111), respectively.[5,21] In both cases, a strong epitaxial stabilization of periodic structures is found. For BaTiO$_3$/Ru(0001), a commensurate triangle–square tiling known as σ-phase approximant or $3^2.4.3.4$ Archimedean tiling is observed.[5] For SrTiO$_3$/Pt(111), a more complex triangle–square–rhombus tiling forms a commensurate phase.[21]

Here, we report on the structure evolution in ultrathin oxide layers derived from BaTiO$_3$ on Pd(111). For this material combination, a nominal lattice mismatch of −2.8% can be calculated, close to the conditions in BaTiO$_3$/Pt(111). Upon annealing in UHV at 930 to 1030 K, reduced Ba–Ti–O forms long-range ordered 2D layers on the Pd substrate. In these wetting layers, a series of structures is identified by means of STM and LEED. In this report, we will focus on single-phase structures with small unit cells. One of these structures is the σ phase, which is a quadratic structure with a base of four vertex atoms.

In the second long-range ordered phase the same four vertex are periodically repeated in a rectangular unit cell. As a consequence, the vertex density is strongly increased. Finally, modifications of the σ phase are observed in which σ-phase patches are connected by periodic antiphase domain boundaries, thus realizing intermediate vertex densities.

2. Results

Ultrathin films of Ba–Ti–O have been deposited by exposing the clean Pd(111) surface at room temperature subsequently to Ba and Ti vapor. Upon post-annealing at 770 K in 10^{-5} mbar O$_2$, this mixed metal layer is fully oxidized. The chemical nature of these films has been investigated by means of X-ray photoelectron spectroscopy (XPS). **Figure 1** shows exemplarily the Ba 3d and Ti 2p core-level regions for a 5 Å thin film of Ba–Ti–O. The film thickness has been determined from the damping of the Pd substrate peaks. The Ba 3d5/2 and Ti 2p3/2 core-level peaks are positioned at 780.3 and 458.0 eV, respectively, which is in good agreement to bulk BaTiO$_3$.[22] Moreover, a first plasmon loss is observed in the Ti 2p region at 13.0 eV higher binding energy with respect to the 2p3/2 peak, which is also characteristic for BaTiO$_3$.[22] Accounting for the differences in the escape depth of the Ba 3 d and Ti 2p photoelectrons, a Ba:Ti composition of 0.5:1 has been

Figure 1. a) XPS spectra of 5 Å Ba–Ti–O on Pd(111) upon full oxidation (top) and UHV annealing (bottom). b) Large-area STM image of the sample upon UHV annealing showing the presence of islands (I) on planar terraces which are covered by a reduced 2D oxide. The different structures formed in this 2D layer will be discussed in the text. b) 500×250 nm^2, 0.4 A, 2.0 V, $\Delta z = 2.8$ nm.

determined for the as prepared 5 Å thin layer. A higher initial Ti content has been chosen intentionally to compensate for Ti segregation into the Pd(111) bulk upon high-temperature treatment.[23] Upon annealing, the ultrathin Ba–Ti–O at temperatures above 900 K in UHV, a second oxide species is formed at the surface, which is recognized most prominently in the Ti 2p region. The bottom spectra of Figure 1a shows the spectrum for the initially 5 Å thin Ba–Ti–O film upon multiple annealing cycles to a maximum temperature of 1030 K in UHV. In this spectrum, a second Ti 2p doublet (blue) shifted by 2.3 eV toward lower binding energies is seen indicating a reduction of the nominal oxidation state. However, the Ba 3d peak remains almost unchanged. Upon reduction, the Ba:Ti ratio of the Ba–Ti–O system reduces by 9%. A quantification of the oxygen content in the layer is not possible due to the superposition of the small O1s intensity with high intensities of the Pd 3p core-level peaks.

Figure 1b shows a large-scale STM image, which corresponds to the reduced state of the aforementioned preparation. In this image, two different oxide species become evident in the morphology of the Ba–Ti–O layer on the Pd(111) surface. On the one hand, islands of different sizes are decorating the substrate step edges, that appear with a rough surface in STM (marked by I in Figure 1b). These islands are attributed to fully oxidized stoichiometric BaTiO$_3$. On the other hand, extended smooth terraces exist, that are fully encapsulated with layers of different structure, which will be introduced in the following text. Following the assumption of a Ba:Ti ratio of 1:1 for the BaTiO$_3$ islands, the global change of the Ba:Ti ratio by 9% upon reduction is indicative for a Ba:Ti composition of the reduced oxide layer significantly below 0.5:1.

The observed behavior is typical for ultrathin ternary oxide films on metal support and has been characterized in 2D Ba–Ti–O films on Pt(111) before, see ref. [24]. The fully oxidized ternary oxide tends to form 3D perovskite islands upon annealing and, therefore, to dewet the metal surface between the islands. Under reducing conditions, a reduced oxide layer is formed starting at a threshold temperature, which fully covers the metal substrate in-between remaining 3D bulk-like islands.[25] Studies of Sr–Ti–O films on Pt(111) and Ba–Ti–O films on Ru(0001) report a similar phenomenon.[5,21]

The fully oxidized Ba–Ti–O films on Pd(111) annealed at 770 K in 10^{-5} mbar O$_2$ do not possess any long-range order in LEED. However, a variety of long-range ordered structures are present upon annealing in UHV, which will be introduced in the following. The onset of long-range order in the reduced oxide has been observed upon annealing at 930 K for 10 min. **Figure 2** shows the corresponding LEED pattern. In addition to the very intense spots of the hexagonal Pd(111) substrate at 2.64 Å^{-1} a ring is visible at 2.41 Å^{-1} in the diffraction pattern of Figure 2a. For Ba–Ti–O on Pt(111), a similar ring has been observed indicating the formation of a 2D reduced oxide wetting layer, which is initially poorly ordered.[25,26] Furthermore, a long-range ordered structure is present that gives rise to sharp superstructure spots in LEED. This superstructure is characterized by 12 intense spots at an reciprocal distance of 1.00 Å^{-1} around the origin of the diffraction pattern and around each of the first-order substrate spots. All these spots are related to a $\begin{pmatrix} 1 & 3 \\ 5 & 1 \end{pmatrix}$ superstructure with respect to Pd(111). It is a rectangular structure with unit
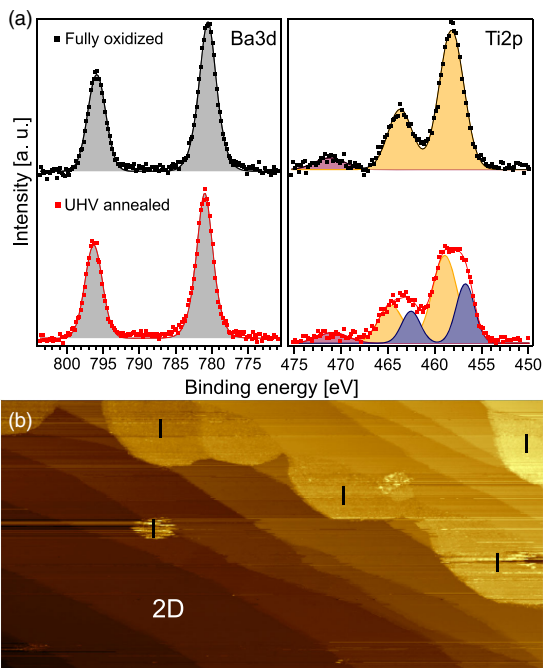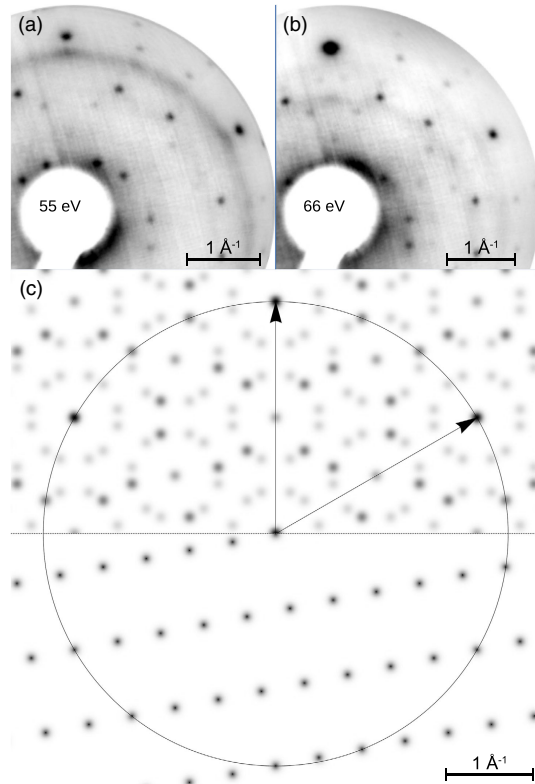
Figure 2. a,b) LEED pattern of 5 Å Ba–Ti–O on Pd(111) upon annealing at 930 K for 10 min in UHV. c) Simulated pattern for a single domain of a rectangular $\begin{pmatrix} 1 & 3 \\ 5 & 1 \end{pmatrix}$ superstructure on Pd(111) (bottom) and the substrate-induced superposition of six rotational and mirror domains (top) reproducing the measured pattern.

Figure 3. STM data of 5 Å Ba–Ti–O on Pd(111) upon annealing at 930 K for 60 min in UHV. a) Large-scale image revealing a homogeneous patterning of the Pd(111) terraces. b) Close-up STM image identifying a rectangular cell with a base of four vertices. c) Schematic representation of the resulting tiling formed from smaller triangles (blue) and larger triangles (orange) and rhombuses with inner angles of 40° and 140°. a) 46 × 23 nm^2, 0.3 A, 1.2 V, $\Delta z = 140$ pm. b) 10.5 × 8.0 nm^2, 0.1 A, 1.2 V, $\Delta z = 30$ pm.

vectors of 12.6 and 7.3 Å. The latter is rotated by 19.1° against the substrate. A simulated diffraction pattern of a single domain of this structure is shown in the lower part of Figure 2c. Due to a lack of STM data giving the unit cell filling, only the unit cell dimensions have been considered. As a consequence of the substrate symmetry, three different rotational and three mirror domains occur. The simulated pattern for a superposition of all six domains is shown in the upper part of Figure 2c. In this pattern intensity differences arise from coinciding spots of different domains. The spots of higher intensities are the ones dominating the measured LEED patterns of Figure 2a,b.

Upon further annealing of this film for 60 min at 930 K, the 2D oxide layer covers the Pd(111) terraces as shown by the STM image of **Figure 3**a. In this densely packed atomic arrangement an almost quadratic array of elongated protrusions can be recognized. Along the two almost perpendicular rows of this grid, neighboring protrusions are rotated by 90° with respect to each other. The close-up STM image in Figure 3b shows that these elongated shapes result
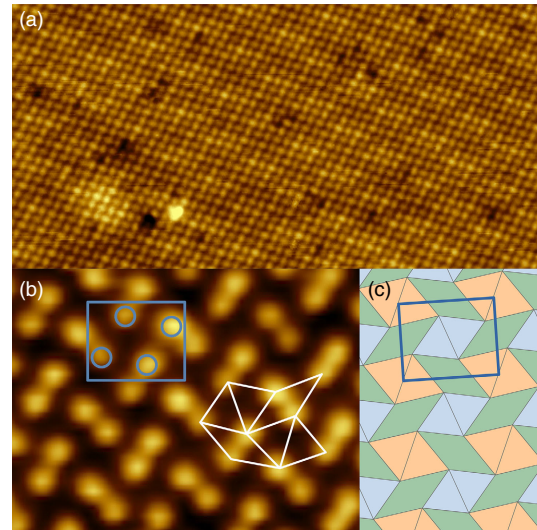
from two protrusions in close vicinity. This structure can be described by a rectangular unit cell that includes a base of four protrusions (marked blue in Figure 3b). The protrusions decorate the vertices of two edge-sharing equilateral triangles. The periodic repetition of this atomic base results in the formation of a second pair of triangles with a 10% larger edge length, which is rotated by 40° against the base. This is shown in the scheme of Figure 3c, in which the small triangles are colored in blue and the larger ones in orange. The remaining voids (green) are rhombuses with inner angles of 40° and 140°. From this scheme, the characteristic building blocks of the tiling can be derived. It consists of two double triangles and two rhombuses of different rotations, as shown in white in Figure 3b. In the larger area STM image in Figure 3a, a moiré pattern is induced from small height variations. A comprehensive analysis of the moiré pattern is provided in the Supporting Information.

Figure 4a,b shows the LEED pattern recorded for this rectangular structure at different electron kinetic energies. Most prominent is a set of three spots with an alternating angular spacing of 28° and 32° centered at a reciprocal distance of 1.2 Å. In addition, 12 or 24 spots are observed at various radii. Therefore, a rotation of the rectangular unit cell out of the mirror planes of the hexagonal substrate can be concluded. The measured diffraction pattern is perfectly reproduced in simulations using a $\begin{pmatrix} 16/3 & 4/3 \\ 11/9 & 38/9 \end{pmatrix}$ superstructure with respect to Pd(111). Figure 4c shows the simulated pattern of a single domain (bottom) and the superposition of all six rotation and mirror domains (top). By including the base of four atoms as determined from STM, the calculated intensities nicely agree with the measured ones. This is remarkable as only
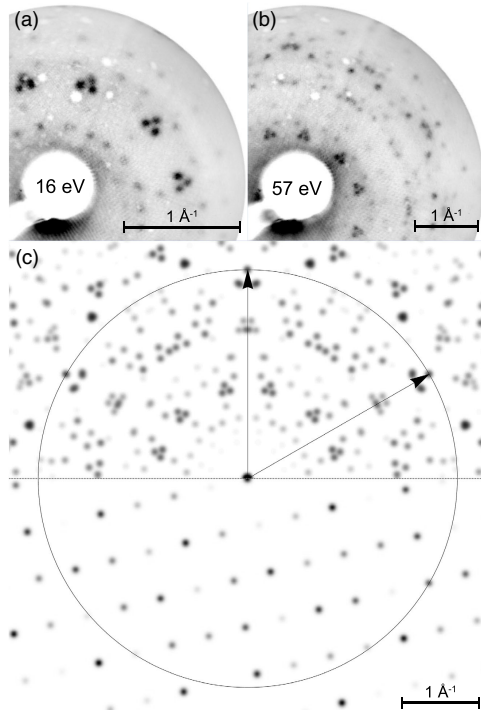
Figure 4. a,b) LEED pattern of a rotated rectangular superstructure formed in 5 Å Ba–Ti–O on Pd(111) upon annealing at 930 K for 60 min in UHV. c) Simulated pattern for a single domain of the rectangular structure (bottom) and the superposition of six domains (top).

Figure 5. a) STM and b–d) LEED data of the σ phase in Ba–Ti–O on Pd(111). The quadratic unit cell and the base of four atoms are marked in blue. The characteristic building block of the triangle–square tiling resulting from the periodic repetition of the base is marked in white. In this STM image, a stripe-like moiré pattern is seen having a periodicity of two unit cells as emphasized by the dashed lines. b,c) Experimentally observed LEED pattern of the σ phase and d) the simulated pattern for a single domain (bottom) and the superposition of six domains (top). a) $11 \times 11\,nm^2$, 100 pA, 1.0 V, $\Delta z = 150\,pm$.

one subgrid of atoms of this ternary compound can be detected by STM, although all atomic species contribute in LEED.[6,7] The given matrix corresponds to a higher-order commensurate structure with unit vectors of 13.2 and 10.3 Å inclining an angle of 89.8°. This structure is rotated by 13.9° against the substrate. The matrix is perfectly in line with the observed moiré pattern in STM data: substrate registry is achieved in one direction by three repetitions of the long unit vector. In the other direction, a linear combination of one long unit vector and three repetitions of the short unit vector are needed. Further explanation is available in the Supporting Information.

Upon multiple cycles of oxygen and UHV annealing with an final annealing step for 30 min to 1020 K, the wetting layer structure changes into the σ phase, which has been reported for Ba–Ti–O on Pt(111) and Ru(0001) before.[5,6,27] This structure is a simple triangle–square tiling, as shown in the STM image in **Figure 5**a.

The unit cell is quadratic and contains a base of four vertex atoms (marked blue in Figure 5a). These four vertices are arranged in a similar fashion as found for the rectangular structure described earlier. It results in a characteristic tiling consisting of four triangles and two squares (white in Figure 5a). In the STM image of the σ phase in Figure 5a, a 1D moiré structure is

present. In an alternating fashion, two rows of atoms running from the upper left to the lower right of Figure 5a appear brighter, whereas the next two rows are dimmer.

This 1D moiré has a periodicity of twice the lattice parameter of the σ-phase unit cell. The σ phase exhibits a very characteristic LEED pattern, which is shown in Figure 5b,c. At various reciprocal distances, 24 groups of three spots each are observed. The simulated pattern of this structure is shown in Figure 5d. The structure is determined by a $\begin{pmatrix} 31/6 & 5/6 \\ 2 & 11/2 \end{pmatrix}$ superstructure matrix with respect to Pd(111). The perfect agreement between the simulated and measured LEED pattern is seen best in the reproducion of the tiny differences in the splitting of the triangles generated by the fifth- and sixth-order spots marked in blue in

Figure 5b,d and the spots cut by the connecting line of the first-order substrate spots marked in red. The unit vectors derived from this superstructure matrix are 13.2 and 13.3 Å in length inclining a 90.3° angle. This results in a next-neighbor distance of 6.85 Å in the triangle–square tiling. The unit cell is rotated by 8.6° against the substrate. As read from the superstructure matrix, a period doubling along the second unit vector of the σ phase results in a snap-into-registry with the substrate, which is in-line with the observed moiré pattern. The configuration of the σ phase on Pd(111) is very close to what has been reported for Pt(111).[6,27] There, the unit cell is slightly compressed along one unit vector, the inner angle is slightly larger, and the rotation against the substrate is reduced to 8°. However, as the differences are small, the LEED pattern are almost indistinguishable for the different substrates. In contrast, on the Ru(0001) substrate the σ phase unit cell is rotated by 15° against the substrate.[5]

In contrast to Ba–Ti–O on all other investigated substrates, local modifications of the σ phase are observed on Pd(111). **Figure 6**a shows a large-scale STM image that demonstrates a high level of perfection in the long-range order of the σ phase. Only two adatoms (bright spots) and a single vacancy (dark hole) are seen in the entire image containing more than 5000 vertices. The second detail to note are compact lines of atoms running in vertical direction. The close-up STM image in Figure 6b shows that these compact rows are created by vertically stacked rhombuses inclining 30° and 150° angles. These rows of rhombuses are enclosed on both sides by a variable number of σ-phase unit cells as marked by white squares in Figure 6a. These σ-phase unit cells are shown in Figure 6b in red and yellow. Both domains are oriented in the same direction, but exhibit a lateral offset of half a unit vector in vertical direction and $\sqrt{3}/2$ perpendicular to it (marked by blue lines in Figure 6b). The phase shift of half a σ-phase unit cell along the domain boundary corresponds to the condition of 1D antiphase domain boundaries. The phase shift across the domain boundary of a $\sqrt{3}/2$ unit cell, however, allows sharing of two (out of four) vertex positions between both domains. As the domain width is only $\sqrt{3}/2$ unit cell wide and contains also four vertex atoms, the domain boundary is denser than the σ phase on both sides. This higher density of vertices results in the formation of rhombuses as new tiling elements. The new characteristic tiling motif generated by this antiphase domain boundary is emphasized in white in Figure 6b. The large-scale image in Figure 6a reveals that the number of σ-phase units between subsequent rows of rhombuses can vary. One, two, or four unit cells are found in this particular measurement. However, no repeating rule could be determined from the sequence of rows.

3. Discussion

In 2D layers of ternary oxides a variety of tilings arises from a combination of equilateral triangles, squares, and rhombuses. The most prominent example is the dodecagonal OQC, but also periodic structures ranging from simple to complex are known.[1,6,8,21]

For 2D Ba–Ti–O on Pd(111), three different characteristic tiling motifs occur, as introduced earlier. These are the triangle–square patch of the σ phase, the triangle–square–rhombus patch observed at the antiphase domain boundaries, and the triangle–rhombus patch, which is an idealization of the motif found in the
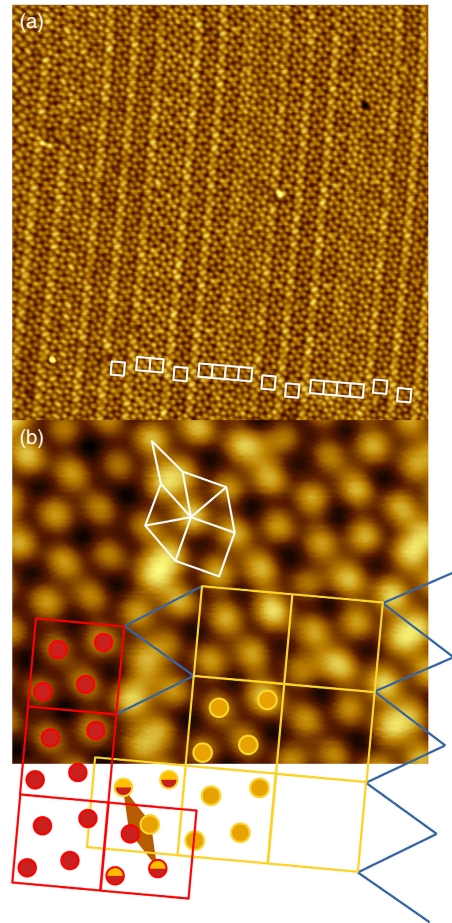
Figure 6. a) Large-scale STM image of σ-phase patches with incorporated rows of rhombuses. b) Schematics illustrating the formation of rhombuses as a result of 1D antiphase domain boundaries of neighboring σ-phase patches of identical orientation (red and yellow). a) $44 \times 44\,nm^2$, b) $6 \times 5\,nm^2$, a,b) 40 pA, 2.0 V, $\Delta z = 170$ pm.

small aspect ratio rectangular structure shown in Figure 3 and 4. **Figure 7** shows, how all three tiling motifs can be traced back to the very same base of four vertices in different periodic repetitions. In Figure 7a, four vertices are arranged in a base such that they form two edge-sharing equilateral triangles. By periodically repeating this base in rectangular, quadratic, or hexagonal unit cells of appropriate size, periodic structures with different triangle–square–rhombus tiling motifs can be created. For the periodic repetition of all structures in Figure 7a, the unit vector length is $\sqrt{(2+\sqrt{3})}$ times larger than the vertex separation and the unit vectors are rotated by 15° against the edges of the triangles. In case of the rectangular structure, this applies for the long unit vector only. The short unit vector has a length of $\sqrt{2}$ and is rotated by 45°. In the periodic repetition, new tiles are created by

2100389 (5 of 8)
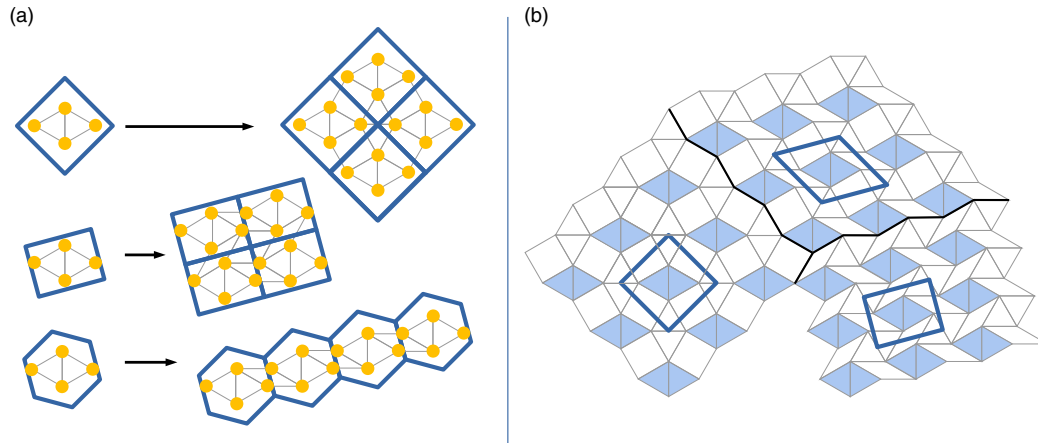
Figure 7. a) Three different structures that evolve from an identical base, which is periodically repeated in either quadratic, rectangular, or hexagonal fashion. The upper two examples resemble the σ phase and the rectangular structure observed in Ba–Ti–O on Pd(111), the lower one the conditions that apply at antiphase domain boundaries. b) The three tilings of (a) form smooth boundaries between extended patches. All three tilings are formed from tiles of constant edge length.

connecting the vertices across the unit cell boundaries. Due to the specific orientation of the base with respect to the unit vectors and the particular relation between the vertex separation and the unit cell dimensions, only triangles, squares, and rhombuses of constant edge length are formed. The magic factor of $\sqrt{(2+\sqrt{3})}$ is the inflation factor of the dodecagonal Niizeki–Gähler tiling, which produces a self-similar pattern under a rotation of $15°$.[2,3] While the upper two examples of Figure 7a exist in Ba–Ti–O on Pd(111) in extended patches in the rectangular structure and the σ phase, the bottom example periodically repeats in one dimension only along the antiphase domain boundaries between σ-phase patches. Due to the common unit vector length the three patches can be smoothly combined in neighboring domains, as shown in Figure 7b.

As an immediate consequence of the different unit cell areas, all three structures differ significantly in their vertex density. The pure σ phase exhibits the lowest density of 2.28 vertices per nm^2. The density of the triangle-rhombus tiling in the rectangular structure amounts to 2.94 vertices per nm^2. And the hypothetical hexagonal triangle–square–rhombus tiling would result in a density of 2.65 vertices per nm^2. The inclusion of antiphase domain boundaries shown in Figure 6 can be rationalized in this context as a mechanism to accommodate an increasing vertex density in the σ phase. In the self-organized growth of 2D crystals of organic and inorganic materials, the formation of antiphase domain boundaries is observed frequently, which can produce denser or more dilute packing. At low temperatures, antiphase domain boundaries result from the intergrowth of immobilized nuclei.[28] However, they also represent a way of releasing strain induced by increasing adsorbate coverages of organic and inorganic materials.[29–32] In rare cases, they can be condensed into ordered arrays, thus forming a new structural phase as for surface layers of Pb and In.[31,32] The latter scenario also applies for the ultrathin Ba–Ti–O layer on

Pd(111). The experimental observation of a variable spacing between subsequent domain boundaries indicates that the vertex density can be tuned in small increments. The minimum spacing between neighboring domain boundaries of one complete unit cell of the σ phase has been observed in experiments. This implies that based on the incorporation of domain boundaries, the vertex density can be tuned to a maximum of 2.45 vertices per nm^2. We note that this maximum is equivalent to the vertex density in the Niizeki–Gähler tiling of the $BaTiO_3$-derived OQC on Pt(111). In other words, a periodic repetition of one σ-phase unit cell and the tiling motif formed at the antiphase domain boundary, resembles a similar vertex density, as given in the aperiodic Niizeki–Gähler tiling. While on Pt(111), the general scheme of demixing into phases of different composition is observed, which results in the coexistence of different structures in adjacent domains,[8] the antiphase domain boundary formation on Pd(111) represents a fascinating alternative for mediating atom density variations.

4. Conclusion

The structure formation in ultrathin reduced layers of Ba–Ti–O on Pd(111) has been investigated. Three long-range ordered phases with small unit cells exist: two rectangular structures and the quadratic σ-phase approximant. One of the rectangular structure and the σ phase share a common base, which results in the formation of a triangle–rhombus and a triangle–square tiling, respectively. In contrast to other related systems, the incorporation of antiphase domain boundaries in the triangle–square tiling of the σ phase is observed on Pd(111). The systematic incorporation of domain boundaries is identified as a mechanism to tune the vertex density of the tiling from the low-density σ phase conditions toward that of the dodecagonal triangle–square–rhombus tiling found in OQC.

5. Experimental Section

Sample growth, LEED, and XPS measurements were carried out in an UHV system operating at a base pressure of 1×10^{-10} mbar. Pd(111) substrates (Mateck, Germany) were cleaned by repeated cycles of Ar^+-ion sputtering at 1 keV and a two-step annealing process. In the first step, the crystal was briefly annealed at 1170 K for 30 s to heal out sputter-induced surface roughening. In the second step, the crystal was annealed at 900 K for 10 min at an oxygen partial pressure of 1×10^{-6} mbar. During the second step, residual carbon contaminations were oxidized to CO, which immediately desorbed at high temperatures. Due to the low sticking probability of oxygen on palladium at elevated temperatures, a clean metal surface was obtained. For temperature measurements, a pyrometer (Pyrospot DG40N, DIAS, $\lambda = 1600$ nm) was used at an emissivity of 0.17. Ba was supplied from a commercial Ba dispenser source (SAES Getters). Ti was evaporated from a rod out of a three-cell electron beam evaporator (Focus). Film thickness was estimated using a quartz crystal microbalance maintained at 345 K. Metal layers were deposited at room temperature and postoxidized by annealing in an oxygen atmosphere of 1×10^{-5} mbar for 20 min at 770 K. The XPS measurements were carried out using nonmonochromatized Al Kα excitation. For detection, a 127° analyzer equipped with a single channeltron was used. From the measured data, Al Kα satellites, an experimentally determined background of the bare substrate, and an additional Shirley background were subtracted prior to fitting. The XPS binding energy axis was calibrated to a Pd 3d5/2 core level energy of 335.2 eV.[33] The STM measurements were carried out in a home-build STM. All measurements presented here were conducted at liquid nitrogen temperatures.

Custom code was used for LEED pattern calculation using point-like atoms under kinematic scattering with atomic form factor set to unity for all atoms, similar to earlier work.[21] The unit cell base was defined according to the protrusions seen by STM. Calculated single domain patterns were further duplicated, symmetrically rotated, and mirrored according to the substrate symmetry. To compare the calculated pattern with experiment, the calculated intensities were plotted as 2D Gaussian profiles.

Conflict of Interest

The authors declare no conflict of interest.

Data Availability Statement

Research data are not shared.

[1] S. Förster, K. Meinel, R. Hammer, M. Trautmann, W. Widdra, *Nature* **2013**, *502*, 215.

[2] N. Niizeki, H. Mitani, *J. Phys. A: Math. Gen.* **1987**, *20*, L405.

[3] F. Gähler, in *Proc. of the ILL/CODEST Workshop*, World Scientific, Singapore **1988**, p. 13.

[4] S. Schenk, E. M. Zollner, O. Krahn, B. Schreck, R. Hammer, S. Förster, W. Widdra, *Acta Crystallogr., Sect. A: Found. Adv.* **2019**, *75*, 307.

[5] E. M. Zollner, F. Schuster, K. Meinel, P. Stötzner, S. Schenk, B. Allner, S. Förster, W. Widdra, *Phys. Status Solidi B* **2020**, *257*, 1900655.

[6] S. Förster, M. Trautmann, S. Roy, W. A. Adeagbo, E. M. Zollner, R. Hammer, F. O. Schumann, K. Meinel, S. K. Nayak, K. Mohseni, W. Hergert, H. L. Meyerheim, W. Widdra, *Phys. Rev. Lett.* **2016**, *117*, 095501.

[7] E. Cockayne, M. Mihalkovič, C. L. Henley, *Phys. Rev. B* **2016**, *93*, 020101.

[8] S. Förster, K. Meinel, K.-M. Schindler, W. Widdra, *Surf. Interface Anal.* **2012**, *44*, 628.

[9] J. Yuhara, K. Horiba, R. Sugiura, X. Li, T. Yamada, *Phys. Rev. Mater.* **2020**, *4*, 103402.

[10] X. Li, K. Horiba, R. Sugiura, T. Yamada, J. Yuhara, *Appl. Surf. Sci.* **2021**, *561*, 150099.

[11] T. T. Dorini, F. Brix, C. Chatelier, A. Kokalj, É. Gaudry, *Nanoscale* **2021**, *13*, 10771.

[12] M. Maniraj, L. V. Tran, O. Krahn, S. Schenk, W. Widdra, S. Förster, *Phys. Rev. Mater.* **2021**, *5*, 084006.

[13] C. Wu, M. S. J. Marshall, M. R. Castell, *J. Phys. Chem. C* **2011**, *115*, 8643.

[14] F. Sedona, G. A. Rizzi, S. Agnoli, F. X. Llabrés i Xamena, A. Papageorgiou, D. Ostermann, M. Sambi, P. Finetti, K. Schierbaum, G. Granozzi, *J. Phys. Chem. B* **2005**, *109*, 24411.

[15] C. Breinlich, M. Buchholz, M. Moors, S. L. Moal, C. Becker, K. Wandelt, *J. Phys. Chem. C* **2014**, *118*, 6186.

[16] G. Barcaro, A. Fortunelli, *Phys. Chem. Chem. Phys.* **2019**, *21*, 11510.

[17] J. Liu, T. Lin, Z. Shi, F. Xia, L. Dong, P. N. Liu, N. Lin, *J. Am. Chem. Soc.* **2011**, *133*, 18760.

[18] M. Dunin von Przychowski, H. Wiechert, G. K. Marx, G. Schonhense, *Surf. Sci.* **2003**, *541*, 46.

[19] G. E. Poirier, *Langmuir* **1999**, *15*, 1167.

[20] U. Stahl, D. Gador, A. Soukopp, R. Fink, E. Umbach, *Surf. Sci.* **1998**, *414*, 423.

[21] S. Schenk, S. Förster, K. Meinel, R. Hammer, B. Leibundgut, M. Paleschke, J. Pantzer, C. Dresler, F. O. Schumann, W. Widdra, *J. Phys.: Condens. Matter* **2017**, *29*, 134002.

[22] L. T. Hudson, R. L. Kurtz, S. W. Robey, D. Temple, R. L. Stockbauer, *Phys. Rev. B* **1993**, *47*, 1174.

[23] M. H. Farstad, D. Ragazzon, H. Groenbeck, M. D. Strömsheim, C. Stavrakas, J. Gustafson, A. Sandell, A. Borg, *Surf. Sci.* **2016**, *649*, 80.

[24] S. Förster, S. Schenk, E. M. Zollner, O. Krahn, C.-T. Chiang, F. O. Schumann, A. Bayat, K.-M. Schindler, M. Trautmann, R. Hammer, K. Meinel, W. A. Adeagbo, W. Hergert, J. I. Flege, J. Falta, M. Ellguth, C. Tusche, M. DeBoissieu, M. Muntwiler, T. Greber, W. Widdra, *Phys. Status Solidi B* **2020**, *257*, 1900624.

[25] S. Förster, J. I. Flege, E. M. Zollner, F. O. Schumann, R. Hammer, A. Bayat, K.-M. Schindler, J. Falta, W. Widdra, *Ann. Phys. (Berlin)* **2017**, *529*, 1600250.

[26] S. Förster, W. Widdra, *Surf. Sci.* **2010**, *604*, 2163.

[27] S. Roy, K. Mohseni, S. Förster, M. Trautmann, F. Schumann, E. Zollner, H. Meyerheim, W. Widdra, *Z. Kristallogr.—Crystall. Mater.* **2016**, *231*, 749.

[28] L. Gross, C. Seidel, H. Fuchs, *Org. Electron.* **2002**, *3*, 1.

[29] P. Studer, S. R. Schofield, G. Lever, D. R. Bowler, C. F. Hirjibehedin, N. J. Curson, *Phys. Rev. B* **2011**, *84*, 041306.

[30] W. Hösler, W. Moritz, *Surf. Sci.* **1986**, *175*, 63.

[31] C. Nagl, E. Platzgummer, O. Haller, M. Schmid, P. Varga, *Surf. Sci.* **1995**, *331–333*, 831.

[32] A. A. Saranin, A. V. Zotov, M. Kishida, Y. Murata, S. Honda, M. Katayama, K. Oura, D. V. Gruznev, A. Visikovskiy, H. Tochihara, *Phys. Rev. B* **2006**, *74*, 035436.

[33] M. C. Militello, S. J. Simko, *Surf. Sci. Spectra* **1994**, *3*, 387.
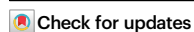
nature communications

2D honeycomb transformation into dodecagonal quasicrystals driven by electrostatic forces

Sebastian Schenk[1], Oliver Krahn[1], Eric Cockayne [2], Holger L. Meyerheim[3], Marc de Boissieu[4], Stefan Förster [1] & Wolf Widdra [1]

Dodecagonal oxide quasicrystals are well established as examples of long-range aperiodic order in two dimensions. However, despite investigations by scanning tunneling microscopy (STM), low-energy electron diffraction (LEED), low-energy electron microscopy (LEEM), photoemission spectroscopy as well as density functional theory (DFT), their structure is still controversial. Furthermore, the principles that guide the formation of quasicrystals (QCs) in oxides are elusive since the principles that are known to drive metallic QCs are expected to fail for oxides. Here we demonstrate the solution of the oxide QC structure by synchrotron-radiation based surface x-ray diffraction (SXRD) refinement of its largest-known approximant. The oxide QC formation is forced by large alkaline earth metal atoms and the reduction of their mutual electrostatic repulsion. It drives the $n = 6$ structure of the 2D Ti_2O_3 honeycomb arrangement via Stone–Wales transformations into an ordered structure with empty $n = 4$, singly occupied $n = 7$ and doubly occupied $n = 10$ rings, as supported by DFT.

Dodecagonal oxide quasicrystals (QCs) are two-dimensional metal-oxide ultrathin films that exhibit a sharp 12-fold diffraction pattern[1,2]. They have been identified for Ba-Ti-O and for Sr-Ti-O metal-oxide layers on hexagonally closed-packed metal substrates[1–8]. The dodecagonal symmetry is associated with a distinct square-triangle-rhomb tiling that was derived independently as a mathematical model a quarter of a century ago by Niizeki and Mitani and by Gähler, the Niizeki-Gähler tiling (NGT)[9,10]. The bright spots observed by atomically resolved STM images for the Ba-Ti-O and the Sr-Ti-O QCs closely match the vertices of this mathematical model[11]. As in many other QC systems, oxide QCs come along with a family of approximants that are periodic arrangements composed of the very same building blocks. They differ in complexity and unit cell size, classified by the number of tiling elements. The known approximants range from 4:2:0 to 48:18:6 with respect to the number of triangles, squares, and rhombi within the unit cell[2–4,12–15]. How these approximants are related to or evolve from

oxide quasicrystals are open questions, since the atomic structure is still under debate. Earlier studies on the 4:2:0 approximant, the smallest square-triangle tiling commonly known as sigma phase, suggested that Ti atoms decorate the triangle and square vertices for Ba-Ti-O on Pt(111) based on STM, SXRD and density functional theory (DFT) calculations[4,5]. In contrast, a DFT study proposed a structural model for various approximants where the tiling vertices are decorated by Ba instead[3], for which an uplifting into the four-dimensional hyperspace has been proposed also[16]. A third structure with a different stoichiometry was proposed by Yuhara et al. based on STM, XPS and Rutherford backscattering experiments[6,7]. This controversial situation arises from the lack of experimental data for a full structure determination. Though atomically resolved STM images pin down the dodecagonal quasicrystalline vertex structure as seen by bright features of protruding atoms, their chemical nature is debated. Furthermore, despite several attempts, information about the second and third atomic

[1]Institute of Physics, Martin-Luther-Universität Halle-Wittenberg, 06099 Halle, Germany. [2]Material Measurement Laboratory, National Institute of Standards and Technology, Gaithersburg, MD 20899, USA. [3]Max Planck Institute of Microstructure Physics, 06120 Halle, Germany. [4]Universite Grenoble Alpes, CNRS, SIMaP, St Martin d'Heres, France. ✉e-mail: stefan.foerster@physik.uni-halle.de

Article

species in the ternary oxide is not experimentally accessible either from STM or from non-contact AFM[1,17].

In the present work using SXRD, we will resolve these issues and present a complete structural analysis in accordance with DFT for a large-scale quasicrystal approximant. From the proposed structure we derive a tiling decoration scheme that also applies to the quasicrystalline NGT. For the formation process of the dodecagonal oxide QC, we identify Stone–Wales transformations as key elements that drive 2D hexagonal honeycomb lattices into QC approximant structures with square-triangle tiling. The Stone–Wales defect is known as a low-energy structural transformation in many 2D honeycomb lattices, including graphene, h-BN, silicene, and Ti_2O_3[18,19]. It converts four adjacent six-fold honeycomb rings, Ti_nO_n with $n = 6$, into two $n = 7$ and two $n = 5$ rings. For many 2D materials such as, e.g., graphene, the transformation stops upon a few Stone–Wales conversions and results in a disordered structure consisting of $n = 5$, 6, and 7 rings. Fully random, but also continuous structures with a broad ring size distribution are known from 2D silica films, which are 2D analogs of the Zachariasen model for glass formation[20,21]. For the Ti_2O_3-based QC and its approximants we demonstrate that their long-range order results from the self-organization of alkaline earth metal atoms stabilizing Ti_nO_n ring sizes with $n \geq 7$.

Results

Structure determination for a large-scale approximant

For the dodecagonal QC structure determination, we focus on the largest-known oxide QC approximant[12]. It shows a periodic tiling with 48 triangles, 18 squares, and 6 rhombi in the unit cell (Fig. 1a, c, e). It is prepared by deposition of Sr and Ti on Pt(111) followed by post-annealing in an oxygen atmosphere of 10^{-4} Pa. The long-range order forms upon high-temperature annealing at 1250 K under ultrahigh vacuum conditions (see Supplementary Fig. 1). Atomically resolved STM images clearly show the vertex structure

of the square-triangle-rhomb tiling as depicted in Fig. 1a. The Fourier-transform (FT) taken from large-area STM data (Supplementary Fig. 2) identifies the large unit cell of an almost square lattice as fine grid with reciprocal lattice vectors of 0.14 Å^{-1}. Twelve reflections of higher intensity are located at a distance of 1.0 Å^{-1} from the center. They resemble the characteristic diffraction intensities of the dodecagonal QC. The close resemblance of the approximant and the QC diffraction pattern indicates their structural similarity where 48 vertex atoms are arranged in 72 tiles with only minor modifications from the dodecagonal NGT (Fig. 1c). The latter include chains of three rhombi in the approximant, while pairs of rhombi dominate the oxide QC tiling meeting in the center of a characteristic dodecagon[11]. Our SXRD experiments carried out at the synchrotron radiation facility Soleil allow to determine the unit cell dimensions more accurately (Supplementary Fig. 3): the periodic square lattice as shown in Fig. 1b has lattice parameters of $a = 44.3$ and $b = 43.2$ Å equivalent to a commensurate $\begin{pmatrix} 16 & 0 \\ 9 & 18 \end{pmatrix}$ superstructure with respect to the primitive hexagonal unit cell of the Pt(111) substrate. The structure with this tiling pattern has p2gg plane-group symmetry due to the presence of two orthogonal glide lines. Therefore, the size of the symmetrically independent part is equal to one-quarter of the unit cell only (filled region in Fig. 1a). Owing to the fact that the rectangular p2gg unit cell grows on the p6mm symmetric surface, six rotational and mirror domains of this superstructure exist. From the full SXRD reciprocal space maps, which are partly shown in Fig. 1e (Supplementary Fig. 3 for full data), the integrated intensities of 460 reflections of type (hk0) were collected which reduce to 182 symmetry-inequivalent ones with an average agreement factor of 0.15. After correction for instrumental factors, the structure factor magnitudes $|F_{obs}(hk0)|$ were considered for the structural analysis. For the structural
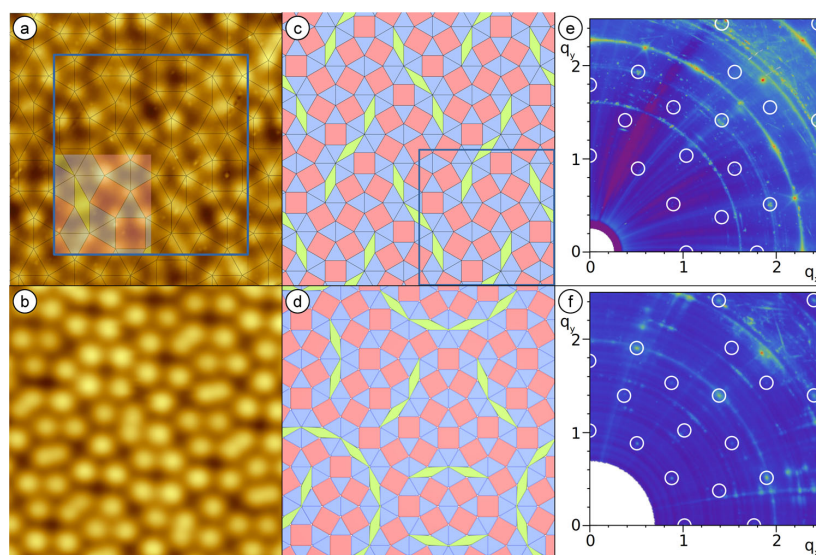
Fig. 1 | Comparison of the 48:18:6 approximant structure with the oxide quasicrystal. a The atomic-resolution STM image of the Sr-Ti-O approximant reveals 48 protrusions in the unit cell (blue square). The semi-transparent tiling highlights the asymmetric unit. **b** The vertex atoms of the Ba-Ti-O oxide quasicrystal arrange in similar elementary tiles. **c** The approximant tiling is characterized by chains of three rhombuses, while pairs of rhombuses meeting in the center of a dodecagon dominate the QC tiling (**d**). In reciprocal space, the most intense spots of the

approximant (**e**) are centered around the spot positions of the dodecagonal pattern (**f**) as marked by white circles in the SXRD data. The close correspondence of spot positions and intensities for both structures is demonstrated in Supplementary Fig. 8. The spot splitting in (**e**) results from the occurrence of multiple domains of the approximant structure. **a** 6 × 6 nm², 0.1 nA, 1.0 V. **b** 6 × 6 nm², 0.015 nA, −1.0 V.
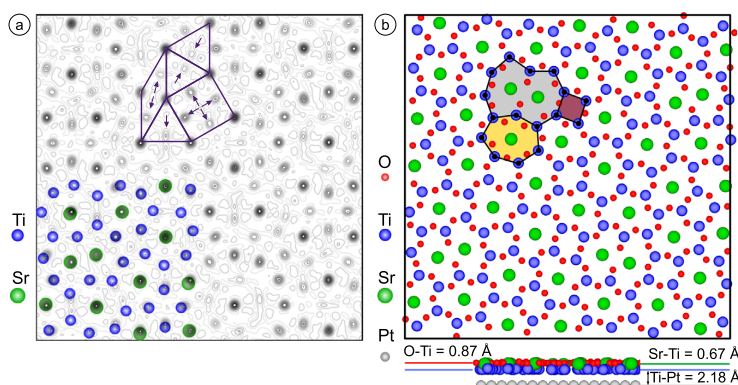
Fig. 2 | Atomic structure of the 48:18:6 approximant. a SXRD-derived electron density map calculated from the best fit model for the unit cell of the 48:18:6 approximant in Sr-Ti-O on Pt(111). The heavy Sr atoms (green) reside at positions of the highest electron densities. By connecting the Sr atoms the tiling seen in STM is formed (emphasized in the upper part). The weaker electron densities are attributed to Ti atoms (blue). Their positions inside the tiling elements are marked by purple arrows. **b** Relaxed atomic structure containing the oxygen sublattice calculated by DFT in top and side views. The Ti atoms are attracted toward the Pt interface. The average height of the Sr and O atoms above the Pt substrate is by 0.67 and 0.82 Å larger as compared to Ti. The characteristic features of this structure are Ti_nO_n rings with $n = 4$, 7 and 10 hosting 0, 1 and 2 Sr atoms, respectively (highlighted in purple, orange and gray).
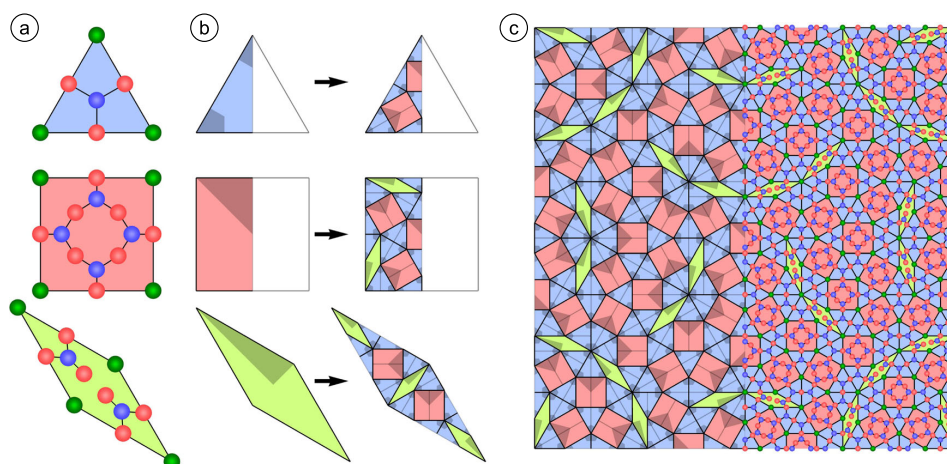

Fig. 3 | Generalization of the atomic structure to all related ternary oxides. a Decoration scheme for the three tiles of the oxide QC. Green, blue and red spheres represent A-side (Sr or Ba), Ti, and O atoms, respectively. **b** Inflation rule for the Niizeki-Gähler tiling of oxide quasicrystals based on three tiling elements. Shaded areas indicate the symmetry inherent to the tiling elements. The definition of the recursion rule based on half a triangle and half a square determines an overlap-free dodecagonal square-triangle-rhomb tiling. **c** Square supertile after three iterations of recursion. The decoration scheme of (**a**) has been applied to the right part of (**c**).

refinement process, two complementary models have been used as a starting point, where the vertex positions of the tiling are occupied either by the alkaline earth metal Sr or by Ti atoms. These complementary assignments correspond to the proposed oxide QC models based on DFT or STM, respectively[3,4]. Despite the complexity of the large unit cell with 72 tiling elements for an SXRD structural refinement, the positions of the vertex atoms as well as those of the second (non-vertex) atomic species have been optimized by a constrained least-squares refinement using the program SHELXL[22]. Oxygen atoms within the structure are not considered due to their small scattering cross-section. With regard to all agreement factors (Goodness of fit (GOF), weighted residuum (wR2), and unweighted residuum (R1))[22,23], the structural model including Sr atoms occupying the vertex positions leads to substantially better fits (GOF = 1.5, wR2 = 0.21, R1 = 0.11) as compared to the alternative with Ti atoms at the vertices (GOF = 4.2, wR2 = 0.73, R1 = 0.45)[4,5].

This leads us to conclude that the SXRD analysis is in agreement with the theoretical model developed by Cockayne et al.[3] The arrangement of the Sr and Ti atoms can be directly visualized by the calculation of the charge density contour map, $\rho(x, y)$, using the observed structure factor magnitudes ($|F_{obs}|$) and the calculated scattering phases α derived from the structural model (due to the centrosymmetry of the z-projected structure, the condition $\alpha = 0$ or π holds). The highest-density features as marked in green in Fig. 2a correspond to the positions of the heaviest atom, Sr. They form the vertices of the square-triangle-rhomb tiling. The Ti atoms are located at positions of the second highest electron density, as emphasized in
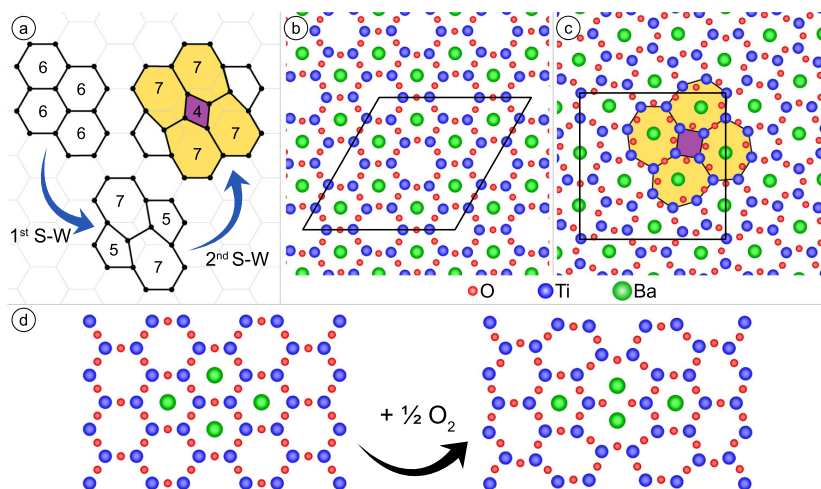
Fig. 4 | Stone–Wales transformation converting honeycomb structure into square-triangle tiling and rhombus formation by incorporation of additional oxygen. a Transition from a honeycomb lattice by subsequent Stone–Wales (S–W) transformations into a structure of four- and seven-member rings. **b** Comparison of the DFT relaxed structures of the Ba-decorated Ti_2O_3 honeycomb structure and **c** the Ba-Ti-O sigma-phase approximant on Pt(111). The DFT calculations were performed for these commensurate $Ba_8Ti_{24}O_{36}$ supercells ontop of three layers of Pt(111) (Pt not shown). The lowest energy phase is the sigma-phase approximant. **d** The addition of one oxygen atom to a Ti-O-Ti edge of two adjoining hexagons leads upon relaxation to the $n = 10$ ring of the oxide QC (compare central $n = 10$ ring with those in Fig. 2).

blue and by the black arrows in Fig. 2a. Note that the weak intensities in between the refined atomic positions as well as the small deviation between ideal positions and maxima of the calculated electron density result from Fourier series truncation errors due to the limited number of experimentally available diffraction intensities.

Theoretical description

DFT calculations for the 48:18:6 approximant on Pt(111) provide further insights into the full atomic structure especially the oxygen positions. The fully relaxed structure is shown in Fig. 2b and can be understood as a partially Sr-decorated Ti_2O_3 network, in which every Ti atom is coordinated by three O atoms at an average distance of 1.89 Å (standard deviation 0.02 Å). This value is slightly larger than the 1.84 Å reported for DFT calculations of freestanding Ti_2O_3 in a planar honeycomb geometry[24]. The positions of each species above the Pt surface are quite uniform: Sr 2.85 Å (standard deviation 0.02 Å), Ti 2.18 Å (0.05 Å), and O 3.00 Å (0.06 Å). The average Sr-Sr distance corresponding to a tile edge is 6.75 Å (0.18 Å), which is in line with the experimentally determined value of 6.72 Å for the oxide QC[2]. The average Sr-Sr distance corresponding to the short diagonal of the 30° tile is 3.79 Å (0.07 Å), about 8% larger than that for a perfect 30° rhombus of edge length 6.75 Å but comparable to the 3.905 Å lattice parameter of perovskite $SrTiO_3$. Merchan et al. also reported results for a DFT relaxation of the Cockayne et al. structure model, and found similar structural features in spite of differences in the computational details[12].

Whereas Ti_2O_3 honeycomb structures consist of hexagonal arrangements of planar Ti_6O_6 rings, the oxide QC approximant contains Ti_nO_n rings with $n = 4$, 7 and 10 only (colored in Fig. 2b). The smallest $n = 4$ rings are empty, whereas the larger Ti_7O_7 rings are decorated and stabilized by Sr, as we show below. The $n = 10$ pores host two Sr and two additional O atoms. These additional oxygen atoms screen the positively charged Sr cations thus allowing a shorter Sr-Sr next-neighbor distance in these rings.

From the structure solution presented, a decoration scheme for all tiles of the two-dimensional ternary oxide phase is confirmed, which universally applies to the quasicrystalline NGT and all related

approximant structures (Fig. 3a)[3]. By combining the tiling element ratio in the respective unit cell with the atom density given by the decoration scheme, the stoichiometry of a given structure can be derived. For the 48:18:6 approximant a composition of $Sr_{48}Ti_{132}O_{204}$ and Sr:Ti:O ratio of approximately 0.364: 1: 1.545 is obtained. For the oxide QC, the Sr:Ti:O ratio is very similar: $(\sqrt{3} - 1)/2:1:(3\sqrt{3} + 1)/4 \approx$ 0.366:1:1.549.

The atomic network of the oxide QC can be constructed from a combination of recursion and decoration (Fig. 3b, c). The definition of the NGT based on a recursion rule using half a triangle, half a square and the full rhombus given in Fig. 3b is the first that defines an overlap-free NGT, in contrast to earlier attempts[25]. The tiling as well as the atomic network formed from decoration are illustrated in Fig. 3c after three inflation steps. The equivalent tiling decoration scheme of the 48:18:6 approximant and the oxide QC leads to a high level of agreement of the corresponding diffraction intensities of both systems as demonstrated in Supplementary Fig. 8. While the average tiling decoration is well-defined from the DFT results, there are some local deviations. In particular, the three oxygen atoms surrounding a given Ti are frequently rotated clockwise or counterclockwise with respect to their average positions, associated with a tendency for each Sr atom to form bonds of length 2.4–2.7 Å with 3 or 4 of its oxygen neighbors.

Discussion

Driving force toward quasicrystal approximant formation

Many 2D threefold coordinated networks display disorder that can be described as the application of one or more Stone–Wales-type transformations to a hexagonal honeycomb lattice[19,26–28]. The Stone–Wales defect, discussed originally for icosahedral C_{60}, twists one edge in the network and converts four adjacent $n = 6$ honeycomb rings into $n = 7$ and $n = 5$ rings[18]. Typical threefold networks with disorder are characterized by an approximate Gaussian size distribution peaking at $n = 6$. In sharp contrast to these previously reported structures, the oxide QC approximant structure solved here, is composed of Ti_nO_n rings characterized by $n = 4$, 7, and 10 only (hosting 0, 1, and 2 alkaline earth metal atoms respectively). The stabilization of such low symmetry Ti_nO_n rings with $n = 7$ and $n = 10$ by the alkaline earth metal

5.12 2D honeycomb transformation into dodecagonal quasicrystals driven by electrostatic forces

atoms Sr or Ba, which will be called A-type atoms, are the essential features to explain.

Ultrathin film Ti_2O_3 has the well-known hexagonal honeycomb structure with $n = 6$ rings whereas the sigma 4:2:0 approximant (under the decoration scheme in this paper) has only $n = 4$ and $n = 7$ rings. In fact, it is possible to convert the honeycomb structure into the sigma approximant via a sequence of Stone–Wales transformations: A single transformation first generates $n = 5$ and 7 rings (Fig. 4a). Reapplying the concept of Stone–Wales transformation to the $n = 5$ and 6 rings, yields $n = 4$ and 7 rings (Fig. 4a). Thus, the stabilization of the $n = 7$ rings is characteristic to the full conversion of an initial honeycomb lattice into an ordered structure consisting of $n = 4$ and 7 rings only, according to:

$$12 \times Ti_6O_6 \rightarrow 4 \times Ti_5O_5 + 4 \times Ti_6O_6 + 4 \times Ti_7O_7 \,(1.\,Stone - Wales\,transformation)$$
$$\rightarrow 4 \times Ti_4O_4 + 8 \times Ti_7O_7 \,(2.\,Stone - Wales\,transformation)$$
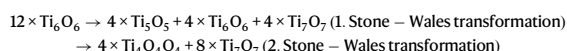
This process converts 2/3 of all hexagonal rings to those with $n = 7$.

The unit cell areas of the honeycomb and the sigma phase are similar while their composition $Ti_{24}O_{36}$ is identical. By decorating 2/3 of the honeycomb Ti_6O_6 rings and all of the sigma-phase Ti_7O_7 rings with Ba as shown in Fig. 4b, c, structures of identical composition $Ba_8Ti_{24}O_{36}$ are derived. As detailed in the Supplementary Notes, DFT calculations were used to optimize the strains and atomic positions of each structure on a Pt substrate. In absence of decorating atoms, the honeycomb structure is favored, as expected. By contrast, Ba decoration leads to an energy lowering of 0.034 eV per Ti_2O_3 unit in favor of the sigma phase. This provides evidence that large A-type atoms drive Stone–Wales-type transformations to form $n = 7$ rings. This energy lowering is directly related to the reduction of the electrostatic dipole-dipole energy, which can be understood by the larger separation of the positively charged large A-type cation within the sigma phase: DFT shows that Ba atoms in the sigma phase have five closest Ba neighbors at an average distance of 6.96 Å, which is about 17% larger than for the honeycomb structure, 5.89 Å (this work) or 5.95 Å[29]. Also, the average height of the Ba atoms above the metal surface is 3.18 Å for the sigma structure, which corresponds to a reduction by 0.24 Å as compared to the honeycomb structure. Both, the larger separation and the smaller dipole moment, reduce the electrostatic dipole-dipole repulsion between the Ba ions and, therefore, support the sigma structure. On the other hand, rings with $n > 7$ are energetically unfavorable as in this case the A-O bond becomes too large. Finally, we suggest that the energy penalty of the $n = 4$ ring formation is overcompensated by the reduction of the electrostatic repulsion. Consequently, the nature of the long-range order should depend on the A-type ion coverage relative to the number of rings.

A coverage of 2/3 Ba per ring is obtained for the sigma phase, also known as the $3^2.4.3.4$ Archimedean tiling[30]. This QC approximant has been observed experimentally for Ba-Ti-O on Pt(111), Ru(0001), and Pd(111) surfaces[4,13,15]. In principle, a higher fraction of $n = 7$ rings and thus higher A-type atom density could be obtained if Stone–Wales transformations to form $n = 3$ rings were allowed, but we suspect that the energy penalty of $n = 3$ rings is too large. Instead, higher A-type atom density is obtained via the $n = 10$ rings associated with the short diagonal of the rhombus tile. By hosting two A-type atoms at a relatively short distance, they allow for a higher coverage than would be possible via Stone–Wales transformations alone. Two nearby oxygen atoms, which are not interconnected via additional Ti reduce the Coulomb repulsion between the A-type atoms. While there is not a Stone–Wales type transformation for generating an $n = 10$ ring, one can be formed by expanding the shared edge of a pair of adjoined $n = 6$ rings, adding another interior O, and moving the two interior O to be near the appropriate Ti atoms (Fig. 4d). The additional O atoms change the overall Ti:O ratio from 2:3. We hypothesize that the $n = 10$ ring of Fig. 4d lowers the (free) energy under relatively A-rich conditions,

allowing for triangle-square-rhombus tilings. Experimentally, such a transformation from a hexagonal honeycomb structure to the 48:18:6 quasicrystal approximant has been followed by LEED (Supplementary Fig. 1b, c).

For a Ba-decorated Ti_2O_3 honeycomb on Au(111), the honeycomb lattice is not modified up to 873 K and a coverage of 0.63[31]. In case of Ba-Ti-O on Pt(111), annealing at above $T = 1100$ K produces a variety of ordered structures[8,32] that have been interpreted as networks with $n = 7$ rings occupied by Ba[3]. For a coverage of 50% of all rings by an A-type atom, structures made from $n = 5$ and 7 rings only have been reported[3,32]. For coverages between 50% and 67%, a transition to a square-triangle tiling occurs. The sigma phase (Fig. 4) represents the highest Ba coverage in $n = 7$ rings that is realized in a pure square-triangle tiling. This is even by 5.1% higher than in a quasicrystalline square-triangle tiling[33] using the decoration scheme presented above. Thus, higher Ba coverages require the formation of $n = 10$ rings, which hosts two Ba atoms. Together with two neighboring $n = 7$ rings, the two A-type atoms form the vertices of a 30° rhombus, which is essential as the third tiling element for the formation of the dodecagonal structure of oxide QCs.

In summary, we have used a combination of SXRD experiments and DFT calculations to analyze the structure of an ultrathin film Sr-Ti-O approximant, which allows the structural solution of the directly related dodecagonal oxide quasicrystal. The structures of the quasicrystal and of the related quasicrystal approximants are based on 2D networks of interconnected Ti_nO_n rings with $n = 4$, 7, and 10. We have shown that the formation of the oxide quasicrystal is governed by a fundamental principle which is based on the low-energy phase transformation (Stone–Wales transformation) in which the reduction of the electrostatic interaction between positively charged large cations located within the rings is the major driving mechanism. By exploiting this mechanism of ring size modifications, we expect that 2D structures of similar flexibility as, e.g., made from V_xO_y, $FeWO_3$, Nb_2O_3, and SiO_4 units[20,34–41], might also be driven into oxide quasicrystals.

Methods
Experimental setup
Sample growth, LEED, and STM characterization were carried out in a UHV system operating at a base pressure of 1×10^{-8} Pa. For thin film deposition, a four-pocket e-beam evaporator (EBE4, SPECS, Berlin) was used (certain commercial equipment and software are identified in this paper to adequately describe the methodology used. Such identification does not imply recommendation or endorsement by the National Institute of Standards and Technology, nor does it imply that the equipment and software identified is necessarily the best available for the purpose). Sr-Ti-O has been sublimed by heating a $SrTiO_3$ single crystal clamped between Ta plates. Additional evaporation of Ti can be supplied from a Ti rod. Evaporation rates were determined using a quartz crystal microbalance. SXRD measurements have been performed at the SixS beamline at the synchrotron SOLEIL. The UHV endstation of this beamline was used in which the diffractometer is coupled to standard UHV tools for sample preparation and analysis (LEED, STM). For temperature measurements, a pyrometer (Pyrospot DG40N, DIAS, $\lambda = 1600$ nm) was used at an emissivity of 0.17.

Sample preparation
Ultrathin films of Sr-Ti-O have been grown onto Pt(111) at room temperature using molecular beam epitaxy. 8 Å of $SrTiO_3$ were deposited at an oxygen background pressure of 10^{-4} Pa with a rate of 1.0 Å/min. To balance Ti deficiencies in the film, 3 Å of Ti was added under the same conditions. The ultrathin films were post-annealed for 10 min at 950 K in 10^{-4} Pa of oxygen. Annealing for 20 min at 1150 K in UHV resulted in the formation of the 48:18:6 approximant homogeneously covering the Pt(111) single crystal. Such prepared samples were transferred through air to the SixS beamline. At the beamline, the samples

Article https://doi.org/10.1038/s41467-022-35308-z

have been annealed at 850 K in 10^{-4} Pa oxygen atmosphere to remove residual carbon impurities originating from the air transfer. The approximant structure was recovered by UHV annealing at the beamline. Several annealing steps were performed to optimize the structural perfection as monitored by LEED prior to the SXRD characterization.

SXRD analysis
The SXRD measurements were carried out at the UHV diffractometer of the SIXS beamline at Synchrotron SOLEIL in Paris, France. Monochromatic x-rays with photon energy of 11 keV were used to avoid Pt fluorescence (at 11.1 and 13 keV) and to reduce the background signal. The diffraction experiment was performed under grazing incidence at an angle of 0.2°. A 2D hybrid pixel XPad detector with 560 × 240 pixel was used for data collection. For the 48:18:6 approximant, the reciprocal space has been mapped in continuous rotation mode covering 120° of the azimuthal angles for polar angles ranging from 5 to 52° in increments of 0.1 and 1.5°, respectively. In case of the oxide QC, the reciprocal space map covered an azimuth of 182° at a polar angle variation from 4 to 40° in increments of 0.07 and 2°, respectively. The integration time was 0.3 s per frame. The 2D raw data were processed using the binoculars software[42] to generate 3D reciprocal voxel map data. For structure optimization and calculations of the unweighted residuum, the software package SHELXL was used[22].

DFT calculations
DFT calculations were performed using the commercial software VASP (certain commercial equipment and software are identified in this paper to adequately describe the methodology used. Such identification does not imply recommendation or endorsement by the National Institute of Standards and Technology, nor does it imply that the equipment and software identified is necessarily the best available for the purpose)[43,44]. Projector-augmented-wave pseudopotentials[45,46] from the VASP library were used for each element. A Hubbard U correction was applied to the d-electrons of Ti[47,48]. Non-local dispersions were included[49,50]. Further details are given in the Supplementary Notes.

Data availability
Source data are provided with this paper. The SXRD data generated in this study have been deposited in the Zenodo repository under the accession code https://doi.org/10.5281/zenodo.6787572. The DFT structure files and sample input files have been deposited in the Zenodo repository under the accession code https://doi.org/10.5281/zenodo.7007289.

References
1. Förster, S., Meinel, K., Hammer, R., Trautmann, M. & Widdra, W. Quasicrystalline structure formation in a classical crystalline thin-film system. *Nature* **502**, 215–218 (2013).
2. Schenk, S. et al. Observation of a dodecagonal oxide quasicrystal and its complex approximant in the SrTiO₃-Pt(111) system. *J. Phys. Condens. Matter* **29**, 134002 (2017).
3. Cockayne, E., Mihalkovič, M. & Henley, C. L. Structure of periodic crystals and quasicrystals in ultrathin films of Ba-Ti-O. *Phys. Rev. B* **93**, 020101 (2016).
4. Förster, S. et al. Observation and structure determination of an oxide quasicrystal approximant. *Phys. Rev. Lett.* **117**, 095501 (2016).
5. Roy, S. et al. The Kepler tiling as the oldest complex surface structure in history: X-ray structure analysis of a two-dimensional oxide quasicrystal approximant. *Z. Kristallogr* **231**, 749 (2016).
6. Yuhara, J., Horiba, K., Sugiura, R., Li, X. & Yamada, T. Growth and composition of an ultrathin Ba-Ti-O quasicrystal film and its crystalline approximant on Pt(111). *Phys. Rev. Materials* **4**, 103402 (2020).
7. Li, X., Horiba, K., Sugiura, R., Yamada, T. & Yuhara, J. Growth of Ba–O ultrathin films on Pt(111) followed by Ti incorporation to prepare oxide crystalline approximants and quasicrystals. *Appl. Surf. Sci.* **561**, 150099 (2021).
8. Förster, S. et al. Quasicrystals and their approximants in 2D ternary oxides. *Phys. Status Solidi B* **257**, 1900624 (2019).
9. Niizeki, N. & Mitani, H. Two-dimensional dodecagonal quasi-lattices. *J. Phys. A Math. Gen.* **20**, L405 (1987).
10. Gähler, F. in *Quasicrystalline Materials* (eds Janot, D & Dubois, J. M.) 272–284 (World Scientific, Singapore, 1988).
11. Schenk, S. et al. Full real-space analysis of a dodecagonal quasicrystal. *Acta Cryst.* **A75**, 307 (2019).
12. Merchan, C. et al. Two-dimensional square and hexagonal oxide quasicrystal approximants in SrTiO₃ films grown on Pt(111)/Al₂O₃(0001). *Phys. Chem. Chem. Phys.* **24**, 7253 (2022).
13. Zollner, E. M. et al. Two-dimensional wetting layer structures of reduced ternary oxides on Ru(0001) and Pt(111). *Phys. Status Solidi B* **257**, 1900655 (2020).
14. Maniraj, M. et al. Hexagonal approximant of the dodecagonal oxide quasicrystal on Pt(111). *Phys. Rev. Mater.* **5**, 084006 (2021).
15. Wührl, F. E., Krahn, O., Schenk, S., Förster, S. & Widdra, W. Anti-phase domain boundary formation in two-dimensional Ba-Ti-O on Pd(111): an alternative to phase separation. *Phys. Status Solidi B* **259**, 2100389 (2022).
16. Yamada, T. A four-dimensional model for the Ba–Ti–O dodecagonal quasicrystal. *Acta Cryst.* **B78**, 247–252 (2022).
17. Zollner, E. M., Schenk, S., Setvin, M. & Förster, S. Perfect monolayers of the BaTiO₃-derived 2D oxide quasicrystals investigated by scanning tunneling microscopy and noncontact atomic force microscopy. *Phys. Status Solidi B* **257**, 1900620 (2020).
18. Stone, A. J. & Wales, D. J. Theoretical studies of icosahedral C60 and some related species. *Chem. Phys. Lett.* **128**, 501–503 (1986).
19. Wang, S., Hu, X., Goniakowski, J., Noguera, C. & Castell, M. R. Influence of the support on stabilizing local defects in strained monolayer oxide films. *Nanoscale* **11**, 2412–2422 (2019).
20. Lichtenstein, L., Heyde, M. & Freund, H.-J. Crystalline-vitreous interface in two dimensional silica. *Phys. Rev. Lett.* **109**, 106101 (2012).
21. Zachariasen, W. H. The atomic arrangement in glass. *J. Am. Chem. Soc.* **54**, 3841 (1932).
22. Sheldrick, G. M. Crystal structure refinement with SHELXL. *Acta Cryst.* **C71**, 3–8 (2015).
23. Abrahams, A. C. Indicators of accuracy in structure factor measurement. *Acta Cryst.* **A25**, 165 (1969).
24. Goniakowski, J. & Noguera, C. Properties of M₂O₃/Au(111) honeycomb monolayers (M = Sc, Ti, V, Cr, Mn, Fe, Co, Ni). *J. Phys. Chem. C* **123**, 9272–9281 (2019).
25. Liao, L.-G., Zhang, W.-B., Yu, T.-X. & Cao, Z.-X. A single cluster covering for dodecagonal quasiperiodic ship tiling. *Chin. Phys. Lett.* **30**, 026102 (2013).
26. Kotakowski, J. et al. Stone-Wales-type transformations in carbon nanostructures driven by electron irradiation. *Phys. Rev.B* **83**, 245420 (2011).
27. Björkman, T. et al. Defects in bilayer silica and graphene: common trends in diverse hexagonal two-dimensional systems. *Sci. Rep.* **3**, 3482 (2013).
28. Huang, P. Y. et al. Imaging atomic rearrangements in two-dimensional silica glass: watching silica's dance. *Science* **342**, 224–227 (2013).
29. Sedona, F. et al. Ultrathin TiOₓ films on Pt(111): a LEED, XPS, and STM investigation. *J. Phys. Chem. B* **109**, 24411 (2005).
30. Grünbaum, B. & Shephard, G. C. Tilings by regular polygons. *Math. Mag.* **50**, 227 (1977).

Article

31. Wu, C., Castell, M. R., Goniakowski, J. & Noguera, C. Stoichiometry engineering of ternary oxide ultrathin films: $Ba_xTi_2O_3$ on Au(111). *Phys. Rev. B* **91**, 155424 (2015).

32. Förster, S., Meinel, K., Schindler, K.-M. & Widdra, W. Oxygen-deficient ordered phases of ultrathin $BaTiO_3$ films on Pt(111). *Surf. Interface Anal.* **44**, 628 (2012).

33. Stampfli, P. A dodecagonal quasiperiodic lattice in two dimensions. *Helvetica Phys. Acta* **59**, 1260 (1986).

34. Surnev, S. et al. Growth and structure of ultrathin vanadium oxide layers on Pd(111). *Phys. Rev. B* **61**, 13945 (2000).

35. Schoiswohl, J. et al. Planar vanadium oxide clusters: two-dimensional evaporation and diffusion on Rh(111). *Phys. Rev. Lett.* **92**, 206103 (2004).

36. Schoiswohl, J. et al. Reduction of vanadium-oxide monolayer structures. *Phys. Rev. B* **71**, 165437 (2005).

37. Pomp, S. et al. Two-dimensional iron tungstate: a ternary oxide layer with honeycomb geometry. *J. Phys. Chem. C.* **120**, 7629–7638 (2016).

38. Wang, S., Goniakowski, J., Noguera, C. & Castell, M. Atomic and electronic structure of an epitaxial Nb_2O_3 honeycomb monolayer on Au(111). *Phys. Rev. B* **100**, 125408 (2019).

39. Barcaro, G. & Fortunelli, A. 2D oxides on metal materials: concepts, status, and perspectives. *Phys. Chem. Chem. Phys.* **21**, 11510 (2019).

40. van Gog, H. et al. Thermal stability and electronic and magnetic properties of atomically thin 2D transition metal oxides. *npj 2D Mater. Appl.* **3**, 18 (2019).

41. Lewandowski, A. L. et al. Growth and atomic-scale characterization of ultrathin silica and germania films: the crucial role of the metal support. *Chem. Eur. J.* **27**, 1870–1885 (2021).

42. Roobol, S., Onderwaater, W., Drnec, J., Felici, R. & Frenken, J. BINoculars: data reduction and analysis software for two-dimensional detectors in surface X-ray diffraction. *J. Appl. Cryst.* **48**, 1324–1329 (2015).

43. Kresse, G. & Furthmüller, J. Efficient iterative schemes for ab initio total-energy calculations using a plane-wave basis set. *Phys. Rev. B* **54**, 11169–11186 (1996).

44. Kresse, G. & Furthmüller, J. Efficiency of ab-initio total energy calculations for metals and semiconductors using a plane-wave basis set. *Comput. Mater. Sci.* **6**, 15–50 (1996).

45. Kresse, G. & Hafner, J. Norm-conserving and ultrasoft pseudopotentials for first-row and transition elements. *J. Phys. Condens. Matter* **6**, 8245–8257 (1994).

46. Kresse, G. & Joubert, D. From ultrasoft pseudopotentials to the projector augmented-wave method. *Phys. Rev. B* **59**, 1758–1775 (1999).

47. Liechtenstein, A. I., Anisimov, V. I. & Zaanen, J. Density-functional theory and strong interactions: orbital ordering in Mott-Hubbard insulators. *Phys. Rev. B* **52**, R5467–R5470 (1995).

48. Hu, Z. & Metiu, H. Choice of U for DFT+U calculations for titanium oxides. *J. Phys. Chem. C.* **115**, 5841–5845 (2011).

49. Dion, M., Rydberg, H., Schröder, E., Langreth, D. C. & Lundqvist, B. I. Van der Waals density functional for general geometries. *Phys. Rev. Lett.* **92**, 109902 (2004).

50. Klimeš, J., Bowler, D. R. & Michaelides, A. Van der Waals density functionals applied to solids. *Phys. Rev. B* **83**, 195131 (2011).

Author contributions
O.K. and S.S. prepared the samples. S.S., S.F., M.d.B., and W.W. performed the SXRD experiments. O.K. measured and analyzed STM and LEED data. S.S. and H.L.M. were involved in the SXRD analysis and structure solution. S.S., S.F., and W.W. developed decoration scheme and inflation rule. E.C. carried out the DFT calculations. S.F., E.C., H.L.M. and W.W. discussed the results and wrote the manuscript.

Competing interests
The authors declare no competing interests.

Additional information
Supplementary information The online version contains supplementary material available at https://doi.org/10.1038/s41467-022-35308-z.

Correspondence and requests for materials should be addressed to Stefan Förster.

Peer review information *Nature Communications* thanks Marek Mihalkovič and the other, anonymous, reviewer(s) for their contribution to the peer review of this work. Peer reviewer reports are available.

Reprints and permissions information is available at http://www.nature.com/reprints

Publisher's note Springer Nature remains neutral with regard to jurisdictional claims in published maps and institutional affiliations.

Bibliography

[1] S. Förster, K. Meinel, R. Hammer, M. Trautmann, and W. Widdra. Quasicrystalline Structure Formation in a Classical Crystalline Thin-Film System. *Nature* **502,** 215–218 (2013).

[2] S. Schenk, S. Förster, K. Meinel, R. Hammer, B. Leibundgut, M. Paleschke, J. Pantzer, C. Dresler, F. O. Schumann, and W. Widdra. Observation of a Dodecagonal Oxide Quasicrystal and Its Complex Approximant in the SrTiO₃-Pt(111) System. *J. Phys.: Condens. Matter* **29,** 134002 (2017).

[3] D. Shechtman, I. Blech, D. Gratias, and J. W. Cahn. Metallic Phase with Long-Range Orientational Order and No Translational Symmetry. *Phys. Rev. Lett.* **53,** 1951–1953 (1984).

[4] D. Levine and P. J. Steinhardt. Quasicrystals: A New Class of Ordered Structures. *Phys. Rev. Lett.* **53,** 2477–2480 (1984).

[5] T. Ishimasa, H.-U. Nissen, and Y. Fukano. New Ordered State between Crystalline and Amorphous in Ni-Cr Particles. *Phys. Rev. Lett.* **55,** 511–513 (1985).

[6] N. Wang, H. Chen, and K. H. Kuo. Two-Dimensional Quasicrystal with Eightfold Rotational Symmetry. *Phys. Rev. Lett.* **59,** 1010–1013 (1987).

[7] H. Chen, D. X. Li, and K. H. Kuo. New Type of Two-Dimensional Quasicrystal with Twelvefold Rotational Symmetry. *Phys. Rev. Lett.* **60,** 1645–1648 (1988).

[8] M. Conrad, F. Krumeich, and B. Harbrecht. A Dodecagonal Quasicrystalline Chalcogenide. *Angew. Chem. Int. Ed.* **37,** 1383–1386 (1998).

[9] X. Zeng, G. Ungar, Y. Liu, V. Percec, A. E. Dulcey, and J. K. Hobbs. Supramolecular Dendritic Liquid Quasicrystals. *Nature* **428,** 157–160 (2004).

[10] K. Hayashida, T. Dotera, A. Takano, and Y. Matsushita. Polymeric Quasicrystal: Mesoscopic Quasicrystalline Tiling in ABC Star Polymers. *Phys. Rev. Lett.* **98,** 195502 (2007).

[11] D. V. Talapin, E. V. Shevchenko, M. I. Bodnarchuk, X. Ye, J. Chen, and C. B. Murray. Quasicrystalline Order in Self-Assembled Binary Nanoparticle Superlattices. *Nature* **461,** 964–967 (2009).

[12] C. Xiao, N. Fujita, K. Miyasaka, Y. Sakamoto, and O. Terasaki. Dodecagonal Tiling in Mesoporous Silica. *Nature* **487,** 349–353 (2012).

[13] J. I. Urgel, D. Écija, G. Lyu, R. Zhang, C.-A. Palma, W. Auwärter, N. Lin, and J. V. Barth. Quasicrystallinity Expressed in Two-Dimensional Coordination Networks. *Nature Chemistry* **8,** 657–662 (2016).

[14] L. Liu, Z. Li, Y. Li, and C. Mao. Rational Design and Self-Assembly of Two-Dimensional, Dodecagonal DNA Quasicrystals. *J. Am. Chem. Soc.* **141,** 4248–4251 (2019).

[15] T. Ishimasa, S. Iwami, N. Sakaguchi, R. Oota, and M. Mihalkovič. Phason Space Analysis and Structure Modelling of 100 Å-scale Dodecagonal Quasicrystal in Mn-based Alloy. *Phil. Mag.* **95,** 3745–3767 (2015).

[16] S. Fischer, A. Exner, K. Zielske, J. Perlich, S. Deloudi, W. Steurer, P. Lindner, and S. Förster. Colloidal Quasicrystals with 12-Fold and 18-Fold Diffraction Symmetry. *Proc. Natl. Acad. Sci.* **108,** 1810–1814 (2011).

[17] J. Mikhael, J. Roth, L. Helden, and C. Bechinger. Archimedean-like Tiling on Decagonal Quasicrystalline Surfaces. *Nature* **454,** 501–504 (2008).

[18] M. Schmiedeberg and H. Stark. Comparing Light-Induced Colloidal Quasicrystals with Different Rotational Symmetries. *J. Phys.: Condens. Matter* **24,** 284101 (2012).

[19] M. Schmiedeberg and H. Stark. Colloidal Ordering on a 2D Quasicrystalline Substrate. *Phys. Rev. Lett.* **101,** 218302 (2008).

[20] M. Schmiedeberg, J. Mikhael, S. Rausch, J. Roth, L. Helden, C. Bechinger, and H. Stark. Archimedean-like Colloidal Tilings on Substrates with Decagonal and Tetradecagonal Symmetry. *Eur. Phys. J. E* **32,** 25–34 (2010).

[21] J. A. Kromer, M. Schmiedeberg, J. Roth, and H. Stark. What Phasons Look Like: Particle Trajectories in a Quasicrystalline Potential. *Phys. Rev. Lett.* **108,** 218301 (2012).

[22] J. Kromer, M. Schmiedeberg, J. Roth, and H. Stark. Phason-Induced Dynamics of Colloidal Particles on Quasicrystalline Substrates. *Eur. Phys. J. E* **36,** 25 (2013).

[23] J. Hielscher, M. Martinsons, M. Schmiedeberg, and S. C. Kapfer. Detection of Phonon and Phason Modes in Intrinsic Colloidal Quasicrystals by Reconstructing Their Structure in Hyperspace. *J. Phys.: Condens. Matter* **29,** 094002 (2017).

[24] A. Gemeinhardt, M. Martinsons, and M. Schmiedeberg. Growth of Two-Dimensional Dodecagonal Colloidal Quasicrystals: Particles with Isotropic Pair Interactions with Two Length Scales vs. Patchy Colloids with Preferred Binding Angles. *Eur. Phys. J. E* **41,** 126 (2018).

[25] T. Ishimasa. Dodecagonal Quasicrystals Still in Progress. *Isr. J. Chem.* **51,** 1216–1225 (2011).

[26] U. T. Lieu and N. Yoshinaga. Formation and Fluctuation of Two-Dimensional Dodecagonal Quasicrystals. *Soft Matter* **18,** 7497–7509 (2022).

[27] P. M. de Wolff. The Pseudo-Symmetry of Modulated Crystal Structures. *Acta Cryst. A* **30,** 777–785 (1974).

[28] A. Janner and T. Janssen. Symmetry of Periodically Distorted Crystals. *Phys. Rev. B* **15,** 643–658 (1977).

[29] A. Janner and T. Janssen. Symmetry of Incommensurate Crystal Phases. I. Commensurate Basic Structures. *Acta Cryst. A* **36,** 399–408 (1980).

[30] T. Janssen, G. Chapuis, and M. de Boissieu. *Aperiodic Crystals: From Modulated Phases to Quasicrystals*. Oxford University Press 2. edition (2018).

[31] A. Yamamoto. Crystallography of Quasiperiodic Crystals. *Acta Cryst. A* **52,** 509–560 (1996).

[32] T. Dotera. Toward the Discovery of New Soft Quasicrystals: From a Numerical Study Viewpoint. *J. Polym. Sci. B Polym. Phys.* **50,** 155–167 (2012).

[33] A. Haji-Akbari, M. Engel, A. S. Keys, X. Zheng, R. G. Petschek, P. Palffy-Muhoray, and S. C. Glotzer. Disordered, Quasicrystalline and Crystalline Phases of Densely Packed Tetrahedra. *Nature* **462,** 773–777 (2009).

[34] R. Lifshitz and D. M. Petrich. Theoretical Model for Faraday Waves with Multiple-Frequency Forcing. *Phys. Rev. Lett.* **79,** 1261–1264 (1997).

[35] S. Savitz, M. Babadi, and R. Lifshitz. Multiple-Scale Structures: From Faraday Waves to Soft-Matter Quasicrystals. *IUCrJ* **5,** 247–268 (2018).

[36] J. J. Oppenheim, G. Skorupskii, and M. Dinca. Aperiodic Metal–Organic Frameworks. *Chemical Science* **11,** 11094–11103 (2020).

[37] N. Niizeki and H. Mitani. Two-Dimensional Dodecagonal Quasilattices. *J. Phys. A Math. Theor.* **20,** L405 (1987).

[38] F. Gähler. *Crystallography of Dodecagonal Quasicrystals*. Proceedings of the ILL/CODEST Workshop. World Scientific Singapore (1988).

[39] M. Baake, R. Klitzing, and M. Schlottmann. Fractally Shaped Acceptance Domains of Quasiperiodic Square-Triangle Tilings with Dedecagonal Symmetry. *Physica A: Statistical Mechanics and its Applications* **191,** 554–558 (1992).

[40] M. Baake, D. Écija, and U. Grimm. A Guide to Lifting Aperiodic Structures. *Zeitschrift für Kristallographie - Crystalline Materials* **231,** (2016).

[41] M. Oxborrow and C. L. Henley. Random Square-Triangle Tilings: A Model for Twelvefold-Symmetric Quasicrystals. *Phys. Rev. B* **48,** 6966–6998 (1993).

[42] L.-G. Liao, W.-B. Zhang, T.-X. Yu, and Z.-X. Cao. A Single Cluster Covering for Dodecagonal Quasiperiodic Ship Tiling. *Chinese Physics Letters* **30,** 026102 (2013).

[43] S. Schenk, E. M. Zollner, O. Krahn, B. Schreck, R. Hammer, S. Förster, and W. Widdra. Full Real-Space Analysis of a Dodecagonal Quasicrystal. *Acta Cryst. A* **75,** 307–313 (2019).

[44] S. Förster, S. Schenk, E. M. Zollner, O. Krahn, C.-T. Chiang, F. O. Schumann, A. Bayat, K.-M. Schindler, M. Trautmann, R. Hammer, K. Meinel, W. A. Adeagbo, W. Hergert, J. I. Flege, J. Falta, M. Ellguth, C. Tusche, M. DeBoissieu, M. Muntwiler, T. Greber, and W. Widdra. Quasicrystals and Their Approximants in 2D Ternary Oxides. *Phys. Stat. Solidi B* **257,** 1900624 (2020).

[45] S. Förster and W Widdra. Ultrathin Perovskites: From Bulk Structures to New Interface Concepts in *Oxide Materials at the Two-Dimensional Limit*. Editor: Netzer, F P. and Fortunelli, A volume 234 pages 361–380. Springer International Publishing Cham (2016).

[46] E. M. Zollner, F. Schuster, K. Meinel, P. Stötzner, S. Schenk, B. Allner, S. Förster, and W. Widdra. Two-Dimensional Wetting Layer Structures of Reduced Ternary Oxides on Ru(0001) and Pt(111). *Phys. Stat. Solidi B* **257,** 1900655 (2020).

[47] F. E. Wührl, O. Krahn, S. Schenk, S. Förster, and W. Widdra. Antiphase Domain Boundary Formation in 2D Ba-Ti-O on Pd(111): An Alternative to Phase Separation. *Phys. Stat. Solidi B* **259,** 2100389 (2022).

[48] S. Förster, J. I. Flege, E. M. Zollner, F. O. Schumann, R. Hammer, A. Bayat, K.-M. Schindler, J. Falta, and W. Widdra. Growth and Decay of a Two-Dimensional Oxide Quasicrystal: High-temperature in Situ Microscopy. *Annalen der Physik* **529,** 1600250 (2017).

[49] S. J. Tauster, S. C. Fung, and R. L. Garten. Strong Metal-Support Interactions. Group 8 Noble Metals Supported on Ti02. *J. Am. Chem. Soc.* **100,** 6 ().

[50] S. Shaikhutdinov and H.-J. Freund. Ultrathin Oxide Films on Metal Supports: Structure-Reactivity Relations. *Ann. Rev. Phys. Chem.* **63,** 619–633 (2012).

[51] Z. Luo, G. Zhao, H. Pan, and W. Sun. Strong Metal–Support Interaction in Heterogeneous Catalysts. *Adv. Energy Mater* **,** 2201395 (2022).

[52] Sebastian Schenk, Oliver Krahn, Eric Cockayne, Holger L. Meyerheim, Marc de Boissieu, Stefan Förster, and Wolf Widdra. 2D Honeycomb Transformation into Dodecagonal Quasicrystals Driven by Electrostatic Forces. *Nat. Commun.* **13,**(1) 7542 (2022).

[53] E. M. Zollner, S. Schenk, M. Setvin, and S. Förster. Perfect Monolayers of the BaTiO3-derived 2D Oxide Quasicrystals Investigated by Scanning Tunneling Microscopy and Noncontact Atomic Force Microscopy. *Phys. Stat. Solidi B* **257,** 1900620 (2020).

[54] S. Förster, K. Meinel, K.-M. Schindler, and W. Widdra. Oxygen-Deficient Ordered Phases of Ultrathin BaTiO3 Films on Pt(111). *Surf. Interface Anal.* **44,** 628–634 (2012).

[55] S. Förster, M. Trautmann, S. Roy, W. A. Adeagbo, E. M. Zollner, R. Hammer, F. O. Schumann, K. Meinel, S. K. Nayak, K. Mohseni, W. Hergert, H. L. Meyerheim, and W. Widdra. Observation and Structure Determination of an Oxide Quasicrystal Approximant. *Phys. Rev. Lett.* **117,** 095501 (2016).

[56] M. Maniraj, L. V. Tran, O. Krahn, S. Schenk, W. Widdra, and S. Förster. Hexagonal Approximant of the Dodecagonal Oxide Quasicrystal on Pt(111). *Phys. Rev. Mater.* **5,** 084006 (2021).

[57] C. R. Merchan, T. Dorini, F. Brix, L. Pasquier, M. Jullien, D. Pierre, S. Andrieu, K. Dumesnil, S. Parapari, S. Šturm, J. Ledieu, M. Sicot, O. Copie, E. Gaudry, and V. Fournée. Two-Dimensional Square and Hexagonal Oxide Quasicrystal Approximants in SrTiO_3 Films Grown on Pt(111)/Al_2O_3 (0001). *Phys. Chem. Chem. Phys.* **24,** 7253–7263 (2022).

[58] F. E. Wührl. Strukturanalyse oxidischer Quasikristallapproximanten auf Palladium Pd(111). Dissertation, Martin-Luther-Universität Halle-Wittenberg Halle (Saale), Germany (2021).

[59] S. Roy, K. Mohseni, S. Förster, M. Trautmann, F. Schumann, E. Zollner, H. Meyerheim, and W. Widdra. The Kepler Tiling as the Oldest Complex Surface Structure in History: X-ray Structure Analysis of a Two-Dimensional Oxide Quasicrystal Approximant. *Z. Kristallogr. Cryst. Mater.* **231,** (2016).

[60] E. Cockayne, M. Mihalkovič, and C. L. Henley. Structure of Periodic Crystals and Quasicrystals in Ultrathin Films of Ba-Ti-O. *Phys. Rev. B* **93,** 020101 (2016).

[61] G. M. Sheldrick. Crystal Structure Refinement with SHELXL. *Acta Cryst. C* **71,** 3–8 (2015).

[62] A. J. Stone and D. J. Wales. Theoretical Studies of Icosahedral C60 and Some Related Species. *Chem. Phys. Lett.* **128,** 501–503 (1986).

[63] S. Wang, X. Hu, J. Goniakowski, C. Noguera, and M. R. Castell. Influence of the Support on Stabilizing Local Defects in Strained Monolayer Oxide Films. *Nanoscale* **11,** 2412–2422 (2019).

[64] F. Sedona, G. A. Rizzi, S. Agnoli, F. X. Llabrés i Xamena, A. Papageorgiou, D. Ostermann, M. Sambi, P. Finetti, K. Schierbaum, and G. Granozzi. Ultrathin TiO_x Films on Pt(111): A LEED, XPS, and STM Investigation. *J. Phys. Chem. B* **109,** 24411–24426 (2005).

[65] C. Wu, M. R. Castell, J. Goniakowski, and C. Noguera. Stoichiometry Engineering of Ternary Oxide Ultrathin Films: Ba_xTi_2O_3 on Au(111). *Phys. Rev. B* **91,** 155424 (2015).

[66] S. Surnev, L. Vitali, M. G. Ramsey, F. P. Netzer, G. Kresse, and J. Hafner. Growth and Structure of Ultrathin Vanadium Oxide Layers on Pd(111). *Phys. Rev. B* **61,** 13945–13954 (2000).

[67] C. Wu, M. S. J. Marshall, and M. R. Castell. Surface Structures of Ultrathin TiOx Films on Au(111). *J. of Phys. Chem. C* **115,** 8643–8652 (2011).

[68] B. Yang, W. E. Kaden, X. Yu, J. A. Boscoboinik, Y. Martynova, L. Lichtenstein, M. Heyde, M. Sterrer, R. Włodarczyk, M. Sierka, J. Sauer, S. Shaikhutdinov, and H.-J.m Freund. Thin Silica Films on Ru(0001): Monolayer, Bilayer and Three-Dimensional Networks of [SiO4] Tetrahedra. *Phys. Chem. Chem. Phys.* **14,** 11344–11351 (2012).

[69] S. Pomp, D. Kuhness, G. Barcaro, L. Sementa, V. Mankad, A. Fortunelli, M. Sterrer, F. P. Netzer, and S. Surnev. Two-Dimensional Iron Tungstate: A Ternary Oxide Layer With Honeycomb Geometry. *J. Phys. Chem. C* **120,** 7629–7638 (2016).

[70] S. Wang, J. Goniakowski, C. Noguera, and M. R. Castell. Atomic and Electronic Structure of an Epitaxial Nb_2O_3 Honeycomb Monolayer on Au(111). *Phys. Rev. B* **100,** 125408 (2019).

[71] J. Goniakowski and C. Noguera. Intrinsic Properties of Pure and Mixed Monolayer Oxides in the Honeycomb Structure: M_2O_3 and $MM'O_3$ (M, M' = Ti, V, Cr, Fe). *J. Phys. Chem. C* **123,** 7898–7910 (2019).

[72] A. Barcaro, G.and Fortunelli. 2D Oxides on Metal Materials: Concepts, Status, and Perspectives. *Phys. Chem. Chem. Phys.* **21,** 11510–11536 (2019).

[73] A. Hashmi, K. Nakanishi, M. U. Farooq, and T. Ono. Ising Ferromagnetism and Robust Half-Metallicity in Two-Dimensional Honeycomb-Kagome Cr2O3 Layer. *NPJ 2D Mater. Appl* **4,** 1–8 (2020).

[74] L. Lichtenstein, C. Büchner, B. Yang, S. Shaikhutdinov, M. Heyde, M. Sierka, R. Wlodarczyk, J. Sauer, and H.-J. Freund. The Atomic Structure of a Metal-Supported Vitreous Thin Silica Film. *Angew. Chem. Int. Ed.* **51,** 404–407 (2012).

[75] L. Lichtenstein, M. Heyde, and H.-J. Freund. Crystalline-Vitreous Interface in Two Dimensional Silica. *Phys. Rev. Lett.* **109,** 106101 (2012).

[76] L. Lichtenstein, M. Heyde, and H.-J. Freund. Atomic Arrangement in Two-Dimensional Silica: From Crystalline to Vitreous Structures. *J. Phys. Chem. C* **116,** 20426–20432 (2012).

[77] M. Heyde. Structure and Motion of a 2D Glass. *Science* **342,** 201–202 (2013).

[78] A. L. Lewandowski, S. Tosoni, L. Gura, Z. Yang, A. Fuhrich, M. J. Prieto, T. Schmidt, D. Usvyat, W.-D. Schneider, M. Heyde, G. Pacchioni, and H.-J. Freund. Growth and Atomic-Scale Characterization of Ultrathin Silica and Germania Films: The Crucial Role of the Metal Support. *Eur. J. Chem.* **27,** 1870–1885 (2021).

[79] O. Krahn. Topografie und elektronische Struktur des zweidimensionalen oxidischen Quasikristalls in Ba-Ti-O und des (48:18:6)-Approximanten in Sr-Ti-O auf Pt(111). Dissertation, Martin-Luther-Universität Halle-Wittenberg Halle (Saale), Germany (2022).

[80] C.-T. Chiang, M. Ellguth, F. O. Schumann, C. Tusche, R. Kraska, S. Förster, and W. Widdra. Electronic Band Structure of a Two-Dimensional Oxide Quasicrystal. *Phys. Rev. B* **100,** 125149 (2019).

[81] S. Doniach and M. Sunjic. Many-Electron Singularity in X-ray Photoemission and X-ray Line Spectra from Metals. *J. Phys. C Solid State Phys.* **3,** 285–291 (1970).

[82] E. M. Zollner, S. Schenk, S. Förster, and W. Widdra. C_{60} Adsorption on a Dodecagonal Oxide Quasicrystal. *Phys. Rev. B* **100,**(20) 205414 (2019).

[83] E. M. Zollner. Moleküladsorption auf einem oxidischen Quasikristall. Dissertation, Martin-Luther-Universität Halle-Wittenberg Halle (Saale), Germany (2020).

Lebenslauf

Persönliche Daten

Name	Dr. Stefan Förster
E-Mail	stefan.foerster@physik.uni-halle.de

Wissenschaftlicher Werdegang

Seit 01/2018	Leiter der Nachwuchsgruppe „Zweidimensionale oxidische Quasikristalle" am Institut für Physik der Martin-Luther-Universität Halle-Wittenberg
12/2016-01/2017	Elternzeit
Seit 04/2016	Habilitand in der Gruppe Oberflächen- und Grenzflächenphysik von Prof. W. Widdra an der Martin-Luther-Universität Halle-Wittenberg
10/2014-03/2016	P.R.I.M.E.-PostDoc-Stipendiat des DAAD in der Gruppe von Prof. J. Osterwalder und Prof. T. Greber an der Universität Zürich
06/2012-09/2012	Elternzeit
01/2012-09/2014	PostDoc in der Gruppe Oberflächen- und Grenzflächenphysik der Martin-Luther-Universität Halle-Wittenberg: „Aufbau einer UHV-kompatiblen Elektrospray-Depositionsanlage zur Abscheidung von Polymerketten auf idealen Oberflächen"
09/2008-12/2008	Elternzeit
05/2006-12/2011	Promotion „Wachstum und Struktur ultradünner, epitaktischer $BaTiO_3$-Schichten auf Platin-Substraten"
April 2006	Physikdiplom "Oberflächenuntersuchung zur Sulfatierung von ZrO2-Schichten auf Pt(111)"
2000-2006	Physikstudium an der Martin-Luther-Universität Halle-Wittenberg
1999	Abitur am Johann-Gottfried-Herder-Gymnasium Halle (Saale)

Dr. Stefan Förster

Halle (Saale), 15.08.2023

Eidesstattliche Erklärung

Hiermit erkläre ich, dass ich die vorliegende Habilitationsschrift

Quasicrystals in two-dimensional ternary oxides

selbständig und ohne fremde Hilfe verfasst, andere als die von mir angegebenen Quellen und Hilfs-

mittel nicht benutzt und die den benutzten Werken wörtlich oder inhaltlich entnommenen Stellen als

solche kenntlich gemacht habe.

Dr. Stefan Förster

Halle (Saale), 15.08.2023

Acknowledgements

My scientific journey over the past six years was accompanied by a number of people that have supported me in one way or another and to whom I'm very grateful.

In her capacity as spokes-person of the "Forschungschwerpunkt Nanostrukturierte Materialien" of the state Saxony-Anhalt I thank **Prof. Ingrid Mertig** for her effort in promoting young researchers. Her commitment allowed me to establish a junior research group entitled "Zweidimensionale oxidische Quasikristalle".

Prof. Wolf Widdra was so kind to host me and my small team in his surface science group at the Institute of Physics. Besides providing access to almost unlimited experimental possibilities he taught me lessons in academic administration and assisted me in my transformation from an inquisitive researcher towards a team leader. Most of all I thank him for sharing my passion for quasicrystals and motivating me to push my limits.

Numerous students have been attracted towards quasicrystal research throughout the years. I'm thankful to **Eva Maria Zollner**, **Sebastian Schenk**, **Oliver Krahn**, **Loi Vinh Tran**, **Martin Haller**, **Christoph Dresler**, **Bettina Allner**, **Jonas Pantzer**, **Philine Stötzner**, **Friederike Wührl**, **Maria Nitzsche** and **Rajesh Chirala** for making this small group a great and very successful team. You folks challenged me to excite you for the topic and to teach you in making the first steps before becoming independent. A great experience.

For broadening my mind with all kinds of inputs and creating a stimulating scientific environment I want to express my gratitude to **Dr. Cheng-Tien Chiang**, **Dr. Maximilian Palescheke**, **Dr. Karl-Michael Schindler**, **Prof. Maniraj Mahalingam** and all other members of the surface science group.

I would not have enjoyed my daily work so much without **Ralf Kulla**. I thank him for being a strong supporter and a good friend.

Last but not least, I thank **Kristin, Hugo, Agathe** and **Egon** for bringing me down to real life by showing to me how much waits to be explored beyond this scientific journey.